

---

2           **Consolidation and longevity of the CMS**  
3           **Resistive Plate Chamber system in view of the**  
4           **High-Luminosity LHC Upgrade**

---

5



Alexis Fagot

Thesis to obtain the degree of  
Doctor of Philosophy in Physics  
Academic year 2018-2019





<sup>7</sup>

<sup>8</sup> Promotors: Dr. Michael Tytgat  
Prof. Dr. Dirk Ryckbosch

<sup>9</sup>  
<sup>10</sup> Ghent University  
<sup>11</sup> Faculty of Sciences  
<sup>12</sup> Department of Physics and Astronomy  
<sup>13</sup> Proeftuinstraat 86, B-9000 Ghent, Belgium  
<sup>14</sup> Tel.: +32 9 264.65.28  
<sup>15</sup> Fax.: +32 9 264.66.97

<sup>16</sup>



Alexis Fagot

Thesis to obtain the degree of  
Doctor of Philosophy in Physics  
Academic year 2018-2019





17

## Acknowledgements

18

19

*XX/XX/2018*

*Alexis Fagot*



# Table of Contents

21	<b>Acknowledgements</b>	i
22	<b>Nederlandse samenvatting</b>	vii
23	<b>English summary</b>	ix
24	<b>1 Introduction</b>	1-1
25	<b>2 Investigating the TeV scale</b>	2-1
26	2.1 The Standard Model of Particle Physics . . . . .	2-1
27	2.1.1 A history of particle physics . . . . .	2-2
28	2.1.2 Construction and validation of the Standard Model . . . . .	2-14
29	2.1.3 Investigating the TeV scale . . . . .	2-15
30	2.2 The Large Hadron Collider & the Compact Muon Solenoid . . . . .	2-20
31	2.2.1 LHC, the most powerful particle accelerator . . . . .	2-20
32	2.2.2 Timeline of operation . . . . .	2-23
33	2.2.3 High Luminosity LHC . . . . .	2-25
34	2.2.4 The Compact Muon Solenoid experiment . . . . .	2-25
35	2.2.4.1 The silicon tracker . . . . .	2-27
36	2.2.4.2 The calorimeters . . . . .	2-27
37	2.2.4.3 The muon system . . . . .	2-28
38	<b>3 Muon Phase-2 Upgrade</b>	3-1
39	3.1 Motivations for HL-LHC and the upgrade of CMS . . . . .	3-1
40	3.2 Description of the muon system . . . . .	3-5
41	3.2.1 The Drift Tubes . . . . .	3-5
42	3.2.2 The Cathode Strip Chambers . . . . .	3-6
43	3.2.3 The Resistive Plate Chambers . . . . .	3-7
44	3.3 Necessity for improved electronics . . . . .	3-8
45	3.4 New detectors and increased acceptance . . . . .	3-10
46	3.4.1 Gas electron multipliers . . . . .	3-12
47	3.4.2 Improved forward resistive plate chambers . . . . .	3-15
48	3.5 Impact on Level-1 Trigger and physics performance . . . . .	3-17
49	3.6 Ecofriendly gas studies . . . . .	3-20
50	<b>4 Physics of Resistive plate chambers</b>	4-1
51	4.1 Principle . . . . .	4-1
52	4.2 Rate capability and time resolution of Resistive Plate Chambers . . . . .	4-3
53	4.2.1 Operation modes . . . . .	4-3
54	4.2.2 Standard gas mixture for RPCs operated in collider experiments . . . . .	4-5
55	4.2.3 Detector designs and performance . . . . .	4-9

---

56	4.2.3.1	Double-gap RPC . . . . .	4-12
57	4.2.3.2	Multigap RPC (MRPC) . . . . .	4-13
58	4.2.3.3	Charge distribution and performance limitations . . . . .	4-17
59	4.3	Signal formation . . . . .	4-19
60	4.3.1	Energy loss at intermediate energies . . . . .	4-20
61	4.3.2	Primary ionization . . . . .	4-24
62	4.3.3	Development and propagation of avalanches . . . . .	4-28
63	4.3.4	Drift and diffusion of the electron cloud . . . . .	4-32
64	4.3.5	Space charge effect & streamers . . . . .	4-34
65	4.4	Effect of atmospherical conditions on the detector's performance . . . . .	4-38
66	<b>5</b>	<b>Longevity studies and Consolidation of the present CMS RPC subsystem</b>	<b>5-1</b>
67	5.1	Testing detectors under extreme conditions . . . . .	5-2
68	5.1.1	GIF . . . . .	5-4
69	5.1.2	GIF++ . . . . .	5-5
70	5.2	Preliminary studies at GIF . . . . .	5-7
71	5.2.1	RPC test setup . . . . .	5-7
72	5.2.2	Geometrical acceptance of the setup layout to cosmic muons . . . . .	5-9
73	5.2.2.1	Description of the simulation layout . . . . .	5-10
74	5.2.2.2	Simulation procedure . . . . .	5-11
75	5.2.2.3	Results and limitations . . . . .	5-12
76	5.2.3	Photon flux at GIF . . . . .	5-14
77	5.2.4	Results and discussions . . . . .	5-17
78	5.3	Longevity tests at GIF++ . . . . .	5-20
79	5.3.1	Selection and characterization of CMS RPCs for longevity at GIF++ . . . . .	5-20
80	5.3.2	RPC test setup . . . . .	5-22
81	5.3.3	GIF++ data flow . . . . .	5-24
82	5.3.4	Measurements performed during beam periods . . . . .	5-26
83	5.3.4.1	Efficiency scans . . . . .	5-26
84	5.3.4.2	Rate scans . . . . .	5-26
85	5.3.4.3	Offline analysis and Data Quality Monitoring . . . . .	5-27
86	5.3.5	Measurements performed during irradiation periods . . . . .	5-28
87	5.3.5.1	Longevity scans . . . . .	5-29
88	5.3.5.2	Daily rate monitoring scans . . . . .	5-30
89	5.3.5.3	Weekly noise monitoring scans . . . . .	5-31
90	5.3.5.4	Weekly source scans . . . . .	5-31
91	5.3.5.5	Weekly current scans . . . . .	5-32
92	5.3.5.6	Resistivity measurements . . . . .	5-32
93	5.3.6	Results and discussions . . . . .	5-32
94	<b>6</b>	<b>Improved RPC investigation and preliminary electronics studies</b>	<b>6-1</b>
95	6.1	FEE candidates for the production of iRPCs . . . . .	6-1
96	6.1.1	CMS RPCROC: the RPC upgrade baseline . . . . .	6-2
97	6.1.2	INFN Front-End Electronics: a robust back-up solution . . . . .	6-3
98	6.2	Preliminary tests at CERN . . . . .	6-3
99	6.2.1	INFN preamplifiers . . . . .	6-3
100	6.2.2	INFN preamplifiers mounted onto CMS Front-End Board . . . . .	6-7
101	6.2.3	HARDROC 2 readout panel . . . . .	6-18

---

102	<b>7 Conclusions and outlooks</b>	<b>7-1</b>
103	7.1 Conclusions . . . . .	7-1
104	7.2 Outlooks . . . . .	7-1
105	<b>A A data acquisition software for CAEN VME TDCs</b>	<b>A-1</b>
106	A.1 GIF++ DAQ file tree . . . . .	A-1
107	A.2 Usage of the DAQ . . . . .	A-2
108	A.3 Description of the readout setup . . . . .	A-3
109	A.4 Data read-out . . . . .	A-3
110	A.4.1 V1190A TDCs . . . . .	A-4
111	A.4.2 DataReader . . . . .	A-7
112	A.4.3 Data quality flag . . . . .	A-10
113	A.5 Communications . . . . .	A-12
114	A.5.1 V1718 USB Bridge . . . . .	A-13
115	A.5.2 Configuration file . . . . .	A-14
116	A.5.3 WebDCS/DAQ intercommunication . . . . .	A-17
117	A.5.4 Example of inter-process communication cycle . . . . .	A-17
118	A.6 Software export . . . . .	A-18
119	<b>B Details on the offline analysis package</b>	<b>B-1</b>
120	B.1 GIF++ Offline Analysis file tree . . . . .	B-1
121	B.2 Usage of the Offline Analysis . . . . .	B-2
122	B.2.1 Output of the offline tool . . . . .	B-3
123	B.2.1.1 ROOT file . . . . .	B-3
124	B.2.1.2 CSV files . . . . .	B-5
125	B.3 Analysis inputs and information handling . . . . .	B-6
126	B.3.1 Dimensions file and IniFile parser . . . . .	B-7
127	B.3.2 TDC to RPC link file and Mapping . . . . .	B-8
128	B.4 Description of GIF++ setup within the Offline Analysis tool . . . . .	B-9
129	B.4.1 RPC objects . . . . .	B-9
130	B.4.2 Trolley objects . . . . .	B-10
131	B.4.3 Infrastructure object . . . . .	B-10
132	B.5 Handeling of data . . . . .	B-12
133	B.5.1 RPC hits . . . . .	B-13
134	B.5.2 Clusters of hits . . . . .	B-14
135	B.6 DAQ data Analysis . . . . .	B-15
136	B.6.1 Determination of the run type . . . . .	B-16
137	B.6.2 Beam time window calculation for efficiency runs . . . . .	B-17
138	B.6.3 Data loop and histogram filling . . . . .	B-18
139	B.6.4 Results calculation . . . . .	B-21
140	B.6.4.1 Rate normalisation . . . . .	B-21
141	B.6.4.2 Rate and activity . . . . .	B-23
142	B.6.4.3 Correction of muon performance parameters . . . . .	B-25
143	B.6.4.4 Strip masking tool . . . . .	B-27
144	B.6.4.5 Output CSV files filling . . . . .	B-29
145	B.7 Current information extraction . . . . .	B-31



146

## Nederlandse samenvatting –Dutch Summary–

147



## English summary



# List of Figures

149

- |     |      |   |      |
|-----|------|---|------|
| 150 | 2.1  | Solar spectrum with spectral lines as it visually appeared to Fraunhofer. . . . .   | 2-2  |
| 151 | 2.2  | Through the gold foil experiment, Rutherford could show that most of the mass of atoms was contained in a positively charged nucleus and could then propose a more accurate atomic model than that of Thomson. . . . .  | 2-3  |
| 152 |      |   |      |
| 153 |      |   |      |
| 154 | 2.3  | Figure 2.3a: The orbits in which the electron may travel according to the Bohr model of the hydrogen atom. An electron jumps between orbits and is accompanied by an emitted or absorbed amount of electromagnetic energy ( $h\nu$ ). The orbits radius increases as $n^2$ . Figure 2.3b: Elliptical orbits with the same energy and quantized angular momentum $l = 0, 1, \dots, n - 1$ in the case $n = 5$ . Figure 2.3c: Illustration of quantum mechanical orbital angular momentum. The cones and plane represent possible orientations of the angular momentum vector for $l = 2$ and $m = -2, -1, 0, 1, 2$ . . . . . | 2-5  |
| 155 |      |   |      |
| 156 |      |   |      |
| 157 |      |   |      |
| 158 |      |   |      |
| 159 |      |   |      |
| 160 |      |   |      |
| 161 | 2.4  | Figure 2.4a: The spectral lines of mercury vapor lamp anomalous Zeeman effect without magnetic field (A) and with magnetic field (B - transverse Zeeman effect & C - longitudinal Zeeman effect). Figure 2.4b: Stern-Gerlach experiment: Silver atoms traveling through an inhomogeneous magnetic field and being deflected up or down depending on their spin. . . . .   | 2-6  |
| 162 |      |   |      |
| 163 |      |   |      |
| 164 |      |   |      |
| 165 |      |   |      |
| 166 | 2.5  | Figure 2.5a: decay of a $\mu$ -meson in an emulsion. Figure 2.5b: track of a $\pi$ -meson in an emulsion signed by Lattes, Powell, and Occhialini. . . . .  | 2-8  |
| 167 |      |   |      |
| 168 | 2.6  | Figure 2.6a: Meson octet. Figure 2.6b: Baryon octet. Figure 2.6c: Baryon decuplet. . . . .  | 2-9  |
| 169 | 2.7  | Discovery of the $J/\Psi$ by both SPEAR (SLAC [74]) in Figure 2.7a and AGS (BNL [75]) in Figure 2.7b. In Figure 2.7a, the cross section versus energy is showed for (a) multi hadron final states, (b) $e^+e^-$ final states, and (c) $\mu^+\mu^-$ , $\pi^+\pi^-$ and $K^+K^-$ final states. . . . .  | 2-10 |
| 170 |      |   |      |
| 171 |      |   |      |
| 172 | 2.8  | Figure 2.8a: the color field of QCD only allows for "white" baryons, particles composed of quarks, to exist. Examples are given for mesons, composed of a quark and its anti-quark, and hadrons, composed of three differently colored quarks or anti-quarks. Other exotic baryons have been predicted and observed, such as tetraquarks and pentaquarks. Figure 2.8b: a crossed analysis performed thanks to the data collected by various experiments at different energies have showed that the coupling constant evolves as predicted by the mechanism of asymptotic freedom [87]. . . . .                              | 2-11 |
| 173 |      |   |      |
| 174 |      |   |      |
| 175 |      |   |      |
| 176 |      |   |      |
| 177 |      |   |      |
| 178 |      |   |      |
| 179 | 2.9  | Energy spectrum of beta particles emitted by a source of $^{210}Bi$ . . . . .   | 2-12 |
| 180 | 2.10 | As explained through Figure 2.10a, the Wu experiment consisted in measuring the preferred direction of emission of beta rays of a Cobalt source placed in a stable magnetic field aligned, in one case, and anti-aligned, in the other case, with the nuclear spin. The result of Figure 2.10b showed a violation of parity. . . . .  | 2-13 |
| 181 |      |   |      |
| 182 |      |   |      |
| 183 |      |   |      |

184	2.11	The elementary particles of the Standard Model are shown along with their properties. Their interactions with the strong, weak and electromagnetic forces have been made explicit using color squares. In the left column, the scalar Higgs boson is depicted. The center is focused on the matter particles, the fermions, and the right column on the force carriers, the gauge bosons. The role of the Higgs boson in electroweak symmetry breaking is highlighted, and the corresponding way properties of the various particles differ in the (high-energy) symmetric phase (top) and the (low-energy) broken-symmetry phase (bottom) are shown. . . . .	2-15
185			
186			
187			
188			
189			
190			
191			
192	2.12	Figure 2.12a: Total proton-proton cross-section as a function of the collisions center-of-mass energy $\sqrt{s}$ [116] with cosmic-ray data from Akeno Observatory and Fly's Eye Collaboration. Figure 2.12b: Total proton-(anti)proton and interaction channel cross-sections in the TeV scale. . . . .	2-16
193			
194			
195			
196	2.13	Rotation curve (points) of the galaxy M33 compared with best fitting model (line). The short-dashed line represents the rotation profile that would be expected from the observation of the stellar disc alone [128]. . . . .	2-17
197			
198			
199	2.14	Cosmic Microwave Background as measured by the space observatory Planck which mean temperature is $T_\gamma = (2.7255 \pm 0.0006)\text{K}$ with anisotropies of the order of a few $\mu\text{K}$ . . . . .	2-18
200			
201			
202	2.15	CERN accelerator complex. . . . .	2-20
203	2.16	Pictures of the different accelerators. From top to bottom: first the LINAC 2 and the $Pb$ source of LINAC 3. Then the Booster and the LEIR. Finally, the PS, the SPS and the LHC. . . . .	2-21
204			
205			
206	2.17	Figure 2.17a: schematics of the LHC cryodipoles. 1: Superconducting Coils, 2: Beam pipe, 3: Heat exchanger Pipe, 4: Helium-II Vessel, 5: Superconducting Bus-bar, 6: Iron Yoke, 7: Non-Magnetic Collars, 8: Vacuum Vessel, 9: Radiation Screen, 10: Thermal Shield, 11: Auxiliary Bus-bar Tube, 12: Instrumentation Feed Throughs, 13: Protection Diode, 14: Quadrupole Bus-bars, 15: Spool Piece Bus-bars. Figure 2.17b: magnetic field and resulting motion force applied on the beam particles. . . . .	2-22
207			
208			
209			
210			
211			
212			
213	2.18	The LHC quadrupoles (Figure 2.18a) showed together with the magnetic fields and resulting focussing force applied on the beam by two consecutive quadrupoles (Figure 2.18b). . . . .	2-23
214			
215			
216	2.19	Distribution of the four-lepton invariant mass for the $ZZ \rightarrow 4l$ analysis as presented by both ATLAS [112] and CMS [113] in 2012. . . . .	2-23
217			
218	2.20	Detailed timeline projection of LHC and HL-LHC operation until 2039 showing the evolution of the instantaneous and integrated luminosity as designed (Figure 2.20a) and in the ultimate case where the instantaneous luminosity is increased to $7.5 \times 10^{34}\text{cm}^{-2}\text{s}^{-1}$ thanks to a new increase of instantaneous luminosity during Run 5 (Figure 2.20b) [175–177]. . . . .	2-24
219			
220			
221			
222			
223	2.21	Picture of the CMS barrel. The red outer layer is the muon system hosted into the red iron return yokes. The calorimeters are the blue cylinder inside in magnet solenoid and the tracker is the inner yellow cylinder built around the beam pipe. . . . .	2-26
224			
225			
226	2.22	View of the CMS apparatus and of its different components. . . . .	2-26
227	2.23	Slice showing CMS sub-detectors and how particles interact with them. . . . .	2-27
228	2.24	The CMS tracker. . . . .	2-27
229	2.25	Figure 2.25a: The electromagnetic calorimeter. Figure 2.25b: The lead tungstate crystals composing the ECAL. . . . .	2-28
230			
231	2.26	The CMS hadron calorimeter barrel. . . . .	2-28

232	2.27	A quadrant of the muon system, showing DTs (yellow), RPCs (blue), and CSCs (green). . . . .	2-29
233			
234	3.1	The measured transit time of an HSCP in CMS is compared to the transit time of a particle traveling at near the speed of light [177]. . . . .	3-2
235			
236	3.2	Slice of the CMS detector showing examples of passage of SM particles and R-hadrons. On the one hand, lepton-like HSCPs will appear to behave like slow and heavy muons. On the other hand, R-hadrons are likely to convert into other kind of charged or neutral R-hadrons due to interactions inside the detector volume. . . . .	3-2
237			
238	3.3	Distribution of the energy-loss $dE/dx$ as described by Bethe-Bloch formula through the estimator $I_h$ with increasing particle momentum for tracks in the 13 TeV data. The estimator depends on the charge deposition of the particles per unit length in the silicon detectors of CMS which is related to their energy loss as explained in a publication by the CMS Collaboration [181]. The simulated HSCPs are singly or multiply charged particles with masses of 400 and 1000 GeV. . . . .	3-3
239			
240	3.4	Distribution of the average number of interactions per crossing (pileup) for pp-collisions in 2011 (red), 2012 (blue), 2015 (purple), 2016 (orange), 2017 (light blue), and 2018 (navy blue). The overall mean values and the minimum bias cross sections are also shown [189]. . . . .	3-4
241			
242	3.5	Absorbed dose in the CMS Cavern after an integrated luminosity of $3000 \text{ fb}^{-1}$ . Using the interaction point as reference, R is the transverse distance from the beamline and Z is the distance along the beamline [177]. . . . .	3-4
243			
244	3.6	Figure 3.6a: Barrel wheel with its detector rings and return yokes. Figure 3.6b: CSC endcap disk with the two CSC stations. The outer station is made of 10 deg detectors while the inner station is made of 20 deg detectors. Figure 3.6c: RPC endcap disk. The inner station is not equipped, leaving the inner CSC station visible. . . . .	3-5
245			
246	3.7	Figure 3.7a: Cross section of a DT module showing the two superlayers measuring the $\phi$ coordinate, perpendicular to the cross section plane, and the superlayer measuring the $\eta$ coordinate, placed in between the two others with a honeycomb plate and parallel to the cross section plane. The DT detector is sandwiched in between 2 RPCs whose readout strips are perpendicular to the cross section plane, measuring the $\phi$ coordinate. Figure 3.7b: A DT cell is shown together with its electric field. The path of a muon through a superlayer is shown. . . . .	3-6
247			
248	3.8	Figure 3.8a: Cathode strips and anode wire layout of a CSC panel. Figure 3.8b: Avalanche development and charge collection by anode wires and induction on cathode strips inside of a CSC panel. . . . .	3-7
249			
250	3.9	Muon track reconstruction through the six panels of a CMS CSC using the information of anode wire groups and cathode strip charge distribution combined with comparator bits to decide on which half strip the muon is more likely to have passed. . . . .	3-7
251			
252	3.10	Double-gap layout of CMS RPCs. Muons passing through the gas volumes will create electron-ions pairs by ionising the gas. This ionisation will immediately translate into a developing avalanche. . . . .	3-8
253			
254	3.11	Extrapolated fraction of failing channels of the present DT MiC1 electronics as a function of the integrated luminosity for different scenarios until LS4 [177]. . . . .	3-8
255			
256	3.12	The event loss fractions as a function of the instantaneous luminosity is compared for CFEBs (Phase-1) and DCFEBs (Phase-2) at different CSC locations. HL-LHC luminosity is marked with the dashed brown line [177]. . . . .	3-9
257			
258	3.13	Comparison of the simulated time residuals in between reconstructed and true muon times without (blue) and with (red) the upgraded RPC link system [177]. . . . .	3-9
259			



328	3.24	Measured average charge per avalanche as a function of the effective electric field for different gas gap thickness in double-gap RPCs using HPL electrodes [177]. . . . .	3-17
329	3.25	Level-1 Trigger data flow during Phase-2 operations [177]. . . . .	3-17
330	3.26	Efficiency of the L1 trigger in the endcap region after Phase-2 upgrade in the case CSC/GEM/RPC hits are requested in at least two stations out of four (3.26a) and in all four stations (3.26b) [177]. . . . .	3-18
331	3.27	Comparison of L1 trigger performances for prompt muons with and without the ad- dition of GEMs in the region $2.1 <  \eta  < 2.4$ at Phase-2 conditions [177]. GEMs would allow a reduction of the trigger accept rate by an order of magnitude (Fig- ure 3.27a) while increasing the trigger efficiency (Figure 3.27b). . . . .	3-19
332	3.28	The angular resolution on reconstructed muon tracks in the GEM overlap region $2.0 <  \eta  < 2.15$ is compared for Phase-2 conditions in the case CSC are alone (Figure 3.28a) and in the case the GEMs' data, including ME0, is combined to which of CSCs (Figure 3.28b) [177]. . . . .	3-19
333	3.29	Resolution of the LCT ambiguous events thanks to the combination of CSC and iRPC readout data. Using CSCs only, two pairs of hits are possible [177]. . . . .	3-20
334	3.30	Efficiency (Figure 3.30a [202]) and cluster size (Figure 3.30b) of a standard double- gap RPC operated with $CO_2$ mixtures for different ratios of $SF_6$ . . . . .	3-21
335	3.31	Efficiency of a CMS double-gap RPC operated with 30% of $HFO$ , 4.5% of $iC_4H_{10}$ , 1% of $SF_6$ and 64.5% of $CO_2$ [202]. . . . .	3-21
336	3.32	The efficiency (solid lines) and streamer probability (dashed lines) of $HFO/CO_2$ (Figure 3.32a) and $CF_3I/CO_2$ (Figure 3.32b) based gas mixtures as a function of the effective high-voltage are compared with the present CMS RPC gas mixture represented in black [177, 202]. The detector used for the study is a single-gap RPC with similar properties than CMS RPCs. The streamer probability is defined as the proportion of events with a deposited charge greater than 20 pC. . . . .	3-22
337	3.33	Efficiency (open symbols) and cluster size (full symbols) of an iRPC as a function of the effective voltage for the standard CMS gas mixture and an environmental- friendly gas mixture [177]. . . . .	3-22
357	4.1	Different phases of the avalanche development in the RPC gas volume subjected to a constant electric field $E_0$ . a) An avalanche is initiated by the primary ionisation caused by the passage of a charged particle through the gas volume. b) Due to its growing size, the avalanche starts to locally influence the electric field. c) The electrons, lighter than the cations reach the anode first. d) The ions reach the cathode. While the charges have not recombined, the electric field in the small region around the avalanche stays affected and locally blinds the detector. . . . .	4-2
358	4.2	Movement of the charge carriers in an RPC. Figure 4.2a: Voltage across an RPC whose electrodes have a relative permittivity of 5 at the moment the tension is ap- plied. Figure 4.2b: After the charge carriers moved, the electrodes are charged and there is no voltage drop over the electrodes anymore. The full potential is applied on the gas gap only. Figure 4.2c: The streamer discharge initiated by a charged particle transports electrons and cations towards the anode and cathode respectively. . . . .	4-4
359	4.3	Typical oscilloscope pulses in streamer mode (Figure 4.3a) and avalanche mode(Figure 4.3b). In the case of streamer mode, the very small avalanche signal is visible. . . . .	4-4
360	4.4	Rate capability comparison for the streamer and avalanche mode of operation. An order of magnitude in rate capability for a maximal efficiency drop of 10% is gained by using the avalanche mode over the streamer mode. . . . .	4-5

- 375        4.5 Comparison of the charge distribution of signals induced by cosmic muons in an  
376            RPC operated with a gas mixture of argon, butane and bromotrifluoromethane ( $CF_3Br$ ).  
377            The  $Ar/C_4H_{10}$  is kept constant at 60/40 in volume while the total amount of  $CF_3Br$   
378            in the mixture is varied: 0% (Figure 4.5a), 4% (Figure 4.5b) and 8% (Figure 4.5c) [209]. . . . . 4-6
- 379        4.6 Comparison of the efficiency and streamer probability, defined as the fraction of  
380            events with an induced charge 10 times larger than that of the average avalanche,  
381            with and without irradiation by a 24 GBq  $^{137}Cs$  source of an RPC successively  
382            operated with a 90/10 mixture  $C_2H_2F_4/i-C_4H_{10}$  (Figure 4.6a) and a 70/5/10/15  
383            mixture of  $Ar/i-C_4H_{10}/CO_2/C_2H_2F_4$  (Figure 4.6b) [210]. . . . . 4-6
- 384        4.7 Comparison of the fast charge ratio with and without irradiation by a 24 GBq  $^{137}Cs$   
385            source of an RPC successively operated with a 90/10 mixture  $C_2H_2F_4/i-C_4H_{10}$   
386            (Figure 4.7a) and a 70/5/10/15 mixture of  $Ar/i-C_4H_{10}/CO_2/C_2H_2F_4$  (Figure 4.7b).  
387            The results are provided for both single-gap and double-gap operation [210]. . . . . 4-7
- 388        4.8 Efficiency (circles and stars with 30 mV and 100 mV thresholds respectively) and  
389            streamer probability (opened circles) as function of the operating voltage of a 2 mm  
390            single-gap HPL RPC flushed with a gas mixture containing (a) 5%, (b) 2%, (c) 1%  
391            and (d) no  $SF_6$  [212]. . . . . 4-8
- 392        4.9 Evolution of the efficiency, working voltage, and voltage at 50% of maximum ef-  
393            ficiency for CMS Barrel (Figure 4.9a) and Endcap (Figure 4.9b) RPCs obtained  
394            through yearly voltage scans since 2011. The working voltage of each RPC is up-  
395            dated after each voltage scan to ensure optimal operation [227]. . . . . 4-9
- 396        4.10 Comparison of the rate capability of 8 mm and 2 mm wide RPCs. The lines are  
397            linear fits on the data [229]. . . . . 4-10
- 398        4.11 Distributions of the induced charge of fast signals on 2 mm (Figure 4.11a) and 8 mm  
399            (Figure 4.11b) RPCs exposed to a radiation rate of 100 Hz/cm<sup>2</sup>. Average induced  
400            charge of fast signals as a function of the high voltage applied on 2 mm and 8 mm  
401            RPCs (Figure 4.11c). In the case of the 2 mm RPC, a saturation of the pre-amplifier  
402            was observed. The average of the distribution is underestimated, and the median is  
403            showed together with the average to account for this bias [229]. . . . . 4-11
- 404        4.12 Time distributions of the leading, trailing, and average of both leading and trailing  
405            edges for 2 mm (top row) and 8 mm (bottom row) RPCs exposed to a 100 Hz/cm<sup>2</sup>  
406            radiation rate. The data was collected with RPCs operated at the voltage correspond-  
407            ing to the knee of the efficiency distribution, defined as the point where 95% of the  
408            maximum efficiency is obtained [229]. . . . . 4-12
- 409        4.13 Possible double-gap RPC layouts: a) "standard" 1D double-gap RPC, as used in  
410            CMS experiment, where the anodes are facing each other and a 1D read-out plane  
411            is sandwiched in between them, b) double read-out double-gap RPC as used in AT-  
412            LAS experiment, where the cathodes are facing each other and 2 read-out planes  
413            are used on the outer surfaces. This last layout can offer the possibility to use a 2D  
414            reconstruction by using orthogonal read-out planes. . . . . 4-13
- 415        4.14 Comparison of performance of CMS double and single-gap RPCs using cosmic  
416            muons [225]. Figure 4.14a: Comparison of efficiency sigmoid. Figure 4.14b: Volt-  
417            age distribution at 95% of maximum efficiency. Figure 4.14c:  $\Delta_{10\%}^{90\%}$  distribution. . . . . 4-13
- 418        4.15 Representation of different RPC layouts (wide gap on Figure (a), double-gap on  
419            Figure (b) and multigap on Figure (c)), of the corresponding sensitive volume in  
420            gray, and of the associated avalanche size [215]. . . . . 4-14

421	4.16 Time distributions of the leading, trailing, and average of both leading and trailing edges for multigap RPCs consisting in two 4 mm (Figure 4.16a) and four 2 mm (Figure 4.16b) exposed to a 100 Hz/cm <sup>2</sup> radiation rate. The data was collected with RPCs operated at the voltage corresponding to the knee of the efficiency distribution, defined as the point where 95% of the maximum efficiency is obtained [215]. . . . .	4-15
422		
423		
424		
425		
426	4.17 Presentation of a study of a possible ALICE MRPC cell using 250 µm gas gaps, 620 µm outer glass electrodes, and 550 µm inner floating electrodes (Figure 4.17a), and of its time resolution performance as a function of the applied high voltage for different radiation levels referred through different filter settings of the 740 GBq <sup>137</sup> Cs source the former CERN GIF facility [230]. . . . .	4-15
427		
428		
429		
430		
431	4.18 Particle identification applied to electrons in the STAR experiment. The identification is performed combining ToF and $dE/dx$ measurements [235]. . . . .	4-16
432		
433	4.19 Comparison of the detector performance of ALICE ToF MRPC [236] at fixed applied voltage (in blue) and at fixed effective voltage (in red). The effective voltage is kept fixed by increasing the applied voltage accordingly to the current drawn by the detector.	4-17
434		
435		
436	4.20 Ratio between total induced and drifting charge have been simulated for single-gap, double-gap and multigap layouts [237]. The total induced charge for a double-gap RPC is a factor 2 higher than for a multigap. . . . .	4-18
437		
438		
439	4.21 Charge spectra have been simulated for single-gap, double-gap and multigap layouts [237]. It appears that when single-gap shows a decreasing spectrum, double and multigap layouts exhibit a spectrum whose peak is detached from the origin. The detachment gets stronger as the number of gaps increases. . . . .	4-18
440		
441		
442		
443	4.22 The maximal theoretical efficiency is simulated for single-gap, double-gap and multi-gap layouts [237] at a constant gap thickness of 2 mm and using an effective Townsend coefficient of 9 mm <sup>-1</sup> . . . . .	4-19
444		
445		
446	4.23 Mass stopping power as a function of $\beta\gamma = p/Mc$ for positive muons in copper [115]. The total stopping power is indicated with a solid line and local components with dashed lines. The vertical bands are used to indicate boundaries between different approximations used at different energy range. . . . .	4-19
447		
448		
449		
450	4.24 Mean mass stopping power for liquid hydrogen, as used in bubble chambers, gaseous helium, carbon, aluminum, iron, tin, and lead without the inclusion of radiative effect at higher $\beta\gamma$ necessary for pions and muons in denser materials [115]. . . . .	4-21
451		
452		
453	4.25 Mean excitation energies normalized to the atomic number as adopted by the ICRU [115, 241, 242]. . . . .	4-22
454		
455	4.26 Mean mass stopping power at minimum ionization as a function of the atomic number [115]. . . . .	4-22
456		
457	4.27 Example of straggling function $f(\Delta)$ of particles passing through 1.2 cm of Argon gas with a $\beta\gamma$ of 3.6 and represented with a solid line. The original Landau distribution is showed with a dashed line [243]. . . . .	4-23
458		
459		
460	4.28 Evolution of straggling functions $f(\Delta)$ of particles passing through a volume of Argon gas with a $\beta\gamma$ of 3.6 with increasing thickness $x$ [243]. . . . .	4-23
461		
462	4.29 Photoabsorption cross section as computed by HEED for nobles gases with different electric shell numbers [239]. . . . .	4-25
463		
464	4.30 Photoabsorption cross section as computed by HEED for typical RPC gas mixtures [239]. The RPC mixture with CO <sub>2</sub> corresponds to the mixture used by CALICE SD-HCAL [247] while the other one was foreseen for the experiment ATLAS [248] but has been changed since then. . . . .	4-26
465		
466		
467		

468	4.31 Distributions of number of electrons (left) and energy loss (right) for a 5 GeV/c muon passing through 1.2 mm of Helium (Figure 4.31a), Argon (Figure 4.31b) or a typical RPC gas mixture (Figure 4.31c) [239]. . . . .	4-27
471	4.32 Figure 4.32a: Mean cluster density for muons through different gas volumes [239]. Figure 4.32b: Distribution of the number of electrons per cluster for a 5 GeV/c muon traveling through a mixture of 96.7% $C_2H_2F_4$ , 3% i- $C_4H_{10}$ and 0.3% $SF_6$ [239, 248]. . . . .	4-28
475	4.33 Townsend and attachment coefficient for a typical 96.7/3/0.3 mixture of $C_2H_2F_4$ /i- $C_4H_{10}$ / $SF_6$ , at a temperature $T = 296.15$ K and a pressure $P = 1013$ hPa [239, 248]. . . . .	4-29
478	4.34 Comparison of the distribution law of Furry and the Poisson law for $\bar{n} = 5$ [251]. . . . .	4-29
479	4.35 Single-electron avalanche size distribution in a proportional counter filled with methanol at different $E/p$ values. (a) 70, (b) 76.5, (c) 105, (d) 186.5, (e) 426V/cm torr [252].	4-30
481	4.36 Figure 4.36a: Comparison of avalanche size distributions for different values of Townsend and attachment coefficients. The effective Townsend coefficient is the same for both distributions. Figure 4.36b: Fluctuation in avalanches size for avalanche started by a single electron with $\alpha = 13 \text{ mm}^{-1}$ and $\eta = 3.5 \text{ mm}^{-1}$ [248]. . . . .	4-32
485	4.37 Figure 4.37a: Electrons mean drift velocity $v_D$ in pure $C_2H_2F_4$ and typical RPC gas mixtures. Figure 4.37b: Transverse diffusion coefficient in pure $C_2H_2F_4$ and a typical RPC gas mixture. Figure 4.37c: Longitudinal diffusion coefficient in pure $C_2H_2F_4$ and a typical RPC gas mixture. All results are given with a pressure $P = 760$ Torr and a temperature $T = 296.15$ K [239]. . . . .	4-33
490	4.38 Comparison of the free charge carriers in the gas after a time $t = 7.90$ ns in the case where no diffusion is taken into account to simulate the avalanche (Figure 4.38a) and in the case where the diffusion is implemented (Figure 4.38b) [239]. . . . .	4-33
493	4.39 Schematic representation of an avalanche and of the electric field deformation it causes due to the local concentration of charge carriers [221]. . . . .	4-35
495	4.40 Evolution of the charge induced by an avalanche started by a single electron in a 1.2 mm thick RPC with an applied electric field of 54 kV/cm in the case space charge is not taken into account (Figure 4.40a) and in the case it is implemented into the simulation (Figure 4.40b). The total induced charge is correlated to the size of the avalanche [239]. . . . .	4-36
500	4.41 Distributions of charge carriers within the gas volume of a 1.2 mm thick RPC and the corresponding deformation of the electric field at different time steps with an applied electric field of 55.5 kV/cm [239]. . . . .	4-37
503	4.42 Representation of the weighting field in the volume of an RPC and the resulting induced current in the strip placed at 1 V and its neighbour connected to the ground. The induced current corresponds, as can be understood from Formula 4.22 [221]. . . . .	4-38
506	4.43 Schematics of CMS RPC FEE logic. . . . .	4-39
507	4.44 Equivalence in between the charge of the induced signal in input of the CMS FEE and the signal strength on the output of the pre-amplifier. . . . .	4-39

509	4.45 Description of the principle of a CFD. A comparison of threshold triggering (left) 510 and constant fraction triggering (right) is shown in Figure 4.45a. Constant fraction 511 triggering is obtained thanks to zero-crossing technique as explained in Figure 4.45b. 512 The signal arriving at the input of the CFD is split into three components. A first 513 one is delayed and connected to the inverting input of a first comparator. A sec- 514 ond component is connected to the noninverting input of this first comparator. A 515 third component is connected to the noninverting input of another comparator along 516 with a threshold value connected to the inverting input. Finally, the output of both 517 comparators is fed through an AND gate. . . . .	4-40
518	4.46 Typical efficiency sigmoid of a CMS RPC detector. The black dots correspond to the 519 data, the blue line to the sigmoid fit and the opened cross to the knee and working 520 extracted from the fit line. . . . .	4-41
521	4.47 Effect of the temperature variation on the rate (Figure 4.47a) and the efficiency (Fig- 522 ure 4.47b) of an RPC [253]. . . . .	4-42
523	4.48 Effect of the pressure variation on the rate (Figure 4.48a) and the efficiency (Fig- 524 ure 4.48b) of an RPC [254]. . . . .	4-43
525	 5.1 Mean RPC Barrel (left column) and Endcap (right column) rate (top row) and current 526 (bottom row) as a function of the instantaneous luminosity as measured in 2017 $p$ - 527 $p$ collision data. . . . .	5-2
528	5.2 Figure 5.2a: The hit rate per region (Barrel, Endcap) is linearly extrapolated to 529 HL-LHC highest instantaneous luminosity ( $5 \times 10^{34} \text{ cm}^{-2} \text{ s}^{-1}$ ) using the rate as 530 a function of instantaneous luminosity recorded by RPCs in 2017 showing a linear 531 dependence. Figure 5.2b: The integrated charge per region (Barrel, Endcap) is ex- 532 trapolated to HL-LHC integrated luminosity ( $3000 \text{ fb}^{-1}$ ) using the data accumulated 533 in 2016 in every HV channel. . . . .	5-3
534	5.3 CMS RPC mean integrated charge in the Barrel region (Figure 5.3a) and the Endcap 535 region (Figure 5.3b). The integrated charge per year is shown in blue. The red curve 536 shows the evolution of the accumulated integrated charge through time. The blank 537 period in 2013 and 2014 corresponds to LS1. The total integrated charge for the 538 entire operation period (Oct.2009 - Dec.2017) is estimated to be about $1.66 \text{ mC/cm}^2$ 539 in the Barrel and $4.58 \text{ mC/cm}^2$ in the Endcap. . . . .	5-3
540	5.4 Layout of the test beam zone called X5c GIF at CERN. Photons from the radioactive 541 source produce a sustained high rate of random hits over the whole area. The zone is 542 surrounded by 8 m high and 80 cm thick concrete walls. Access is possible through 543 three entry points. Two access doors for personnel and one large gate for material. 544 A crane allows installation of heavy equipment in the area. . . . .	5-4
545	5.5 $^{137}\text{Cs}$ decays by $\beta^-$ emission to the ground state of $^{137}\text{Ba}$ (BR = 5.64%) and via the 546 662 keV isomeric level of $^{137}\text{Ba}$ (BR = 94.36%) whose half-life is 2.55min. . . . .	5-5
547	5.6 Floor plan of the GIF++ facility. When the facility downstream of the GIF++ takes 548 electron beam, a beam pipe is installed along the beam line (z-axis). The irradiator 549 can be displaced laterally (its center moves from $x = 0.65 \text{ m}$ to $2.15 \text{ m}$ ), to increase 550 the distance to the beam pipe. . . . .	5-6
551	5.7 Simulated unattenuated current of photons in the xz plane (Figure 5.7a) and yz plane 552 (Figure 5.7b) through the source at $x = 0.65 \text{ m}$ and $y = 0 \text{ m}$ [263]. With angular 553 correction filters, the current of 662 keV photons is made uniform in xy planes. . . . .	5-6

- 554        5.8 Description of the RPC setup. Dimensions are given in mm. A tent containing RPCs  
 555        is placed at 1720 mm from the source container. The source is situated in the center  
 556        of the container. RE-4-2-BARC-161 chamber is 160 mm inside the tent. This way,  
 557        the distance between the source and the chambers plan is 2060 mm. Figure 5.8a  
 558        provides a side view of the setup in the  $xz$  plane while Figure 5.8b shows a top view  
 559        in the  $yz$  plane. . . . . 5-7
- 560        5.9 RE-4-2-BARC-161 chamber is inside the tent as described in Figure 5.8. In the  
 561        top right, the two scintillators used as trigger can be seen. This trigger system has an  
 562        inclination of  $10^\circ$  relative to horizontal and is placed above half-partition B2 of the  
 563        RPCs. PMT electronics are shielded thanks to lead blocks placed in order to protect  
 564        them without stopping photons from going through the scintillators and the chamber. 5-8
- 565        5.10 Hit distributions over all three partitions of RE-4-2-BARC-161 chamber is showed.  
 566        Top, middle and bottom figures respectively correspond to partitions A, B, and C.  
 567        The profiles show that some events still occur in other half-partitions than B2, which  
 568        corresponds to strips 49 to 64, in front of which the trigger is placed, contributing to  
 569        the inefficiency of detection of cosmic muons. In the case of partitions A and C, the  
 570        very low amount of data can be interpreted as noise. On the other hand, it is clear  
 571        that a little portion of muons reach the half-partition B1, corresponding to strips 33  
 572        to 48. . . . . 5-8
- 573        5.11 Signals from the RPC strips are shaped by the FEE described on Figure 5.11a.  
 574        Output LVDS signals are then read-out by a TDC module connected to a computer or  
 575        converted into NIM and sent to scalers. Figure 5.11b describes how these converted  
 576        signals are put in coincidence with the trigger. . . . . 5-9
- 577        5.12 Results are derived from data taken on half-partition B2 only. On the 18<sup>th</sup> of June  
 578        2014, data has been taken on chamber RE-4-2-BARC-161 at CERN building 904  
 579        (Prevessin Site) with cosmic muons providing us a reference efficiency plateau of  
 580         $(97.54 \pm 0.15)\%$  represented by a black curve. A similar measurement has been done  
 581        at GIF on the 21<sup>st</sup> of July with the same chamber giving a plateau of  $(78.52 \pm 0.94)\%$   
 582        represented by a red curve. . . . . 5-10
- 583        5.13 Representation of the layout used for the simulations of the test setup. The RPC  
 584        read-out plane is represented as a yellow trapezoid while the two scintillators as blue  
 585        cuboids looking at the sky. The green plane corresponds to the muon generation  
 586        plane within the simulation. Figure 5.8a shows a global view of the simulated setup.  
 587        Figure 5.8b shows a zoomed view that allows to see the two scintillators as well as  
 588        the full RPC plane. . . . . 5-11
- 589        5.14 Geometrical acceptance distribution as provided by the Monte Carlo simulation. . . . 5-12
- 590        5.15 Correction of the efficiency without source. The efficiency after correction gets  
 591        much closer to the Reference measurement performed before the study in GIF by  
 592        reaching a plateau of  $(93.52 \pm 2.64)\%$ . . . . . 5-13
- 593        5.16 Hit distributions over read-out partition B of RE-4-2-BARC-161 chamber to-  
 594        gether with skew distribution fits corresponding to forward and backward coming  
 595        muons. . . . . 5-14
- 596        5.17 Figure 5.17a shows the linear approximation fit performed on data extracted from  
 597        table 5.2. Figure 5.17b shows a comparison of Formula 5.5 with the simulated flux  
 598        using  $a$  and  $b$  given in figure 5.17a in formulae 5.3 and the reference value  $D_0 =$   
 599        50 cm and the associated flux for each absorption factor  $F_0^{ABS}$  from table 5.1. . . . . 5-16

600	5.18 Efficiency (Figure 5.18a) and cluster size (Figure 5.18b) of chamber RE-4-2-BARC-161 measured at GIF with Source OFF (red) and Source ON using different absorber settings: ABS 5 (green), ABS 2 (blue) and ABS 1 (yellow). The results are compared to the Reference values obtained with cosmics. . . . .	5-17
604	5.19 Rates in chamber RE-4-2-BARC-161 measured at GIF with Source OFF (red) and Source ON using different absorber settings: ABS 5 (green), ABS 2 (blue) and ABS 1 (yellow). On Figure 5.19b, the rates of Figure 5.19a were normalized to the measured efficiency, and constant fits are performed on Source ON data showing the gamma rate in the chamber. . . . .	5-18
609	5.20 Evolution of the voltages at half maximum and at 95% of the maximum efficiency (Figure 5.20a), and of the maximum efficiency (Figure 5.20b) as a function of the rate in chamber RE-4-2-BARC-161. The data is extracted from the fits in Figures 5.18a and 5.19b. . . . .	5-18
613	5.21 Presentation of a double-gap endcap RPC with its three RPC gaps. Due to the partitioning of the read-out strips into three rolls, the TOP layer of gap is divided into two gaps: TOP NARROW (TN) and TOP WIDE (TW). The BOTTOM (B) only consists in one gap. . . . .	5-19
617	5.22 Current density and charge deposition per gamma avalanche, defined as the current density normalized to the measured rate taken from Figure 5.19a as a function of the effective high voltage in chamber RE-4-2-BARC-161 measured at GIF with Source ON using different absorber settings: ABS 5 (green), ABS 2 (blue) and ABS 1 (yellow). . . . .	5-20
622	5.23 Characterization of CMS RPC detectors foreseen to be used at GIF++ for longevity studies of the present system. Using cosmic muons, efficiency (Figure 5.23a) and cluster size (Figure 5.23b) were measured as well as noise rate (Figure 5.23c) and current density (Figure 5.23d). For each detector, the working voltage, defined as in Formula 4.25, was extracted from sigmoid fits performed in Figure 5.23a and the values of efficiency, cluster size, noise rate and current density at this voltage are reported using open crosses. . . . .	5-21
629	5.24 CMS RPC setup inside of GIF++ bunker during test beam (Figure 5.24a) and ageing periods (Figure 5.24b). The space in between the RPCs and the source is usually used by other detectors while the space in between T1 and the upstream wall is not filled. Due to the presence of the beam pipe, the trolley is moved away from the beam line during irradiation periods and placed farther away from the source for less intense irradiation. The position of the trolley can vary due to the use of the space by other setups and is then not exact. In the contrary, the position of the chambers in the trolley is fixed and given in Figure 5.24c. . . . .	5-23
637	5.25 Visualisation of the main data flows in GIF++. The yellow flow lines correspond to the DIP flow used for source, environmental and gas information. The red flow lines are for the CAEN flow through which the WebDCS communicates the voltages to be applied on the detectors using pressure and temperature information and retrieves the monitored voltages and currents. Finally, the blue flow lines correspond to the DAQ flow through which the RPC data is collected from the TDCs by the computer. . . . .	5-24
643	5.26 DIP monitoring history accessed through GIF++ WebDCS interface. . . . .	5-25
644	5.27 Example of DQM page available on CMS RPC WebDCS in GIF++. The rate measured in one of the tracking chambers, namely GT1_20_20-BKL_JUL16_4, is presented here. The DQM page allows clicking on each histogram to extend its view and to navigate through the histograms thanks to the left and right arrows. . . . .	5-27

648	5.28 Example of DQM ROOT Browser page available on CMS RPC WebDCS in GIF++. The strip activity profile, defined as the rate profile normalized to the mean rate, in one of the tracking chambers, namely GT1_20_20-BKL_JUL16_4, is presented here. Available ROOT files and histograms can be browsed thanks to the left panel showing the directory and files structures. . . . .	5-28
653	5.29 Longevity statistics of chamber RE2-2-NPD-BARC-9 in GIF++. For each month since July 2017, the integrated charge (in blue) as well as the time efficiency of irradiation (in gray) is reported. . . . .	5-28
656	5.30 Example of current monitoring (Figure 5.30a) and of corresponding integrated charge (Figure 5.30b) of chamber RE2-2-NPD-BARC-09. The decrease of current is related to a decrease of the voltage due to the daily rate scan procedure or to periods during which the source was turned OFF. . . . .	5-29
660	5.31 Example of rate (Figure 5.31a) and current (Figure 5.31b) monitoring of chamber RE2-2-NPD-BARC-09 with increasing integrated charge. The variations of the rate and current are correlated and corresponds to change of source irradiation, gas flow, gas humidity, or environmental conditions. . . . .	5-30
664	5.32 Example of strip activity of chamber RE2-2-NPD-BARC-09 monitoring through time. The activity of a strip is defined as the rate of the individual channel normalized to the mean rate measured in the corresponding read-out partition. . . . .	5-31
667	5.33 Total integrated charge in the irradiated RPCs, RE2-2-NPD-BARC-9 and RE4-2-CERN-165, before starting August 2018 test beam period. The irradiation of the RE2 chamber started in June 2016 while the RE4 chamber couldn't be irradiated before November 2016. . . . .	5-33
671	6.1 PETIROC 2A block diagram. . . . .	6-2
672	6.2 The PETIROC time jitter as a function of the input signal amplitude, measured with and without internal clocks. . . . .	6-3
674	6.3 The four channels of INFN preamplifiers are mounted directly on a CMS RPC and connected to the four outermost read-out strips of the detector. . . . .	6-4
676	6.4 Experimental setup used to test the INFN preamplifier with respect to the CMS FEEs. . . . .	6-5
677	6.5 The block diagrams corresponding to the signal treatment for both INFN preamplifier (Figure 6.5a) and CMS FEEs (Figure 6.5b) are shown. The digitized signals are then counted in coincidence with the trigger signals provided by PMTs (Figure 6.5c). . . . .	6-6
680	6.6 Efficiency (Figure 6.6a) and noise rate per unit area (Figure 6.6b) of the CMS RE2-2 detector tested with the standard CMS FEBs (black) and with the INFN preamplifier at different thresholds (red and blue). An extra HV scan was performed with better conditions to measure the noise with a threshold of 3 fC on the INFN preamplifiers. . . . .	6-7
684	6.7 Figure reffig:Setup-INFN-904:A: Shielded Front-End Board on which the INFN preamplifiers are to be mounted. Figure reffig:Setup-INFN-904:B: Three INFN preamplifiers connected onto the test FEB. Figure reffig:Setup-INFN-904:C: Experimental setup used to test the INFN preamplifier single mounted on a FEB similar to the CMS FEB. . . . .	6-8
689	6.8 Similarly to Figure 6.5c, the signals are counted in coincidence with the trigger signals provided by PMTs. To estimate the cluster size, the channels are counted by groups of three, two but also alone. . . . .	6-9
692	6.9 Efficiency (Figure 6.9a), cluster size (Figure 6.9b) and noise rate per unit area (Figure 6.9c) of the CMS RE2-2 detector tested with the standard CMS FEBs (black and red) and with the INFN preamplifier mounted onto the CMS FEB at different thresholds (blue, pink, green and purple). . . . .	6-10

696	6.10 The glass RPC developped by Ghent uses a double-gap design (Figure 6.10a). The 697 electrodes are made of four pieces of float glass glued into a single plate (Fig- 698 ure 6.10b). Indeed a gluing technique has been investigated as most new low re- 699 sistivity materials foreseen for RPCs of the new generation are not available in large 700 areas. . . . .	6-11
701	6.11 Figure 6.11a: A gap used to concieve the gRPC tested at CERN. Figure 6.11b: 702 Both gaps with their read-out panel are placed into a faraday made out of copper. 703 Figure 6.11c: The faraday cage containing the double-gap gRPC is finally placed 704 into its aluminium case. . . . .	6-12
705	6.12 Experimental setup used to test the INFN preamplifier mounted on the CMS like 706 FEB with the glass RPC build by Ghent. . . . .	6-13
707	6.13 Efficiency (Figure 6.13a), cluster size (Figure 6.13b) and noise rate per unit area 708 (Figure 6.13c) of the Ghent gRPC detector tested with the standard CMS FEBs (red) 709 and with the INFN preamplifier mounted onto the CMS FEB at different thresholds 710 (blue, pink, green and purple). . . . .	6-14
711	6.14 Figure 6.14a: Time difference between the first and last hit composing a cluster in 712 the gRPC. The maximum time difference is set to 300 ns. Figure 6.14b: Variation of 713 the reconstructed average cluster size as a function of the time constraint used in the 714 algorithm. . . . .	6-15
715	6.15 Evolution of the cluster size distribution with increasing voltage for the gRPC tested 716 with the INFN preamplifiers using a threshold of 5 fC. . . . .	6-16
717	6.16 Map of the cluster size distribution as a function of the cluster position with increas- 718 ing voltage for the gRPC tested with the INFN preamplifiers using a threshold of 719 5 fC. . . . .	6-16
720	6.17 Noise profile measured in the glass RPC built by Ghent tested with the standard 721 CMS FEB (Figure 6.17a) and the INFN preamplifiers mounted on a CMS-like FEB 722 (Figure 6.17b). . . . .	6-17
723	6.18 The arrival time of the hits recorded in the gRPC tested with the CMS FEB (Fig- 724 ure 6.18a) and with the INFN preamplifiers (Figure 6.18b), and recorded in the CMS 725 RE2 RPC tested with the INFN preamplifiers (Figure 6.18c). . . . .	6-18
726	6.19 Experimental setups used to test the HARDROC2 electronics with a CMS RE4-3 727 gap (Figure 6.19a) and a gRPC gap built in Ghent (Figure 6.19b). . . . .	6-19
728	6.20 HARDROC2 control chip with its "Mezzanine" used to collect the data from the 729 different HARDROC ASICs and communicate with the computer. On top of the 730 picture, the trigger is brought by a coaxial cable. The connection with the computer 731 is assured by both the USB cables. . . . .	6-19
732	6.21 Efficiency (Figure 6.21a), cluster size (Figure 6.21b) and noise rate per unit area 733 (Figure 6.21c) of the CMS RE4-3 detector tested in single gap mode with the stan- 734 dard CMS FEBs (black) and with the HARDROC 2 readout panel at different thresh- 735 olds (red, blue and pink). . . . .	6-20
736	6.22 Measured muon (Figure 6.22a) and noise (Figure 6.22a) profiles in the read-out pads 737 of the HARDROC 2 over a CMS RE4-3 gap. The inner structure of the gap and the 738 presence of the spacers in the volume is visible. . . . .	6-21
739	6.23 Efficiency (Figure 6.21a), cluster size (Figure 6.21b) and noise rate per unit area 740 (Figure 6.21c) of the UGent gRPC tested in double-gap mode with the standard CMS 741 FEBs (black) and in single-gap with the HARDROC 2 readout panel at a threshold 742 of 143 fC (red). . . . .	6-22

743	6.24 Measured muon (Figure 6.22a) and noise (Figure 6.22a) profiles in the read-out pads of the HARDROC 2 over a CMS RE4-3 gap. The inner structure of the gap and the presence of the spacers in the volume is visible. . . . .	6-23
746	A.1 (A.1a) View of the front panel of a V1190A TDC module [264]. (A.1b) View of the front panel of a V1718 Bridge module [265]. (A.1c) View of the front panel of a 6U 6021 VME crate [279]. . . . .	A-3
749	A.2 Module V1190A <i>Trigger Matching Mode</i> timing diagram [264]. . . . .	A-4
750	A.3 Structure of the ROOT output file generated by the DAQ. The 5 branches ( <code>EventNumber</code> , <code>number_of_hits</code> , <code>Quality_flag</code> , <code>TDC_channel</code> and <code>TDC_TimeStamp</code> ) are visible on the left panel of the ROOT browser. On the right panel is visible the histogram cor- responding to the variable <code>nHits</code> . In this specific example, there were approximately 50k events recorded to measure the gamma irradiation rate on the detectors. Each event is stored as a single entry in the <code>TTree</code> . . . . .	A-10
756	A.4 The effect of the quality flag is explained by presenting the content of <code>TBranch</code> <code>number_of_hits</code> of a data file without <code>Quality_flag</code> in Figure A.4a and the con- tent of the same <code>TBranch</code> for data corresponding to a <code>Quality_flag</code> where all TDCs were labelled as <code>GOOD</code> in Figure A.4b taken with similar conditions. It can be noted that the number of entries in Figure A.4b is slightly lower than in Figure A.4a due to the excluded events. . . . .	A-12
762	A.5 Using the same data as previously showed in Figure A.4, the effect of the quality flag is explained by presenting the reconstructed hit multiplicity of a data file with- out <code>Quality_flag</code> in Figure A.5a and the reconstructed content of the same RPC partition for data corresponding to a <code>Quality_flag</code> where all TDCs were labelled as <code>GOOD</code> in Figure A.5b taken with similar conditions. The artificial high content of bin 0 is completely suppressed. . . . .	A-12
768	A.6 WebDCS DAQ scan page. On this page, shifters need to choose the type of scan (Rate, Efficiency or Noise Reference scan), the gamma source configuration at the moment of data taking, the beam configuration, and the trigger mode. These in- formation will be stored in the DAQ ROOT output. Are also given the minimal measurement time and waiting time after ramping up of the detectors is over before starting the data acquisition. Then, the list of HV points to scan and the number of triggers for each run of the scan are given in the table underneath. . . . .	A-14
775	B.1 Example of expected hit time distributions in the cases of efficiency (Figure B.1a) and noise/gamma rate per unit area (Figure B.1b) measurements as extracted from the raw ROOT files. The unit along the x-axis corresponds to ns. The fact that "the" muon peak is not well defined in Figure B.1a is due to the contribution of all the RPCs being tested at the same time that don't necessarily have the same signal arrival time. Each individual peak can have an offset with the ones of other detectors. The inconsistancy in the first 100 ns of both time distributions is an artefact of the TDCs and are systematically rejected during the analysis. . . . .	B-16
783	B.2 The effect of the quality flag is explained by presenting the reconstructed hit multi- plicity of a data file without <code>Quality_flag</code> . The artificial high content of bin 0 is the effect of corrupted data. . . . .	B-21

- 786 B.3 Display of the masking tool page on the webDCS. The window on the left allows the  
787 shifter to edit `ChannelsMapping.csv`. To mask a channel, it only is needed to set the  
788 3rd field corresponding to the strip to mask to 0. It is not necessary for older mapping  
789 file formats to add a 1 for each strip that is not masked as the code is versatile and  
790 the default behaviour is to consider missing mask fields as active strips. The effect  
791 of the mask is directly visible for noisy channels as the corresponding bin turns red.  
792 The global effect of masking strips will be an update of the rate value showed on the  
793 histogram that will take into consideration the rejected channels. . . . . B-28



# List of Tables

794

795	3.1	Details of the greenhouse fluorinated gases used in CMS and of their GWP [177]. . .	3-20
796	4.1	Properties of the most used electrode materials for RPCs. . . . .	4-3
797	5.1	Total photon flux ( $E\gamma \leq 662$ keV) with statistical error predicted considering a $^{137}\text{Cs}$ activity of 740 GBq at different values of the distance $D$ to the source along the x-axis of irradiation field [261]. . . . .	5-14
798	5.2	Correction factor $c$ is computed thanks to Formula 5.4 taking as reference $D_0 = 50$ cm and the associated flux $F_0^{ABS}$ for each absorption factor available in table 5.1.	5-15
799	5.3	The data at $D_0$ in 1997 is taken from [261]. Using Formula 5.5, the flux at $D$ , including an error of 1 cm, can be estimated in 1997. Then, taking into account the attenuation of the source activity, the flux at $D$ can be estimated at the time of the tests in GIF in 2014. Assuming a sensitivity of the RPC to $\gamma s = 2 \times 10^{-3}$ , an estimation of the hit rate per unit area is obtained. . . . .	5-16
800	5.4	Summary of the characterization measurement performed in Ghent on CMS RPC detectors foreseen to be used at GIF++ for longevity studies of the present system. For each detector, the working voltage, defined as in Formula 4.25, was extracted from sigmoid fits performed in Figure 5.23a and the values of efficiency, cluster size, noise rate and current density at this voltage are reported. . . . .	5-22
801	6.1	Results of the sigmoid fit (Formula 4.24) performed on the data presented in Fig- ure 6.6a. The working point and its corresponding efficiency are computed using Formulas 4.24 and 4.25. . . . .	6-7
802	6.2	Results of the sigmoid fit (Formula 4.24) performed on the data presented in Fig- ure 6.9a. The working point and its corresponding efficiency are computed using Formulas 4.24 and 4.25. . . . .	6-10
803	6.3	Results of the sigmoid fit (Formula 4.24) performed on the data presented in Fig- ure 6.13a. The working point and its corresponding efficiency are computed using Formulas 4.24 and 4.25. . . . .	6-14
804	6.4	Results of the sigmoid fit (Formula 4.24) performed on the data presented in Fig- ure 6.21a. The working point and its corresponding efficiency are computed using Formulas 4.24 and 4.25. . . . .	6-20
805	6.5	Results of the sigmoid fit (Formula 4.24) performed on the data presented in Fig- ure 6.23a. The working point and its corresponding efficiency are computed using Formulas 4.24 and 4.25. . . . .	6-22
806	A.1	Inter-process communication cycles in between the webDCS and the DAQ through file string signals. . . . .	A-18



# List of Acronyms

## List of Acronyms

831	AFL	Almost Full Level
832	ALCTs	Anode local charged track boards
833	BARC	Bhabha Atomic Research Centre
834	BCS	Bardeen–Cooper–Schrieffer
835	BLT	Block Transfer
836	BMTF	Barrel Muon Track Finder
837	BNL	Brookhaven National Laboratory
838	BSM	Physics beyond the Standard Model
839	BR	Branching Ratio
840	CAEN	Costruzioni Apparecchiature Elettroniche Nucleari S.p.A.
841	CERN	European Organization for Nuclear Research
842	CFD	Constant Fraction Discriminator
843	CFEBs	cathode front-end boards
844	CKM	Cabibbo–Kobayashi–Maskawa
845	CMB	Cosmic Microwave Background
846	CMS	Compact Muon Solenoid
847	CSC	Cathode Strip Chamber
848	CuOF	copper-to-optical-fiber translators
849	DAQ	Data Acquisition
850	DCS	Detector Control Software
851	DMBs	Data acquisition mother boards
852	DQM	Data Quality Monitoring
853	DT	Drift Tube
854	EDM	electric dipole moment
855	ECAL	electromagnetic calorimeter
856	EMTF	Endcap Muon Track Finder
857	FCC	Future Circular Collider
858	FEB	Front-End Board
859	FEE	Front-End Electronics
860	FWHM	full-width-at-half-maximum
861	GEANT	GEometry ANd Tracking - a series of software toolkit platforms developed by CERN
862		
863	GEB	GEM Electronics board
864	GEM	Gas Electron Multiplier
865	GIF	Gamma Irradiation Facility
866	GIF++	new Gamma Irradiation Facility
867	gRPCs	glass RPCs
868	GWP	Global Warming Potential

---

869	HARDROC	HAdronic RPC Digital Read-Out Chip
870	HCAL	hadron calorimeter
871	HEP	High-Energy Physics
872	HL-LHC	High Luminosity LHC
873	HPL	High-pressure laminate
874	HSCPs	Heavy Stable Charged Particles
875	HV	High Voltage
876	ICRU	International Commission on Radiation Units & Measurements
877	ILC	International Linear Collider
878	IPNL	Institut de Physique Nucléaire de Lyon
879	iRPC	improved RPC
880	IRQ	Interrupt Request
881	ISR	Intersecting Storage Rings
882	LEIR	Low Energy Ion Ring
883	LEP	Large Electron-Positron
884	LHC	Large Hadron Collider
885	LS1	First Long Shutdown
886	LS2	Second Long Shutdown
887	LS3	Third Long Shutdown
888	LSP	lightest supersymmetric particle
889	LV	Low Voltage
890	LVDS	Low-Voltage Differential Signaling
891	MC	Monte Carlo
892	MCNP	Monte Carlo N-Particle
893	MiC	Minicrate electronics
894	MiC1	first version of Minicrate electronics
895	mip's	minimum ionizing particles
896	MRPC	Multigap RPC
897	MSSM	Minimal Supersymmetric Standard Model
898	mSUGRA	minimal SUper GRAvity
899	NIM	Nuclear Instrumentation Module logic signals
900	OH	Optohybrid Board
901	OMTF	Overlap Muon Track Finder
902	OTMBs	Optical TMBs
903	PAI	Photo-Absorption Ionisation
904	PAIR	Photo-Absorption Ionisation with Relaxation
905	PMT	PhotoMultiplier Tube
906	PS	Proton Synchrotron
907	PU	pile-up
908	QCD	Quantum Chromodynamics
909	QED	Quantum Electrodynamics
910	RADMON	Radiation Monitoring
911	RMS	Root Mean Square
912	ROOT	a framework for data processing born at CERN
913	RPC	Resistive Plate Chamber
914	SC	Synchrocyclotron
915	SDHCAL	Semi-Digital HCAL
916	SiPM	Silicon Photomultiplier
917	SLAC	Stanford Linear Accelerator Center

918	SM	Standard Model
919	SPS	Super Proton Synchrotron
920	SUSY	supersymmetry
921	TDC	Time-to-Digital Converter
922	TDR	Technical Design Report
923	TMBs	Trigger mother boards
924	ToF	Time-of-flight
925	TPG	trigger primitives
926	webDCS	Web Detector Control System
927	WIMPs	Weakly Interacting Massive Particles
928	YETS	Year End Technical Stop



# 1

929

930

## Introduction

931 Grasping an understanding of the world in which they are leaving in has always been part of human  
932 life. Beyond the metaphysical questioning of our origins and purpose, curiosity has brought mankind  
933 to question its surroundings. Following the philosophy of the ancient Greeks and Indians came  
934 the development of the sciences as the systematic experimentation aimed at testing hypothesis and  
935 reproducing results obtained by fellow natural philosophers. With the industrial revolution and the  
936 organisation of science, it became possible to go always further in the understanding of the universe  
937 and of the matter in particular. Investigation on the constituent of matter proved to require more  
938 and more powerful machines in order to break apart the bricks of the world into ever smaller pieces,  
939 study their behaviour and extract new knowledge to help the development of humanity. So far, the  
940 largest and most powerful machine that was built to study the particles composing matter and test  
941 the models thought by physicists to explain their behaviour is the Large Hadron Collider (LHC),  
942 a circular particle accelerator used to collide protons and heavy ions. After only a few years of  
943 investigations conducted thanks to the LHC, several discoveries, predicted by the existing models,  
944 have been made. In the future, in order to boost the discovery potential on the LHC and be able to  
945 test hypotheses lying beyond the already acknowledged models, the instantaneous luminosity, i.e.  
946 the rate of particle interactions, will be slightly increased into a so-called High Luminosity phase to  
947 boost its discovery potential.

948 As the Large Hadron Collider will see its instantaneous luminosity be increased, the detectors  
949 on the different experimental sites will have to suffer an increased background irradiation due to the  
950 byproducts of the interaction of the beams with the infrastructure. This will cause for the detectors  
951 a stress which implications need to be understood throughout the High Luminosity LHC (HL-LHC)  
952 phase of operations. In the case of the Compact Muon Solenoid (CMS) experiment, it is important  
953 to understand if the detectors that will be subjected to the higher levels of radiation will be able to  
954 sustain higher detection rates while displaying the same performance they have so far been operated  
955 at and if this level of performance of the detectors will stay stable for a period longer than ten years.  
956 More specifically, the detectors placed very close to the beam line will be the most subjected to the  
957 change of luminosity. In CMS, the endcap detectors will then be particularly affected by the stronger

background radiation. The endcap detectors compose a part of the muon system of CMS and among them, the Resistive Plate Chamber (RPC) plays a key role in providing the experiment a reliable trigger on potentially interesting data. This PhD work takes place into this very specific context of muon detector consolidation and certification for the HL-LHC period in order to provide the CMS experiment with robust new detectors and confirm that the present system will survive through the next 20 years.

CMS experiment main focus revolves around testing the Standard Model (SM) of particle physics using a multipurpose detector design to detect the interaction products of the protons and ions colliding along the LHC. Looking at the successive evolution of the theoretical models that gave birth to the SM, the need for very intense particle beams in high energy physics experiment becomes clear in that the higher the center-of-mass energy for each interaction, the greater the probe on very small cross-section processes predicted by the theory, justifying the successive increase in beam energy and intensity at LHC.

The implications for LHC experiments and in particular for the CMS detector explain the need for longevity and rate capability studies conducted on the Resistive Plate Chambers which are an important part of its Muon System as it is needed to certify the quality of operation of the trigger detectors throughout the lifetime of HL-LHC.

RPCs are gaseous detectors which physics principles are non trivial and are still being investigated. Nevertheless, key processes driving the electron multiplication in the gas volume, rate capability and ageing have been successfully identified and will define the parameters that will have to be taken into consideration while producing the detectors extending the pseudo-rapidity coverage of RPCs toward the beam line as well as the ones to be monitored during the on-going longevity and rate capability certification campaign.

On the one hand, the present RPC sub-system consists in two different RPC productions. Indeed, most of the RPC detectors were produced in view of the start of LHC activities in 2010. These detectors were build in between 2007 and 2008 to equip the barrel and the three disks of each endcaps of the CMS apparatus. But during the First Long Shutdown (LS1) of LHC in between end of 2012 and 2015, a fourth disk of endcap was added in order to reinforce the redundancy of the endcap trigger. Hence, new RPC detectors using the same technology were built in between 2012 and 2013. These two sets of detector productions only differ in the properties of the High-pressure laminate (HPL) used for their electrodes that could lead to a different ageing rate. This is why spare detectors of both production periods have been tested over the past years to certify their good operation through HL-LHC.

On the other hand, producing detectors to equip a highly irradiated region such as the extension of CMS RPC endcaps requires to substantially improve the ageing properties of the chosen technology by reducing the charge deposition per ionizing particle. This can be achieved both by modifying the design of the detector volume or by improving the signal to noise ratio of the Front-End Electronics (FEE) used to process the charge collected by the read-out strips making them more sensitive to weaker signals. Two improved RPC (iRPC) designs were selected and tested in order to extend of CMS endcap coverage.

Thanks to the study presented in this document, preliminary conclusions will be brought on the production of iRPCs and on the longevity of the present RPC system, providing with a better understand of the future performance of the RPC sub-system within the CMS experiment.

# 2

1001

1002

## Investigating the TeV scale

1003 Throughout history, physics experiment became more and more powerful in order to investigate finer  
1004 details of nature to help understanding the building blocks of matter and the fundamental interactions  
1005 that bind them in the microscopic world. Nowadays, the Standard Model of particle physics is the  
1006 most accurate theory designed to explain the behaviour of particles and is able to make very precise  
1007 predictions that are constantly verified. Nevertheless, some hints of new physics are visible as bricks  
1008 are still missing to obtain a global description of the Universe.

1009 To highlight the limits of the SM and test the different alternative theories, evermore powerful  
1010 machines are needed. It is in this context that the Large Hadron Collider has been thought and built  
1011 to accelerate and collide particles at energies exceeding anything that had been done before. Higher  
1012 collision energies and high pile-up imply the use of enormous detectors to measure the properties of  
1013 the interaction products. The Compact Muon Solenoid is a multipurpose experiment that have been  
1014 designed to study the proton-proton collisions of the LHC and give answers on various high-energy  
1015 physics scenarios such as different supersymmetry (SUSY) extensions to the Standard Model or  
1016 Extra Dimensions models.

1017 This Chapter will be the occasion to go through the history of the Standard Model of Particle  
1018 Physics to understand the research conducted today in High-Energy Physics (HEP) facilities. From  
1019 the discovery of the atom and of its inner structure to the development of the theories governing  
1020 the fundamental interactions, all the elements leading to the construction SM will be discussed.  
1021 Furthermore, highlights on the Physics beyond the Standard Model (BSM) will be given to replace  
1022 the document in the context of today's research. Finally, a full description of the LHC and of the  
1023 CMS detector will be provided.

### 1024 **2.1 The Standard Model of Particle Physics**

1025 In the early 21<sup>st</sup> century it is now widely accepted that matter is made of elementary blocks referred  
1026 to as *elementary particles*. The physics theory that classifies and describes the best the behaviour and  
1027 interaction of such elementary particles is the so-called Standard Model. The SM formalizes three of

1028 the four fundamental interactions (electromagnetic, weak and strong interactions). Its development  
 1029 happened since the 1960s thanks to a strong collaboration between theoretical and experimental  
 1030 physicists.

### 1031 2.1.1 A history of particle physics

1032 The idea that nature is composed of elementary bricks, called *atomism*, is not contemporary as it  
 1033 was already discussed by Indian or Greek philosophers during antiquity. In Greece, atomism has  
 1034 been rejected by *Aristotelianism* as the existence of *atoms* would imply the existence of a void that  
 1035 would violate the physical principles of Aristotle philosophy. Aristotelianism has been considered  
 1036 as a reference in the european area until the 15<sup>th</sup> century. With the *Rinascimento*, antic text and  
 1037 history started to be more deeply studied. The re-discovery of Platon's philosophy allowed opening  
 1038 the door to alternative theories and give a new approach to natural sciences where experimentation  
 1039 would become central. A new era of knowledge was starting. By the beginning of the 17<sup>th</sup> century,  
 1040 atomism was re-discovered by philosophers. The very first attempt at estimating the number of  
 1041 *particles* in a volume was provided by Magnenus in 1646 by calculating that the number of *particles*  
 1042 in a stick of incense [1]. He found a value of the order of  $10^{18}$  simply by considering the time  
 1043 necessary to smell it everywhere in a large church after the stick was lit on. It is now known that this  
 1044 number only falls short only by 1 order of magnitude.

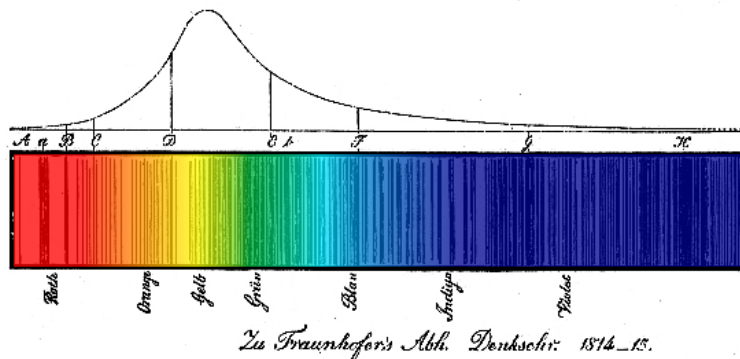
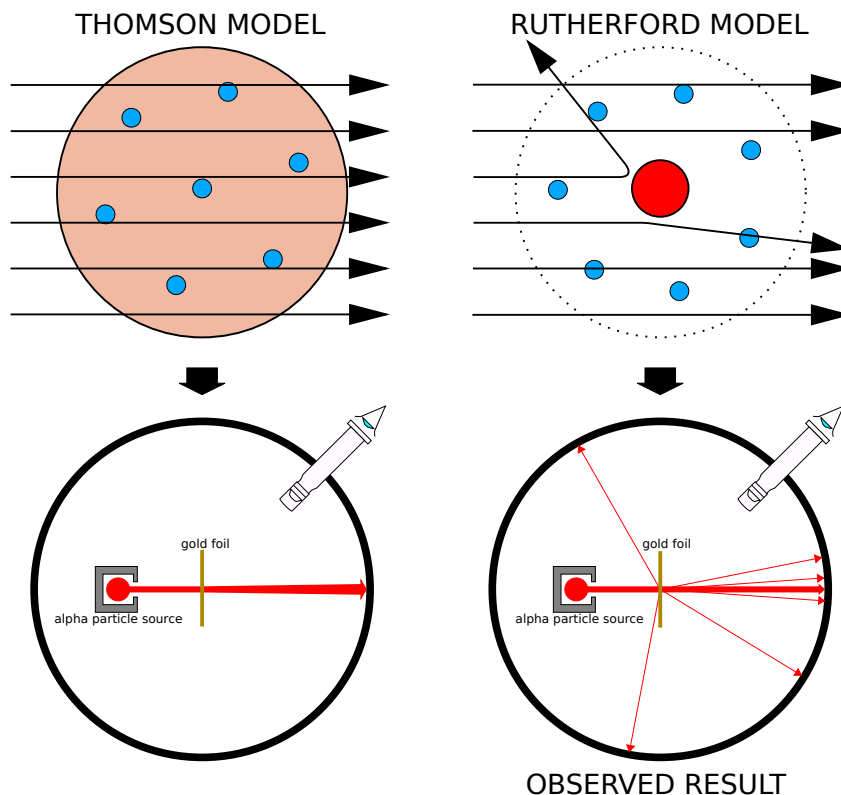


Figure 2.1: Solar spectrum with spectral lines as it visually appeared to Fraunhofer.

1045 An alternative philosophy to atomism popularized by Descartes was *corpuscularianism*. Built on  
 1046 ever divisible corpuscles, contrary to atoms, its principles were mainly used by alchemists like New-  
 1047 ton who would later develop a corpuscular theory of light. Boyle combined together ideas of both  
 1048 atomism or corpuscularianism leading to mechanical philosophy. The 18<sup>th</sup> century has seen the  
 1049 development of engineering providing philosophical thought experiments with repeatable demon-  
 1050 stration and a new point of view to explain the composition of matter. Lavoisier greatly contributed  
 1051 to chemistry and atomism by publishing in 1789 a list of 33 chemical elements corresponding to  
 1052 what are now called *atoms* [2]. In the early 19<sup>th</sup> century Dalton summarized the knowledge on  
 1053 composition of matter [3]. In his atomic model, the atoms are ball-like constituents of the chemical  
 1054 elements. All atoms of a given element are identical, in size, mass, and other properties while the  
 1055 atoms of different elements differ. He also considered that atoms cannot be divided into smaller  
 1056 particles, created nor destroyed and that they combine into chemical compounds. The essence of  
 1057 chemical reaction was then the combination, separation or rearrangement of atoms. Soon after,

1058 Fraunhofer invented the spectrometer and discovered the spectral lines in the sunlight spectrum, as  
 1059 showed in Figure 2.1 [4]. These were later linked to the absorption by chemical elements present in  
 1060 the solar atmosphere by Kirchhoff and Bunsen. The rise of atomic physics, chemistry and mathematical  
 1061 formalism unraveled the different atomic elements and ultimately, the 20<sup>th</sup> century saw the  
 1062 very first sub-atomic particles.

1063 **Discovery of the inner structure of the atom**



*Figure 2.2: Through the gold foil experiment, Rutherford could show that most of the mass of atoms was contained in a positively charged nucleus and could then propose a more accurate atomic model than that of Thomson.*

1064 The negatively charged *electron* was the first to be discovered in 1897 by Thomson after three  
 1065 decades of research on cathode rays [5]. He proved that the electrification observed in an elec-  
 1066 troscope, as reported by Perrin [6], was due to the rays themselves. Hence, they had to be composed  
 1067 of electrically charged particles. In 1900, Becquerel showed the *beta rays* emitted by radium had the  
 1068 same charge over mass ratio as was measured by Thomson for cathode rays, pointing to electrons as  
 1069 a constituent of atoms [7]. This discovery leads to Thomson's plum pudding atomic model in which  
 1070 electrons are embed into a uniform positively charged atom [8]. In 1907, Rutherford and Royds  
 1071 showed that *alpha* particles were helium ions [9]. Indeed, once captured in a tube and subjected to  
 1072 an electric spark causing an electron avalanche, they could combine with two electrons to form a  
 1073  ${}^4\text{He}$ .

This discovery was directly followed by the constraint of the atom structure in between 1908 and 1913 through the Geiger–Marsden gold foil experiments in which the deflection angle of alpha particles fired at a very thin gold foil was measured [10–13]. It highlighted that atoms were mainly empty with nearly all their mass contained into a tiny positively charged *nucleus*. With these two observations, Rutherford could formulate the Rutherford planetary model of the atom in 1911 [14], shown together with the Thomson plum pudding model in Figure 2.2. The link between atomic number and number of positive and negative charges contained into the atoms would fast be understood. Hence, the different kinds of element transmutations appeared to be purely nuclear processes making clear that the electromagnetic nature of chemical transformations could not possibly change nuclei. A new branch in physics appeared to exclusively study nuclei: *nuclear physics*. By studying alpha emission and the product of their interaction with nitrogen gas, Rutherford reported in 1919 the very first nuclear reaction [15]. It leads to the discovery that the hydrogen nucleus was composed of a single positively charged particle that was later baptised *proton* [16]. This idea came from 1815 Prout's hypothesis proposing that all atoms are composed of "protyles" (i.e. hydrogen atoms) [17, 18]. By using scintillation detectors, Rutherford could highlight typical hydrogen nuclei signature and understand that the impact of alpha particles with nitrogen would knock out a hydrogen nucleus and produce an oxygen 17, as showed in Formula 2.1 and would then postulate that protons are building bricks of all elements.



With this assumption and the discovery of *isotopes* together with Aston, elements with identical atomic number but different masses, Rutherford proposed that all elements' nuclei but hydrogen are composed of both charged particles, protons, and of chargeless particles, which he called *neutrons* [16, 19]. These neutral particles helped maintaining nuclei as one, as charged protons were likely to electrostatically repulse each other. He then introduced the idea of a new force, a *nuclear* force. The first idea concerning neutrons was a bond state of protons and electrons as it was known that the beta decay, emitting electrons, was taking place in the nucleus. However, it was then shown that electrons being confined into the nucleus would hardly be possible due to Heisenberg's uncertainty principle. Finally, in 1932, following the discovery of a new neutral radiation, Chadwick could discover the neutron as an uncharged particle with a mass similar to that of the proton which would solve the nucleus puzzle [20–24].

### 1103 Development of the Quantum Electrodynamics

Historically, the development of the quantum theory revolved around the question of emission and absorption of discrete amount of energy through light. Einstein used the initial intuition of Planck about the black-body radiation to develop in 1905 a model to explain the photoelectric effect in which light was described by discrete *quanta* now called *photons* [25, 26]. For this model, Einstein introduced the concept of wave-particle duality as classical theory was not able to describe the phenomenon. With the new understanding of atoms and of their structure, classical theories also proved unable to explain atoms' stability. Indeed, using classical mechanics, electrons orbiting around a nucleus should radiate an energy proportional to their angular momentum and hence, loose energy through time and the spectrum of energy emission should then be continuous. However, it was known since the 19<sup>th</sup> century and the discovery of spectral lines that the emission spectrum of material was discrete [4].

In 1913, quantum physics was introduced into the atomic model by Bohr to overcome the electron's energy loss due to orbiting radiation emission [27]. Using the correspondence principle stating that for large enough numbers the quantum calculations should give the same results than the classical theory, he proposed the very first quantum model of the hydrogen atom explaining the line spectrum by introducing the *principal quantum number*  $n$  describing the electron shell. The same year, Moseley confirmed Bohr's model through the Moseley's law [28]. Debye and then Sommerfeld extended it by introducing the quantization of the angular momentum [29]. The quantization the z-component of the angular momentum led to the *second and third quantum numbers*, or *azimuthal and magnetic quantum number*,  $l$  and  $m$ . The second defines the orbital angular momentum of the electrons on their shells and hence, the shape of the orbital, while the third the available orbital on the subshell for each electron as shown in Figure 2.3.

Nevertheless, although the model was not only limited to spherical orbitals anymore, making the atom more realistic, the Zeeman effect couldn't be completely explained by just using  $n$ ,  $l$  and  $m$  [30–33] nor could the result of the Stern-Gerlach experiment [34]. Both experiments are shown in Figure 2.4. A solution was brought after Pauli in 1925 proposed together with his exclusion principle the idea of a new quantum degree of freedom in order to resolve the apparent problem [35, 36]. This degree of freedom was interpreted as an intrinsic angular momentum vector associated to the particle itself, not to the orbital [37], and associated to a new quantum number  $s$ , the *spin projection quantum number* explaining the lift of degeneracy to an even number of energy levels [38]. The new quantum number helped in theorizing the neutron as a neutral particle rather than a bond state of a proton and an electron confined in the nucleus itself.

The introduction of the *spin* happened one year after another attempt of improvement of the theory was made by De Broglie in his Ph.D. thesis [39]. The original formulation of the quantum theory only considered photons as energy quanta behaving as both *waves* and *particles*. De Broglie proposed that *all* matter are described by waves and that

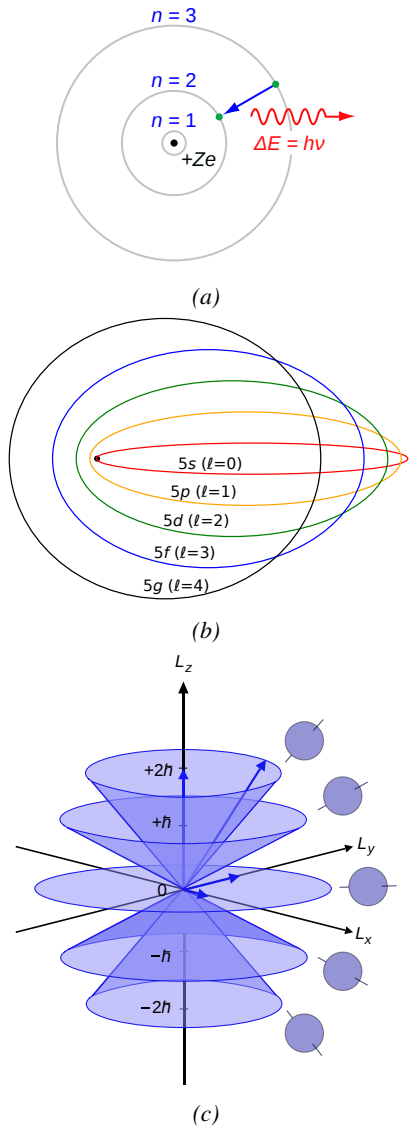


*Figure 2.3: Figure 2.3a: The orbits in which the electron may travel according to the Bohr model of the hydrogen atom. An electron jumps between orbits and is accompanied by an emitted or absorbed amount of electromagnetic energy ( $h\nu$ ). The orbits radius increases as  $n^2$ . Figure 2.3b: Elliptical orbits with the same energy and quantized angular momentum  $l = 0, 1, \dots, n - 1$  in the case  $n = 5$ . Figure 2.3c: Illustration of quantum mechanical orbital angular momentum. The cones and plane represent possible orientations of the angular momentum vector for  $l = 2$  and  $m = -2, -1, 0, 1, 2$ .*

*all* matter are described by waves and that

<sup>1161</sup> their momentum is proportional to the oscillation of quantized electromagnetic field oscillators. This  
<sup>1162</sup> interpretation was able to reproduce the previous version of the quantum energy levels by showing  
<sup>1163</sup> that the quantum condition involves an integer multiple of  $2\pi$ , as shown by Formula 2.2.

$$(2.2) \quad p = \hbar k \Leftrightarrow \int pdx = \hbar \int kdx = 2\pi\hbar n$$

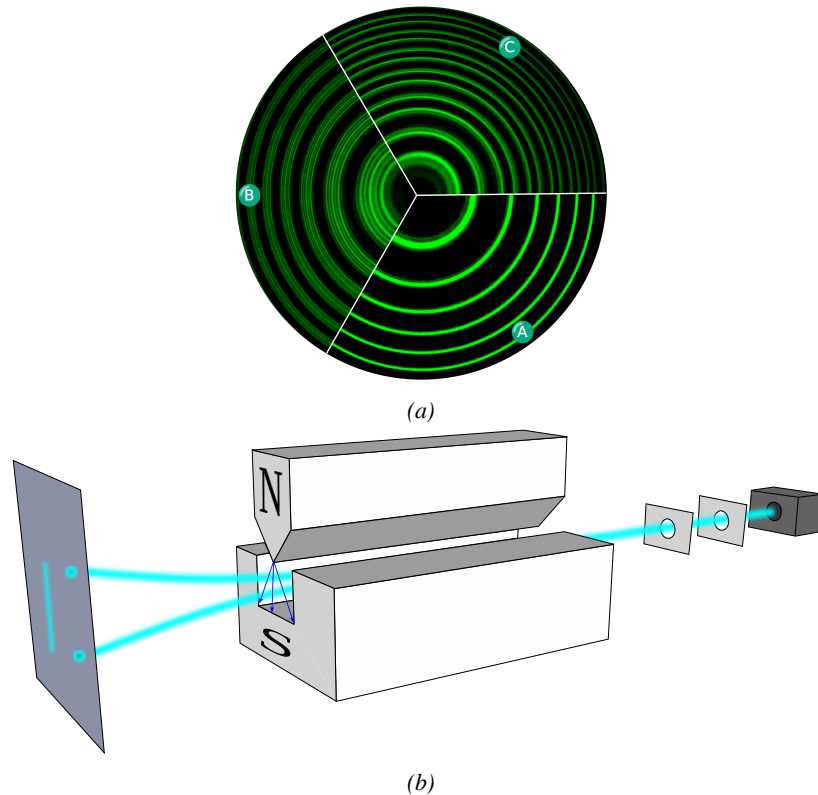


*Figure 2.4: Figure 2.4a: The spectral lines of mercury vapor lamp anomalous Zeeman effect without magnetic field (A) and with magnetic field (B - transverse Zeeman effect & C - longitudinal Zeeman effect). Figure 2.4b: Stern-Gerlach experiment: Silver atoms traveling through an inhomogeneous magnetic field and being deflected up or down depending on their spin.*

<sup>1164</sup> Although the intuition of De Broglie about the wave-particle duality of all matter was a step in the  
<sup>1165</sup> right direction, his interpretation was semiclassical and it is in 1926 that the first full quantum wave  
<sup>1166</sup> equation would be introduced by Schrödinger to describe electron-like particles, reproducing the  
<sup>1167</sup> previous semiclassical formulation without inconsistencies [40]. This complex equation describes  
<sup>1168</sup> the evolution of the wave function  $\Psi$  of the quantum system, defined by its position vector  $\mathbf{r}$  and time  
<sup>1169</sup>  $t$  as an energy conservation law, in which the hamiltonian of the system  $\hat{H}$  is explicit, by solving the  
<sup>1170</sup> Equation 2.3.

$$(2.3) \quad i\hbar \frac{\partial}{\partial t} |\Psi(\mathbf{r}, t)\rangle = \hat{H} |\Psi(\mathbf{r}, t)\rangle$$

1171     The spin was then included into Schrödinger equation by Pauli to take into account the interaction  
 1172     with an external magnetic field, as shown in Equation 2.4 in which the Hamiltonian operator is a  $2 \times 2$   
 1173     matrix operator due to the Pauli matrices [38].  $\mathbf{A}$  is the vector potential and  $\phi$  is the scalar electric  
 1174     potential.

$$(2.4) \quad i\hbar \frac{\partial}{\partial t} |\Psi\rangle = \left[ \frac{1}{2m} (\sigma \cdot (\mathbf{p} - q\mathbf{A})^2 + q\phi) \right] |\Psi\rangle$$

1175     Later in 1927, Dirac went further in his paper about emission and absorption of radiation by  
 1176     proposing a second quantization not only of the physical process at play but also of the electromagnetic  
 1177     field [41]. His equation provided the ingredients to the first formulation of *Quantum Electrodynamics (QED)*  
 1178     and the description of photon emission by electrons dropping into a lower energy state  
 1179     in which the final number of particles is different than the initial one. Nevertheless, in order to properly  
 1180     treat electromagnetism, the incorporation of the special relativity developed by Einstein was  
 1181     necessary. Derived in 1928, the Dirac equation, shown as Equation 2.5, similarly to Schrödinger  
 1182     equation, is a single-particle equation but it incorporates special relativity in addition to quantum  
 1183     mechanics rules [42].

$$(2.5) \quad i\hbar\gamma^\mu \partial_\mu \psi - mc\psi = 0$$

1184     It features the  $4 \times 4$  gamma matrices  $\gamma^\mu$  built using  $2 \times 2$  Pauli matrices and the unitary matrix,  
 1185     the 4-gradient  $\partial_\mu$ , the rest mass  $m$  of any half integer spin massive particle described by the wave  
 1186     function  $\psi(x, t)$ , also called a Dirac spinor and the speed of light  $c$ . In addition to perfectly reproduce  
 1187     the results obtained with quantum mechanics so far, it also provided *negative-energy solutions* that  
 1188     would later be interpreted as a new form of matter, *antimatter* [43, 44]. In the non-relativistic limit,  
 1189     the Dirac equation gives a theoretical justification to the Pauli equation that was phenomenologically  
 1190     constructed to account for the spin.

1191     The successes of the QED were soon followed with theoretical problems as computations of any  
 1192     physical process involving photons and charged particles were shown to be only reliable at the first  
 1193     order of the *perturbation theory* [45]. At higher order of the theory, divergent contributions were  
 1194     appearing giving nonsensical results. Only two effects were contributing to these infinities.

- 1195       • The self-energy of the electron (or positron), the energy that the particle has due to its own  
     1196       interaction with its environment.
- 1197       • The vacuum polarization, virtual electron–positron pairs produced by a background electro-  
     1198       magnetic field in the vacuum which is not an "empty" space. These virtual pairs affect the  
     1199       charge and current distributions generated by the original electromagnetic field.

1200     Solving this apparent problem was done by carefully defining the concepts of each observable,  
 1201     for example mass or charge, as these quantities are understood within the context of a non-interacting  
 1202     field equation. From the experimental point of view, they are abstractions as what is measured is  
 1203     "renormalized observables" shifted from their "bare" value by the interaction taking place in the  
 1204     measuring process. The infinities needed to be connected to corrections of mass and charge as those  
 1205     are fixed to finite values by experiment. This was the intuition of Bethe in 1947 who successfully  
 1206     computed the effect of such *renormalization* in the non-relativistic case [46]. Full covariant formula-  
 1207     tions of QED including renormalization were achieved by 1949 by Tomonaga, Schwinger, Feynman,

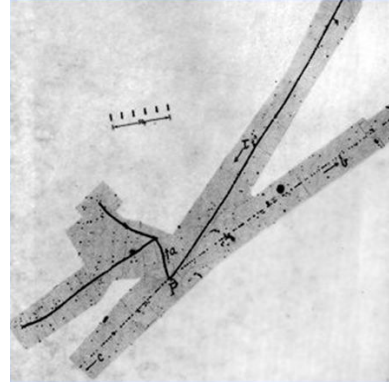
1208 and Dyson [47]. With the resolution of infinities, QED had mostly reached its final form, being still  
 1209 today the most accurate physical theory, and would serve as a model to build all other quantum field  
 1210 theories.

1211 **Development of the quark model and Quantum Chromodynamics**

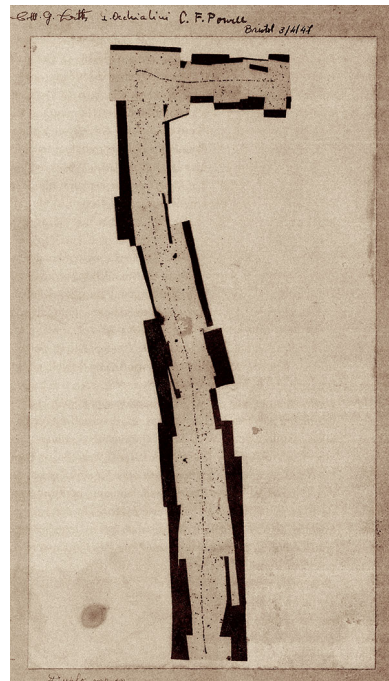
1212 To explain the nuclear force that holds *nucleons*  
 1213 (protons and neutrons) together, Yukawa proposed  
 1214 in 1934 the existence of a force carrier called *meson*  
 1215 due to its predicted mass in the range in between the  
 1216 electron and nucleon masses [48]. Discovered in  
 1217 1936 by Anderson and Neddermeyer [49, 50], and  
 1218 confirmed using bubble chambers in 1937 by Street  
 1219 and Stevenson [51], a first meson candidate was ob-  
 1220 served in the decay products of cosmic rays. As-  
 1221 suming it had the same electric charge as electrons  
 1222 and protons, this particle was observed to have a  
 1223 curvature due to magnetic field that was sharper  
 1224 than protons but smoother than electrons resulting  
 1225 in a mass in between the two. But its properties  
 1226 were not compatible with Yukawa's theory, which  
 1227 was emphasized by the discovery of a new candi-  
 1228 date in 1947, again in cosmic ray products using  
 1229 photographic emulsions [52–54]. The detections of  
 1230 the mu-meson and of the pi-meson in emulsions are  
 1231 showed in Figure 2.5.

1232 This new candidate, although it had a similar  
 1233 mass than the already believed *meson*, would rather  
 1234 decay into it. For distinction, the first candidate  
 1235 would then be renamed "*mu meson*" when the sec-  
 1236 ond would be the "*pi meson*". The *mu meson* was  
 1237 behaving like a heavy electron and didn't partici-  
 1238 pate in the strong interaction whereas the pion was  
 1239 believed to be the carrier of the nuclear interaction.  
 1240 This led to classify the *mu* in a new category of par-  
 1241 ticles that shared similar properties called *leptons*  
 1242 under the name of *muon* together with the electron.  
 1243 The *pi meson* was finally found to be a triplet of par-  
 1244 ticles: a positively charged, a negatively charged,  
 1245 and a neutral particle. The neutral *pi meson* has  
 1246 been more difficult to identify as it wouldn't leave  
 1247 tracks on emulsions nor on bubble chambers and  
 1248 needed to be studied via its decay products. It was  
 1249 ultimately identified in University of California's  
 1250 cyclotron in 1950 through the observation of its decay into 2 photons [55].

1251 Also discovered in 1947 but in cloud chamber photographs, the *K meson* has also been an impor-



(a)



(b)

Figure 2.5: Figure 2.5a: decay of a  $\mu$ -meson in an emulsion. Figure 2.5b: track of a  $\pi$ -meson in an emulsion signed by Lattes, Powell, and Occhialini.

tant step towards the establishment of the Standard Model [56]. A triplet of particles, two charged and a neutral, with a mass roughly half that of a proton, were reported. These particles were baptised *K meson* in contrast to the "light" *pi* and *mu* "L-mesons". The particularity of the *K* is their very slow decays with a typical lifetime of the order of  $10^{-10}$ s much longer than the  $10^{-23}$ s of *pi*-proton reactions. The concept of *strangeness*, a new quantum number was then introduced thanks to an idea of Pais as an attempt to explain this phenomenon as *strange* particles appeared as the pair production of a strange and anti-strange particle [57].

With the development of synchrotrons, the particle *zoo* grew to several dozens during the 1950s as higher energies were reachable through acceleration. In 1961, a first classification system, called *Eightfold Way*, was proposed by Gell-Mann [58]. It found its roots in the Gell-Mann–Nishijima formula, which relates the electric charge  $Q$ , the third component of the isospin  $I_3$ , the *baryon* number  $B$  and the strangeness  $S$ , as showed in Formula 2.6 [59–61].

$$(2.6) \quad Q = I_3 + \frac{1}{2}(B + S)$$

The isospin is a quantum number introduced in 1932 to explain symmetries of the newly discovered neutron using representation theory of SU(2) [62]. The baryon number, was introduced by Nishijima as a quantum number for baryons, i.e. particles of the same family as nucleons [59]. The mesons were classified in an octet and baryons of spin  $\pm \frac{1}{2}$  and  $\pm \frac{3}{2}$  were respectively classified into an octet and a decuplet, as shown in Figure 2.6. To complete the baryon decuplet, Gell-Mann predicted the existence of baryon  $\Omega^-$  which would later be discovered in 1964 [63].

Gell-Mann, and independently Zweig, then proposed a full theoretical model in which *hadrons* (strongly interacting particles, i.e. mesons and baryons) were not elementary particles anymore [64–66]. They were rather composed of three flavors of particles called *quarks* and their anti-particles. The three flavors were called *up*, *down* and *strange*. *Up* and *down* were used to explain the nucleons and non-strange mesons, while *strange* came into the composition of hadrons showing strangeness. *Up* and *down* flavors were discovered in 1968 thanks to the deep inelastic scattering experiments conducted at the Stanford Linear Accelerator Center (SLAC) [67, 68], and *strange* could only be indirectly validated even though it provided a robust explanation to *kaon* (*K*) and *pion* ( $\pi$ ).

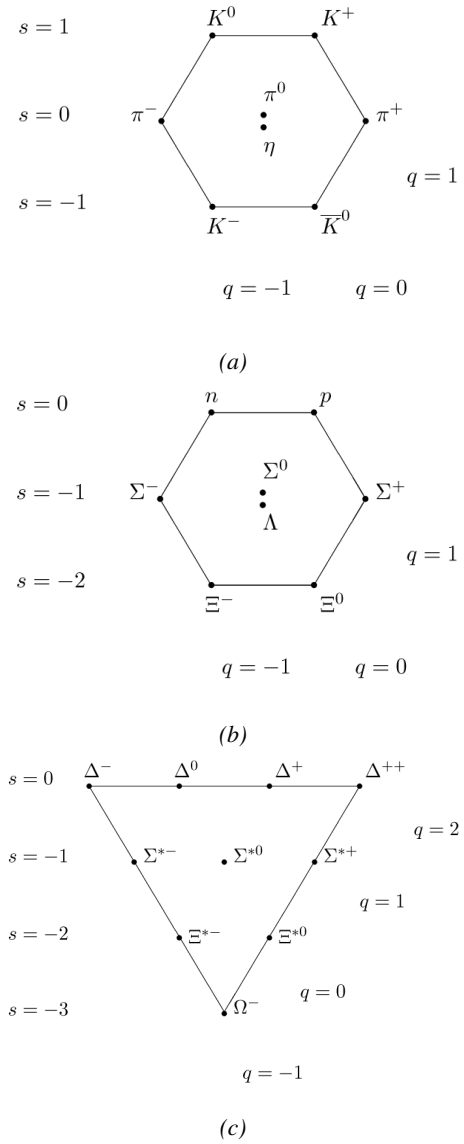
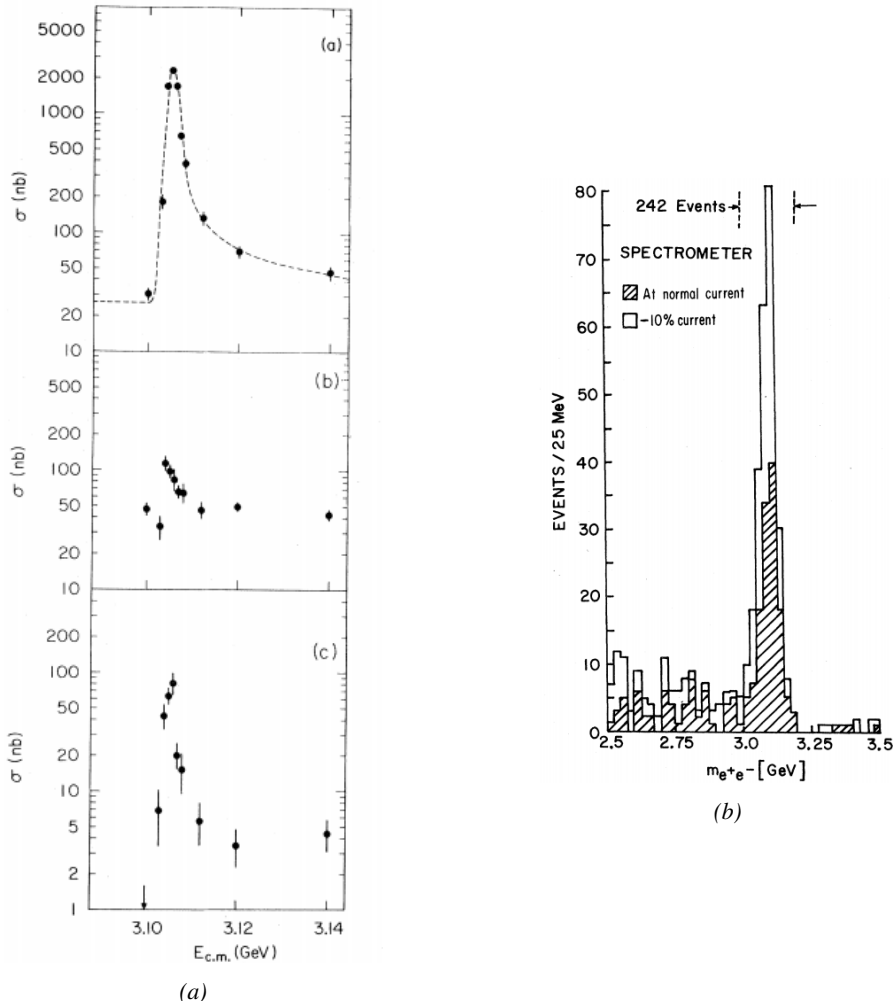


Figure 2.6: Figure 2.6a: Meson octet. Figure 2.6b: Baryon octet. Figure 2.6c: Baryon decuplet.

However, in the decade following the Gell-Mann-Zweig quark model proposition, several improvement to the model were brought. First by Glashow and Bjorken the same year that predicted the existence of a fourth quark flavor, the *charm*, that would equalize the then known number of quarks and leptons [69, 70]. Finally in 1973 by Kobayashi and Maskawa that increased the number of quarks to six to explain the experimental observation of CP violation [71, 72]. These two quarks were referred to as *top* and *bottom* for the first time in 1975 [73]. It's only after these additions to the quark model that finally the *charm* was discovered in 1974 at both SLAC and Brookhaven National Laboratory (BNL) [74, 75]. A meson in which the *charm* is bonded with an *anti-charm*, called  $J/\psi$  and presented in Figure 2.7, helped convince the physics community of the validity of the model. The *bottom* was discovered soon after in 1977 in Fermilab [76] and indicated the existence of the *top* that resisted to discovery until Fermilab's experiments CDF and D $\emptyset$  in 1995 due its very large mass and the energy needed to produce it [77, 78].



*Figure 2.7: Discovery of the  $J/\Psi$  by both SPEAR (SLAC [74]) in Figure 2.7a and AGS (BNL [75]) in Figure 2.7b. In Figure 2.7a, the cross section versus energy is showed for (a) multi hadron final states, (b)  $e^+e^-$  final states, and (c)  $\mu^+\mu^-$ ,  $\pi^+\pi^-$  and  $K^+K^-$  final states.*

As remarked by Struminsky, due to mesons such as  $\Omega^-$  or  $\Delta^{++}$ , the first SU(3) model already should have possessed an additional quantum number [79]. Indeed, these mesons are composed of three identical quarks, respectively three *strange* and *up* quarks, with parallel spins, which should be forbidden by the exclusion principle. Independently, Greenberg, and Han and Nambu proposed an additional SU(3) degree of freedom for the quarks [80, 81]. It was later referred to as *color charge gauge*, that could interact through *gluons*, the gauge boson octet corresponding to this degree of freedom. The color field is presented in Figure 2.8a. Nevertheless, as observing free quarks to prove their existence proved to be impossible, two visions of the quarks were argued. On one side, Gell-Mann proposed to see quarks as mathematical construct instead of real particles, as they are always confined, implying that quantum field theory would not describe entirely the strong interaction. He promoted the S-matrix approach to treat the strong interaction. Opposed to this vision, Feynman on the contrary argued that quarks are real particles, that he would call *partons*, that should be described as all other particles by a distribution of position and momentum [82]. The implications of quarks as point-like particles were verified at SLAC and helped abandon the S-matrix to the benefit of QFT [83]. The concept of *color* was then added to the quark model in 1973 by Fritzsch and Leutwyler together with Gell-Mann to propose a description of the strong interaction through the theory of Quantum Chromodynamics (QCD) [84]. The discovery the same year of asymptotic freedom within the QCD by Gross, Politzer, and Wilczek, allowed for very precise predictions thanks to perturbation theory [85, 86]. The evolution of the gauge constant of QCD with respect to the energy as described by asymptotic freedom is showed in Figure 2.8b.

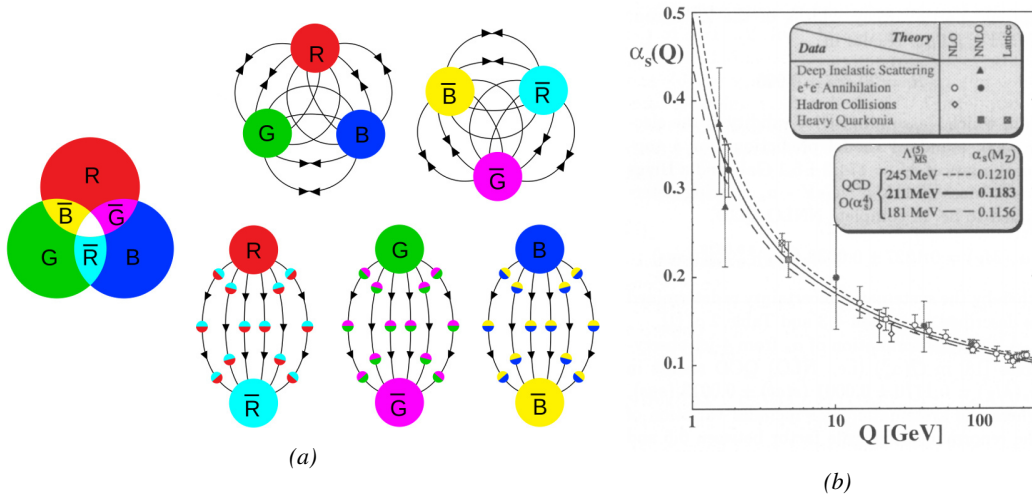
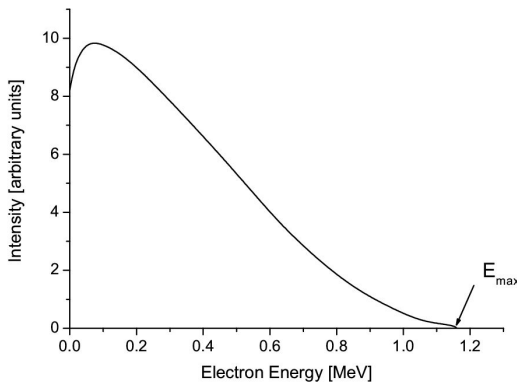


*Figure 2.8: Figure 2.8a: the color field of QCD only allows for "white" baryons, particles composed of quarks, to exist. Examples are given for mesons, composed of a quark and its anti-quark, and hadrons, composed of three differently colored quarks or anti-quarks. Other exotic baryons have been predicted and observed, such as tetraquarks and pentaquarks. Figure 2.8b: a crossed analysis performed thanks to the data collected by various experiments at different energies have showed that the coupling constant evolves as predicted by the mechanism of asymptotic freedom [87].*

1327 **The Weak interaction, spontaneous symmetry breaking, the Higgs mechanism and the Elec-**  
 1328 **treweak unification**

1329 The weak interaction is the process that causes radioactive decays. Thanks to the neutron discov-  
 1330 ery [23], Fermi could explain in 1934 beta radiations through the beta decay process in which the  
 1331 neutron decays into a proton by emitting an electron [88]. Though the missing energy observed dur-  
 1332 ing this process triggered a huge debate about the apparent non-conservation of energy, momentum  
 1333 and spin of the process, Fermi, as Pauli before him [89], proposed that the missing energy was due to  
 1334 a neutral not yet discovered particle that was then baptised *neutrino*. The impossibility to detect such  
 1335 a particle left some members of the scientific community sceptical, but hints of energy conservation  
 1336 and of the existence of the neutrino were provided by measuring the energy spectrum of electrons  
 1337 emitted through beta decay, as there was a strict limit on their energy, as showed in Figure 2.9.



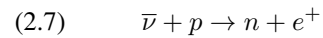
1348 *Figure 2.9: Energy spectrum of beta particles emitted by a source*  
 1349 *of  $^{210}\text{Bi}$ .*

1350 constraint the beta decay theory of Fermi and extend it to the case of the muon, Konopinski and  
 1351 Mahmoud proposed in 1953 that the muon decay would eject a particle similar to the neutrino [91].  
 1352 They predicted the existence of a muon neutrino that would be different to the one involved in the  
 1353 beta decay, related to the electron. With this, the idea of *lepton number* arised. The *muon neutrino*  
 1354 was successfully detected in 1962 by Lederman, Schwartz, and Steinberger [92].

1355 The theory could not be valid though as the probability of interaction, called *cross-section*, would  
 1356 have been increasing without limitation with the square of the energy. Fermi had proposed a two  
 1357 vector current coupling but Lee and Yang noted that an axial current could appear and would violate  
 1358 parity [93]. Gamov and Teller had already tried to account for such parity violation by describ-  
 1359 ing Fermi's interaction through allowed (parity-violating) and superallowed (parity-conserving) de-  
 1360 cays [94]. The Wu experiment in 1956 confirmed the parity violation [95], as showed by Figure 2.10.  
 1361 But the success of QED as a quantum field theory sparked the development of similar theory to de-  
 1362 scribe the weak interaction.

1363 As previously discussed, the great success of QED was built on an underlying symmetry, inter-  
 1364 preted as a gauge invariance so that the effect of the force is the same in all space-time coordinates,  
 1365 and of the possibility to renormalize it in order to resolve infinities. In 1967, Weinberg found a  
 1366 way to unite both the electromagnetic and weak interaction into a gauge theory involving four gauge  
 1367 bosons, three of which are massive and carry out the weak interaction and the last is a massless bo-

1338 It's only 30 years later in 1953  
 1339 that it was discovered by the team of  
 1340 Cowan and Reines using the prin-  
 1341 ciple of inverse beta decay described  
 1342 through Formula 2.7 [90].



1343 The experiment consisted in  
 1344 placing water tanks sandwiched in  
 1345 between liquid scintillators near a  
 1346 nuclear reactor with an estimated  
 1347 neutrino flux of  $5 \times 10^{13} \text{ cm}^{-2} \text{ s}^{-1}$ .  
 1348 However, in order to explain the ab-  
 1349 sence of some reactions in the ex-  
 1350 periment of Cowan and Reines and

son carrying the electromagnetic interaction [96]. Among the three massive bosons, two are charged and one is neutral, similarly to the previously theorized *pi meson* vector of the Yukawa model [48] and all have a mass much greater than nucleons and thus a very short life time implying a finite very short range, contrary to the contact interaction originally proposed by Fermi.

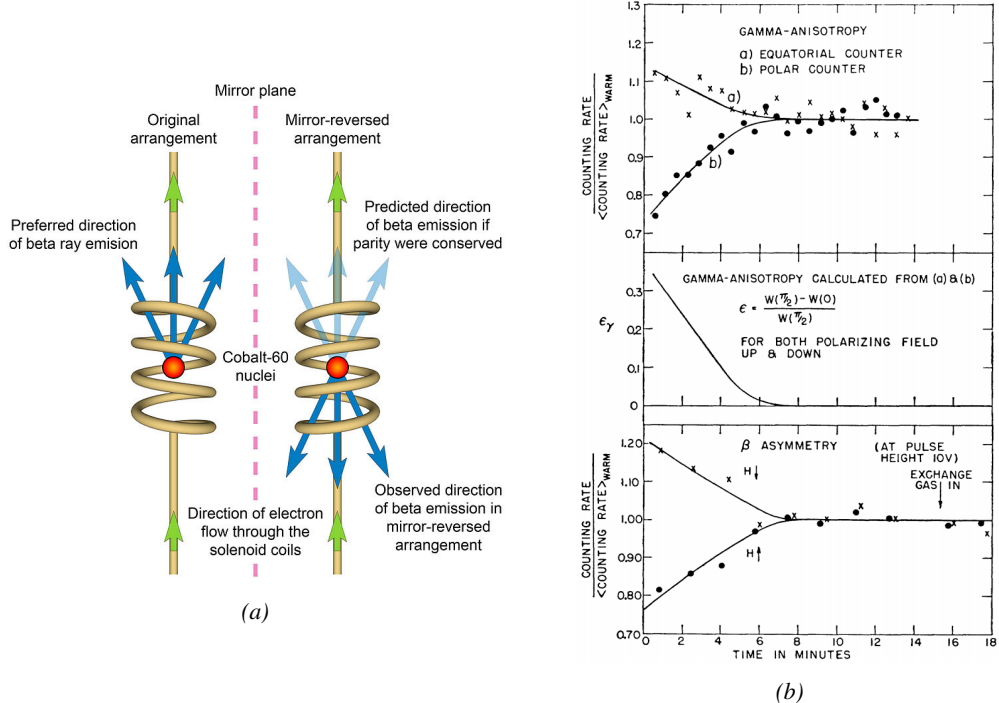


Figure 2.10: As explained through Figure 2.10a, the Wu experiment consisted in measuring the preferred direction of emission of beta rays of a Cobalt source placed in a stable magnetic field aligned, in one case, and anti-aligned, in the other case, with the nuclear spin. The result of Figure 2.10b showed a violation of parity.

Breakthroughs in other fields of physics contributed in giving theoretical support and interpretation to the unified electroweak theory. The stepping stone was the use of spontaneous symmetry breaking that was inspired to Nambu at the beginning of the 1960s [97, 98] following the development of the Bardeen–Cooper–Schrieffer (BCS) superconductivity mechanism in 1957 [99]. Cooper had shown that BCS pairs, pairs of electrons bound together at low temperature, can have lower energy than the Fermi Energy and are responsible for superconductivity. This led to the discovery of Goldstone-Nambu bosons [100, 101] as a result of the spontaneous breaking of the chiral symmetry in a theory describing nucleons and mesons developed by Nambu and Jona-Lasinio in 1961, and now understood as a low-energy approximation of QCD. Similarly to the mechanism of energy gap appearance in superconductivity, the nucleon mass is suggested to be the result of a self-energy of a fermion field and is studied through a four-fermion interaction in which, as a consequence of the symmetry, bound states of nucleon-antinucleon pairs appear and can be regarded as virtual pions. Though the symmetry is maintained in the equations, the ground state is not preserved. Goldstone showed that the bound states correspond to spinless bosons with zero mass [101].

Although the model in itself didn't revolutionize particle physics, spontaneous symmetry breaking was generalized to quantum field theories. As all fundamental interactions are described using

gauge theories based on underlying symmetries, processes such as the chiral symmetry breaking were introduced soon after the publication of Nambu and Jona-Lasinio. In 1962, Anderson, discussed the implications of spontaneous symmetry breaking in particles physics [102]. He did so by following the idea of Schwinger who suggested that zero-mass vector bosons were not necessarily required to describe the conservation of baryons, contrary to the bosons emerging from chiral symmetry breaking [103]. A model was finally independently built in 1964 by Brout and Englert [104], Higgs [105], and Guralnik, Hagen, and Kibble [106], who discovered that combining an additional field into a gauge theory in order to break the symmetry, the resulting gauge bosons acquire a nonzero mass. Moreover, Higgs stated that this implied the existence of at least one new massive, i.e. self-interacting, scalar boson corresponding to this additional field, that is now known as *Higgs boson*. The Higgs mechanism today specifically refers to the process through which the gauge bosons of the weak interaction acquire mass. In 1967, Weinberg could point to the Higgs mechanism to integrate a Higgs field into a new version of the electroweak theory in which the spontaneous symmetry breaking mechanism of the Higgs field would explicitly explain the masses of the weak interaction gauge bosons and the zero-mass of photons [96].

### 2.1.2 Construction and validation of the Standard Model

The Standard Model of particle physics was built in the middle of the 1970s after the experimental confirmation of the existence of quarks [107]. It is based on the assembly of the models previously introduced and describing the fundamental interactions and their gauge bosons, except for gravitation, as well as the way elementary "matter" particles interact with the fields associated with these force carriers. In this sense, the development of QED and the unification of the electroweak interaction, of the Yukawa interaction and of QCD, and of the Higg mechanism made it possible to explain most of the contemporary physics.

In the SM, "matter" particles, are described by twelve fermion fields of spin  $\frac{1}{2}$  obeying the Fermi-Dirac statistics, i.e. subjected to the Pauli exclusion principle. To each fermion is associated its corresponding anti-particle. The fermions are classified according to the way they interact and thus according to the charges they carry. Six of them are classified as quarks ( $u, d, c, s, t$ , and  $b$ ) and are subjected to all interactions and the six others as leptons ( $e^-, \mu^-, \tau^-, \nu_e, \nu_\mu$ , and  $\nu_\tau$ ). Leptons are not subjected to the strong interaction and among them, the three neutrinos only interact weakly as they are neutral particles, which explains why they are so difficult to detect. The gauge boson fields are the gluons  $g$  for the strong interaction, the photon  $\gamma$  for the electromagnetic interaction and the weak bosons  $W^+, W^-$ , and  $Z^0$  for the weak interaction. Finally, the Higgs field  $H^0$  is responsible, through the spontaneous symmetry breaking, of the mixing of the massless electroweak boson fields  $W_1, W_2, W_3$ , and  $B$  leading to the observable states  $\gamma, W^+, W^-$ , and  $Z^0$  that can gain mass while interacting with the Higgs field. This picture of the SM is summarized through Figure 2.11 where the antifermions are not shown.

When the model was first finalized, the existence of the weak gauge bosons, of the charm, of the third quark generation composed of top and bottom quarks to explain the observed CP violation was not proven but the predictions were measured with good precision in the years following [74–78]. The weak bosons  $W$  and  $Z$  were discovered during the next decade in 1983 [108–111]. The very last predicted elementary particle of the model that was not observed yet proved to be very difficult to observe. The Higgs boson needed the start of the LHC to finally be observed in 2012 [112, 113]. A few years more of tests were necessary to measure its properties to confirm the observation of a scalar boson compatible with the predicted Higgs boson  $H^0$  [114].

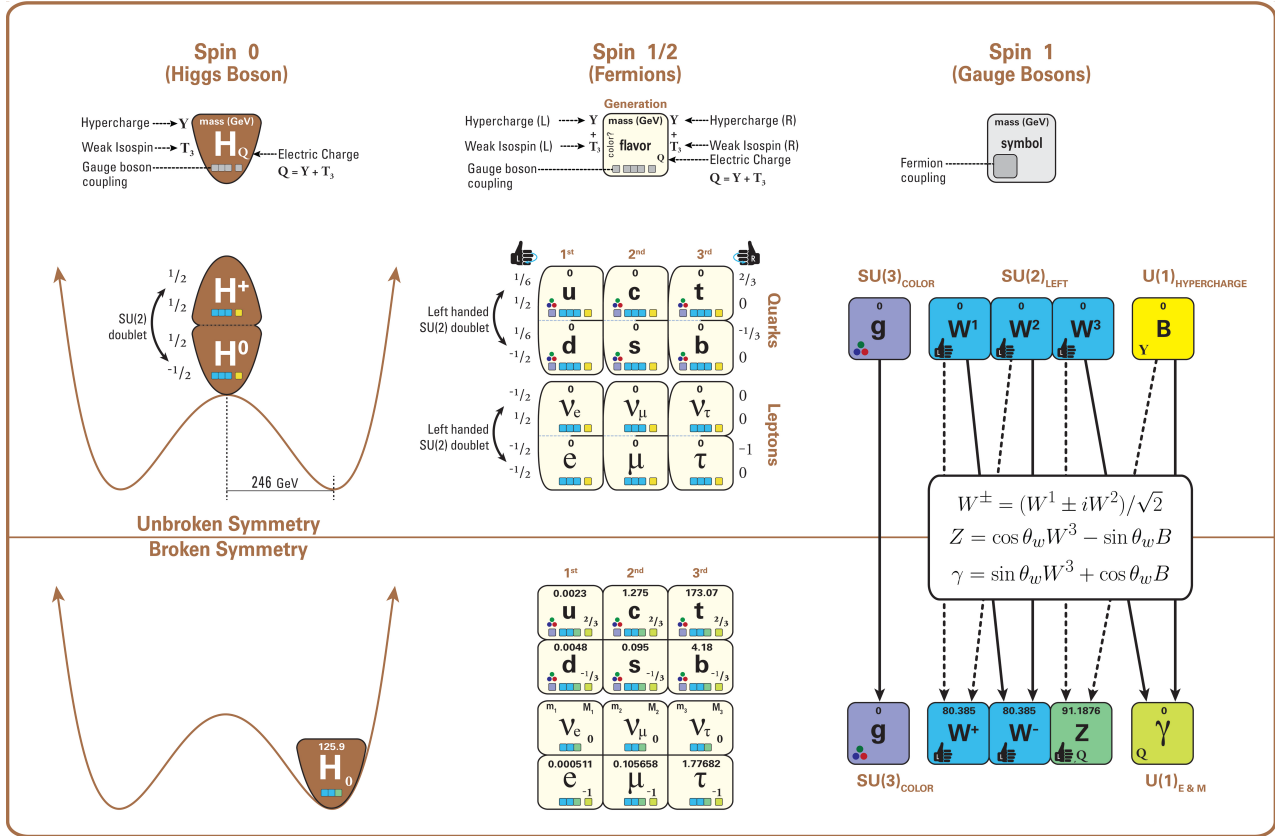


Figure 2.11: The elementary particles of the Standard Model are shown along with their properties. Their interactions with the strong, weak and electromagnetic forces have been made explicit using color squares. In the left column, the scalar Higgs boson is depicted. The center is focused on the matter particles, the fermions, and the right column on the force carriers, the gauge bosons. The role of the Higgs boson in electroweak symmetry breaking is highlighted, and the corresponding way properties of the various particles differ in the (high-energy) symmetric phase (top) and the (low-energy) broken-symmetry phase (bottom) are shown.

### 1433 2.1.3 Investigating the TeV scale

1434 In High-Energy Physics, the number of experimental events depends on the total interaction cross-  
 1435 section of the colliding particles and of the *instantaneous luminosity* [115]. The luminosity is a  
 1436 quantity providing an information on the interaction rate normalised to the interaction cross-section.  
 1437 The relationship between number of events  $N$ , cross-section and instantaneous luminosity  $\mathcal{L}$  is given  
 1438 in Formula 2.8.

$$(2.8) \quad \mathcal{L} = \frac{1}{\sigma} \frac{dN}{dt} \Leftrightarrow N = \sigma \int \mathcal{L} dt = \sigma \mathcal{L}_{int}$$

1439 The integral of the luminosity over time is referred to as the *integrated luminosity*  $\mathcal{L}_{int}$ . In fact,  
 1440 the instantaneous luminosity can be deduced from the beam parameters. New colliders now use  
 1441 bunched beams. The instantaneous luminosity then depends on the bunch crossing frequency  $f_{BX}$ ,  
 1442 on the number of particles contained in each bunch  $n$ , and on the RMS transverse beam sizes in the

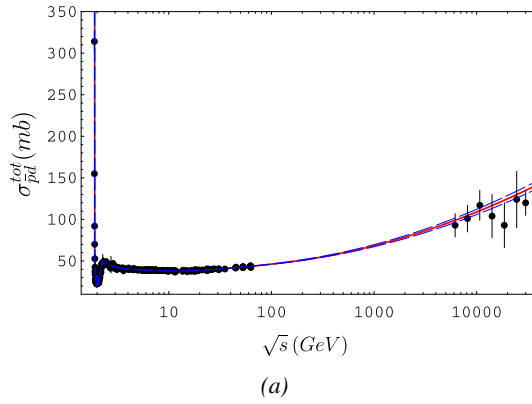
1443 horizontal,  $\sigma_x^*$ , and vertical directions,  $\sigma_y^*$ , at the level of the interaction point. The beam sizes can  
 1444 be assumed to be identical, leading to the relation of Formula 2.9.

$$(2.9) \quad \mathcal{L} = f_{BX} \frac{n^2}{\sigma^*}$$

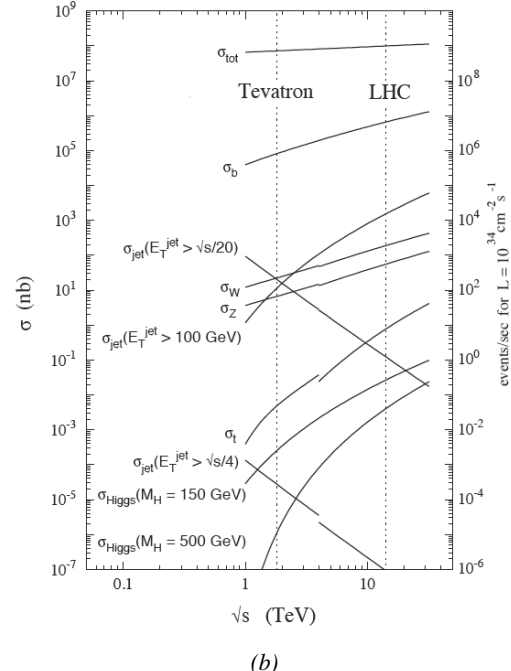
1445 This expression doesn't depend on time  
 1446 anymore and leads to a simple estimation of  
 1447 the integrated luminosity and hence, knowing  
 1448 the cross-section of each available physics  
 1449 channel, to the expected number of events in  
 1450 each channel. The total interaction cross section  
 1451 is the sum of all the different output channels  
 1452 allowed by the interaction process. In the  
 1453 case of highly relativistic protons, the proton-  
 1454 proton (pp) total cross-section increases with  
 1455 the center-of-mass energy of interactions, as  
 1456 can be seen from Figure 2.12.

1457 Enhancing rare processes that allow to  
 1458 finely test the Standard Model is then achieved  
 1459 through an increase in both energy and luminosity.  
 1460 At the energy range that were scanned  
 1461 thanks to high-energy colliders, the SM has so  
 1462 far been a well tested theory. Nevertheless,  
 1463 several hints of physics going beyond its scope  
 1464 have been observed.

1465 **Dark matter and gravity:** The discrepancy  
 1466 of velocity dispersion of stars in galaxies with  
 1467 respect to the visible mass they contain is  
 1468 known since the end of the 19<sup>th</sup> century where  
 1469 Kelvin proposed that this problem could be  
 1470 solved if a great majority of the stars would  
 1471 be dark bodies, idea strongly criticized by  
 1472 Pointcaré [117]. Throughout the 20<sup>th</sup> century,  
 1473 physicists like Kapteyn [118] or Zwicky [119,  
 1474 120], showed the first hints of a *dark matter*  
 1475 by studying star velocities and galactic  
 1476 clusters, followed by robust measurements of  
 1477 galaxy rotation curves by Babcock which sug-  
 1478 gested that the mass-to-luminosity ratio was  
 1479 different from what would be expected from  
 1480 watching the visible light [121]. Later in the  
 1481 1970s, Rubin and Ford from direct light obser-  
 1482 vations [122] and Rogstad and Shostak from  
 1483 radio measurements [123] showed that the ra-  
 1484 dial velocity of visible objects in galaxies was increasing with increasing distance to the center of



(a)



(b)

Figure 2.12: Figure 2.12a: Total proton-proton cross-section as a function of the collisions center-of-mass energy  $\sqrt{s}$  [116] with cosmic-ray data from Akemo Observatory and Fly's Eye Collaboration. Figure 2.12b: Total proton-(anti)proton and interaction channel cross-sections in the TeV scale.

events/sec for  $L = 10^{34} \text{ cm}^{-2} \text{ s}^{-1}$

the galaxy. An example of galaxy rotation curve is provided in Figure 2.13. Finally observation of lensing effect by galaxy clusters, temperature distribution of hot gas in galaxies and clusters, and the anisotropies in the Cosmic Microwave Background (CMB), showed in Figure 2.14, kept on pointing to a *dark matter* [124]. From all the data accumulated, the visible matter would only account to no more than 5% of the total content on the visible universe [125]. Alternative theories have tried to investigate modified versions of the General Relativity as this theory is only well tested at the scale of the solar system but is not sufficiently tested on wider ranges or even theories in which gravitation is not a fundamental force but rather an emergent one [126, 127]. But so far, such theories have difficulties to reproduce all the experimental observations as easily as through dark matter.

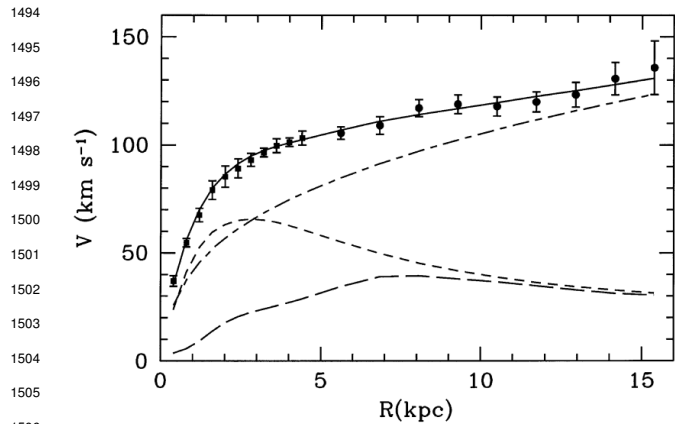


Figure 2.13: Rotation curve (points) of the galaxy M33 compared with best fitting model (line). The short-dashed line represents the rotation profile that would be expected from the observation of the stellar disc alone [128].

into a light Higgs boson compared to the *Planck Mass*. In the SM, the Higgs mass is left to be a measured parameter rather than a calculated one even though the model requires a mass in between 100 and 1000 GeV/c<sup>2</sup> to stay unitary. Nevertheless, quantum corrections to the Higgs mass coming from its interactions with virtual particles should make the scalar boson much heavier than what measured [130]. Through the MSSM, the stability of fermion masses would provide stability to the Higgs boson mass via the introduction of a fermionic super partner.

On top of providing a solution to the Hierarchy Problem, the model comes with heavy dark matter candidates in the TeV scale [131]. Indeed, in the case *R-parity* is not violated, the lightest supersymmetric particle (LSP) cannot decay and could then explain the dark matter. The LSP in the model is neutral and can only interact through the weak and gravitational interactions. Typical candidates are the *neutralino*, the *sneutrino* or the *gravitino*.

Finally, gravity is not explained through the SM, and huge difficulties are encountered when trying to include it. The strength of gravitational interaction is expected to be negligible at the scale of elementary particles, nevertheless, adding gravitation in the perspective of developing a "theory of everything" leads to divergent integrals that could not be fixed through renormalization. Extensions to the MSSM, and in particular minimal SUper GRAvity (mSUGRA), include general relativity as mediator of the symmetry breaking. mSUGRA gives access to the hidden sector in which the MSSM only interacts gravitationally and suppresses the infinities arising from attempts to include gravity into the SM thanks to possible renormalization [132].

Signatures for the MSSM would come from the super partners of quarks and gluons that can

A possible theory to offer dark matter candidates would be *supersymmetry* (SUSY) which proposes a relationship in between bosons and fermions in the frame of the Minimal Supersymmetric Standard Model (MSSM). In this model, each elementary particle, through a spontaneous space-time symmetry breaking mechanism would have a *super partner* from the other family of particles, pairing bosons and fermions together. The model was first introduced as a way to solve the *Hierarchy Problem* [129]. The discrepancy between the strength of the weak force and gravity translates

decay into an LSP that could then be identified as missing energy as it escapes the detectors undetected. But even in the case MSSM predictions are not to be seen, the other models treating dark matter also propose Weakly Interacting Massive Particles (WIMPs) that could be observed in similar ways than LSPs [133]. Moreover alternative models exist to provide solutions to the Hierarchy Problem. The most investigated models are extra dimensions such as Arkani-Hamed Dimopoulos Dvali [134, 135], Kaluza–Klein [136, 137] or Randall-Sundrum models [138, 139] that usually also include gravitation. Finally, alternative models also exist for the production of dark matter candidates. Models with a hidden valley that would unravel the existence of a new group of light particles through the extension of the SM with a new confining gauge group [140].

1540

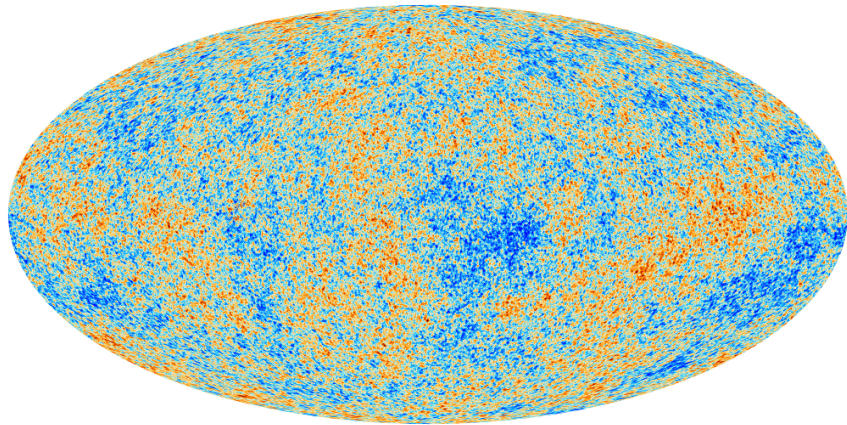


*Figure 2.14: Cosmic Microwave Background as measured by the space observatory Planck which mean temperature is  $T_\gamma = (2.7255 \pm 0.0006)\text{K}$  with anisotropies of the order of a few  $\mu\text{K}$ .*

1541 **Baryon asymmetry:** Another intriguing fact is that the universe is dominated by matter. However,  
 1542 the SM predicted that matter and antimatter should have been created in equal amounts. For an inter-  
 1543 action to produce matter and antimatter at different rates within the SM, three necessary conditions  
 1544 were highlighted by Sakharov[141]. First of all, there must be a violation of the baryon number  $B$ .  
 1545 Then, there must be a C-symmetry and CP-symmetry violation. The C-symmetry violation must  
 1546 happen to make sure that the processes creating more baryons than antibaryons are not compensated  
 1547 by processes creating more anti-baryons and similarly, the CP-symmetry violation makes sure that  
 1548 there are not equal numbers of left-handed baryons and right-handed anti-baryons produced. Fi-  
 1549 nally, the interactions must happen out of thermal equilibrium to make sure that CPT-symmetry does  
 1550 not balance the processes increasing the baryon number with processes doing otherwise [142]. An  
 1551 out-of-equilibrium interaction implies a new unstable heavy particle.

1552 The favoured model to explain this imbalance is the *baryogenesis* that requires electroweak sym-  
 1553 metry breaking to be first order phase transition to fall within the scope of SM [143, 144]. This  
 1554 means that the symmetry breaking process must involve the absorption or release of a fixed latent  
 1555 heat. Through the baryogenesis, the phase transition breaks P-symmetry spontaneously and allows  
 1556 for CP-symmetry violation. In turn, the CP violation makes the amplitude of interactions involving  
 1557 quarks different than the ones involving anti-quarks leading to the greater creation rate of baryons  
 1558 with respect to anti-baryons. The key to this baryon net creation would be found into the *sphaleron*.  
 1559 A sphaleron is a particle-like saddle point of the energy functional that appears at the top of the

1560 transition barrier and that could be created if a sufficiently large amount of energy is brought as the  
 1561 tunneling effect through the barrier is largely suppressed for electroweak interactions. The existence  
 1562 of the sphaleron would allow violation of the conservation of  $B$  but also of the leptonic number  $L$   
 1563 while conserving  $B - L$ . The detection at  $p - p$ -colliders of such a transition is foreseen to be made  
 1564 through processes with high-multiplicity final states such as  $u + u \rightarrow e^+ \mu^+ \tau^+ t\bar{t} b\bar{c} c\bar{s} d\bar{d} + X$  [145]. To  
 1565 be probed, the sphaleron transition requires an energy  $E_{sph} \approx 9$  TeV. Nevertheless, if such transition  
 1566 cannot be observed, other BSM models such as the WIMP baryogenesis could be then observed  
 1567 thanks to the detection of displaced vertices, featuring the decay of a WIMP leading to violation of  
 1568  $B$  [146].

1569 Another possibility to explain the apparent asymmetry would be the existence of an electric  
 1570 dipole moment (EDM) in any fundamental particle that would permit matter and antimatter particles  
 1571 to decay at different rates [147]. Indeed, the presence of an EDM violates in itself both  $P$  and  $T$   
 1572 symmetries. Experiments are able to probe for the EDM of various fundamental particles such as the  
 1573 electron [147], the charm and strange quarks [148] or even a heavy neutrino EDM [149].  
 1574

1575 **Neutrino mass and sterile neutrino scenario:** The SM considers neutrinos to be massless. But  
 1576 it was showed in the late 1960s by the Homestake experiment that the flux of solar neutrinos (i.e.  
 1577  $\nu_e$ ) measured didn't match the predicted values [150]. The mechanism of neutrino oscillations as a  
 1578 solution to the discrepancy was proposed by Pontecorvo [151] and confirmed in the early 2000s by  
 1579 the Sudbury Neutrino Observatory [152]. This oscillation implies that neutrinos that can be observed  
 1580 are a superposition of massive neutrino states. The research on neutrino oscillation is already quite  
 1581 advanced with experiments looking at atmospheric, reactor or beam neutrinos in order to determine  
 1582 the elements of the mixing matrix (Pontecorvo–Maki–Nakagawa–Sakata matrix [153]) similar to the  
 1583 Cabibbo–Kobayashi–Maskawa (CKM) matrix describing the mixing of quarks [72]. Nevertheless,  
 1584 no answer to the origin of neutrino mass is yet provided.

1585 Explaining the light non-zero mass of the neutrinos  $\nu_l$  ( $l = e, \mu, \tau$ ) of the order of the eV can be  
 1586 done through the Seesaw mechanism [154, 155]. This model features heavy Majorana counterparts  
 1587  $N_l$  ( $l = e, \mu, \tau$ ) to the  $\nu_l$ . The masses of the light and heavy neutrinos are linked through a  $2 \times 2$   
 1588 mass matrix  $A$  with eigenvalues  $\lambda_{\pm}$  expressed as in Equation 2.10.

$$(2.10) \quad \begin{aligned} A &= \begin{pmatrix} 0 & M \\ M & B \end{pmatrix} \\ \lambda_{\pm} &= \frac{B \pm \sqrt{B^2 + 4M^2}}{2} \end{aligned}$$

1589 The Majorana mass term  $B$  is assumed to be comparable to the Grand Unified Theory scale  
 1590 ( $10^{16}$  GeV) while the Dirac mass term  $M$  is of the order of electroweak scale (246 GeV). In these  
 1591 conditions, the eigenvalue  $\lambda_+$  is almost  $B$  while  $\lambda_-$  is close to the ratio  $-M^2/B$  compatible with  
 1592 very light neutrinos with masses of the order of 1 eV. Studying the left-right symmetric model  
 1593 seeking for the parity violation in weak interactions leads to the incorporation of three additional  
 1594 gauge bosons  $W_R$  and  $Z'$  as a result of the spontaneous symmetry breaking. The processes that are  
 1595 predicted by the model and can be probed at colliders are processes such as  $pp \rightarrow W_R \rightarrow l + N_l + X$   
 1596 and  $pp \rightarrow Z' \rightarrow N_l + N_l + X$  where the heavy neutrinos decay as  $N_l \rightarrow l + j_1 + j_2$ ,  $j_i$  being  
 1597 jets [156]. Other version of seesaw mechanisms exist to account for the neutrino mass that can also  
 1598 be explained thanks to supersymmetric models [157].

## 1599 2.2 The Large Hadron Collider & the Compact Muon Solenoid

1600 Throughout its history, CERN has played a leading role in high-energy physics. Large regional facil-  
 1601 ities such as CERN were planned after the second world war in an attempt to increase international  
 1602 scientific collaboration and to allow scientists to share the forever increasing costs of experimental  
 1603 facilities. Indeed, it is necessary to use always more powerful tools to improve the fine understanding  
 1604 of our Universe. The construction of the first CERN accelerators at the end of the 50s, the Synchro-  
 1605 cyclotron (SC) and the Proton Synchrotron (PS), was directly followed by the first observation of  
 1606 antinuclei in 1965 [158]. The very first proton-proton collider showing hints of protons not being  
 1607 elementary particles was the Intersecting Storage Rings (ISR). From this experience, the Super Pro-  
 1608 ton Synchrotron (SPS) was built in the 70s to investigate the structure of protons, the preference  
 1609 for matter over antimatter, the state of matter in the early universe or exotic particles, and led to  
 1610 the discovery in 1983 of the W and Z bosons [108–111]. These newly discovered particles and the  
 1611 electroweak interaction were then studied in detail by the Large Electron-Positron (LEP) collider  
 1612 that proved that there only are three generations of elementary particles in 1989 [159]. The LEP was  
 1613 then dismantled in 2000 to allow for the LHC to be constructed in the existing tunnel.

### 1614 2.2.1 LHC, the most powerful particle accelerator

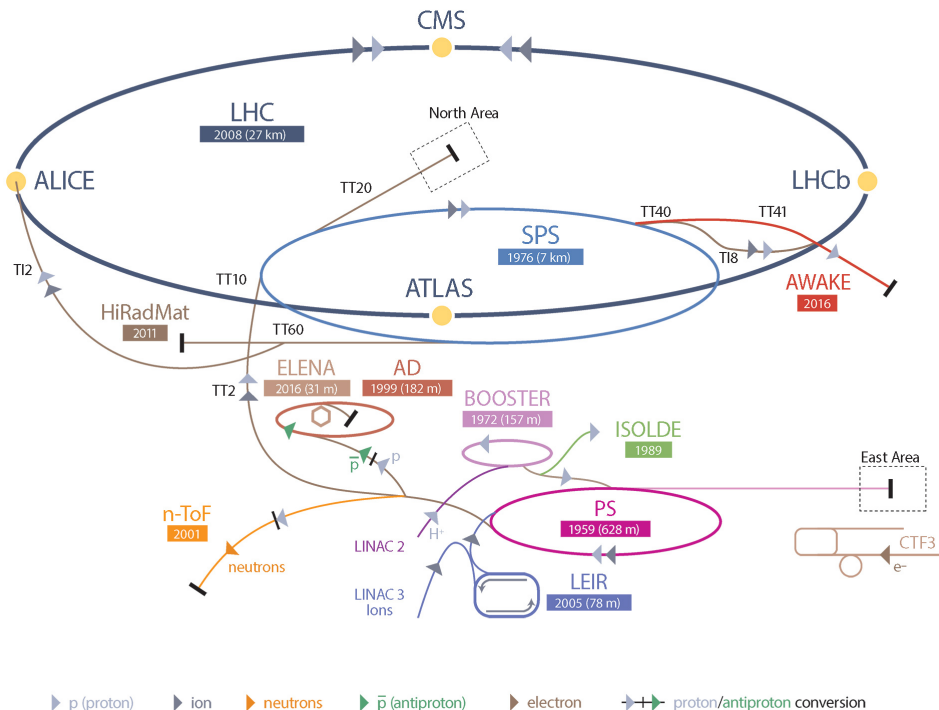


Figure 2.15: CERN accelerator complex.

1615 The different aspects of physics beyond the Standard Model of particle physics and the Standard  
 1616 Model itself can be tested through the use of very energetic and intense hadron and ion colliders.  
 1617 Powerful hadron colliders are suited for searching for strongly interacting particles. The LHC at

1618 CERN is a perfect tool to seek answers to these open questions and the experiments build along its  
 1619 beam lines already started investigating further into the SM and BSM physics.

1620 The LHC has always been considered as an  
 1621 option for the future of CERN. At the moment  
 1622 of the construction of the LEP beneath the border  
 1623 between France and Switzerland, the tunnel was  
 1624 built in order to accommodate what would be a  
 1625 Large Hadron Collider with a dipole field of 10 T  
 1626 and a beam energy in between 8 and 9 TeV [160].  
 1627 In 1985, the creation of a 'Working Group on the  
 1628 Scientific and Technological Future of CERN'  
 1629 took place to investigate such a collider [161].  
 1630 The decision was finally taken almost ten years  
 1631 later, in 1994, to construct the LHC in the LEP  
 1632 tunnel [162] and the approval of the 4 main ex-  
 1633 periments that would take place at the four inter-  
 1634 action points came in 1997 [163] and 1998 [164]:

- 1635 • ALICE [165] has been designed for the  
 1636 purpose of studying the confinement of  
 1637 quarks through exploration of the quark-  
 1638 gluon plasma that is believed to have been  
 1639 a state of matter that existed in the very first  
 1640 moment of the universe.
- 1641 • ATLAS [166] and CMS [167] are general  
 1642 purpose experiments that have been de-  
 1643 signed with the goal of continuing the ex-  
 1644 ploration of the Standard Model and the in-  
 1645 vestigation of new physics.
- 1646 • LHCb [168] has been designed to investi-  
 1647 giate the preference of matter over antimat-  
 1648 ter in the universe through CP violation.

1649 These large-scale experiments, as well as the  
 1650 full CERN accelerator complex, are displayed in  
 1651 Figure 2.15. The LHC is a 27 km long hadron  
 1652 collider and the most powerful accelerator used  
 1653 for particle physics since 2008 [169]. The LHC  
 1654 is designed to collide protons at a center-of-  
 1655 mass energy of 14 TeV and luminosity of  $10^{34}$   
 1656  $\text{cm}^{-2}\text{s}^{-1}$ , as well as  $Pb$  ions at a center-of-mass  
 1657 energy of 2.8 TeV/A with a peak luminosity of  
 1658  $10^{27} \text{ cm}^{-2}\text{s}^{-1}$ . The collider is the last of a long  
 1659 series of accelerating devices. Indeed, before be-  
 1660 ing accelerated by the LHC, the particles need to pass through different acceleration stages. All

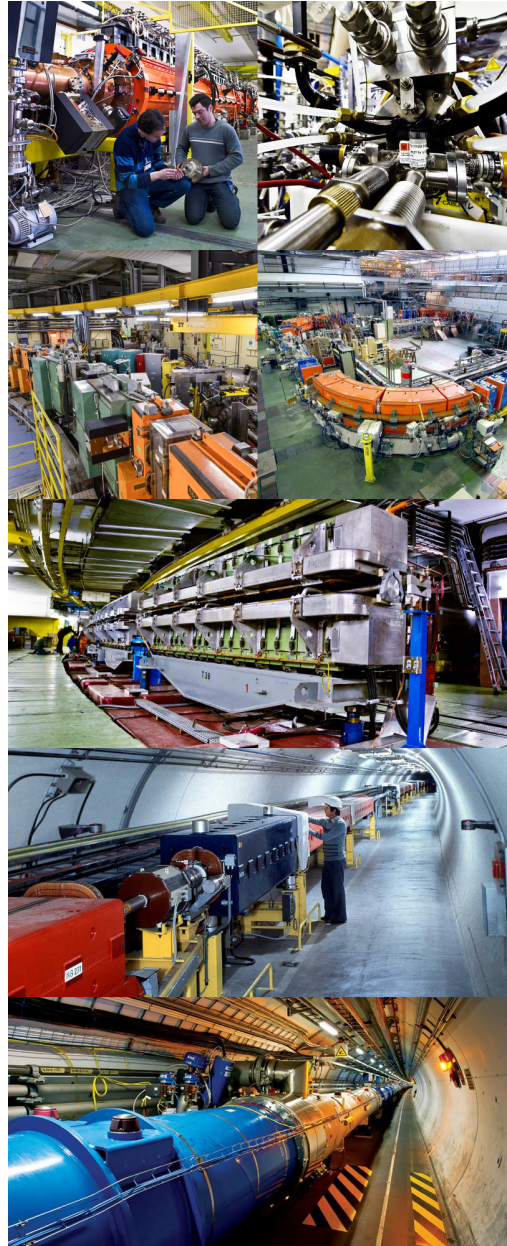


Figure 2.16: Pictures of the different accelerators. From top to bottom: first the LINAC 2 and the Pb source of LINAC 3. Then the Booster and the LEIR. Finally, the PS, the SPS and the LHC.

these acceleration stages are visible on Figure 2.15 and pictures of the accelerators are shown in Figure 2.16.

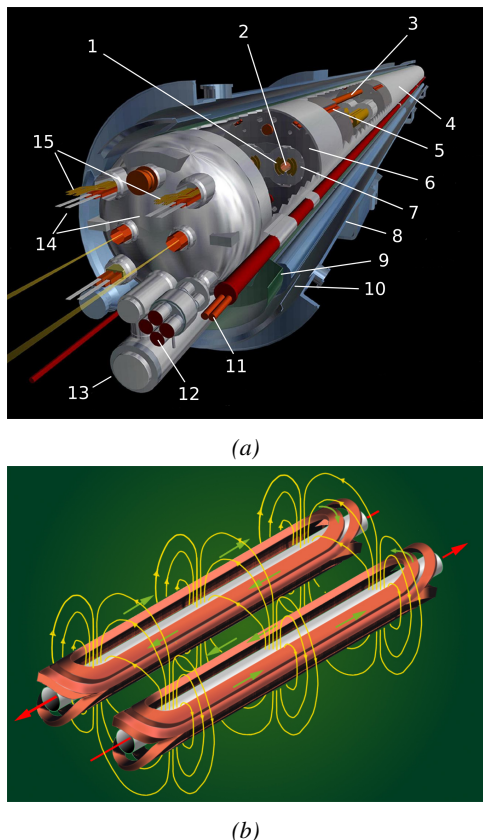
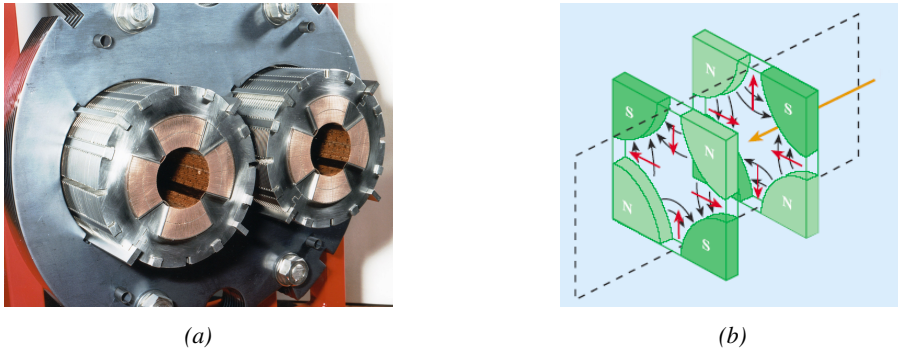


Figure 2.17: Figure 2.17a: schematics of the LHC cryodipoles. 1: Superconducting Coils, 2: Beam pipe, 3: Heat exchanger Pipe, 4: Helium-II Vessel, 5: Superconducting Bus-bar, 6: Iron Yoke, 7: Non-Magnetic Collars, 8: Vacuum Vessel, 9: Radiation Screen, 10: Thermal Shield, 11: Auxiliary Bus-bar Tube, 12: Instrumentation Feed Throughs, 13: Protection Diode, 14: Quadrupole Bus-bars, 15: Spool Piece Bus-bars. Figure 2.17b: magnetic field and resulting motion force applied on the beam particles.

The story of accelerated protons at CERN starts with a bottle of hydrogen gas injected into the source chamber of the linear particle accelerator *LINAC 2* in which a strong electric field strips the electron off the hydrogen molecules only to keep their nuclei, the protons. The cylindrical conductors then accelerate the protons to an energy of 50 MeV. When exiting the *LINAC 2*, the protons are divided into four bunches and injected into the four superimposed synchrotron rings of the *Booster* where they are then accelerated to reach an energy of 1.4 GeV before being injected into the *PS*. The four proton bunches are hence sent as one to the *PS* where their energy eventually reaches 26 GeV. The *PS* not only accelerates protons. It also accelerates heavy ions from the *Low Energy Ion Ring (LEIR)*. Lead is first injected into the dedicated linear collider *LINAC 3*, that accelerates the ions. Electrons are stripped off the lead ions all along the acceleration process and eventually, only bare nuclei are injected in the *LEIR* whose goal is to transform the long ion pulses received into short dense bunches for *LHC*. Ions injected and stored in the *PS* were accelerated by the *LEIR* from 4.2 MeV to 72 MeV. Directly following the *PS*, is finally the last acceleration stage before the *LHC*, the 7 km long *SPS*. The *SPS* accelerates the protons to 450 GeV and inject them in both *LHC* accelerator rings that will increase their energy up to 7 TeV. When the *LHC* runs with heavy lead ions for *ALICE* and *LHCb*, ions are injected and accelerated to reach the energy of 2.8 TeV/A.

The *LHC* beams are not continuous but are rather organised in bunches of particles. When in *pp*-collision mode, the beams are composed of 2808 bunches of  $1.15 \times 10^{11}$  protons separated by

25 ns. When in *Pb*-collision mode, the 592 *Pb* bunches are on the contrary composed of  $2.2 \times 10^8$  ions separated by 100 ns. The two parallel proton beams of the *LHC* are contained in a single twin-bore magnet due to the space restriction in the *LEP* tunnel. Indeed, building two completely separate accelerator rings next to each other was impossible. The dipoles of the 1232 twin-bore magnets are shown in Figure 2.17 alongside the magnetic field generated along the dipole section to accelerate the particles. The dipoles generate a nominal field of 8.33 T, needed to give protons and lead nucleons their nominal energy. Some 392 quadrupoles, presented in Figure 2.18, are also used to focus to the beams, as well as other multipoles to correct smaller imperfections.



*Figure 2.18: The LHC quadrupoles (Figure 2.18a) showed together with the magnetic fields and resulting focussing force applied on the beam by two consecutive quadrupoles (Figure 2.18b).*

## 2.2.2 Timeline of operation

LHC accelerated its first proton in September 2008 but the first collisions only started one year later in November 2009. At this moment the LHC machine officially became the world's most powerful particle accelerator and entered its Physics Run 1 that lasted until February 2013. During Run 1 of the LHC program, the center-of-mass energy was only half of the nominal LHC energy. Nevertheless, the energy and luminosity displayed during Run 1 were enough for both CMS and ATLAS to discover the Higgs boson [112, 113] as showed in Figure 2.19 and for LHCb to discover pentaquarks [170] and confirm the existence of tetraquarks [171]. During this period, ALICE also reported a successful observation of the quark-gluon plasma aimed at studying the early universe [172], ATLAS reported the observation of a new particle before the discovery of the Higgs [173] and a first test of super-symmetric models was performed [174].

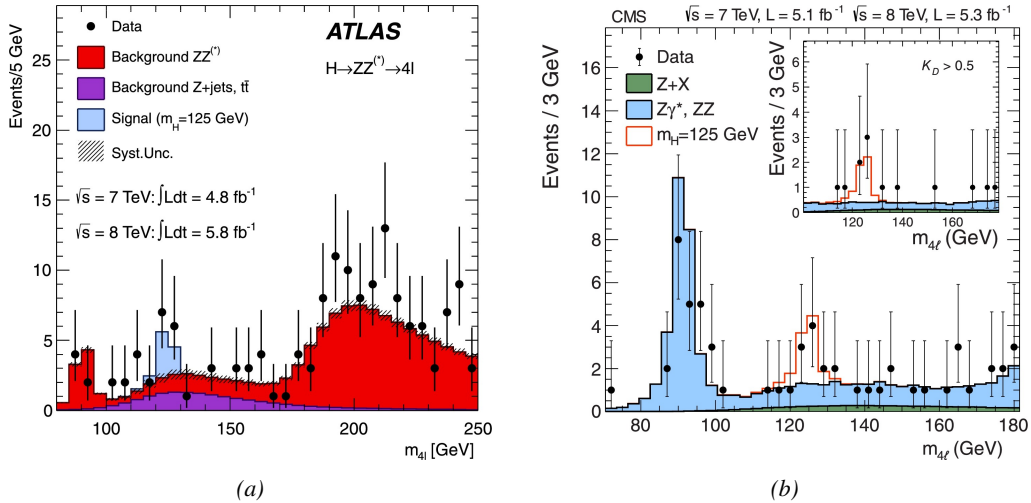


*Figure 2.19: Distribution of the four-lepton invariant mass for the  $ZZ \rightarrow 4l$  analysis as presented by both ATLAS [112] and CMS [113] in 2012.*

Run 1 was brought to an end with the start of the First Long Shutdown, an almost two years technical stop aimed at increasing the energy of the center-of-mass collisions to  $\sqrt{s} = 13$  TeV

as well as the instantaneous luminosity. This maintenance stop was also effectively used by the experiments which upgraded part of their detection systems. Run 2 then started in 2015 and lasted until end of 2018 where the activities ended with a last heavy ion run. During the operation, the instantaneous was successfully brought to a value of  $1.7 \times 10^{34} \text{ cm}^{-2} \text{ s}^{-1}$  exceeding the design value. Run 2 has been the occasion to acquire more data to study the properties of the Higgs boson with more precision. The boson discovered in the first physics run seems to be consistent with the SM Higgs boson [114].

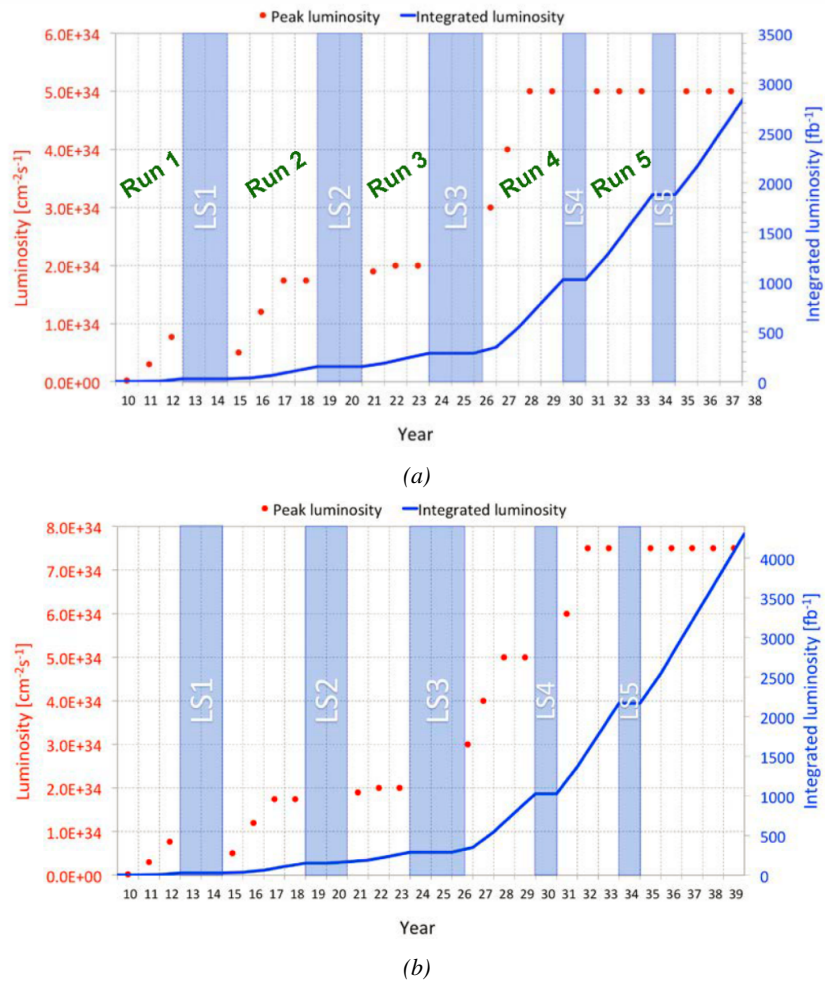


Figure 2.20: Detailed timeline projection of LHC and HL-LHC operation until 2039 showing the evolution of the instantaneous and integrated luminosity as designed (Figure 2.20a) and in the ultimate case where the instantaneous luminosity is increased to  $7.5 \times 10^{34} \text{ cm}^{-2} \text{ s}^{-1}$  thanks to a new increase of instantaneous luminosity during Run 5 (Figure 2.20b) [175–177].

From the end of 2018 to early 2021 the Second Long Shutdown will take place. This second maintenance stop will be the occasion to boost once again the beam energy to finally reach the design energy of LHC, 14 TeV. On the side of the maintenance work, preliminary work for the High Luminosity LHC will be performed. The preparations will consist of detector, on the side of the

1731 experiments, and beam machine upgrades, on the side of LHC. In 2021, the physics program will  
1732 be resumed with an instantaneous luminosity fixed at  $2 \times 10^{34} \text{ cm}^{-2} \text{ s}^{-1}$ . During these 3 years of  
1733 run, the LHC will deliver as much integrated luminosity as what was brought during the almost 7  
1734 years of both Run 1 and 2 of data taking. Phase-1 will end with an overall  $300 \text{ fb}^{-1}$  delivered. The  
1735 timeline so far described is summarized through the evolution of the instantaneous luminosity and  
1736 of the corresponding integrated luminosity provided in Figure 2.20.

1737 After the Third Long Shutdown (2024-2026) that will close the activities of Run 3, the accel-  
1738 erator will enter the HL-LHC configuration [175], increasing the instantaneous luminosity to an  
1739 unprecedented level of  $5 \times 10^{34} \text{ cm}^{-2} \text{ s}^{-1}$  for  $pp$ -collisions ( $4.5 \times 10^{27} \text{ cm}^{-2} \text{ s}^{-1}$  for  $Pb$ -collisions),  
1740 boosting the discovery potential of the LHC. The HL-LHC phase should last at least another 10 years  
1741 depending on the breakthrough this machine would lead to. Already a new accelerating device, the  
1742 FCC, as been proposed and is being investigated to prepare the future of high-energy physics after  
1743 the LHC.

### 1744 2.2.3 High Luminosity LHC

1745 After approximately fifteen years of operation, the LHC will undergo a new series of upgrades during  
1746 the LS3 in order to boost its discovery potential as previously discussed. The period after LS3 is  
1747 what is referred to HL-LHC or Phase-2. The goal is to aim for a luminosity 5 to 7 times stronger  
1748 than the nominal one trying to reach even 10 times this value if possible [175, 176]. Increasing  
1749 the luminosity means that the beam size at the collision points needs to be reduced to boost the  
1750 number of collisions per bunch crossing. For this purpose, new focusing and bending magnets and  
1751 collimators will be installed at the collision points as well as newly developed "*crab cavities*" that  
1752 will tilt the particle bunches just prior to the collisions by giving them transverse momentum and  
1753 thus increasing their meeting area. In addition, the full proton injection line will be upgraded.

1754 On the experiments side, the pile-up (PU) will be increased up to 150 to 200 interactions per  
1755 bunch crossing in ATLAS and CMS, making necessary a strong upgrade of the trigger system and  
1756 of the inner trackers and of the calorimeters. Both ATLAS and CMS will also need to upgrade the  
1757 muon trigger at the level of their endcaps mainly focusing on the coverage near the beam line in  
1758 order to increase the detection acceptance and event selection. Moreover, the increased luminosity  
1759 will also lead to an increased background rate and a faster ageing of the detectors.

1760 The end of 2018 marked the beginning of LS2 and the start of Phase-2 upgrade activities. From  
1761 the HL-LHC period onwards, i.e. past LS3, the performance degradation due to integrated radiation  
1762 as well as the average number of inelastic collisions per bunch crossing will rise substantially. This  
1763 has become a major challenge for all of the LHC experiments, like CMS, that were forced to address  
1764 an upgrade program for Phase-2 [177]. Dealing with the data from the muon detectors will force to  
1765 upgrade the detectors and electronics towards the most recent technologies.

### 1766 2.2.4 The Compact Muon Solenoid experiment

1767 Among the four main LHC experiments is the Compact Muon Solenoid used as a multipurpose  
1768 tool to investigate the SM and the physics beyond its scope. The CMS apparatus in itself is the  
1769 heaviest detector ever built starring a 15 m diameter and a 29 m length for a total weight of 14 kT.  
1770 A thick 4 T solenoid magnet located at the beam interaction point hosts trackers and calorimeters.  
1771 Extending in all directions around the magnet, heavy iron return yokes are installed to extend the  
1772 magnetic field and support a muon system. The apparatus consists of a barrel, referring to the magnet

and the detectors contained in it and the part of the muon system built directly in the cylinder around the magnet, and of two endcaps in the forward and backward region of the detector that closes the apparatus and complete the detection coverage along the beam line. A front view on the barrel is provided in Figure 2.21 while a detailed view of the apparatus is given in Figure 2.22.

In order to efficiently detect all long living particles and measure their properties with good precision, the CMS detector uses an onion like layout around of the interaction point in order to maximize the covered solid angle. As detailed in Figure 2.23, in the innermost region of the detector, closest to the interaction point, the silicon tracker records the trajectory of charged particles. Around it, the electromagnetic calorimeter (ECAL) stops and measures the energy deposition of electrons and photons. In the next layer, the hadron calorimeter (HCAL), hadrons are stopped and their energy measured. These layers are contained inside of the magnet of CMS, the superconducting solenoid. Outside of the magnet are the muon chambers embedded into iron return yokes used to control the magnetic field and gives muons, the only particles traveling completely through the whole detector, a double bending helping in reconstructing their energy and trajectory. Note that photons and neutral hadrons are differentiated from electrons and charged hadrons in the calorimeters by the fact that they don't interact with the silicon tracker and are not influenced by the magnetic field, as can be seen in Figure 2.23.

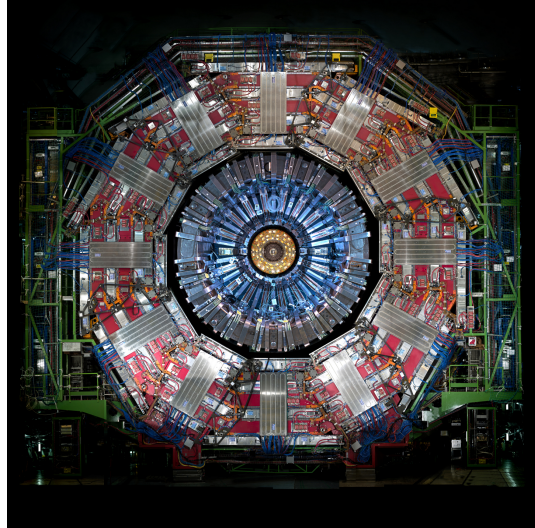


*Figure 2.21: Picture of the CMS barrel. The red outer layer is the muon system hosted into the red iron return yokes. The calorimeters are the blue cylinder inside in magnet solenoid and the tracker is the inner yellow cylinder built around the beam pipe.*

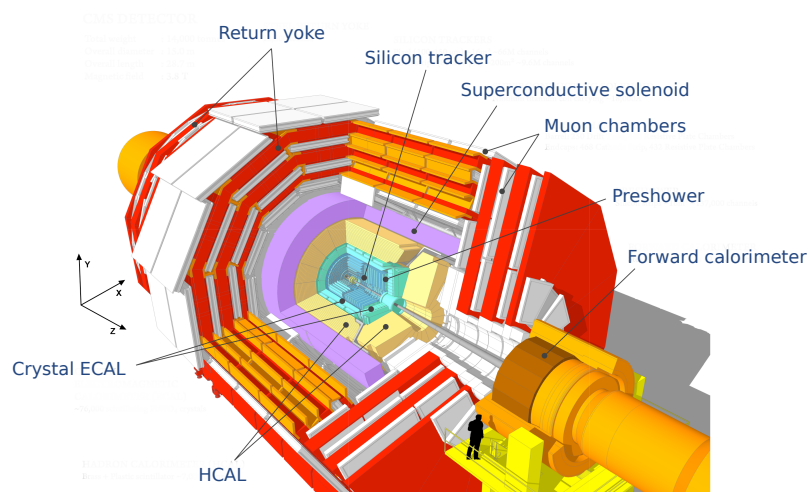


*Figure 2.22: View of the CMS apparatus and of its different components.*

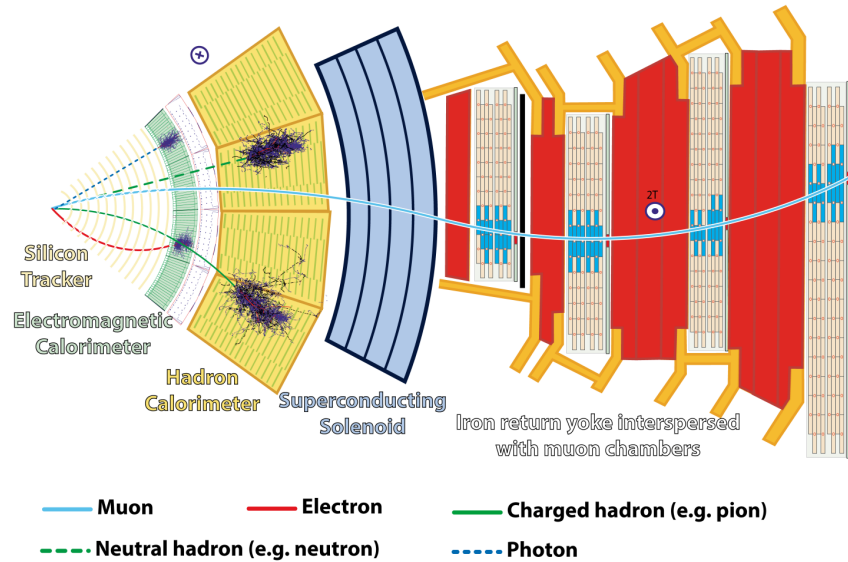


Figure 2.23: Slice showing CMS sub-detectors and how particles interact with them.

#### 1802 2.2.4.1 The silicon tracker

1803 The silicon tracker visible in  
 1804 Figure 2.24 is divided into two  
 1805 different sub-systems: the *pixel*  
 1806 *detector* at the very core and  
 1807 the *microstrip detector* around  
 1808 it. This system is composed  
 1809 of 75 million individual read-  
 1810 out channels with up to 6000  
 1811 channels per squared centime-  
 1812 ter for the pixels making it the  
 1813 world's biggest silicon detec-  
 1814 tor. This density allows for  
 1815 measurements of the particle  
 1816 tracks with a precision of the  
 1817 order of  $10\ \mu\text{m}$ . This is neces-  
 1818 sary to reconstruct all the dif-  
 1819 ferent interaction vertices with precision and have a precise measure of the curvature of the charged  
 1820 particles traveling through the magnetic field to estimate their charge and momentum.

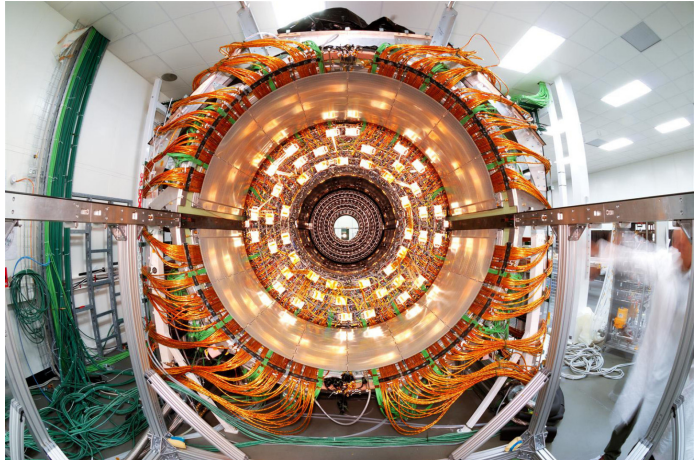
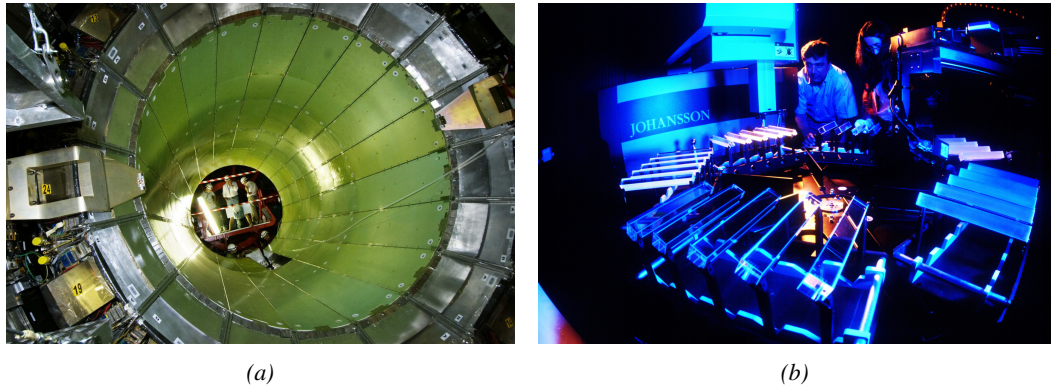


Figure 2.24: The CMS tracker.

#### 1821 2.2.4.2 The calorimeters

1822 The ECAL directly surrounding the tracker is composed of crystals of lead tungstate,  $\text{PbWO}_4$ , a  
 1823 very dense but optically transparent material used to stop high-energy electrons and photons. These  
 1824 crystal blocks basically are extremely dense scintillators which scintillate in fast, short light bursts  
 1825 proportionally to the energy deposition. The light is contained at 80% in the corresponding 25 ns

1826 lasting bunch crossing. Each crystal is isolated from the other by the carbon fiber matrix they are  
 1827 embedded in.



*Figure 2.25: Figure 2.25a: The electromagnetic calorimeter. Figure 2.25b: The lead tungstate crystals composing the ECAL.*

1828 The ECAL is composed of a barrel containing  
 1829 more than 60,000 crystals and of closing  
 1830 endcaps containing another 15,000 crystals.  
 1831 In front of the ECAL endcap is installed  
 1832 a preshower detector made out of two layers  
 1833 of lead and silicon strip detectors to increase  
 1834 the spatial resolution close to the beam line  
 1835 for pion-photon and single-double photon dis-  
 1836 crimination purposes. Figure 2.25 shows the  
 1837 calorimeter inside of the magnet and the crys-  
 1838 tals.

1839 The next layer is the HCAL. The role of  
 1840 these forward calorimeters, made using steel  
 1841 and quartz fibers, is to precisely measure the momentum very energetic hadrons. Several layers  
 1842 of brass or steel are interleaved with plastic scintillators readout by photodiodes using wavelength-  
 1843 shifting fibers. The HCAL is also composed of a barrel, shown in Figure 2.26 and of endcaps. It  
 1844 also features forward calorimeters on both sides of CMS in the region very close to the beam line at  
 1845 high pseudorapidity ( $3.0 < |\eta| < 5.0$ ).



*Figure 2.26: The CMS hadron calorimeter barrel.*

#### 1846 **2.2.4.3 The muon system**

1847 Finally, in the outer region of the apparatus, a muon system is used to trigger on potentially interest-  
 1848 ing event by identifying muons. Three different subsystems compose the muon system as shown in  
 1849 Figure 2.27 in which a quadrant of the CMS detector focuses on muon system. Drift Tubes (DTs)  
 1850 are found in the barrel region covering the low pseudorapidity region where particles transverse  
 1851 momentum is lower and Cathode Strip Chambers (CSCs) are found in the endcap region covering  
 1852 higher pseudorapidity region closer to beam line where particles have a stronger momentum. The  
 1853 redundancy of the system is insured by Resistive Plate Chambers (RPCs) in both the barrel and end-  
 1854 cap. Nevertheless, the region closest to the beam line ( $|\eta| > 1.8$ ) was not equipped with RPCs. This

lack of redundancy in the high pseudo rapidity region will be solved during LS2, the following Year End Technical Stop (YETS) in 2021 and 2022, and LS3 where the necessary services, detectors and Link System, that collects the data and synchronizes them, will be installed.

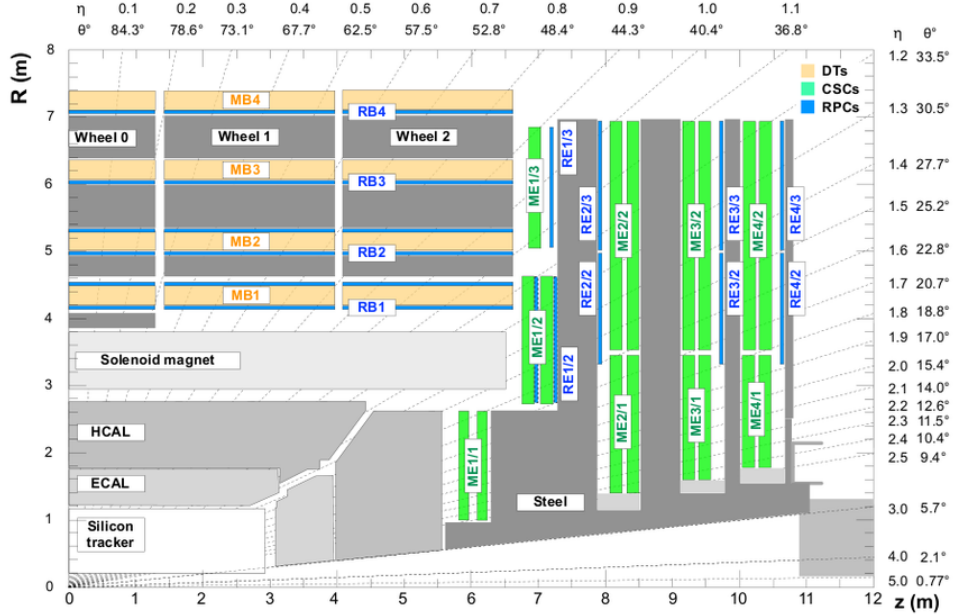


Figure 2.27: A quadrant of the muon system, showing DTs (yellow), RPCs (blue), and CSCs (green).



# 3

1858

1859

## Muon Phase-2 Upgrade

1860 In the previous chapter, the timeline of the LHC has been described and the upcoming High Lumi-  
1861 nosity LHC was introduced. LS3 has now started and the first HL-LHC related upgrade of CMS will  
1862 take place. In order to understand the context in which the work of this thesis was performed as well  
1863 as its motivations, it is necessary to give more insight into the reasons behind the increased instantan-  
1864 eous luminosity of LHC. In a first section of the chapter, these motivations will be discussed.

1865 The muon system of CMS will then be presented in greater details than what was done in the  
1866 previous chapter in order to have a better understanding of the need for upgrades of its different sub-  
1867 systems in the perspective of HL-LHC. Most of the detectors will require new electronics to adapt  
1868 to the new data flow and be integrated into a more robust trigger. Moreover, the redundancy of the  
1869 muon system in the endcaps will need to be improved. This will be achieved by the addition of new  
1870 detectors.

1871 Finally, some insight will be given on ecofriendly gas studies for the specific case of Resistive  
1872 Plate Chambers. These studies don't fall into the scope of the HL-LHC upgrades but the necessity  
1873 of operating the detectors with gas mixtures that are more respectful of the environment is real. The  
1874 European union is starting to press the scientific community for solutions and the research institutes  
1875 are investing time into finding replacements to the gases used while maintaining similar working  
1876 performances.

### 1877 **3.1 Motivations for HL-LHC and the upgrade of CMS**

1878 As detailed in Section 2.2.2, the first data taking period, during which the LHC was only operated  
1879 at a center-of-mass energy of 7 TeV, took place until the start of LS1. It has been sufficient to  
1880 claim the discovery of a new  $125 \text{ GeV}/c^2$  particle compatible with the Higgs boson by both CMS  
1881 and ATLAS in July 2012 and hence achieve a major milestone in the history of science towards the  
1882 understanding of the fundamental nature of the universe. Nevertheless, the LHC machine holds the  
1883 potential to go further and help unravel the remaining mysteries the High-Energy Physics (HEP)  
1884 community is facing.

Over its full lifetime, the HL-LHC is expected to deliver an outstanding integrated luminosity of  $3000 \text{ fb}^{-1}$ , nearly an order of magnitude higher than what will be delivered by LHC until LS3 starts, as shown in Figure 2.20. In the case of Higgs studies, this will lead to measuring the couplings of the boson to a precision of 2 to 5%. Thanks to the estimated 15 millions of Higgs bosons created every year, a more precise measurement of potential deviations from the theoretical predictions is expected. The properties of the boson will hence be tested and compared to the SM Higgs neutral boson. SUSY and heavy gauge boson studies would also see their mass range limits pushed away by at least 1 TeV and could lead to a new breakthrough. Many of the Standard Model extensions discussed in Section 2.1.3 yield Heavy Stable Charged Particles (HSCPs), i.e. heavy long-lived particles. These particles would be produced at the LHC with a high momentum but a velocity significantly lower than the speed of light ( $\beta < 0.9$ ) [178–182] and/or a charge that differs from the elementary charge ( $|Q| = e$ ,  $|Q| < e$  or  $|Q| > e$ ) [181–186]. Depending on the model considered, HSCPs could be lepton-like heavy particles or on the contrary R-hadron, i.e. particles composed of a supersymmetric particle and at least one quark [181].

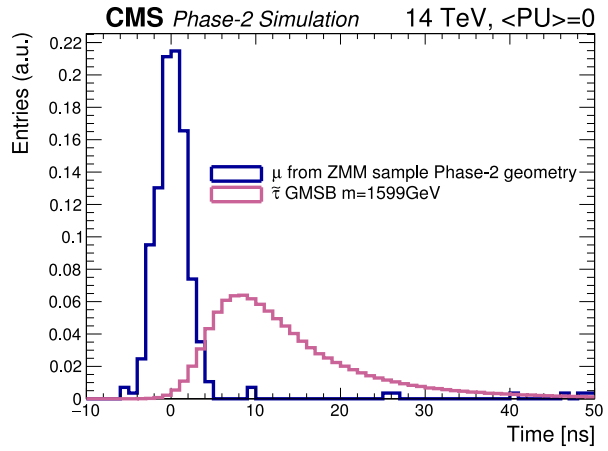


*Figure 3.1: The measured transit time of an HSCP in CMS is compared to the transit time of a particle traveling at near the speed of light [177].*

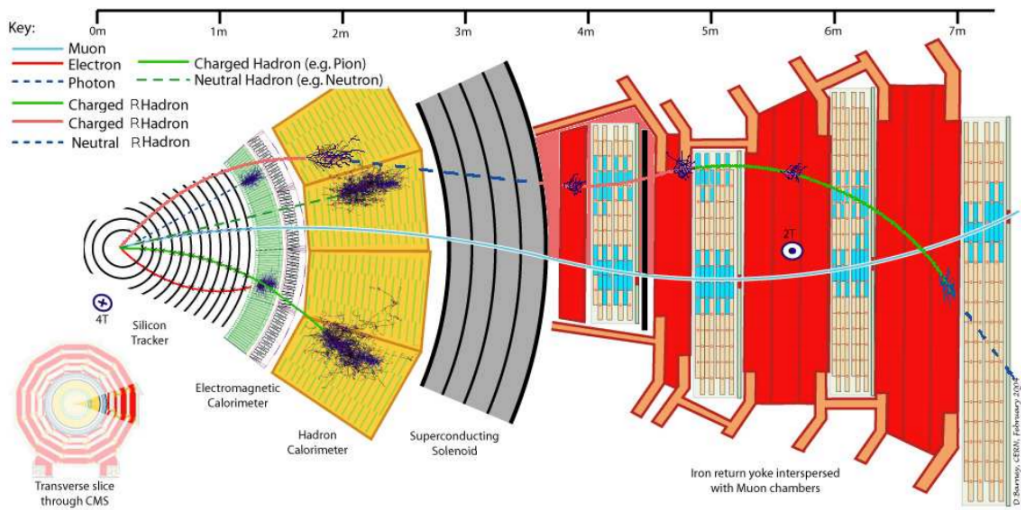


*Figure 3.2: Slice of the CMS detector showing examples of passage of SM particles and R-hadrons. On the one hand, lepton-like HSCPs will appear to behave like slow and heavy muons. On the other hand, R-hadrons are likely to convert into other kind of charged or neutral R-hadrons due to interactions inside the detector volume.*

1911 Due to lifetimes of the order of a few ns,  
 1912 HSCPs would travel for long enough distances  
 1913 to cross through entire typical collider detec-  
 1914 tors while appearing almost stable. Because  
 1915 of their low velocity, they can be reconstructed  
 1916 and assigned to bunch crossings different to  
 1917 the ones they effectively have been produced,  
 1918 as shown in Figure 3.1, if reconstructed at  
 1919 all. Indeed, the trigger algorithms in use at  
 1920 CMS were not designed for such slow parti-  
 1921 cles, and they assume most particles of inter-  
 1922 est will have a velocity close to the speed of  
 1923 light [182, 187].

1924 As HSCPs are long-lived particles, their  
 1925 identification would be possible thanks to the  
 1926 muon system. The main background will con-  
 1927 sist of wrongly measured muons which should  
 1928 have a lower transverse momentum, a near to  
 1929 speed-of-light velocity and a low ionisation  
 1930 energy loss. An example of passage of HSCPs  
 1931 through a slice of the CMS detector is showed  
 1932 in Figure 3.2. The tracks associated to the  
 1933 HSCPs would then have to be reconstructed in  
 1934 both the silicon detectors, for precise  $dE/dx$   
 1935 measurement, and the muon system detectors. In this case, the muon system will be used to perform  
 1936 Time-of-flight (ToF) measurements to discriminate between near speed-of-light particles and slower  
 1937 ones. The full reconstruction will then look for useful signatures such as the large transverse mo-  
 1938 mentum of the candidates, or their large ionisation energy loss alongside the low velocity accurately  
 1939 measured thanks to the muon system as depicted in Figure 3.3. The ToF measurement to identify  
 1940 beyond the Standard Model particles will mostly rely on the time information provided by the Drift  
 1941 Tubes, in the barrel region of the detector, and Cathode Strip Chambers, in the endcaps. From CMS  
 1942 point of view, it will then become necessary to increase the acceptance and redundancy of the end-  
 1943 caps toward higher pseudo-rapidity as the pseudo-rapidity region  $1.6 < |\eta| < 2.5$  is only covered  
 1944 by CSCs.

1945  
 1946 A natural consequence of the higher instantaneous luminosity will be the increase of collisions  
 1947 per bunch crossing. It is estimated that the pile-up will rise from the approximate average of 40  
 1948 collisions per bunch crossing in 2017 and 2018, presented in Figure 3.4, to 140 to 200 depending on  
 1949 the scenario considered [188]. The trigger rate will then be affected in the same way putting a lot  
 1950 of stress on the trigger algorithms. Upgrading the electronics of some of the detectors and working  
 1951 on the data flow within the experiment would help going through HL-LHC with keeping similar  
 1952 performance than during Phase-1. On the other hand, the impact of the increased background will  
 1953 become problematic in many ways and will force for upgrades or many sub-systems of CMS. The  
 1954 main effects will be a large increase of the irradiation of the detectors, mainly close to the beam  
 1955 line. Both the detectors already installed and the new detectors that will extend the coverage of the

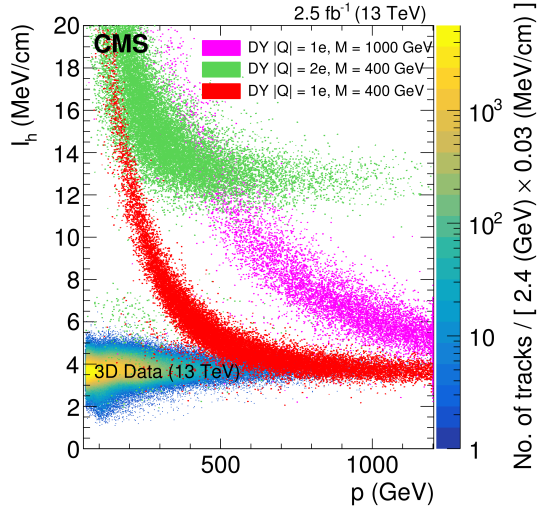


Figure 3.3: Distribution of the energy-loss  $dE/dx$  as described by Bethe-Bloch formula through the estimator  $I_h$  with increasing particle momentum for tracks in the 13 TeV data. The estimator depends on the charge deposition of the particles per unit length in the silicon detectors of CMS which is related to their energy loss as explained in a publication by the CMS Collaboration [181]. The simulated HSCPs are singly or multiply charged particles with masses of 400 and 1000 GeV.

muon system toward higher pseudo-rapidity need to be certified for the irradiation levels they will be subjected to until the end of HL-LHC. Simulations of the expected distribution of absorbed dose in the CMS detector under HL-LHC conditions show, in Figure 3.5, that detectors placed close to the beam line will have to withstand high irradiation, the radiation dose being of the order of a few tens of Gy.

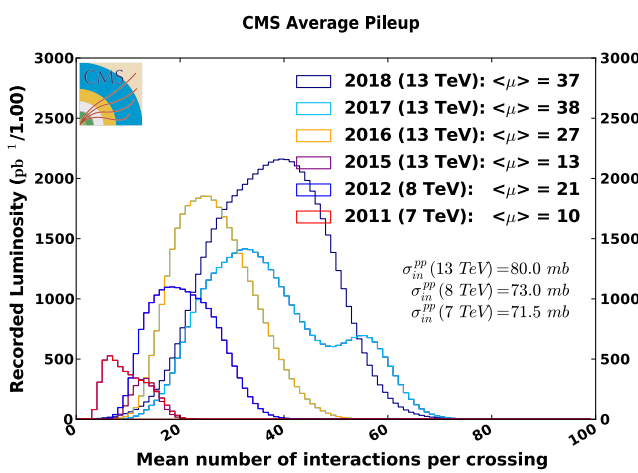


Figure 3.4: Distribution of the average number of interactions per crossing (pileup) for pp-collisions in 2011 (red), 2012 (blue), 2015 (purple), 2016 (orange), 2017 (light blue), and 2018 (navy blue). The overall mean values and the minimum bias cross sections are also shown [189].

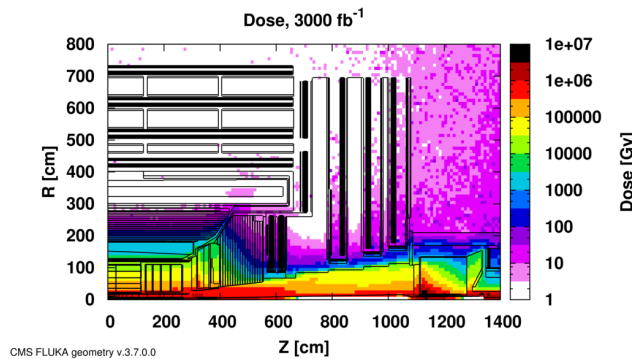


Figure 3.5: Absorbed dose in the CMS Cavern after an integrated luminosity of  $3000 \text{ fb}^{-1}$ . Using the interaction point as reference,  $R$  is the transverse distance from the beamline and  $Z$  is the distance along the beamline [177].

and measurement of their energy with reasonable precision only using the tracker is nearly impossible. Thus, this increased tracker coverage range needs to be put in parallel with a matching muon detector and will open doors to multi-lepton final states in which leptons are likely to have a low transverse momentum and to be found near the beam line.

Finally, as the muon system is composed only of gaseous detectors, strong environmental concerns have risen over the last years as the European directives will restrict the use of fluorine based

Improving this situation will come with the increase of hit numbers recorded along the particle track to reduce the ambiguity on muon versus background detection. Moreover, the measurement of small production cross-section and/or decay branching ratio processes, such as the Higgs boson coupling to charge leptons, and in particular to muons, or the  $B_s \rightarrow \mu^+ \mu^-$  decay, is of major interest. Such considerations give more weight to the upgrade of the forward regions to maximize the physics acceptance to the largest possible solid angle.

To ensure proper trigger performance within the present coverage, the muon system will be completed with new chambers, and the electronics of the present system will need to be upgraded. A first step into this direction will be taken by installing new gaseous detectors in each endcap layer and extend the coverage up to  $|\eta| = 2.8$ . Nevertheless, the region beyond  $|\eta| > 2.8$  and extending to  $|\eta| = 5.0$  only is covered by the forward HCAL detectors and lack redundant muon detector coverage. Extensions of the tracker in the context of HL-LHC will increase its coverage up to  $|\eta| = 4.0$  but the identification of muons

2002 gas mixtures. Both the CSC and RPC subsystems, using  $CF_4$ ,  $C_2H_2F_4$ , or  $SF_6$ , will need to adapt  
 2003 their working gas in order to strongly reduce the greenhouse potential of the mixtures released into  
 2004 the atmosphere due to gas leaks.

2005 **3.2 Description of the muon system**

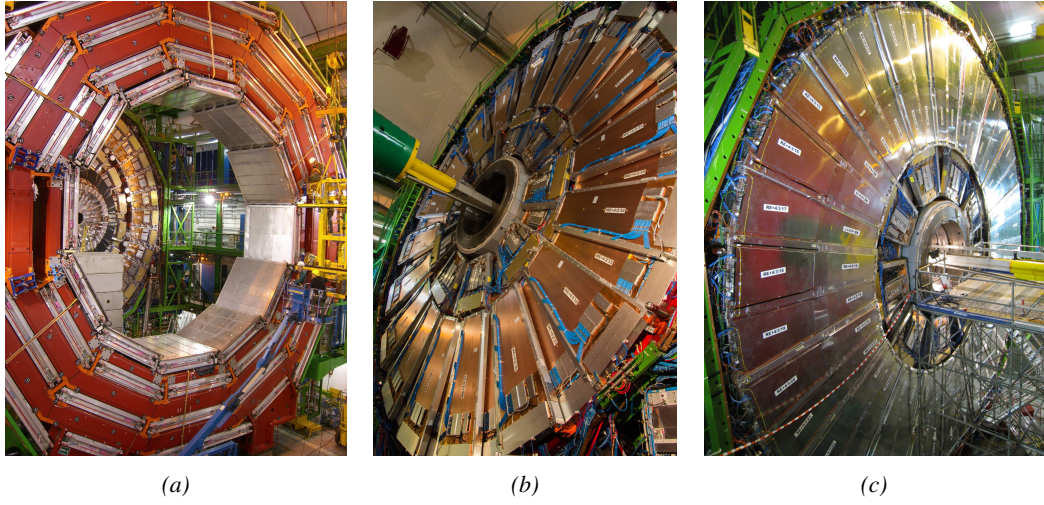


Figure 3.6: Figure 3.6a: Barrel wheel with its detector rings and return yokes. Figure 3.6b: CSC endcap disk with the two CSC stations. The outer station is made of 10 deg detectors while the inner station is made of 20 deg detectors. Figure 3.6c: RPC endcap disk. The inner station is not equipped, leaving the inner CSC station visible.

2006 The barrel region is divided into five *wheels* made out of four *rings* of detectors with iron return yokes  
 2007 in between them whereas the endcaps are made out of four disks, each divided into pseudorapidity  
 2008 stations, two for CSCs (except for the first disk where three stations are equipped) and three for  
 2009 RPCs, although only two RPCs stations are equipped at present. The wheels and disks are shown  
 2010 in Figure 3.6. So far, each subsystem was dedicated to a particular task. DTs, in the barrel, and  
 2011 CSCs, in the endcaps, are used mainly for their spatial resolution. Indeed, DTs' resolution is of  
 2012 the order of 100  $\mu\text{m}$  along both the  $(r - \phi)$  and  $(r - z)$  components while the resolution of CSCs  
 2013 is similar but varies in a range from 50  $\mu\text{m}$  to 140  $\mu\text{m}$  depending on the distance to the beamline.  
 2014 On the other hand, RPCs are used as redundant detection system in the whole muon system. They  
 2015 display a very good intrinsic time resolution of 1.5 ns although the electronics only provide bunch  
 2016 crossing information with a time resolution of 25 ns.

2017 **3.2.1 The Drift Tubes**

2018 The 250 CMS DTs, found in the barrel covering the pseudorapidity region  $0 < |\eta| < 1.2$  and  
 2019 whose structure is shown in Figure 3.7, are composed of three *superlayers* of DT cells. Two of  
 2020 these superlayers are dedicated to measuring the  $\phi$  coordinate of the muons and while the last one  
 2021 measures the  $\eta$  (or  $z$ ) coordinate. Each superlayer consists on four layers of 60 to 70 DT cells  
 2022 arranged in quincunx to allow for a precise reconstruction of the muon path through the DT layers.

2023 Each DT cell is a rectangular aluminium gas volume with a central anode wire. Cathode strips are  
 2024 placed on the narrow surface of the cells and electrode strips are placed on the wide surface to help  
 2025 shaping the electric field to ensure a consistent drift velocity of electrons in the drift volume. These  
 2026 detectors are operated using a 85/15 mixture of Ar and CO<sub>2</sub>. Outside the gas volume of each DT  
 2027 chamber is attached a Minicrate electronics (MiC) that hosts both read-out and trigger electronics.

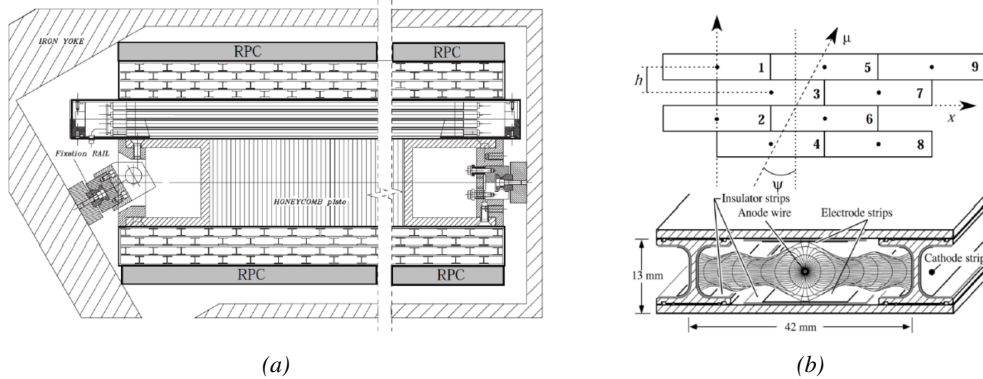


Figure 3.7: Figure 3.7a: Cross section of a DT module showing the two superlayers measuring the  $\phi$  coordinate, perpendicular to the cross section plane, and the superlayer measuring the  $\eta$  coordinate, placed in between the two others with a honeycomb plate and parallel to the cross section plane. The DT detector is sandwiched in between 2 RPCs whose readout strips are perpendicular to the cross section plane, measuring the  $\phi$  coordinate. Figure 3.7b: A DT cell is shown together with its electric field. The path of a muon through a superlayer is shown.

### 2028 3.2.2 The Cathode Strip Chambers

2029 The 540 CMS CSCs are found in the endcaps covering the pseudorapidity region  $0.9 < |\eta| < 2.5$   
 2030 and described through Figures 3.8 and 3.9. Each module is composed of six panels of CSC, each  
 2031 panel consisting in a wide gas volume of 9.5 mm (7 mm in the case of ME1/1 station) containing  
 2032 anode wires and whose surfaces are cathodes. The top cathode is a wide copper plane of the size of  
 2033 the gas volume. The bottom cathode is divided into thin trapezoidal copper strips radially arranged  
 2034 to measure the azimuthal coordinate  $\phi$  with a pitch ranging from 8 to 16 mm. The 0.50  $\mu\text{m}$  anode  
 2035 wires are placed perpendicularly to the strips to measure radial coordinate  $r$  and are grouped by  
 2036 ten to fifteen with a wire to wire space of 3.2 mm. In the specific case of ME1/1 placed against  
 2037 the HCAL endcap, the 0.30  $\mu\text{m}$  anode wires have a wire to wire distance of 2.5 mm and are not  
 2038 disposed perpendicularly to the strips but slightly tilted by an angle of 29 deg to compensate for the  
 2039 lorentz force due to the very strong local magnetic field of 4 T. These detectors are operated with a  
 2040 40/50/10 mixture of Ar, CO<sub>2</sub> and CF<sub>4</sub>. Combining the information of the multiple CSC panels, the  
 2041 detectors achieve a very precise measurement of the muon track. The read-out of the cathode strip  
 2042 signals is performed by cathode front-end boards (CFEBs) mounted on the detectors. The boards  
 2043 are used to collect and digitize the charge of the signals and transfer it to off-chamber electronics  
 2044 called Data acquisition mother boards (DMBs). In parallel, the data from the CFEBs together with  
 2045 the data from the anode wires, after treatment by on-chamber electronics called Anode local charged  
 2046 track boards (ALCTs), is used to build a fast trigger information which is sent other off-chamber  
 2047 electronics called Trigger mother boards (TMBs).

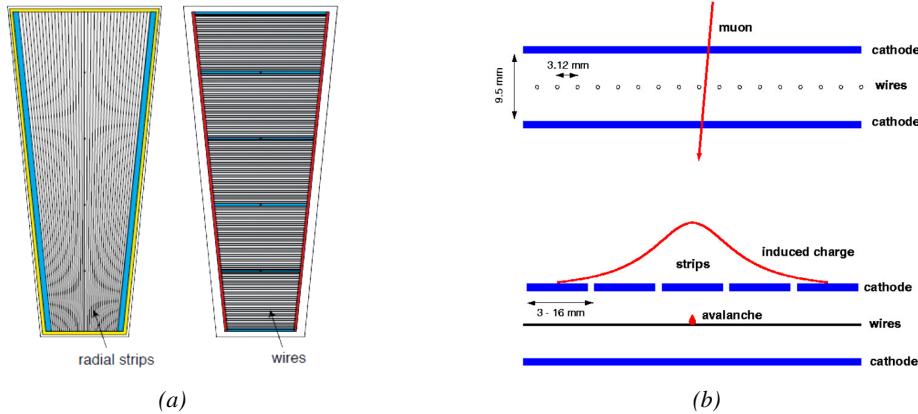


Figure 3.8: Figure 3.8a: Cathode strips and anode wire layout of a CSC panel. Figure 3.8b: Avalanche development and charge collection by anode wires and induction on cathode strips inside of a CSC panel.

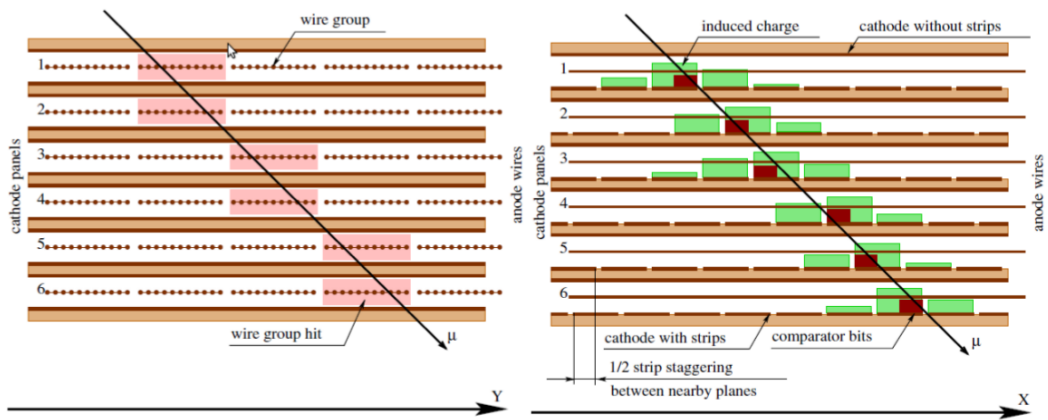


Figure 3.9: Muon track reconstruction through the six panels of a CMS CSC using the information of anode wire groups and cathode strip charge distribution combined with comparator bits to decide on which half strip the muon is more likely to have passed.

### 2048 3.2.3 The Resistive Plate Chambers

Despite their excellent spatial resolution, the wire chambers (DTs and CSCs) are limited in terms of time resolution by the fact that the charge needs to drift towards the anode wire and be collected before having the confirmation that a particle was detected as the drift volume is not used to develop avalanches. Indeed, the stronger electric field close to the anode wire triggers the avalanche and the gain of the detector. Due to the drift, the time resolution is thus limited at best to approximately 2 to 3 ns. In addition, even though the intrinsic time resolution of the tracking chambers is rather good compared to the 25 ns in between successive collisions, the processing time of the trigger system doesn't allow for very fast triggering as it provides a time precision of only 12.5 ns. Thus, detectors fully dedicated to timing measurement have been installed as a redundant system. These detectors are RPCs, also gaseous detectors but that use current induction instead of charge collection allowing for a time resolution of the order of 1 ns only. Theoretically, depending on the design used, RPCs

could reach a time resolution of the order of 10 ps but in the context of LHC where bunch crossing happen every 25 ns, a time resolution of 1 ns is sufficient to accurately assign the right bunch crossing to each detected muon.

The 1056 RPCs equip the CMS muon system both in the barrel and endcap regions and cover the pseudorapidity region  $0 < |\eta| < 1.6$ . They are composed of two layers of RPC *gaps* as described in Figure 3.10. Each gap consists in two resistive electrodes made out of 2 mm thick Bakelite enclosing a 2 mm thick gas volume containing a 95.2/4.5/0.3 mixture of  $C_2H_2F_4$ ,  $i - C_4H_{10}$  and  $SF_6$ . Due to this geometry, the electric field inside of a gap is homogeneous and linear at every point in the gas translating into a uniform development of avalanches in the gas volume as soon as a passing muon ionises the gas. The two gaps sandwich a readout copper strip plane. A negative voltage is applied on the outer electrodes, used as cathodes, and the inner electrodes, the anodes, are simply connected to the ground as well as the readout panel that picks up the current induced by the accumulated charge of the growing avalanches in one or both of the gas gaps. This OR system allows for a lower gain (i.e. a lower electric field) on both gaps to reach the maximal efficiency of such a detector.

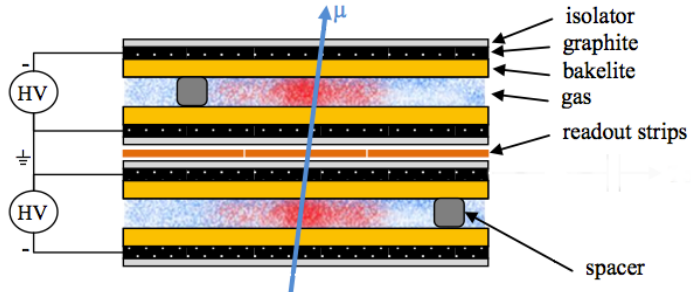


Figure 3.10: Double-gap layout of CMS RPCs. Muons passing through the gas volumes will create electron-ions pairs by ionising the gas. This ionisation will immediately translate into a developing avalanche.

### 3.3 Necessity for improved electronics

Drift Tubes and Cathode Strip Chambers are important components used to identify and measure muons, especially thanks to their spatial resolution of the order of 100  $\mu\text{m}$ . Nevertheless, the luminosity and irradiation during HL-LHC will cause serious event loss and ageing on the electronics of these subsystems that will comprise the triggering and data transferring needs of CMS. Thus, electronics upgrade is foreseen to address these expected problems. While only the RPCs' electronic system is able to operate under Phase-2 requirements [190], DTs and CSCs will need to improve their trigger acceptance rate and latency to ensure that the Level-1 trigger thresh-

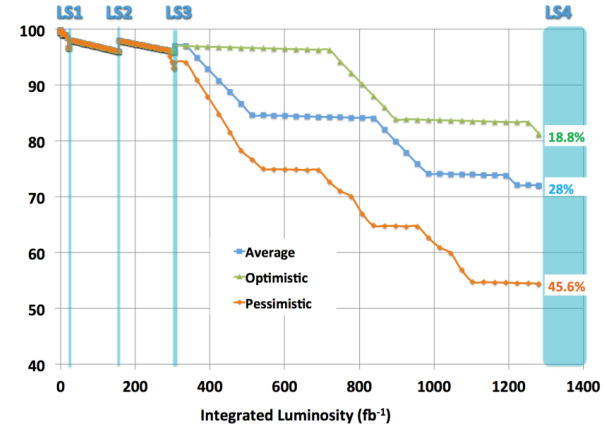


Figure 3.11: Extrapolated fraction of failing channels of the present DT MiC1 electronics as a function of the integrated luminosity for different scenarios until LS4 [177].

old can stay at the same level [191]. The Level-1 trigger consists of custom hardware processors receiving data from the calorimeters and the muon system. In return, they generate a trigger signal within  $3\ \mu\text{s}$ , with a maximum rate of 100 kHz. In the perspective of HL-LHC, each subsystem needs to achieve a minimum rate of 500 kHz with a latency not greater than  $12.5\ \mu\text{s}$ . DTs and CSCs will also need to improve their Data Acquisition (DAQ) transfer rate to reach a minimum near 1 Tbit/s. The foreseen upgrades are expected to exceed the requirements.

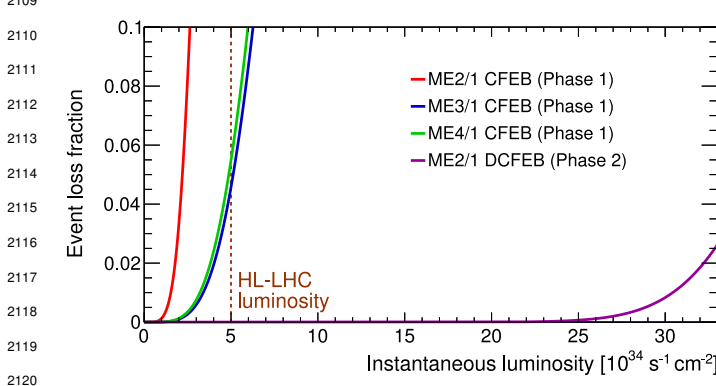


Figure 3.12: The event loss fractions as a function of the instantaneous luminosity is compared for CFEBs (Phase-1) and DCFEBs (Phase-2) at different CSC locations. HL-LHC luminosity is marked with the dashed line [177].

and High Voltage (HV) modules will not need any replacement. On the other hand, CSCs showed that their electronics would be able to live through the 10 years of Phase-2, but the limited buffer depth might cause memory overflows and read-out inefficiencies with a fraction of event loss ranging from 5 to more than 10% at an instantaneous luminosity similar to which of HL-LHC depending on the expected background. The replacement of CSCs' CFEBs by digital ones, DCFEBs, with a deeper buffer would permit to make event loss negligible and satisfy HL-LHC requirements as can be seen in Figure 3.12. All these new DT and CSC electronics will be connected to the trigger electronics via optical links to ensure a faster communication [177].

The upgrade on the side of Resistive Plate Chambers will not be done at the level of the electronics but rather that of the Link System located in the service cavern of CMS. RPC Link System connects the front-end electronics data of RPCs into CMS trigger processors. The main motivation for such an upgrade is that the electronic board composing the link system are built using ob-

The first version of Mini-crake electronics (MiC1) used by DTs don't allow for high enough trigger rate. In addition to this problem, it was shown that these electronics contain components that are not radiation hard enough to sustain HL-LHC conditions and hence, a too large number of channels may fail due to radiations as showed in Figure 3.11. The MiC1 will be replaced on each detector by an improved version referred to as MiC2 while Front-End Electronics (FEE)

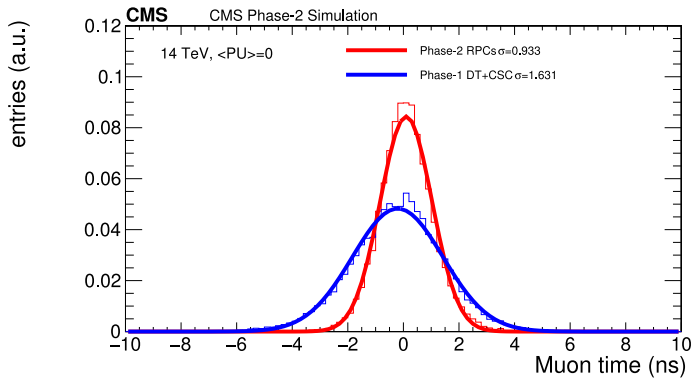


Figure 3.13: Comparison of the simulated time residuals in between reconstructed and true muon times without (blue) and with (red) the upgraded RPC link system [177].

solete and/or weak components that can easily suffer from the electromagnetic noise. These components may become the source of failing channels throughout Phase-2. Moreover, these link boards were originally designed only to match RPC digitized signals with the corresponding bunch crossing. Due to this feature, the time resolution of the full RPC chain is hence limited to 25 ns and does not make use of the full time resolution of the detectors. The time resolution foreseen after the upgrade can be seen through Figure 3.13 and is of the order of 1 ns. The exploitation of the full time resolution would make the synchronization of the RPC system easier and allow to have a finer offline out-of-time background removal within the 25 ns between consecutive bunch crossings. Moreover, this would greatly improve the trigger and reconstruction on HSCPs. Using the TOF information in between consecutive RPC stations, the minimal particle velocity than could be probed will drop from approximately 0.6 to 0.25 times the speed of light as showed in Figure 3.14.

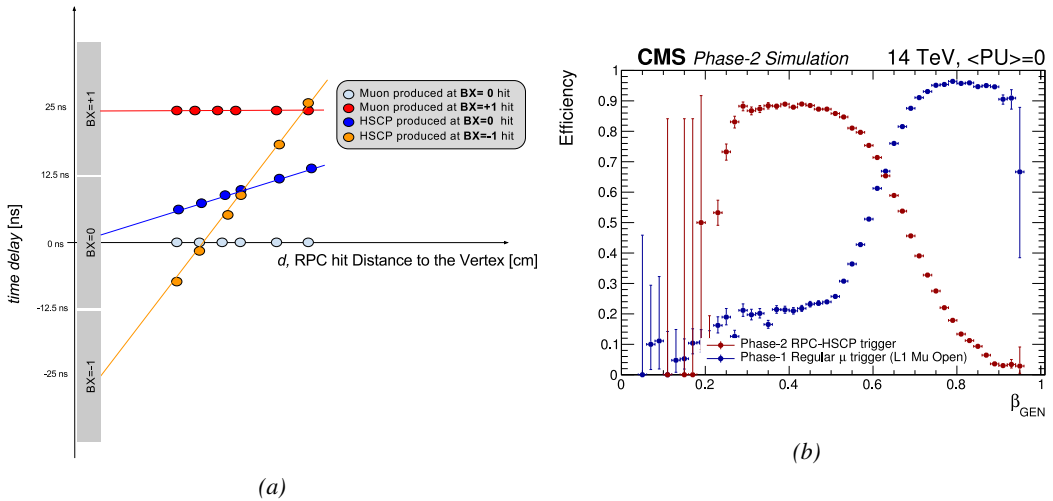


Figure 3.14: Figure 3.14a: Time delay with respect to a particle traveling at the speed of light measured at consecutive RPC stations for particles originating at different bunch crossings and traveling at different velocities [177]. Figure 3.14b: In blue is showed the standard Level-1 muon trigger efficiency as a function of  $\beta$  and in blue is showed the RPC-HSCP trigger efficiency after upgrade of the RPC Link System [177].

Upgrading RPC link system will require the installation of 1376 new link boards and 216 control boards. The new boards will make use of the recent progress made with fast FPGAs and will be a great improvement to the ASICs formerly used as they will be able to process signals from several detectors in parallel.

### 3.4 New detectors and increased acceptance

In the present muon system, the redundancy is assured by RPCs used for their robust bunch crossing assignments. The extension of the muon system towards higher pseudo-rapidity in an effort to complete the redundancy and to contribute to the precision of muon momentum measurements will require muon chambers with a spatial resolution less or comparable to the multiple scattering muons are subjected to while traveling through the detector volume [192].

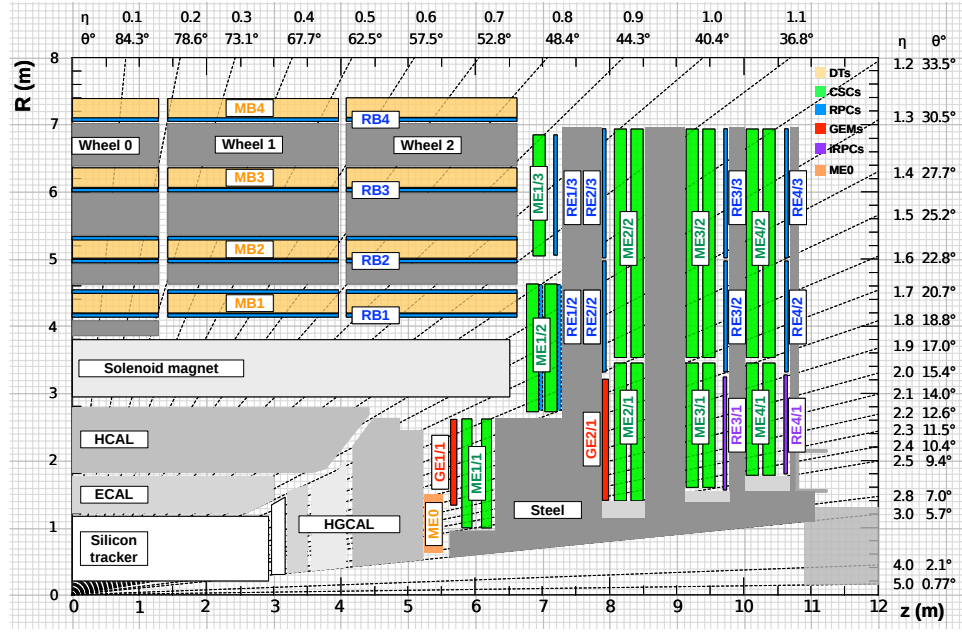


Figure 3.15: A quadrant of the muon system, showing DTs (yellow), RPCs (blue), and CSCs (green). The locations of new forward muon detectors for Phase-2 are contained within the dashed box and indicated in red for GEM stations (ME0, GE1/1, and GE2/1) and dark blue for improved RPC (iRPC) stations (RE3/1 and RE4/1).

Figure 3.15 shows a similar quadrant of CMS than the one presented in Figure 2.27 with the addition of Gas Electron Multiplier (GEM) (ME0, GE1/1 and GE2/1) and improved RPC (iRPC) (RE3/1 and RE4/1) in the pseudo-rapidity region  $1.6 < |\eta| < 2.4$ . The completion of the redundancy was already scheduled in the original CMS Technical Proposal [193] but never addressed. The coming Phase-2I is then the occasion to equip the region with the newest GEM and RPC technology. In order to match CMS requirements, a spatial resolution of  $\mathcal{O}(\text{few mm})$  will be necessary for the proposed new RPC stations while the GEMs will need a resolution better than 1 mm, as showed by the simulation in Figure 3.16. Indeed, most of the plausible physics will be covered only considering muons with  $p_T < 100 \text{ GeV}$ .

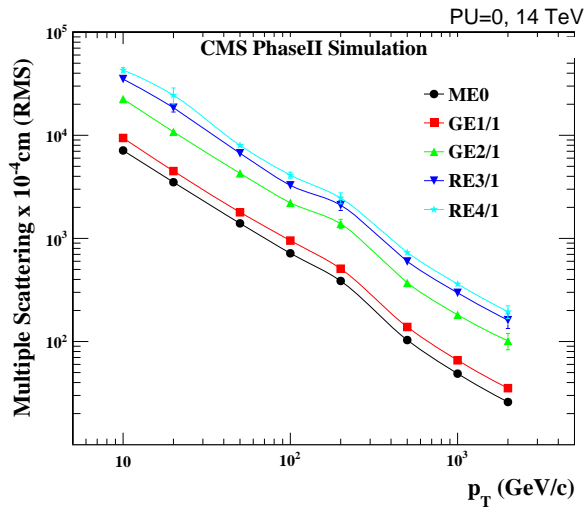


Figure 3.16: RMS of the multiple scattering displacement as a function of muon  $p_T$  for the proposed forward muon stations. All of the electromagnetic processes such as bremsstrahlung and magnetic field effect are included in the simulation.

### 3.4.1 Gas electron multipliers

In the region closer to the interaction point where the spatial resolution is requested for the new detectors to be better than 1 mm (at least for ME0 and GE1/1 according to Figure 3.16) and where the background rate will be the highest for muon detectors, the choice has been made to use triple GEMs, micro pattern gaseous detectors, instead of the originally planned RPCs. The GE1/1 project has been the first to be approved and demonstrators have been installed in CMS already during LS1. The rest of the detectors will be installed during LS2 while the GE2/1 and ME0 projects are still under development. ME0, GE1/1 and GE2/1 will be installed respectively close to the HCAL endcap, on the first and on the second muon endcap disks as can be seen from Figure 3.15.

Gas Electron Multipliers are gaseous detectors [194] whose gas volume is confined between two planar electrodes, the anode serving as read-out panel. The gas volume is divided in two or more regions by a single or multiple *GEM foils* as showed in Figure 3.17. These foils are very thin, of the order of a few tens of  $\mu\text{m}$ , and are pierced with holes as can be seen in Figure 3.18. Both surfaces of the GEM foils are clad with copper in order to apply a strong electric field in between each side that will generate very strong potentials in the holes. The gas region contained in between the cathode and the GEM foil is called the drift region as the electric field is not strong enough to cause avalanches and thus start an amplification. The primary electrons drift toward the foil and are accelerated and amplified by the very high potential within the holes, as showed in Figure 3.18. Then the electrons reach the second drift region where they will induce a signal on the read-out located on the anode. By restraining the amplification process at the level of the holes, the electrons can stay confined in a very little space and thus induce a very localized current, providing the GEMs

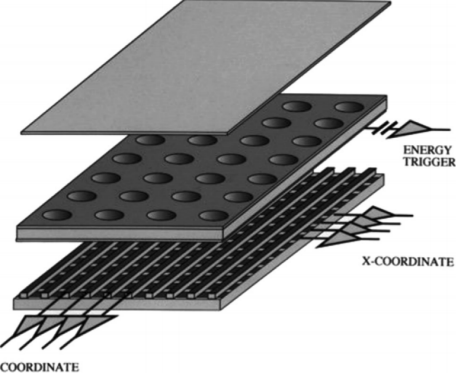


Figure 3.17: Schematics of a GEM. On top is the cathode and on the bottom, the anode on which a 2D read-out is installed. Finally, the GEM foil separates the gas volume into the drift region, in between the cathode and the foil, and the induction region, in between the foil and the anode. A negative voltage is applied on the cathode. The anode is connected to the ground.

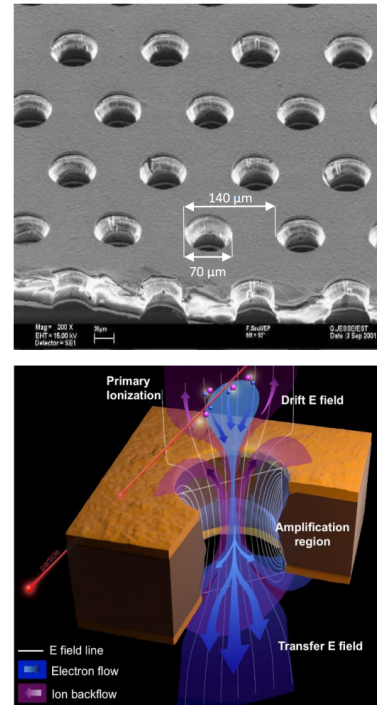


Figure 3.18: Top: Picture of a CMS GEM foil provided by a scanning electron microscope. Bottom: Representation of the electric field in a GEM hole and of the amplification electrons and ions undergo due to the very intense electric field.

with a very good spatial resolution.

The process can be repeated several times in a row, in order to achieve a stronger amplification. The GEMs that will be used in CMS are triple-GEM detectors operated with a 70/30 gas mixture of  $Ar/CO_2$ . They contain three GEM foils and hence three electron amplifications, as can be seen in Figure 3.19. The GEM foils used in CMS are 50  $\mu m$  foils clad with 5  $\mu m$  of copper on each side. The foils are pierced with double-canonical holes which inner and outer diameters are respectively 50 and 70  $\mu m$  which are placed 140  $\mu m$  from each other in a hexagonal pattern, as showed in Figure 3.18. These detectors have a time resolution better than 10 ns and reach very good spatial resolutions of less than 200  $\mu rad$  as indeed the position of the hits is not measured along the strips but following the azimuthal angle granularity of the radially organized trapezoidal strips.

The GEM Upgrade project started with GE1/1 [195]. GE1/1 detectors will already be installed during LS2. GE2/1 and ME0, on the other hand, will profit of the R&D knowledge and skills developed for GE1/1 while the requirements for each subsystem are different as they are not placed at the same distance from the interaction point. In this very forward region, a different position with respect to the center of the detector can dramatically change the conditions in which the detectors will have to be operated. In terms of rate capability, GE2/1, which is the furthest, is required to withstand 2.1 kHz/cm<sup>2</sup> while GE1/1 needs to be better than 10 kHz/cm<sup>2</sup> and ME0, better than 150 kHz/cm<sup>2</sup>. In terms of ageing with respect to charge deposition, ME0 needs to be certified to 840 mC/cm<sup>2</sup>, GE1/1 to 200 mC/cm<sup>2</sup> and GE2/1 only to 9 mC/cm<sup>2</sup>. All 3 detectors need to have a time resolution better than 10 ns and an angular resolution better than 500  $\mu rad$ .

On each GE1/1 ring, 36 super chambers, consisting of two single GEM layers and spanning 10°, will be installed covering the pseudo-rapidity region  $1.6 < |\eta| < 2.2$  together with ME1/1 CSCs. The reach of the muon system will be improved thanks to the GE2/1 that will overlap with the GE1/1 and cover a region from  $|\eta| > 1.6$  to  $|\eta| < 2.4$  and complete the redundancy of ME2/1. The super chambers, built with two triple-GEM layers each consisting of four single GEM modules due to the rather large surface of the GE2/1 chambers, that will be installed on the first ring of the second endcap will span 20° each. Hence, a total of 72 chambers will be assembled to equip the muon system. Finally, the ME0 installed near the HCAL endcap will cover the region  $2.0 < |\eta| < 2.8$ . This subsystem will consist in super modules of six layers of triple-GEM detectors covering an azimuthal angle of 20° leading to the construction of 216 single detectors.

Adding the GEMs into the forward region of the muon system will allow to strongly enhance the Level-1 Trigger performance as shown in Figure 3.20. In the region  $1.6 < |\eta| < 2.4$ , the trigger

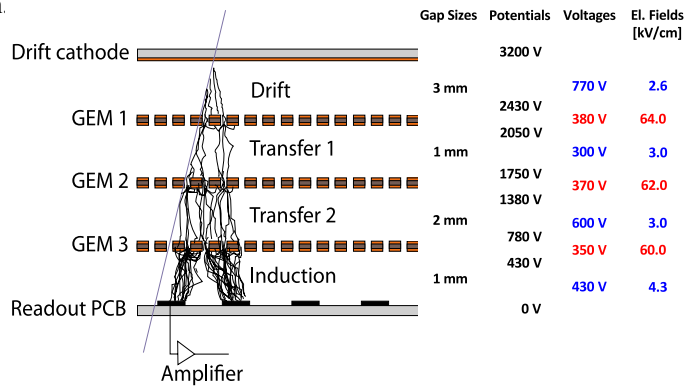


*Figure 3.19: Schematic representation of CMS triple-GEMs. The gas volume is divided into four areas. The drift area is the region where the primary electrons are created before being amplified a first time while passing through the first GEM foil. Then the process of drift and amplification is repeated twice in following two transfer areas and GEM foils. Finally, the charges have been amplified enough to induce current in the read-out strips while in the last drift area. The typical dimensions, potentials and electric fields are provided.*

efficiency of the current system would lie between 80 and 90% under HL-LHC conditions. The installation of GEMs would bring the efficiency to a consistent 92 to 94% on the entire region. At the same time, the trigger rate is expected to fluctuate from 3 to 10 kHz with the current system alone. The addition of detectors to complete the redundancy would allow keeping the rate mostly under 2 kHz. Moreover, benefiting from the good spatial and angular resolution of the GEMs, the precision into the muon measurement will also be improved by an order of magnitude thanks to the addition of GEMs as can be seen from the simulation presented in Figure 3.21.

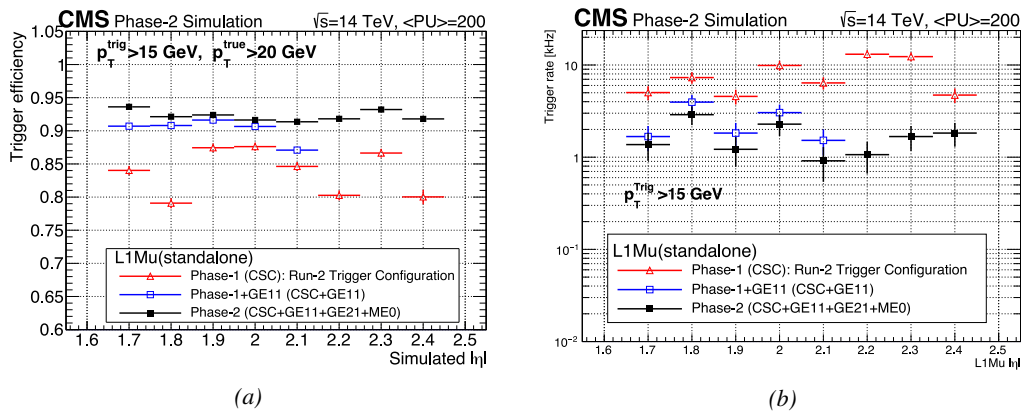


Figure 3.20: Simulated efficiency and rate of the standalone Level-1 muon trigger using tracks reconstructed in CSCs and all GEM stations compared with Phase-1 values in the case where only CSCs are used or CSCs+GE11. The zones of inefficiency of the CSC subsystem are compensated by the addition of GEMs during Phase-2 and the trigger rates is kept from increasing due to the high luminosity [177].

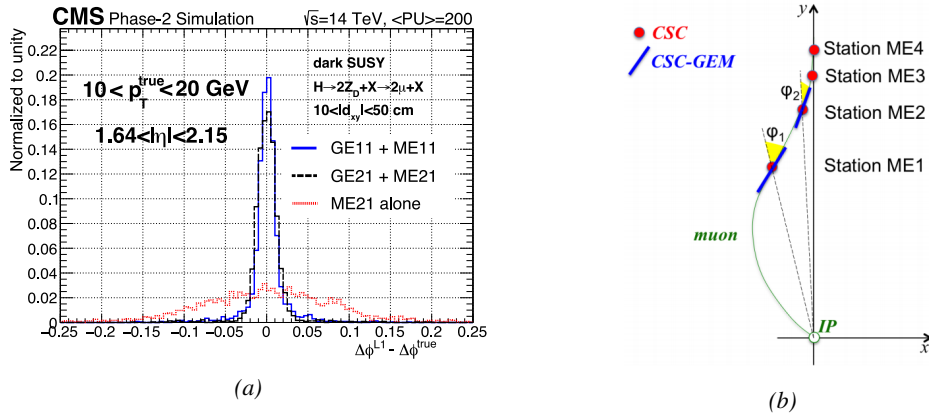


Figure 3.21: Figure 3.21a: Simulated resolution of the muon direction measurement  $\Delta\phi$  with Phase-2 conditions. In the second endcap station, the resolution is compared in the case of CSCs (ME2/1) alone and CSCs+GEMs (GE2/1+ME2/1) while a similar resolution measurement is given in the case of the first station (GE1/1+ME1/1) [177]. Figure 3.21b: The addition of GEM detectors on stations 1 and 2 (ME0 is considered to contribute to station 1) as redundant system to CSCs allows improving the muon momentum improvement through a more accurate measurement of the local bending angles  $\phi_1$  and  $\phi_2$  [177].

### 2290 3.4.2 Improved forward resistive plate chambers

2291 Figure 3.15 shows that the iRPCs that will equip the third and fourth endcap disks in position RE3/1  
 2292 and RE4/1 will finally be the partners of the CSCs in position ME3/1 and ME4/1. They will complete  
 2293 Phase-1 plans by bringing the needed upgrades in the perspective of Phase-2 as the older chambers  
 2294 are not suitable to equip the forward region of CMS due to HL-LHC rates and charge deposition.  
 2295 By completing the redundancy, more hits along the muon track will be available and the lever arm  
 2296 will be improved. The benefits from extending the redundancy of the muon system with iRPCs to  
 2297 the forward most region is shown in Figure 3.22 in which the trigger efficiency is presented with and  
 2298 without RPCs. It is possible to see that the efficiency of the CMS muon trigger with the complete  
 2299 redundancy is consistently improved to a level above 95% in the region  $|\eta| > 1.8$  as the iRPCs help  
 2300 filling the holes in the CSC system.

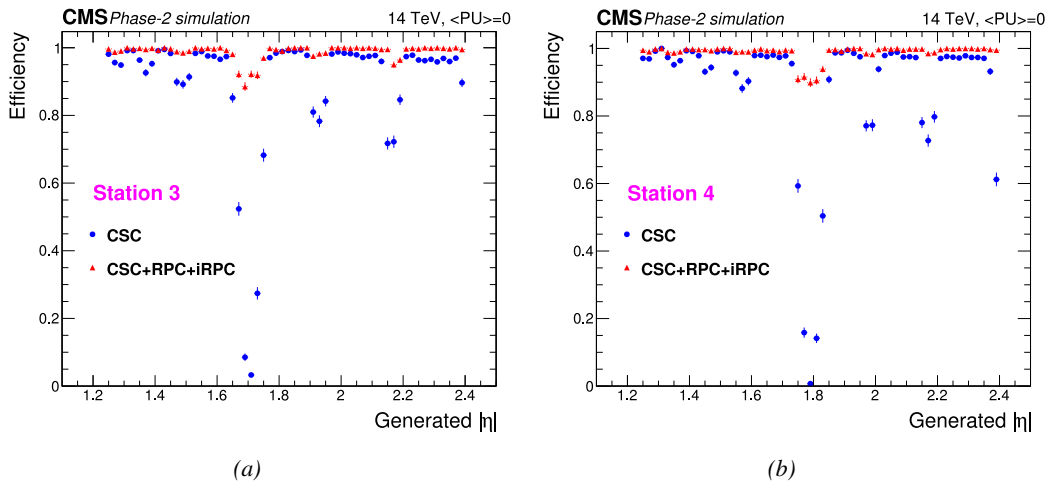
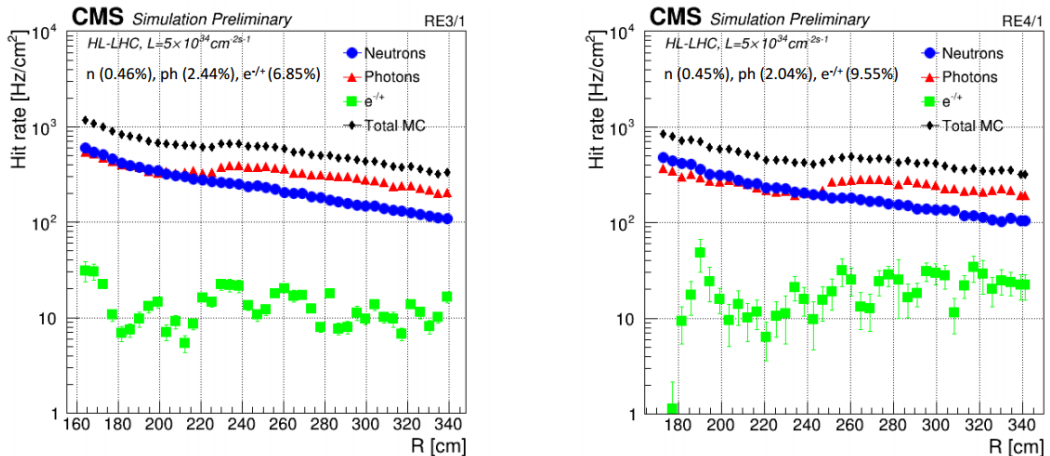


Figure 3.22: Simulation of the impact of RPC hit inclusion onto the local trigger primitive efficiency in station 3 (Figure 3.22a) and station 4 (Figure 3.22b) [177]. The contribution of iRPC starts above  $|\eta| = 1.8$ .

2301 The detectors that will be installed in the coming years will have similarities with the already  
 2302 existing RPC system. 18 of the new chambers, each spanning  $20^\circ$  in  $\varphi$  around the beam axis with  
 2303 96 radially oriented trapezoidal read-out strips, will cover each muon endcap disk leading to the  
 2304 production of 72 iRPCs. The main difference with the old RPC detectors will be found at the level  
 2305 of the read-out panels. Indeed, the new chambers will not feature read-out strips segmented in  $\eta$   
 2306 but rather will favor a read-out on both strip ends to determine the position of the hits along the  
 2307 chamber. By using fast front-end electronics a radial spatial resolution of the order of 2 cm could  
 2308 be achieved to contribute to the better reconstruction of muons in the forward region where the  
 2309 bending due to the magnetic field is low. This technical choice is motivated by the fact that, in  
 2310 the case a  $\eta$  segmentation were to be used, at least five pseudo-rapidity partitions would have been  
 2311 necessary to reach the minimal radial spatial resolution ( $\approx 20$  cm). Having only one strip along the  
 2312 chamber read-out from both ends reduces by 60% the total number of channels and the necessary  
 2313 cabling, and allows for a better spatial resolution. The strip pitch will range from 6.0 mm (5.9 mm)  
 2314 on the high pseudo-rapidity end to 12.3 mm (10.9 mm) on the low one on position RE3/1 (RE4/1).  
 2315 The spatial resolution in the direction perpendicular to the strips should reach approximately 3 mm,  
 2316 better than the minimal needed resolution (Figure 3.16). Finally, the overall time resolution of the

new installation will be equally 1 ns, as for the present due to the same link system being used even though the detector itself can achieve a time resolution of less than 100 ps, necessary for a spatial reconstruction of the hits with a resolution of 2 cm or less along the strip length.

Having only a single strip instead of pseudo-rapidity segmentation will increase the probability of double hits in the same channel. The probability was estimated to be low enough as it shouldn't exceed 0.7%. This estimation was made assuming an average hit rate per unit area of  $600 \text{ Hz/cm}^2$  in the iRPCs (see Figure 3.23), a cluster size (average number of strips fired per muon) of 2, a strip active area of  $158.4 \times 0.87 \text{ cm}^2$  and a safety factor 3. The corresponding rate per strip is estimated to be 380 kHz leading to an average time interval in between two consecutive hits of 2600 ns. This is compared to the minimal time interval of 16 ns necessary to avoid ambiguities. Indeed, a maximum of 10 ns is spent by the signal traveling through the strip to reach the electronics to which can be added 1 ns of dead time and 2 Time-to-Digital Converter (TDC) clock cycles of 2.5 ns to convert the signal arrival time into a digital value in the FEEs. The probability of having ambiguous double hits in a strip is then the ratio between the minimal time interval in between two consecutive hits and the average time interval estimated from the rate the detectors would be subjected to.



*Figure 3.23: Expected hit rate due to neutrons, photons, electrons and positrons at HL-LHC instantaneous luminosity of  $5 \times 10^{34} \text{ cm}^{-2}\text{s}^{-1}$  in RE3/1 and RE4/1 chambers [196, 197]. The sensitivities of iRPCs used in the simulation for each particle are reported and differ from one endcap disk to another as the energies of the considered particles varies with the increasing distance from the interaction point.*

The instantaneous luminosity at HL-LHC being very high, the rates at the position of the new chambers needed to be simulated in order to understand the necessary requirements for these detectors. The simulated results for different background components (neutrons, photons, electrons and positrons) are shown in Figure 3.23 assuming known sensitivities to these particles. It is shown that on average over the iRPC areas the rates would be of the order of  $600 \text{ Hz/cm}^2$  ( $600 \text{ Hz/cm}^2$  seen in RE3/1 and  $480 \text{ Hz/cm}^2$  in RE4/1) [196, 197]. Thus, taking into account a safety factor of about 3, it was decided that improved RPCs should at least be certified for rates reaching  $2 \text{ Hz/cm}^2$  which will be achieved thanks to several improvements on the design and on the electronics. The detectors design will be based on the existing RPCs as they will also feature double RPC gaps. Similarly to the existing RPC system, the electrode material will be HPL although the thickness of the electrodes and of the gas gap will be reduced to 1.4 mm as a thinner gas gap leads to a decrease

of deposited charge per avalanche as showed in Figure 3.24. The charge deposition in the case of 1.4 mm thick electrodes is reduced by a factor greater than 5 when compared to 2 mm electrodes at a similar electric field. The smaller the gas gap, the more the detector becomes sensitive to gap non-uniformities across the electrode planes, making a gap of 1.4 mm a good compromise in between these two competing factors.

A lower charge deposition inside of the detector volume means a slower ageing and a longer lifetime for detectors subjected to high irradiation. But, in order to take advantage of the lower detector gain, more sensitive electronics are required such that part of the gain that was formerly achieved in the gas volume can be moved to the electronics. Achieving this with the technology developed more than ten years ago for the present system is not possible as the signal over noise ratio of such electronics doesn't allow to detect charges as low as 10 fC. Moreover, the new front-end electronics will need to be radiation hard to survive more than ten years of HL-LHC conditions. The new technology that has been chosen is based on the PETIROC ASIC manufactured by OMEGA and is a 64-channel ASIC called CMS RPCROC[177, 198, 199]. The properties of these electronics will be discussed in Chapter 6.

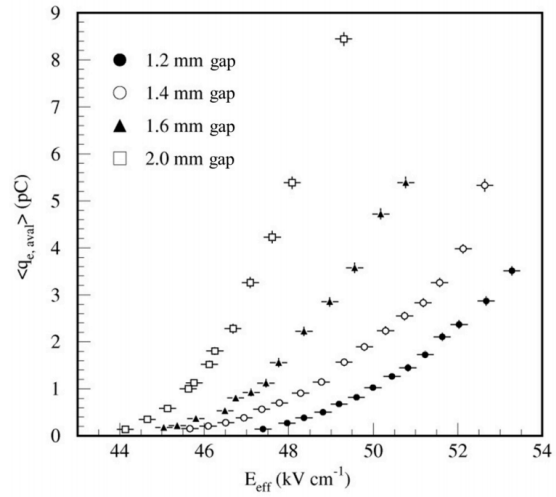


Figure 3.24: Measured average charge per avalanche as a function of the effective electric field for different gas gap thickness in double-gap RPCs using HPL electrodes [177].

The properties of these electronics will be discussed in Chapter 6.

## 3.5 Impact on Level-1 Trigger and physics performance

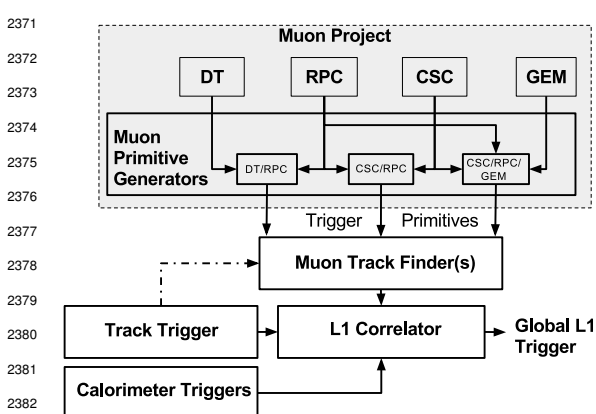


Figure 3.25: Level-1 Trigger data flow during Phase-2 operations [177].

The upgrades of the different subsystems will have a subsequent impact on the Level-1 Trigger. Indeed, although its main scheme will not be affected, the efficiency of the trigger in identifying muons and provide the DAQ with good and fast trigger that can cope with HL-LHC instantaneous luminosity is a major improvement. In addition to the upgrade of the muon system in terms of trigger accept rate and latency, the Level-1 Trigger will get extra information by including the Tracker Trigger into its Muon Track Finder logic and combine the L1 Muon Trigger with Tracker and Calorimeter Triggers to generate a Global L1 Trigger, as shown in Figure 3.25. Using the

track candidates of both the muon system and the tracker in spatial coincidence will allow for a much better momentum resolution thanks to better identified muons and, hence, better measured transverse impulsion as described in reference [177].

In terms of muon trigger, three regions are considered due to their different track finding logic: the Barrel Muon Track Finder (BMTF), the Endcap Muon Track Finder (EMTF) for both the barrel and endcap regions, and finally the Overlap Muon Track Finder (OMTF) which concerns the pseudo-rapidity region in which there is a common coverage by both the barrel and endcap muon systems. This region can be seen in Figure 3.15 for  $0.9 < |\eta| < 1.2$  and requires a specific more complex logic to provide an efficient reconstruction of muons due to the different orientation of the detectors and of the more complex magnetic field of this region. The development of a track finder specific to the overlap region was achieved during the Phase-1 upgrade of the L1-Trigger [200].

The upgraded RPC link system, allowing to take profit of the full 1 ns resolution of the detectors, will help reducing the neutron induced background, slightly improve the bunch crossing assignment, and help increasing the trigger efficiency in every sector. The upgrade of DT electronics is also to take into account as the trigger primitive generator will be renewed through the use of TDCs that will send the digitized signals directly to common DT/RPC back-end electronics instead of having an on-detector trigger logic as it will be the case until the end of Phase-1. The combination of RPC hits together with DT primitives will bring extra improvement in the bunch crossing assignment in the barrel and overlap regions and improve the efficiency of the trigger between the wheels were the quality of DT primitives is the poorest.

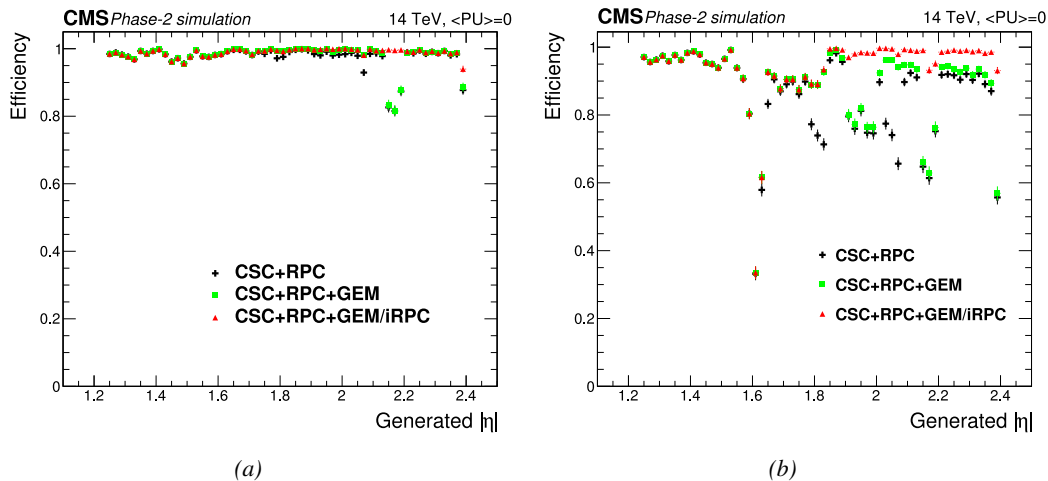


Figure 3.26: Efficiency of the L1 trigger in the endcap region after Phase-2 upgrade in the case CSC/GEM/RPC hits are requested in at least two stations out of four (3.26a) and in all four stations (3.26b) [177].

The current EMTF already uses more sophisticated algorithms by combining together RPC hits and CSC primitives. The GEMs, in stations 1 and 2, and the iRPCs, in stations 3 and 4, will be added into the EMTF algorithm. Both these contributions will help increase the efficiency of the L1 trigger in the endcap region in one hand, as showed by Figure 3.26, and help lowering the L1 trigger rate in the other hand, especially in the most forward region. Similarly to the RPC/CSC algorithms, data from both CSCs and GEMs are combined into the Optical TMBs (OTMBs) to build on each station, GEM/CSC primitives matching space and time information from both subsystems. The efficiency

improvement and rate reduction close to the beam line will be naturally enhanced by the addition of more hits along the muon tracks, as can be seen from Figure 3.27 that focuses especially in the most challenging pseudo-rapidity region. Indeed, the contribution from the GEMs to the lever arm of each track thanks to their high angular resolution will be a great asset in achieving such results, as can be seen in Figure 3.28. The rate will be partly reduced in the forward region thanks to the better spatial resolution of iRPCs, with respect to the current RPC system. The ambiguity brought by multiple local charged tracks in CSCs will be reduced, as explained through Figure 3.29. Indeed, as the rates will increase, the probability to record more than a single local charged track will greatly increase. This is due to the fact that the trigger algorithm uses information from three consecutive bunch crossings to find muon tracks. It is estimated that with iRPCs operated at 95% efficiency the resolution of ambiguous events would be of the order of 99.7%.

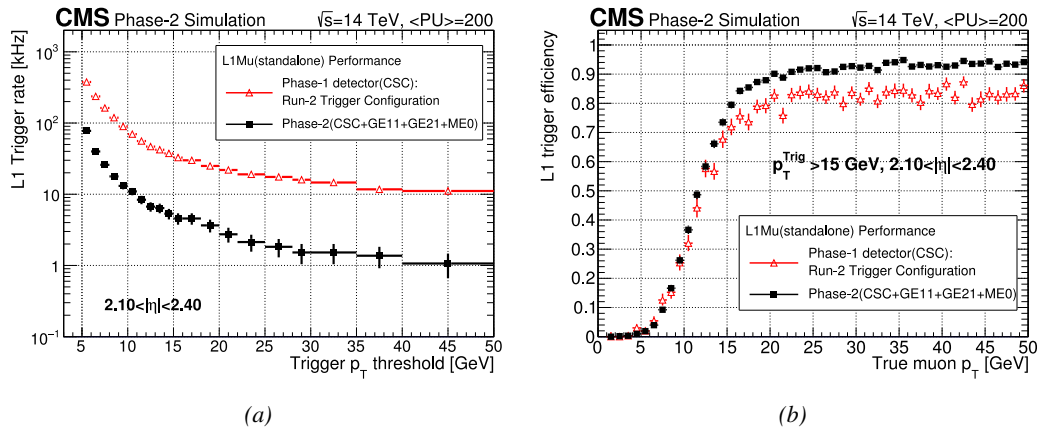


Figure 3.27: Comparison of L1 trigger performances for prompt muons with and without the addition of GEMs in the region  $2.1 < |\eta| < 2.4$  at Phase-2 conditions [177]. GEMs would allow a reduction of the trigger accept rate by an order of magnitude (Figure 3.27a) while increasing the trigger efficiency (Figure 3.27b).

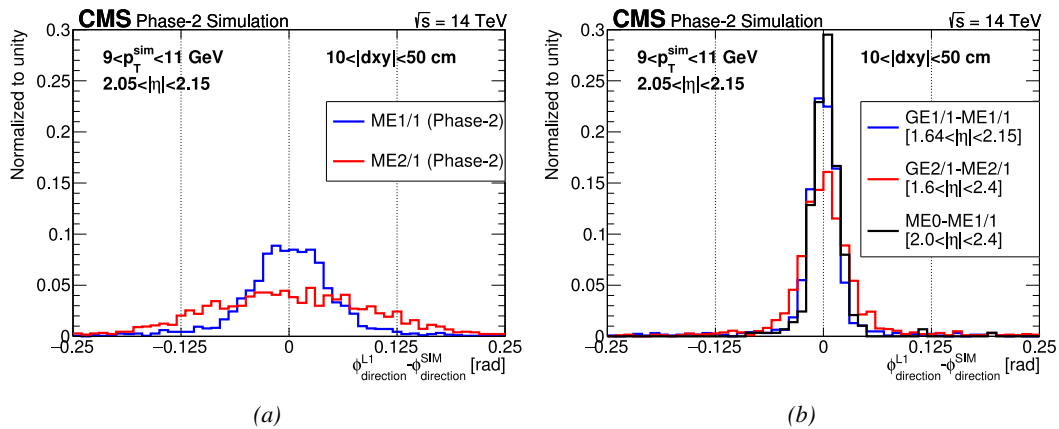
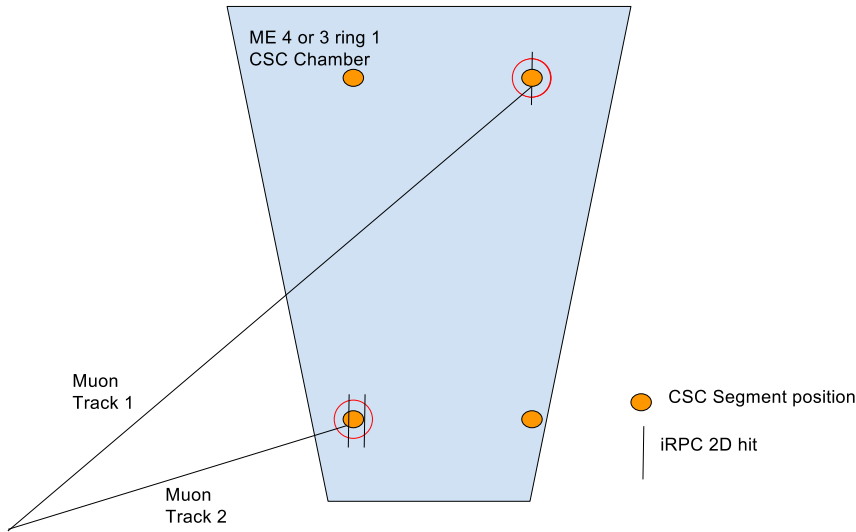


Figure 3.28: The angular resolution on reconstructed muon tracks in the GEM overlap region  $2.0 < |\eta| < 2.15$  is compared for Phase-2 conditions in the case CSC are alone (Figure 3.28a) and in the case the GEMs' data, including ME0, is combined to which of CSCs (Figure 3.28b) [177].



*Figure 3.29: Resolution of the LCT ambiguous events thanks to the combination of CSC and iRPC readout data. Using CSCs only, two pairs of hits are possible [177].*

## 2424 3.6 Ecofriendly gas studies

2425 The European Commission adopted a new "F-gas regulation" in 2014 [201] with the goal to strongly  
 2426 control and reduce the use of fluorinated gases with high Global Warming Potential (GWP). Using  
 2427  $CF_4$ ,  $C_2H_2F_4$  and  $SF_6$ , both CSC and RPC subsystems will need to address this problem by finding  
 2428 new gas mixture for the operation of their detectors. Finding a replacement for these gas components  
 2429 that were used for very specific reasons is a great challenge. Indeed, CSCs use  $CF_4$  in order to  
 2430 enhance the longevity of the detectors, increase the drift velocity of electrons and quench photons  
 2431 with a non-flammable gas mixture. RPCs use a mixture mainly composed of  $C_2H_2F_4$ , or  $R134a$ ,  
 2432 that features a high effective Townsend coefficient and the great average fast charge allowing for  
 2433 operations with a high threshold. The mixture also contains a small fraction of  $SF_6$  that is used  
 2434 for its electronegative properties that prevents the development of delta-rays in the gas volume that  
 2435 might trigger multiple ionization and avalanches.

	CSC	RPC
Greenhouse gases used	$CF_4$	$C_2H_2F_4$ and $SF_6$
Greenhouse gases fraction in the gas mixture	10%	95.2% and 0.3%
Global Warming Potential (relative to $CO_2$ )	6500	1300 and 23900
Gas mixture re-circulation	Yes, 90%	Yes, 85%
Gas mixture replenishing rate (l/hr)	700	1100
F-gas recuperation	Yes, $\approx 40\%$	No
F-gas venting rate (l/hr)	42	1047 and 3.3
$CO_2$ -equivalent rate ( $m^3/h$ )	273	1440
Relative impact (entire muon system = 100%)	16%	84%

*Table 3.1: Details of the greenhouse fluorinated gases used in CMS and of their GWP [177].*

2436 Nevertheless, all these gases have a very high GWP, as reported in Table 3.1, and only few

options are left. The subsystems need to work on strongly decreasing the loss of these gases due to leaks in the gas system or need to completely change their gas mixture for more ecofriendly ones. Reducing the amount of F-gas released in the atmosphere due to leaks on the current gas system will require installation of a F-gas recuperation system on RPCs side and an upgrade of CSCs existing one in addition to the repair of existing leaks. With such measures, it is expected that the total rate of greenhouses gas vented in the atmosphere would represent only 1.6% of the current levels [177]. In the most critical case the F-gas were to be banned, it would be necessary to have replacement mixtures to operate CMS. CSC is presently investigating replacement for  $CF_4$  such as  $CF_3I$ ,  $C_4F_6$ ,  $IC_3F_6$ ,  $C_3F_8$  or  $CHF_3$ . RPCs, in collaboration with the ATLAS RPC group which uses the same gas mixture, have identified  $CF_3I$  ( $GWP \leq 1$ ) and  $C_3H_2F_4$  ( $GWP \sim 6$ ), referred to as *HFO-1234ze*, as potential candidates with mixtures containing  $CO_2$ .  $CO_2$  is already widely used by various RPC experiments in mixtures with argon. More R&D needs to be conducted for both subsystems before concluding on the best alternative. Finding no good alternative to the present mixtures will require very efficient abatement system in CMS to burn and convert the greenhouse gases into less harmful ones. This way, the air pollution would be strongly reduced.

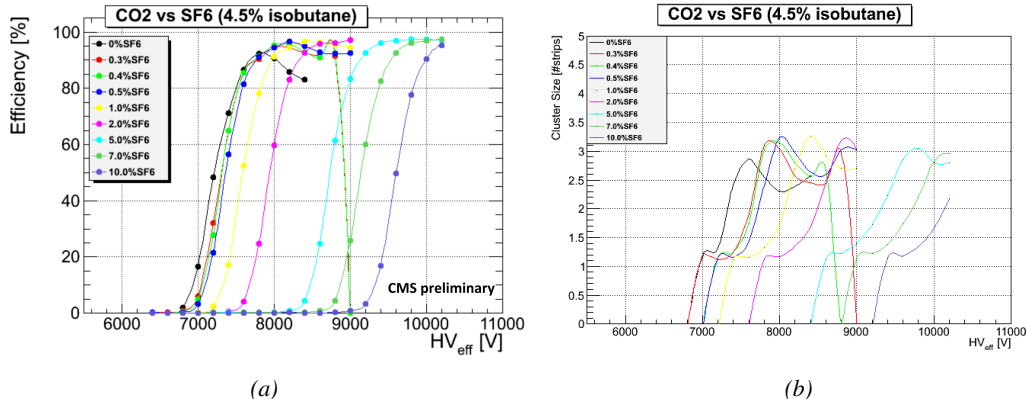


Figure 3.30: Efficiency (Figure 3.30a [202]) and cluster size (Figure 3.30b) of a standard double-gap RPC operated with  $CO_2$  mixtures for different ratios of  $SF_6$ .

Preliminary studies conducted in Ghent confirmed that  $CO_2$  alone would require more than 1% of  $SF_6$  to reach full efficiency, as presented in Figure 3.30. Even though the results obtained in Ghent don't show the streamer probability (the probability to have very large avalanches whose induced charge is greater than 20 pC), the variation of the cluster size indicates that the streamers become predominant before the efficiency plateau is reached. Then, a very first test with an *HFO/CO<sub>2</sub>* was performed. Only one ratio was tested as can be seen from Figure 3.31 that displays a good efficiency with a plateau located at a similar high voltage than with *R134a* based mixtures

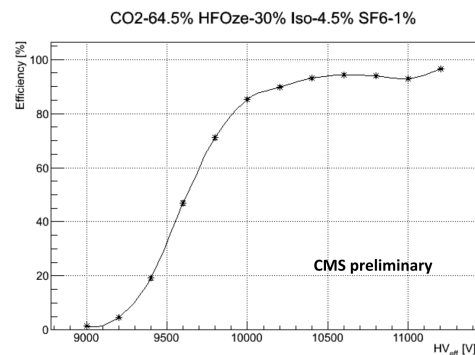
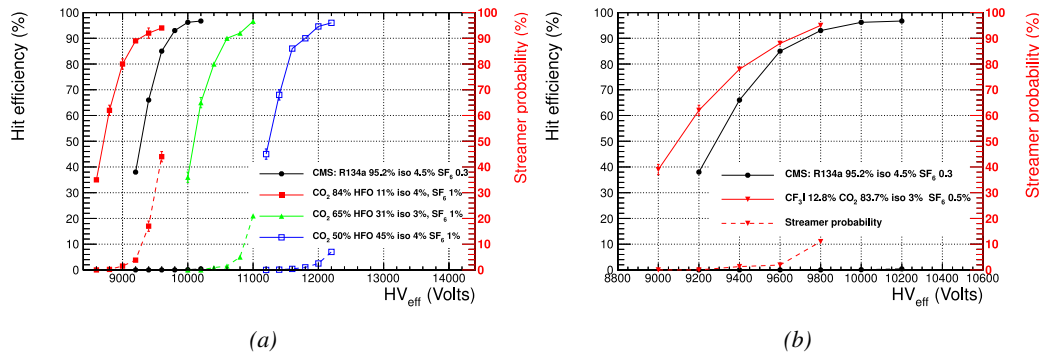


Figure 3.31: Efficiency of a CMS double-gap RPC operated with 30% of  $HFO$ , 4.5% of  $iC_4H_{10}$ , 1% of  $SF_6$  and 64.5% of  $CO_2$  [202].

(Figure 3.32). The status of RPC studies is presented in Figure 3.32 in which the performance (efficiency and streamer probability) of a CMS double-gap RPC operated with alternative gas mixtures is compared to the present CMS RPC mixture. Although the efficiency of detectors operated with mixtures containing  $CO_2/CF_3I$  or  $CO_2/HFO$  as a replacement for  $C_2H_2F_4$  seems to reach similar levels than which of the detectors operated with the present mixture, the new gas mixtures feature a streamer probability that far exceeds which of the present fluorinated mixture. The  $SF_6$  doesn't seem to prevent the formation of streamers as efficiently even when used at levels more than three times higher than with the standard CMS RPC mixture. Nevertheless, it is important to note that these results were obtained with a single-gap RPC while the use of a double-gap RPC reduces the operation voltage by 200 to 300 V, lowering the induced charge. A compromise in between good efficiency and acceptable level of streamer probability, and the fine-tuned composition of potential replacement gas mixtures will be kept on being studied using a standard double-gap CMS RPC.



**Figure 3.32:** The efficiency (solid lines) and streamer probability (dashed lines) of  $HFO/CO_2$  (Figure 3.32a) and  $CF_3I/CO_2$  (Figure 3.32b) based gas mixtures as a function of the effective high-voltage are compared with the present CMS RPC gas mixture represented in black [177, 202]. The detector used for the study is a single-gap RPC with similar properties than CMS RPCs. The streamer probability is defined as the proportion of events with a deposited charge greater than 20 pC.

Although the technology certification was conducted with the standard CMS gas mixture which is a known reference, the iRPCs will need to be operated with new environmental-friendly gas mixtures. Studies have then been conducted with iRPCs, assuming that the  $HFO/CO_2$  mixture containing an almost equal level of both components was the most likely candidate to replace the standard mixture. In this purpose, an iRPC prototype has been built to be tested with an  $HFO/CO_2$  gas mixture. The mixture, referred to as "eco-gas" in Figure 3.33, contained 50% of  $HFO$ , 4.5% of  $iC_4H_{10}$ , 0.3% of  $SF_6$  and 45.2% of  $CO_2$ . In Figure 3.33 is presented a result consistent with the blue curve obtained with 45% of  $HFO$ , 4% of  $iC_4H_{10}$ , 1% of  $SF_6$  and 50%

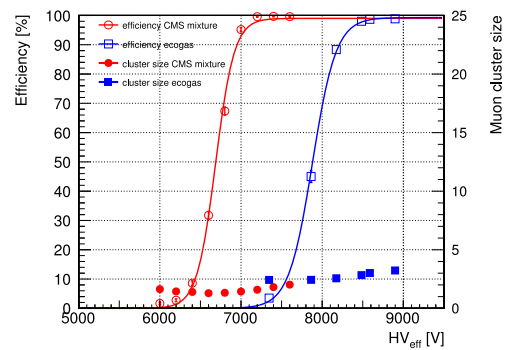


**Figure 3.33:** Efficiency (open symbols) and cluster size (full symbols) of an iRPC as a function of the effective voltage for the standard CMS gas mixture and an environmental-friendly gas mixture [177].

<sup>2496</sup> of  $CO_2$  flushed into a standard double-gap RPC. Instead of the streamer probability, the cluster size  
<sup>2497</sup> is shown. The average number of hits generated by a muon passing through the chamber seem to  
<sup>2498</sup> have increased by 1 at the level of the knee of the sigmoid plateau using the ecogas.



# 4

2499

2500

## Physics of Resistive plate chambers

2501 A Resistive Plate Chamber (RPC) is a gaseous detector used in high-energy physics experiments  
2502 as described in Chapter 3. It has been developed in 1981 by Santonico and Cardarelli [203], under  
2503 the name of *Resistive Plate Counter*, as an alternative to the local-discharge spark counters pro-  
2504 posed in 1978 by Pestov and Fedotovich [204, 205]. Working with spark chambers implied using  
2505 high-pressure gas and high mechanical precision which the RPC simplified by formerly using a gas  
2506 mixture of argon and butane flowed at atmospheric pressure and a constant and uniform electric  
2507 field propagated in between two parallel electrode plates. Moreover, a significant increase in rate  
2508 capability was introduced by the use of electrode plate material with high bulk resistivity, preventing  
2509 the discharge from growing throughout the whole gas gap. Indeed, the effect of using resistive elec-  
2510 trodes is that the constant electric field is locally canceled out by the development of the discharge,  
2511 limiting its growth.

2512 Through its development history, different operating modes [206–208], gas mixtures [203, 208–  
2513 213] and new detector designs [214–216] have been discovered, leading to further improvement of  
2514 the rate capability of such a detector. The low developing costs and easily achievable large detection  
2515 areas offered by RPCs, as well as the wide range of possible designs, made them a natural choice  
2516 to as muon chambers and/or trigger detectors in multipurpose experiments such as CMS [192] or  
2517 ATLAS [217], time-of-flight detectors in ALICE [218], calorimeter with CALICE [219] or even  
2518 detectors for volcanic muography with ToMuVol [220].

### 2519 4.1 Principle

2520 RPCs are ionisation detectors composed of two parallel resistive plate electrodes in between which  
2521 a constant electric field is set. The space in between the electrodes, referred to as *gap*, is filled with  
2522 a dense gas that is used to generate primary ionization into the gas volume. The free charge carriers  
2523 (electrons and cations) created by the ionization of the gas molecules are then accelerated towards the  
2524 electrodes by the electric field, as shown in Figure 4.1 [221]. RPCs being passive detectors, a current  
2525 on pick-up copper read-out placed outside of the gas volume is induced by the charge accumulation

2526 during the growth of the avalanche resulting from the acceleration of the charge carriers. As a  
 2527 consequence, the time resolution of the detector is substantially increased as the output signal is  
 2528 generated while the electrons are still in movement. The advantage of a constant electric field, over  
 2529 multi-wire proportional chambers, is that the electrons are being fully accelerated from the moment  
 2530 charge carriers are freed and feel the full strength of the electric field that doesn't depend on the  
 2531 distance to the readout and that the output signal doesn't need for the electrons to be physically  
 2532 collected.

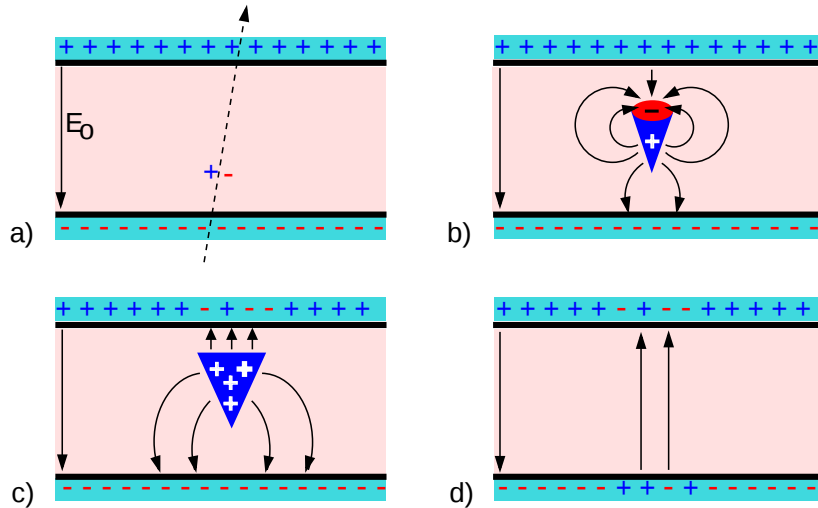


Figure 4.1: Different phases of the avalanche development in the RPC gas volume subjected to a constant electric field  $E_0$ . a) An avalanche is initiated by the primary ionisation caused by the passage of a charged particle through the gas volume. b) Due to its growing size, the avalanche starts to locally influence the electric field. c) The electrons, lighter than the cations reach the anode first. d) The ions reach the cathode. While the charges have not recombined, the electric field in the small region around the avalanche stays affected and locally blinds the detector.

2533 After an avalanche developed in the gas, a time long compared to the development of a discharge  
 2534 is needed to recombine the charge carriers in the electrode material due to their resistivity. This  
 2535 property has the advantage of affecting the local electric field and avoiding sparks in the detector  
 2536 but, on the other hand, the rate capability is intrinsically limited by the time constant  $\tau_{RPC}$  of the  
 2537 detector. Using a quasi-static approximation of Maxwell's equations for weakly conducting media,  
 2538 it can be shown that the time constant  $\tau_{RPC}$  necessary to the charge recombination at the interface  
 2539 in between the electrode and the gas volume is given by the Formula 4.1 [222].

$$(4.1) \quad \tau_{RPC} = \frac{\epsilon_{electrode} + \epsilon_{gas}}{\sigma_{electrode} + \sigma_{gas}}$$

2540 A gas can be assimilated to vacuum, leading to  $\epsilon_{gas} = \epsilon_0$  and  $\sigma_{gas} = 0$ , and the electrodes  
 2541 permittivity and conductivity can be written as  $\epsilon_{electrode} = \epsilon_r \epsilon_0$  and  $\sigma_{electrode} = 1/\rho_{electrode}$ ,  
 2542 showing the strong dependence of the time constant to the electrodes resistivity in Formula 4.2.

$$(4.2) \quad \tau_{RPC} = (\epsilon_r + 1)\epsilon_0 \times \rho_{electrode}$$

Very few materials with a low enough resistivity exist in nature. The resistivity targeted to build RPCs ranges from  $10^9$  to  $10^{12} \Omega \cdot \text{cm}$ . The most common RPC electrode materials are displayed in Table 4.1. When the doped glass and ceramics can offer short time constants of the order of 1 ms, the developing cost of such materials is quite high due to the very low demand. Thus, High-pressure laminate (HPL) is often the choice for high-rate experiments using very large RPC detection areas. Other experiments working at cosmic muon fluxes can safely operate with ordinary float glass.

Material	$\rho_{\text{electrode}} (\Omega \cdot \text{cm})$	$\epsilon_r$	$\tau_{\text{RPC}} (\text{ms})$
Float glass	$10^{12}$	$\sim 7$	$\sim 700$
High-pressure laminate	$10^{10}$ to $10^{12}$	$\sim 6$	$\sim 6$ to 600
Doped glass (LR S)	$10^9$ to $10^{11}$	$\sim 10$	$\sim 1$ to 100
Doped ceramics (SiN/SiC)	$10^9$	$\sim 8.5$	$\sim 1$
Doped ceramics (Ferrite)	$10^8$ to $10^{12}$	$\sim 20$	$\sim 0.2$ to 2000

Table 4.1: Properties of the most used electrode materials for RPCs.

## 4.2 Rate capability and time resolution of Resistive Plate Chambers

The electrode material plays a key role in the maximum intrinsic rate capability of RPCs. R&D is continuously being done to develop at always cheaper costs material with lower resistivity. Nevertheless, the amount of charge released, i.e. the size of the discharge, if reduced leads to a smaller blind area in the detector, increasing the rate capability of the detector. On the other hand, the drift velocity of electrons in the gas volume being quite stable with the applied electric field, the design of a detector and the associated read-out and pulse-processing electronics will be a major component of the time resolution of RPCs. Moreover, the sensitivity of the electronics will also help increasing the rate capability by lowering the gain the gas volume needs to be operated at, increasingly lowering the gas volume in which the signals will develop.

### 4.2.1 Operation modes

Being a gaseous detector using an accelerating electric field to amplify the signal of primary charge carriers, the RPC can be operated into different modes as the electric field intensity varies. Each mode offers different performances for such a detector, and it will be showed that the operating mode corresponding to the lowest electric field possible is best suited for high-rate detectors working in collider experiments.

RPCs where developed early 1980s. At that time it was using an operating mode now referred to as *streamer mode*. Streamers are large discharges that develop in between the two electrodes enough to locally discharge the electrodes. If the electric field inside of the gas volume is strong enough, with electrons being fast compared to ions, a large and dense cloud of positive ions will develop nearby the anode and extend toward the cathode while the electrons are being collected, eventually leading to a streamer discharge due to the increase of the field seen at the cathode. The field is then strong enough so that electrons are pulled out of the cathode. Electrodes, though they are a unique volume of resistive material, can be assimilated to capacitors. At the moment an electric field is applied in between their outer surfaces, the charge carriers inside of the volume will start moving leading to a situation where there is no voltage across the electrodes and a higher density

of negative charges, i.e. electrons, on the inner surface of the cathode. Finally, when a streamer discharge occurs, these electrons are partially released in the gas volume contributing to increase the discharge strength until the formation of a conductive plasma, the streamer. This can be understood through Figure 4.2 [206]. Streamer signals are very convenient in terms of read-out as no further amplification is required with output pulses amplitudes of the order of a few tens to few hundreds of mV as can be seen on Figure 4.3.

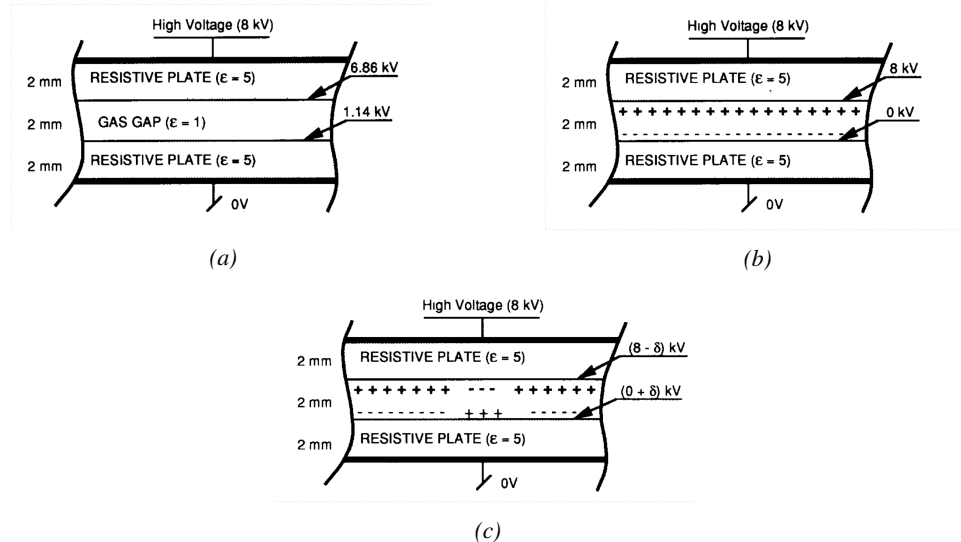


*Figure 4.2: Movement of the charge carriers in an RPC. Figure 4.2a: Voltage across an RPC whose electrodes have a relative permittivity of 5 at the moment the tension is applied. Figure 4.2b: After the charge carriers moved, the electrodes are charged and there is no voltage drop over the electrodes anymore. The full potential is applied on the gas gap only. Figure 4.2c: The streamer discharge initiated by a charged particle transports electrons and cations towards the anode and cathode respectively.*

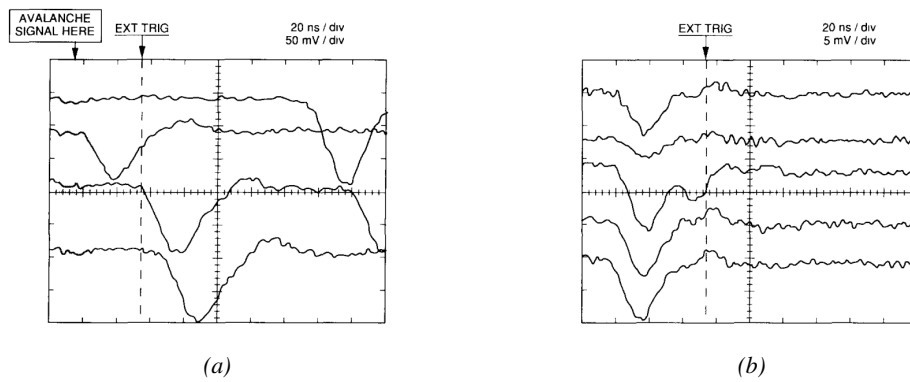


*Figure 4.3: Typical oscilloscope pulses in streamer mode (Figure 4.3a) and avalanche mode (Figure 4.3b). In the case of streamer mode, the very small avalanche signal is visible.*

Though, when the electric field is reduced, the electronic gain is small until the electrons get close enough to the anode and the positive ion cloud is much smaller. The electric field cannot rise

2584 to the point a field emission of electrons on the cathode is possible. The resulting signal is weak,  
 2585 of the order of a few mv as shown on Figure 4.3, and requires amplification. This is the *avalanche*  
 2586 mode of RPC operation. This mode offers a higher rate capability by providing smaller discharges  
 2587 that don't affect the electrodes charge and are more locally contained in the gas volume as was  
 2588 demonstrated by Crotty with Figure 4.4 [206]. The detector only stays locally blind the time the  
 2589 charge carriers are recombined and there is no need for electrode recharge which is a long process  
 2590 affecting a large portion of the detector. Another advantage of avalanche signals over streamer is  
 2591 the great time consistency. Figure 4.3 shows very clearly that avalanche signals have a very small  
 2592 time jitter. Thus, using such a mode is a natural choice for experiments in which the detectors are  
 2593 required to have a high detection rate.

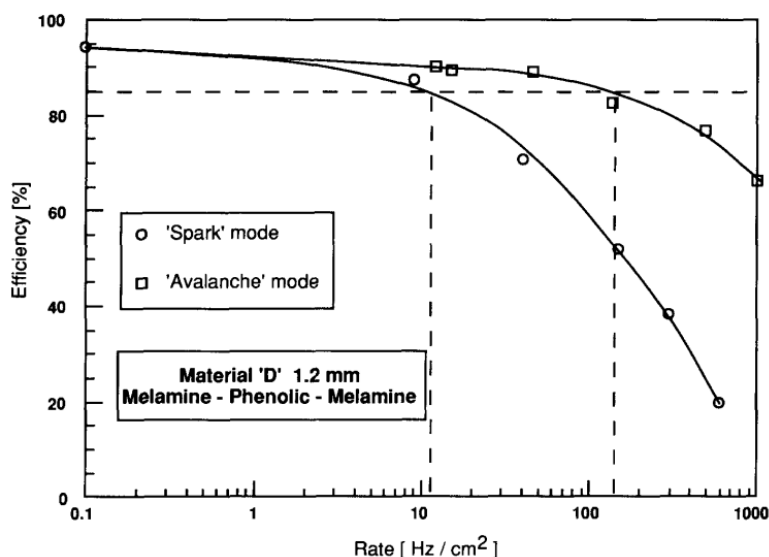


Figure 4.4: Rate capability comparison for the streamer and avalanche mode of operation. An order of magnitude in rate capability for a maximal efficiency drop of 10% is gained by using the avalanche mode over the streamer mode.

#### 2594 4.2.2 Standard gas mixture for RPCs operated in collider experiments

2595 The first RPC working in streamer mode was operated with a 50/50 mixture of argon and butane [203], a standard mixture used at that time in multi-wire proportional chambers, taking profit of  
 2596 the good effective Townsend coefficient of argon to maximize the number of primary charge carriers  
 2597 freed in the gas by ionizing particles and of the quenching properties of butane. Before the discovery  
 2598 of the avalanche mode of RPC operation and concerned about the rate capability of RPCs operated  
 2599 in streamer mode, the performance improvement of the detectors through the increase of fast charge  
 2600 ratio in the signal development, decreasing the charge induced per avalanche as can be seen through  
 2601 Figure 4.5, was studied by adding Freon based gases, such as  $CF_3Br$ , into the typical  $Ar/C_4H_{10}$   
 2602 gas mixture was studied and showed that a lower induced charge could lead to an improvement the  
 2603 rate capability [209]. This consideration led to the discovery of the avalanche mode which confirmed  
 2604 that the smaller the induced charge, the better the rate capability of the RPCs [206]. This discovery  
 2605 could be made thanks to the increased number of lower induced charge events allowed by adding a  
 2606

<sup>2607</sup> fraction of strong quencher in the gas mixture.

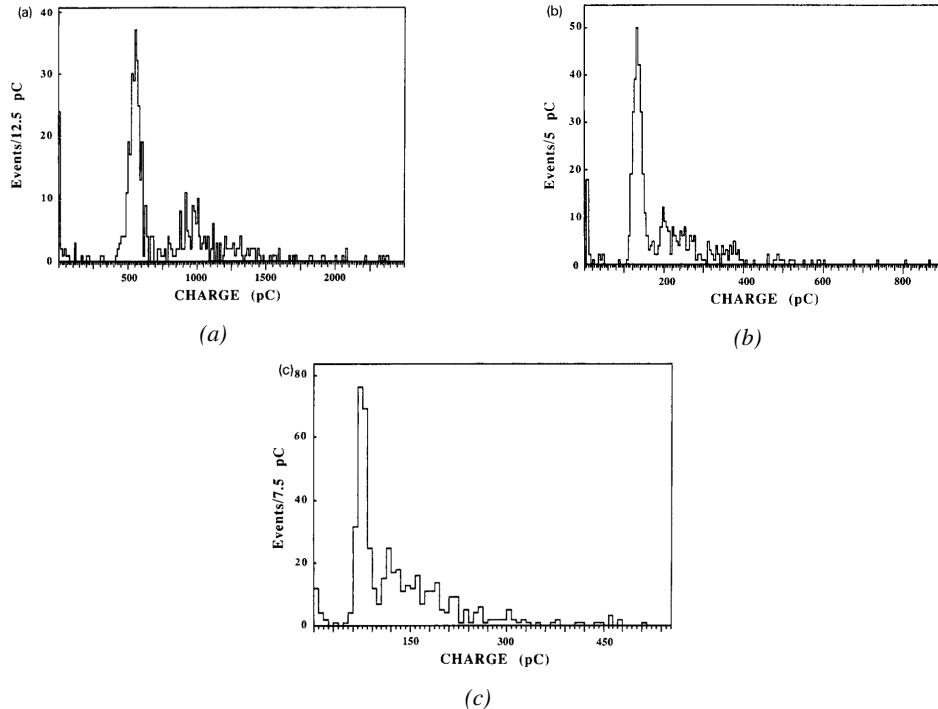


Figure 4.5: Comparison of the charge distribution of signals induced by cosmic muons in an RPC operated with a gas mixture of argon, butane and bromotrifluoromethane ( $CF_3Br$ ). The  $Ar/C_4H_{10}$  is kept constant at 60/40 in volume while the total amount of  $CF_3Br$  in the mixture is varied: 0% (Figure 4.5a), 4% (Figure 4.5b) and 8% (Figure 4.5c) [209].

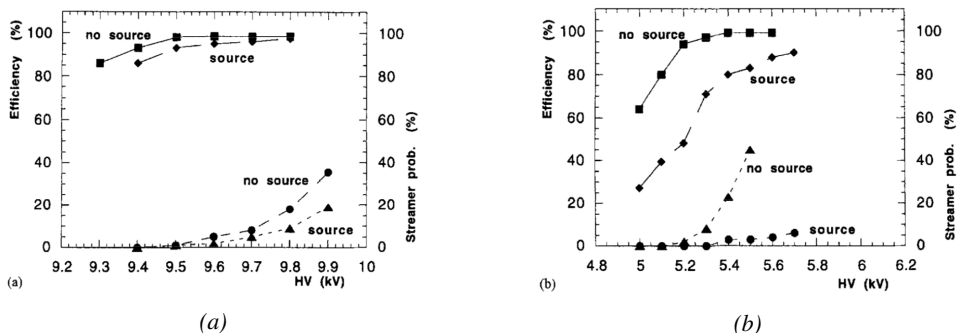


Figure 4.6: Comparison of the efficiency and streamer probability, defined as the fraction of events with an induced charge 10 times larger than that of the average avalanche, with and without irradiation by a 24 GBq  $^{137}Cs$  source of an RPC successively operated with a 90/10 mixture  $C_2H_2F_4/i-C_4H_{10}$  (Figure 4.6a) and a 70/5/10/15 mixture of  $Ar/i-C_4H_{10}/CO_2/C_2H_2F_4$  (Figure 4.6b) [210].

<sup>2608</sup> From this moment onward, more and more studies were conducted in order to find a gas mixture  
<sup>2609</sup> that would allow for the best suppression of streamers for the benefit of low charge avalanches. Most

R&D groups working with narrow gaps started using freon-based gas mixtures while users of wide gap RPCs kept using  $Ar/CO_2$  based mixtures. The differences in between narrow and wide gaps will be later discussed in Section 4.2.3. The  $CF_3Br$  having a high GWP, tetrafluoroethane was preferred to it as more suitable ecofriendly gas in the middle of the 90s. An advantage of this new freon component is that it featured a high primary ionization and a low operating voltage, as reported by Cardarelli [208]. Thus, the new gas mixtures used were mainly composed of tetrafluoroethane alone with lower content of isobutane in order to reduce the flammability of the mixtures in the case it were to be used in accelerator experiments for safety reasons. Performance and models about such mixtures were discussed in papers of Abbrescia [210, 211] and showed a better suitability of such a gas mixture, with respect to argon based ones, for operations with high radiation backgrounds leading to a need for high-rate capability of the detectors, as can be seen from Figures 4.6 and 4.7. Indeed, although the operating voltage of a tetrafluoroethane based mixture is higher than which of an argon based mixture but the efficiency under irradiation is more stable, the voltage range with negligible streamer probability is much wider, and the fast charge ratio available is much greater, providing with more stable operation of the detector.

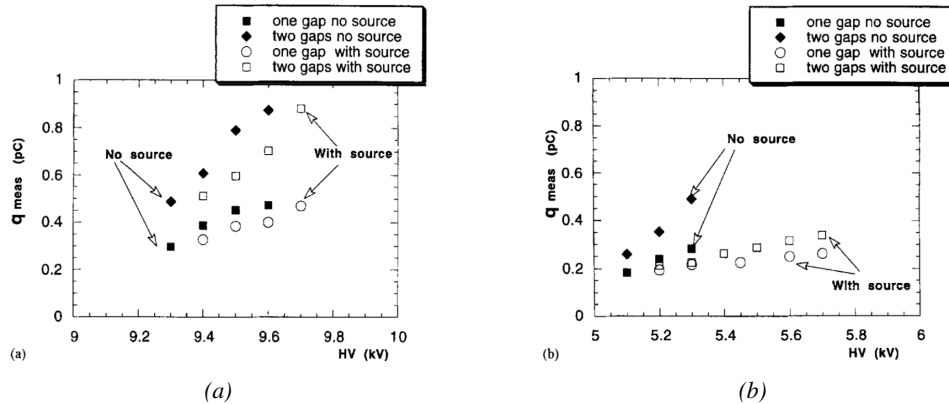


Figure 4.7: Comparison of the fast charge ratio with and without irradiation by a 24 GBq  $^{137}Cs$  source of an RPC successively operated with a 90/10 mixture  $C_2H_2F_4/i-C_4H_{10}$  (Figure 4.7a) and a 70/5/10/15 mixture of  $Ar/i-C_4H_{10}/CO_2/C_2H_2F_4$  (Figure 4.7b). The results are provided for both single-gap and double-gap operation [210].

Aside of the improvement of the rate capability through linseed oil surface treatment of HPL electrodes, which allowed for a lower intrinsic noise rate and dark current of the detectors by improving the smoothness of the electrodes surface [223], it was later found that the streamers could be further suppressed by adding an electronegative compound into the gas mixture. The benefits of adding  $SF_6$  in order to push the transitions from avalanche to streamers towards high voltages has been discussed in 1998 [212, 213] and eventually the high-rate RPC destined to be used in accelerator physics would unanimously start using this compound into RPC gas mixtures. Being able to control the creation of streamers allows for slower ageing of the detector and lower power consumption as the currents driven by the electrodes consecutively to the induced charges would be smaller. In summary, the typical gas mixture RPCs are operated with is generally composed of the following 3 gas compounds, although as mentioned in Chapter 3.6, research is being conducted into new more ecofriendly gas mixture using gases with a much lower Global Warming Potential:

- Tetrafluoroethane ( $C_2F_4H_2$ ), also referred to as *Freon* or *R134a*, is the principal compound

2638 of the RPC gas mixtures, with a typical fraction above 90%. It is used for its high effective  
 2639 Townsend coefficient and the great average fast charge that allows to operate the detector  
 2640 with a high threshold with respect to argon, for example, that has similar effective Townsend  
 2641 coefficient but suffers from a lower fast charge. To operate with similar conditions, argon  
 2642 would require a higher electric field leading to a higher fraction of streamers, thus limiting the  
 2643 rate capability of the detector [210, 211].

- 2644 • Isobutane ( $i\text{-C}_4\text{H}_{10}$ ), only present in a few percent in the gas mixtures, is used for its UV  
 2645 quenching properties [224] helping to prevent streamers due to UV photon emission during  
 2646 the avalanche growth.
- 2647 • Sulfur hexafluoride, ( $\text{SF}_6$ ), simply referred to as  $\text{SF}_6$ , is used in very little quantities for its  
 2648 high electronegativity. Any excess of electrons is absorbed by the compound and streamers  
 2649 are suppressed [212, 213]. Nevertheless, a fraction of  $\text{SF}_6$  higher than 1% will not bring  
 2650 any extra benefit in terms of streamer cancelation power but will lead to higher operating  
 2651 voltage [212], as can be understood through Figure 4.8.

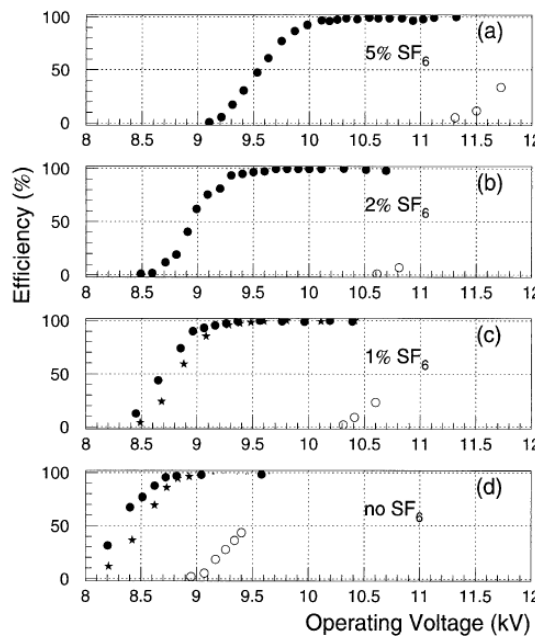
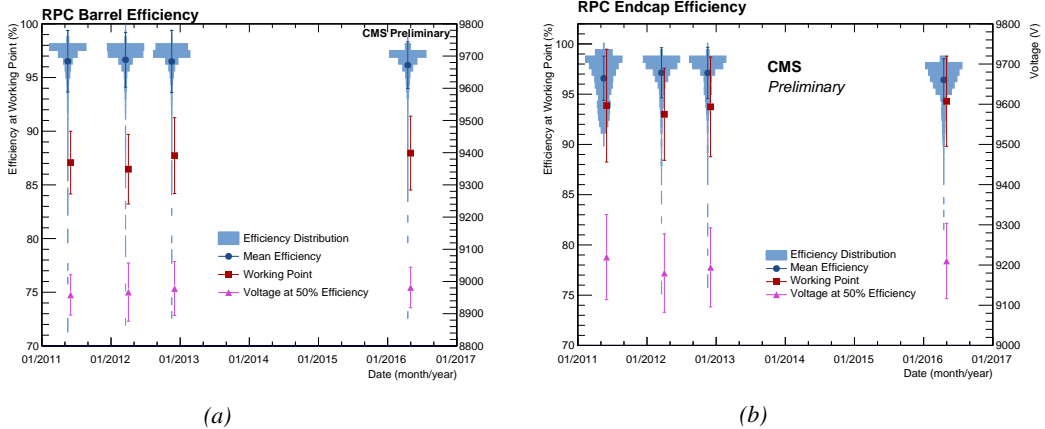


Figure 4.8: Efficiency (circles and stars with 30 mV and 100 mV thresholds respectively) and streamer probability (open circles) as function of the operating voltage of a 2 mm single-gap HPL RPC flushed with a gas mixture containing (a) 5%, (b) 2%, (c) 1% and (d) no  $\text{SF}_6$  [212].

2652 In the last steps of R&D, the gas mixture of CMS RPCs was foreseen to be a 96.2/3.5/0.3 compo-  
 2653 sition of  $\text{C}_2\text{H}_2\text{F}_4/i\text{-C}_4\text{H}_{10}/\text{SF}_6$  [225] but finally it was slightly changed into a 95.2/4.5/0.3 mixture  
 2654 of the same gases [226]. A summary of the operation performance of the RPCs since the start of  
 2655 LHC and of CMS data taking is given in Figure 4.9 [227]. The performance of the detectors is  
 2656 regularly monitored and the operating voltages updated in order to obtain a very stable performance  
 2657 through time. Nevertheless, the detectors will face new challenges during Phase-II during which they

will exposed to more extreme radiation conditions. Description of the longevity tests with extreme irradiation and the conclusions regarding the operation of the present RPC system will be given in Chapter 5.



*Figure 4.9: Evolution of the efficiency, working voltage, and voltage at 50% of maximum efficiency for CMS Barrel (Figure 4.9a) and Endcap (Figure 4.9b) RPCs obtained through yearly voltage scans since 2011. The working voltage of each RPC is updated after each voltage scan to ensure optimal operation [227].*

It was already discussed that in the future, it is likely that the use of freon gases could be banned. As potential replacement for tetrafluoroethane was proposed the trifluoriodomethane ( $CF_3I$ ), a molecule with similar properties than  $CF_3Br$  which was replaced by the tetrafluoroethane, and the 1,3,3,3-tetrafluoropropene ( $C_3H_2F_4$  or HFO-1234re), a molecule with similar properties than the actual tetrafluoroethane and proposed as a replacement in refrigerating and air conditioning systems [228]. These two gases have stronger quenching properties than  $C_2H_2F_4$  which means a much stronger electric field needs to be applied on the parallel electrodes of the RPCs in order to reach full efficiency. But the power supply system of CMS RPC is limited to 15 kV and so is ATLAS power supply system which is participating in a joined R&D. As can be seen from Figure 3.32, reducing the working voltage was achieved by mixing the potential replacements together with  $CO_2$ . Introducing carbon dioxide into the mixture while keeping similar levels of isobutane and  $SF_6$  increases the streamer probability and the best candidate identified for a compromise in between low enough working voltage and acceptable levels of streamers corresponds to a mixture containing 50% of HFO, 4.5% of  $iC_4H_{10}$ , 0.3% of  $SF_6$  and 45.2% of  $CO_2$  but is not yet considered satisfactory. On the other hand, no good replacement for  $SF_6$  has yet been identified. With its very high Global Warming Potential (23900), even small fraction of this gas in the mixture (it only represents 0.3% of CMS standard mixture but more than 5% of its overall GWP) substantially increase the danger for the environment. Although finding a replacement for this gas is less critical than for the tetrafluoroethane composing more than 90% of usual RPC standard mixtures, the problem will need to be addressed.

### 4.2.3 Detector designs and performance

Different RPC designs have been used, and each of them presents its own advantages. Historically, the first type of RPC to have been developed is what is now referred to as *narrow gap* RPC [203,

<sup>2684</sup> 229].

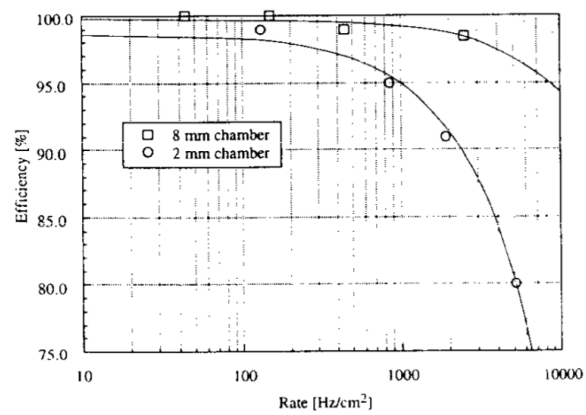


Figure 4.10: Comparison of the rate capability of 8 mm and 2 mm wide RPCs. The lines are linear fits on the data [229].

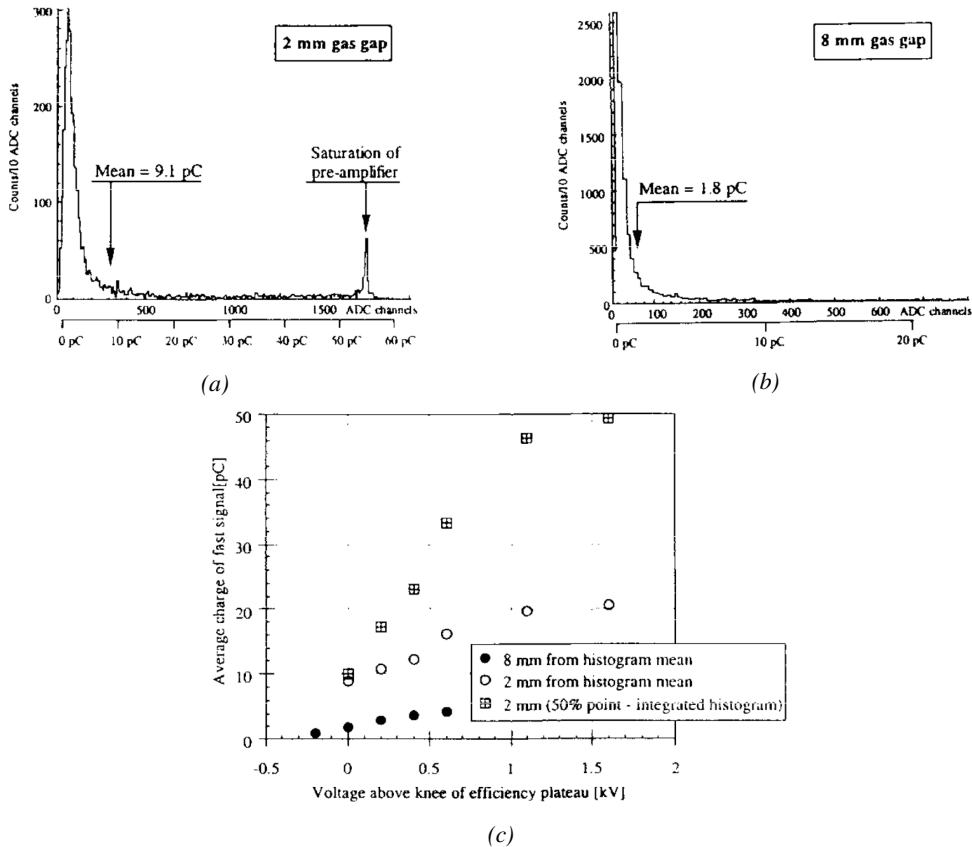
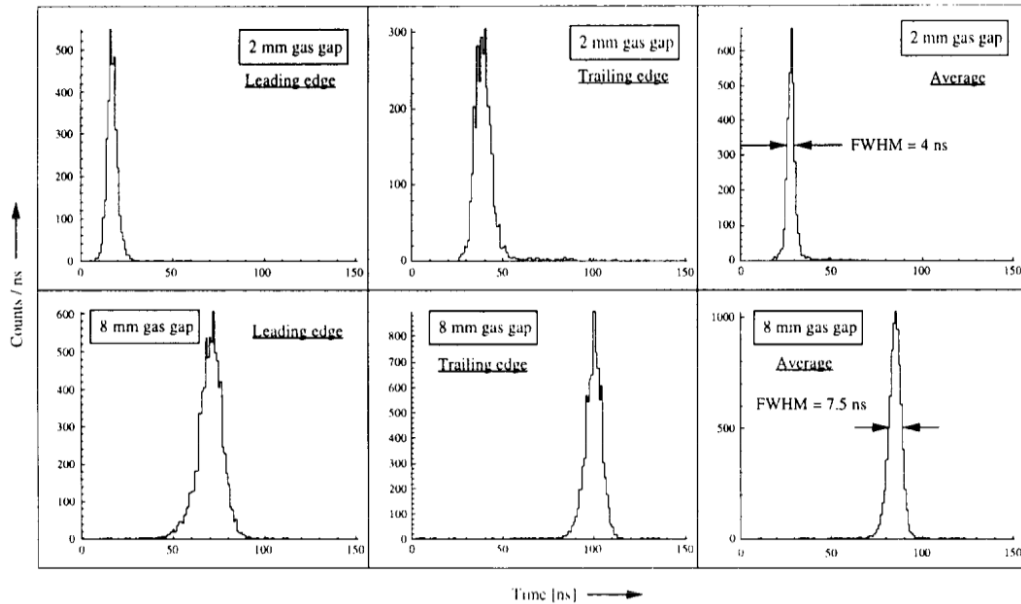


Figure 4.11: Distributions of the induced charge of fast signals on 2 mm (Figure 4.11a) and 8 mm (Figure 4.11b) RPCs exposed to a radiation rate of  $100 \text{ Hz/cm}^2$ . Average induced charge of fast signals as a function of the high voltage applied on 2 mm and 8 mm RPCs (Figure 4.11c). In the case of the 2 mm RPC, a saturation of the pre-amplifier was observed. The average of the distribution is underestimated, and the median is showed together with the average to account for this bias [229].

After the avalanche mode has been discovered [206], it has been shown that increasing the width of the gas gap lead to higher rate capability, due to lower charge deposition per avalanche, and lower power dissipation [229], as is showed in Figures 4.10 and 4.11. The distance in between the electrode being greater, a weaker electric field can be applied and a lower gain used as a longer gas volume will contribute to the signal induction on the read-out circuit. Nevertheless, by increasing the gas gap width, the time resolution of the detector decreases. This is a natural result if the increase of active gas volume in the detector is taken into account. Indeed, for a given detection threshold on the induced charge per signal, only the small fraction of gas closest to the cathode will provide enough gain to have a detectable signal. In the case of a wider gas volume, the active region is then larger and a larger time jitter is introduced with the variation of starting position of the avalanche, as discussed in [214] and showed in Figure 4.12.



*Figure 4.12: Time distributions of the leading, trailing, and average of both leading and trailing edges for 2 mm (top row) and 8 mm (bottom row) RPCs exposed to a  $100 \text{ Hz/cm}^2$  radiation rate. The data was collected with RPCs operated at the voltage corresponding to the knee of the efficiency distribution, defined as the point where 95% of the maximum efficiency is obtained [229].*

2696 To improve both the time resolution and the rate capability, different methods were used trying  
 2697 to take advantage of both narrow and wide gap RPCs into a single design. Thus, double-gap  
 2698 RPCs, combining two narrow gaps into a single detector to increase the effective sensitive volume,  
 2699 and multigap RPCs, which divided the large volume of a wide gap RPC into thinner sub-gaps by  
 2700 adding intermediate electrodes in between the cathode and anode to improve the time resolution by  
 2701 mimicking narrow gap RPCs, were developed starting from the middle of the 90s.

#### 2702 4.2.3.1 Double-gap RPC

2703 Made out of two narrow RPC detectors stacked on top of each other as shown in Figure 4.13, this  
 2704 detector layout, popularized by the two multipurpose experiments CMS [192] and ATLAS [217] at  
 2705 LHC, can be used as an OR system in which each individual chamber participates in the output signal  
 2706 and increases the overall sensitive volume of the detector apparatus. Keeping the copper strip read-  
 2707 out system at the ground, CMS and ATLAS, due to different goals, have chosen different designs as  
 2708 CMS RPCs possess a 1D read-out while ATLAS RPCs offer a 2D read-out. The difference comes  
 2709 from placing the read-out in between the gaps, the anodes facing each other, or to have both RPC  
 2710 gaps in between two layers of read-out panels, one along the X-axis and one along the Y-axis, the  
 2711 cathodes facing each other.

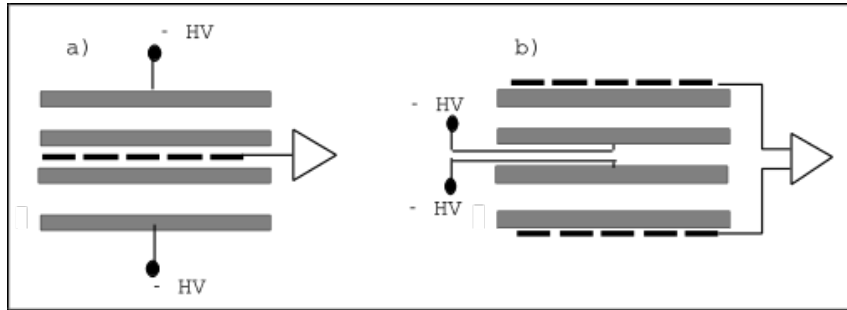


Figure 4.13: Possible double-gap RPC layouts: a) "standard" 1D double-gap RPC, as used in CMS experiment, where the anodes are facing each other and a 1D read-out plane is sandwiched in between them, b) double read-out double-gap RPC as used in ATLAS experiment, where the cathodes are facing each other and 2 read-out planes are used on the outer surfaces. This last layout can offer the possibility to use a 2D reconstruction by using orthogonal read-out planes.

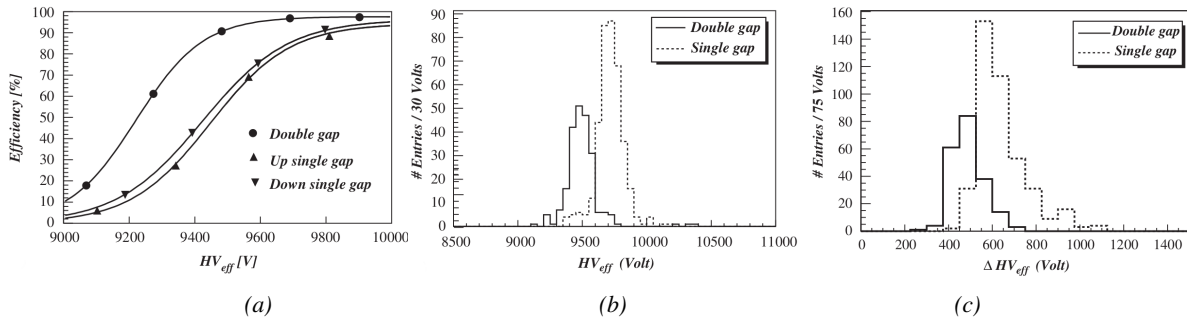
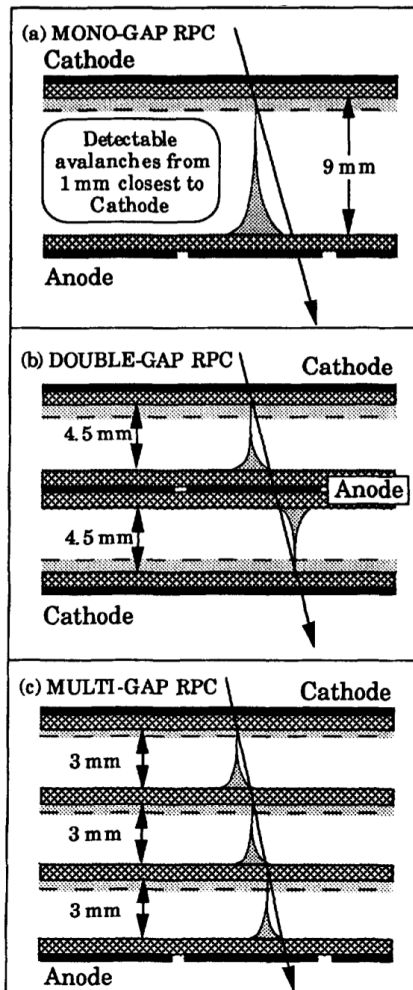


Figure 4.14: Comparison of performance of CMS double and single-gap RPCs using cosmic muons [225].  
Figure 4.14a: Comparison of efficiency sigmoids. Figure 4.14b: Voltage distribution at 95% of maximum efficiency. Figure 4.14c:  $\Delta_{10\%}^{90\%}$  distribution.

The gain of such a detector is reduced by a factor 2 with respect to single-gap RPCs with an efficiency plateau reached at lower voltage, as visible on Figure 4.14, due to the two gas gaps contributing to the signal formation and offering a dynamic range closer to that of a wide gap RPC. A double-gap is then fully efficient while the individual RPC gaps composing it are only 70 to 80% efficient. Naturally, by operating the double-gap at a lower voltage, the rate capability is found to be increased as the induced charge per gap is then lower than in the case of a single-gap detector also leading to a reduction of the streamer probability and a better extraction of the fast charge of the total signal as could be seen through previously presented Figure 4.7.

#### 4.2.3.2 Multigap RPC (MRPC)

MRPCs are layouts in which floating sub electrode plates are placed into a wide gap RPC to divide the gas volume and create a sum of narrow gaps [214, 215]. Similarly to the double-gap RPC for which the gain could be reduced by increasing the dynamic range, the multigap reduces the gain while keeping a total dynamic range similar to that of a wide gap RPC by reducing the size of each individual sub-gap composing the detector. The dynamic range, associated to the sensitive volume, and the comparison of each detector layout to the wide gap RPC is showed in Figure 4.15.



*Figure 4.15: Representation of different RPC layouts (wide gap on Figure (a), double-gap on Figure (b) and multigap on Figure (c)), of the corresponding sensitive volume in gray, and of the associated avalanche size [215].*

2727 By operating the detector with thinner gaps, the time resolution is improved. Comparatively to  
2728 the time resolution presented in Figure 4.12 for the wide gap RPC of 8 mm, a complementary study  
2729 was conducted on multigaps using two 4 mm and four 2 mm subgaps and showed, via Figure 4.16,  
2730 an improvement of the time resolution with the reduction of the gap width and of the number of gaps  
2731 while the same sensitive volume was kept [215].

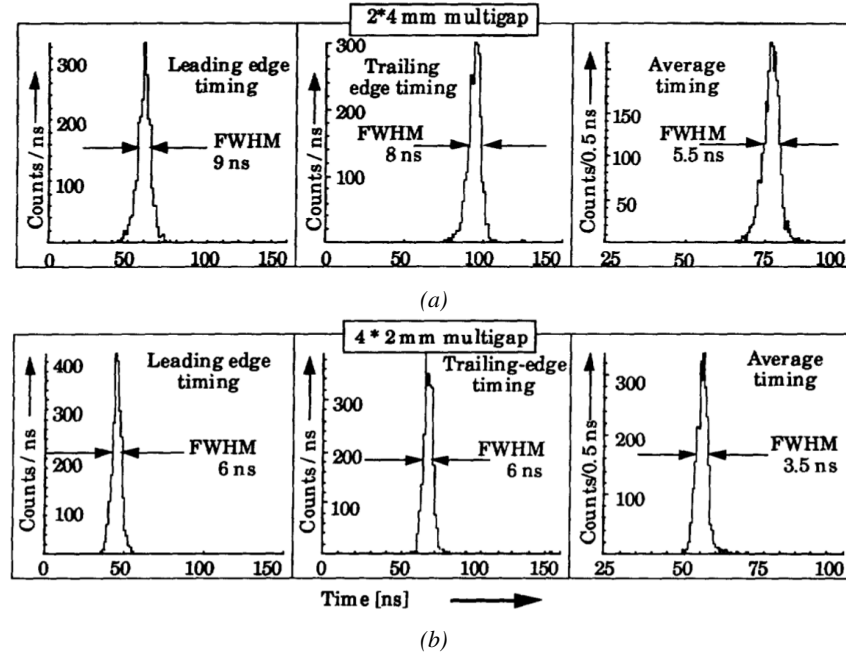


Figure 4.16: Time distributions of the leading, trailing, and average of both leading and trailing edges for multigap RPCs consisting in two 4 mm (Figure 4.16a) and four 2 mm (Figure 4.16b) exposed to a 100 Hz/cm<sup>2</sup> radiation rate. The data was collected with RPCs operated at the voltage corresponding to the knee of the efficiency distribution, defined as the point where 95% of the maximum efficiency is obtained [215].

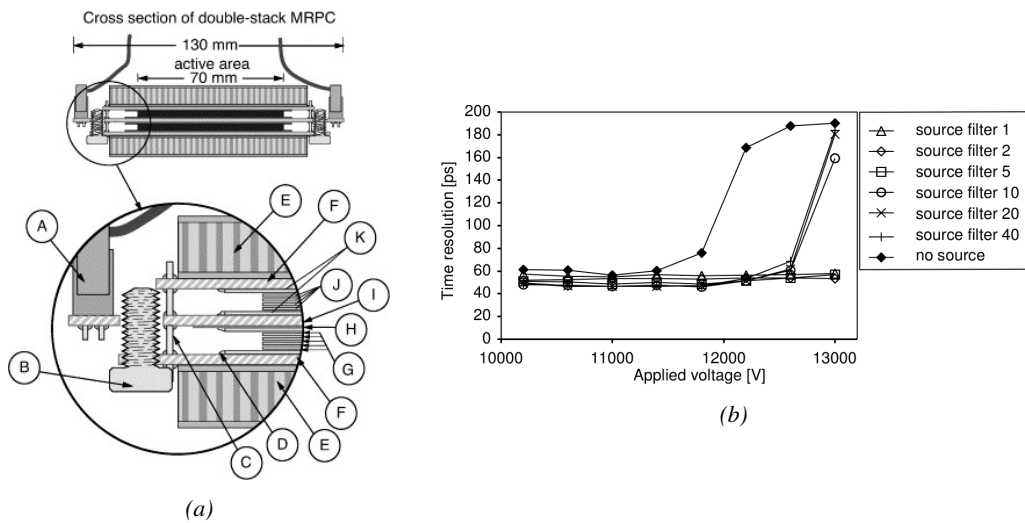


Figure 4.17: Presentation of a study of a possible ALICE MRPC cell using 250 µm gas gaps, 620 µm outer glass electrodes, and 550 µm inner floating electrodes (Figure 4.17a), and of its time resolution performance as a function of the applied high voltage for different radiation levels referred through different filter settings of the 740 GBq <sup>137</sup>Cs source the former CERN GIF facility [230].

2732 After the problem of streamers was solved by adding SF<sub>6</sub> into the gas mixture, the size of the

2733 MRPCs decreased as the research groups started applying the concept of dividing the gas volume  
 2734 into subvolumes to the narrow gap RPCs leading to the, now, widely used micro gap MRPCs. The  
 2735 time resolution of such a detector can reach of few tens of ps, with gas gaps of the order of a few  
 2736 hundred  $\mu\text{m}$  as showed in Figure 4.17 representing a single cell of ALICE Time-of-flight (ToF)  
 2737 system consisting of double MRPCs, as it was studied in the early 2000s [230].

2738 Sometimes used as a double multigap RPC, taking advantage of the OR of double-gap RPCs to  
 2739 both be able to operate a higher number of gaps while keeping a reasonable high voltage applied  
 2740 in between the cathode and anode and to further reduce the gain, the MRPC is mainly used as ToF  
 2741 detector [230–234] due to its excellent timing properties that allow to perform particle identification  
 2742 as explained by Williams in [235]. The principle of particle identification using ToF is simply the  
 2743 measurement of the velocity of a particle. Indeed, particles are defined by their mass (for the parameter  
 2744 of interest here, their electric charge being measured using the bending angle of the particles  
 2745 traveling through a magnetic field) and this mass can be calculated by measuring the velocity  $\beta$  and  
 2746 momentum of the particle:

$$(4.3) \quad \beta = \frac{p}{\sqrt{p^2 + m^2}}$$

2747 Intuitively, it is trivial to understand that 2 different particles having the same momentum will  
 2748 have a different velocity due to the mass difference and thus a different flight time  $T_1$  and  $T_2$  through  
 2749 the detector and this is used to separate and identify particles. The better the time resolution of the  
 2750 ToF system used, the stronger will the separation be:

$$(4.4) \quad T = \frac{L}{v} = \frac{L}{c \cdot \beta}, \quad \Delta T = T_1 - T_2 = \frac{L}{c} \left( \sqrt{1 + m_1^2/p^2} - \sqrt{1 + m_2^2/p^2} \right) \cong (m_1^2 - m_2^2) \frac{L}{2cp^2}$$

2751 An example of particle identification is given for the case of STAR experiment in Figure 4.18.

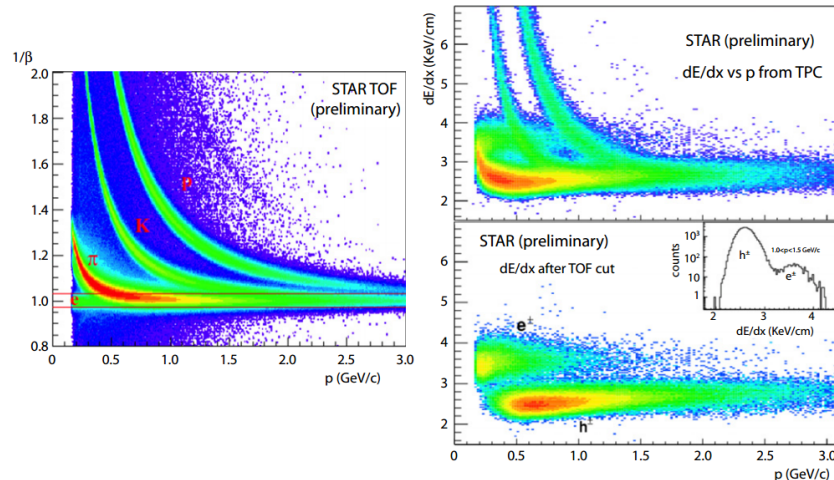


*Figure 4.18: Particle identification applied to electrons in the STAR experiment. The identification is performed combining ToF and  $dE/dx$  measurements [235].*

Taking into account the distortion effect on the electric field inside of an MRPC built using micro gaps due to the exposition to irradiation, distortion that can be understood by monitoring the current drawn by the detector which should stay constant at constant electric field, another benefice of using such small gas gaps is the strong reduction of the average avalanche volume and thus of the blind spot on MRPCs leading to an improved rate capability. Multigaps can sustain backgrounds of several kHz/cm<sup>2</sup> as demonstrated in Figure 4.19.

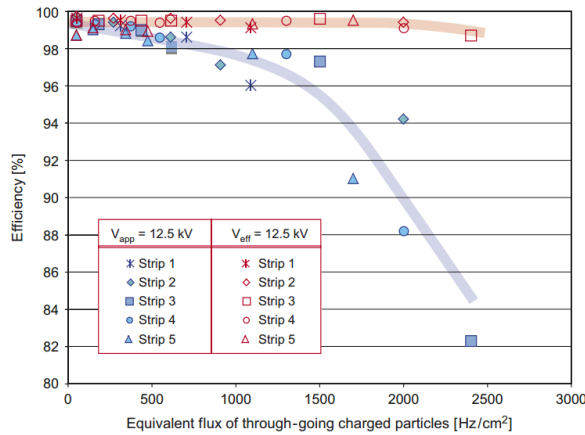


Figure 4.19: Comparison of the detector performance of ALICE ToF MRPC [236] at fixed applied voltage (in blue) and at fixed effective voltage (in red). The effective voltage is kept fixed by increasing the applied voltage accordingly to the current drawn by the detector.

#### 4.2.3.3 Charge distribution and performance limitations

[This part could be moved in the next section of the chapter and deepened using the perspective of the avalanche physics.]

The direct consequence of the different RPC layouts is a variation of intrinsic time resolution of the RPC as the gap size decreases and of the rate capability when the deposited charge per event is spread over a larger number of amplification volumes, allowing for a reduction of the overall gain of the detectors which is replaced by an on-electronics pre-amplification of the signals. In this sense, an advantage is given to multigaps whose design use sub-millimeter gas volumes providing very consistent signals.

From the charge spectrum point of view, each layout has its own advantages. When the double-gap has the highest induced-over-drifting charge ratio, as seen in Figure 4.20, the multigap has a charge spectrum strongly detached from the origin, as visible in Figure 4.21. A high induced-over-drifting charge ratio means that the double-gap can be safely operated at a high threshold or that at a similar threshold it can be operated with a twice smaller drifting charge, meaning a higher rate capability if operated with sensitive enough electronics. On the other hand, the strong detachment of the charge spectrum from the origin in the MRPC case allows reaching a higher efficiency with increasing threshold as most of the induced charge is not low due to the convolution of several single-gap spectra. The range of stable efficiency increases with the number of gaps, as presented in Figure 4.22.

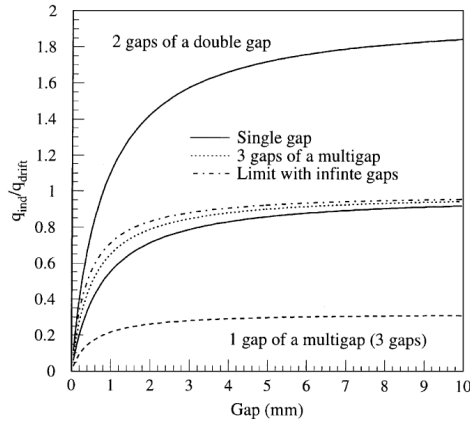


Figure 4.20: Ratio between total induced and drifting charge have been simulated for single-gap, double-gap and multigap layouts [237]. The total induced charge for a double-gap RPC is a factor 2 higher than for a multigap.

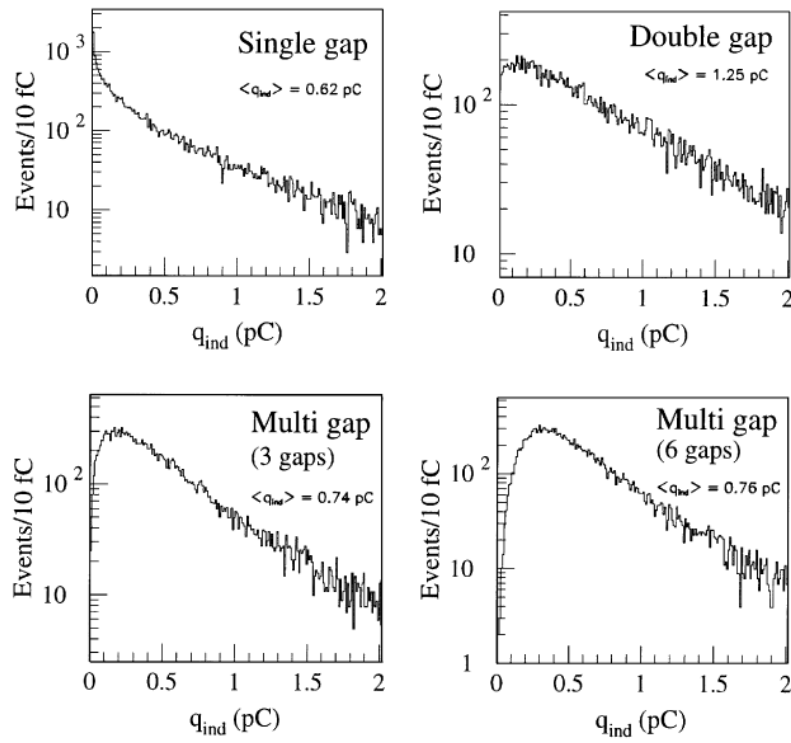


Figure 4.21: Charge spectra have been simulated for single-gap, double-gap and multigap layouts [237]. It appears that when single-gap shows a decreasing spectrum, double and multigap layouts exhibit a spectrum whose peak is detached from the origin. The detachment gets stronger as the number of gaps increases.

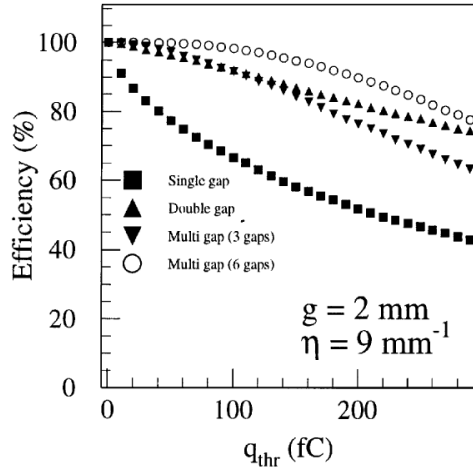


Figure 4.22: The maximal theoretical efficiency is simulated for single-gap, double-gap and multigap layouts [237] at a constant gap thickness of 2 mm and using an effective Townsend coefficient of  $9 \text{ mm}^{-1}$ .

### 2777 4.3 Signal formation

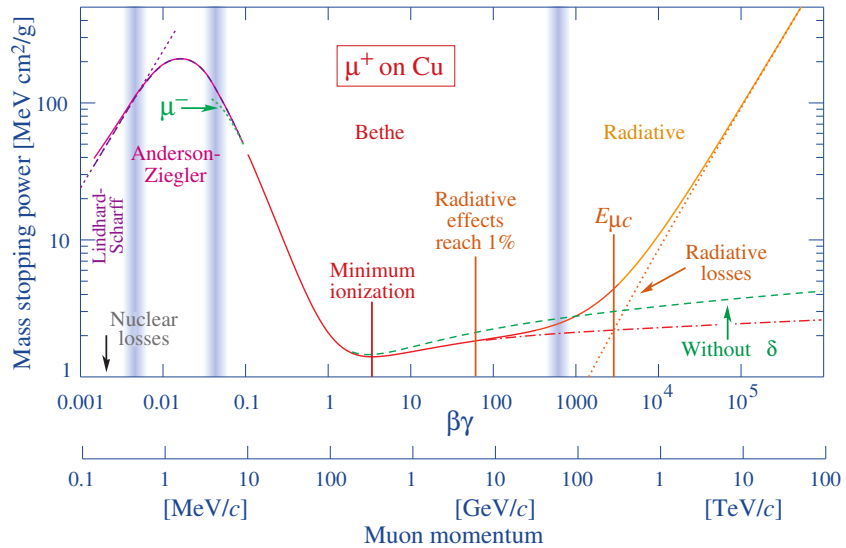


Figure 4.23: Mass stopping power as a function of  $\beta\gamma = p/Mc$  for positive muons in copper [115]. The total stopping power is indicated with a solid line and local components with dashed lines. The vertical bands are used to indicate boundaries between different approximations used at different energy range.

2778 The physics of Resistive Plate Chambers still is far from being fully understood and work is regularly  
 2779 being accomplished in trying to model these detectors the best way possible by phenomenological  
 2780 models using well-defined physics [221, 238, 239]. These theoretical works have nevertheless led to  
 2781 a better understanding of the key principles that account for RPCs signal formation. As previously

discussed, the typical mixture of such a detector is in great majority composed by a ionizing gas with some quenching properties and a low ionization potential to easily produce electrons, with the addition of UV quencher and electronegative compounds. The electronic avalanche formation will be triggered by a charged particle passing through the gas, typically a muon in the case of most uses of RPCs. The production of electrons in the gas of a detector is related to the energy lost by the incoming particle traveling through a material medium. The example of the mass stopping power of copper on muons is given in Figure 4.23 on which the different energy loss mechanisms at different energy ranges are visible. Once primary electrons have been freed in the gas volume, the electric field applied in between the electrodes of the RPC will make the charges move and there will be a competition in the gas in between the Townsend and attachment coefficient which describe the evolution of the number of electrons in an avalanche. While drifting through the gas, the electrons are also subjected to diffusion that will affect the evolution of the avalanches. Finally, when the avalanche is big enough, the accumulation of negative (electrons) and positive (ions) charges in the gas volume will start affecting the local electric field. This effect is known as space charge effect.

### 4.3.1 Energy loss at intermediate energies

Intuitively, a particle traveling through a medium will interact with its components, losing energy. When a muon travels through the gas of a gaseous detector, at the energy range usually observed, it interacts with the molecules of the gas leading to dissipation of the transferred energy in the form of inelastic diffusion or ionization. The photons and electron-ion pairs resulting from these interactions can trigger avalanches in the gas which will contribute to feed the avalanche growth thanks to the strong electric field applied in between the two electrodes of an RPC.

The mass stopping power of moderately relativistic ( $0.1 \lesssim \beta\gamma \lesssim 1000$ ) heavy particles ( $M \gg m_e$ ) traveling through a medium via excitation and ionization processes was studied by Bethe in 1930 [240] and is well described by the so called the Bethe Formula given in Equation 4.5.

$$(4.5) \quad \left\langle -\frac{dE}{dx} \right\rangle = K z^2 \frac{Z}{A} \frac{1}{\beta^2} \left( \frac{1}{2} \ln \frac{2m_e c^2 \beta^2 \gamma^2 W_{max}}{I^2} - \beta^2 - \delta(\beta\gamma) \right)$$

The different parameters used in this equation are

$E$	- incident particle energy $\gamma Mc^2$	MeV
$x$	- mass per unit area	$\text{g cm}^{-2}$
$N_A$	- Avogadro's number	$6.022\ 140\ 857(74) \times 10^{23} \text{ mol}^{-1}$
$c$	- speed of light in vacuum	$299\ 792\ 458 \text{ m s}^{-1}$
$\mu_0$	- permeability of free space	$4\pi \times 10^{-7} \text{ N A}^{-2}$
$\epsilon_0$	- permittivity of free space $\epsilon_0 = 1/\mu_0 c^2$	$8.854\ 187\ 817\dots \times 10^{-12} \text{ F m}^{-1}$
$\alpha$	- fine structure constant $\alpha = e^2/4\pi\epsilon_0\hbar c$	$1/137.035\ 999\ 139(31)$
$r_e$	- classical electron radius $r_e = e^2/4\pi\epsilon_0 m_e c^2$	$2.817\ 940\ 3227(19) \text{ fm}$
$e$	- elementary charge of the electron	$-1.6021766208(98) \times 10^{-19} \text{ C}$
$m_e c^2$	- electron mass $\times c^2$	$0.510\ 998\ 9461(31) \text{ MeV}$
$K$	- constant defined as $K = 4\pi N_A r_e^2 m_e c^2$	$0.307\ 075 \text{ MeV mol}^{-1} \text{ cm}^2$
$z$	- charge number of incident particle	
$Z$	- atomic number of absorbing medium	
$A$	- atomic mass of absorbing medium	$\text{g mol}^{-1}$
$\beta$	- velocity of particle $\beta = v/c$	
$\gamma$	- Lorentz factor $\gamma = (1 - \beta^2)^{-1/2}$	

$W_{max}$	-	maximum energy transfer through a single collision	MeV
$I$	-	mean excitation energy of absorbing medium	eV
$\delta(\beta\gamma)$	-	density effect correction to ionization energy loss	

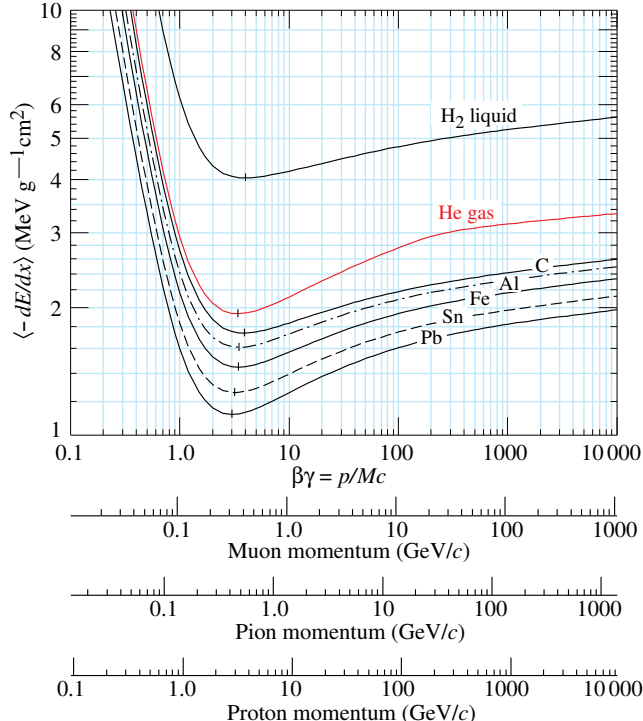


Figure 4.24: Mean mass stopping power for liquid hydrogen, as used in bubble chambers, gaseous helium, carbon, aluminum, iron, tin, and lead without the inclusion of radiative effect at higher  $\beta\gamma$  necessary for pions and muons in denser materials [115].

In this equation, the maximum energy transfer  $W_{max}$  is defined as function of the incident particle mass  $M$ , expressed in  $\text{MeV}/c^2$

$$(4.6) \quad W_{max} = \frac{2m_e c^2 \beta^2 \gamma^2}{1 + 2\gamma m_e / M + (m_e / M)^2}$$

and the mean excitation energy  $I$  depends on the absorber. Its determination is non-trivial but recommendations are given by the International Commission on Radiation Units & Measurements (ICRU) based on experimental measurements and interpolations as showed in Figure 4.25.

For the case of copper, the mean stopping power is visible in Figure 4.23. The mean stopping power corresponding only to the Bethe range for other materials is given in Figure 4.24 and shows that  $\langle -dE/dx \rangle$  is similar for each material with a slow decrease with  $Z$ . The factor affecting the equation the most is  $\beta$  as the dependence on  $M$  is introduced at higher energies in the logarithm via the max transfer energy per single collision but in most practical cases, only the dependence on  $\beta$  is considered as most of the relativistic particles are close to the lowest mean energy loss rate and are

referred to as minimum ionizing particles (mip's). The almost logarithmic relation in between the mean energy loss rate for minimum ionizing particles and  $Z$  is showed in Figure 4.26.

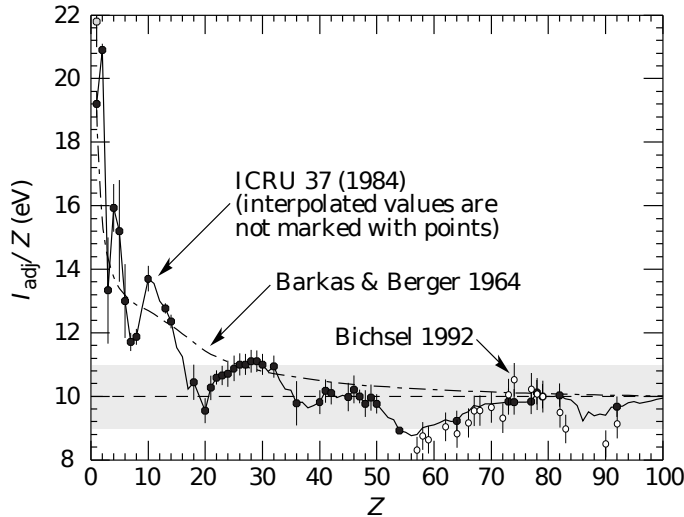


Figure 4.25: Mean excitation energies normalized to the atomic number as adopted by the ICRU [115, 241, 242].

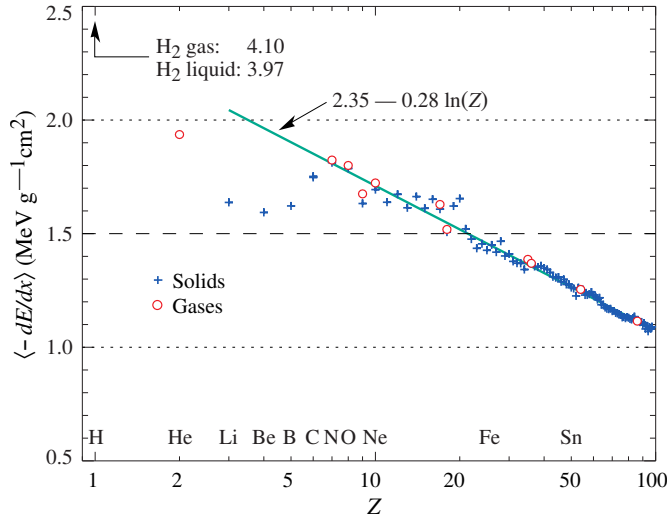


Figure 4.26: Mean mass stopping power at minimum ionization as a function of the atomic number [115].

Finally, the term  $\delta(\beta\gamma)/2$  corresponds to the density effect correction introduced to account for the polarization of a real media that limits the spatial extension of the electric field of relativistic particles. Indeed, as the energy of a particle increases, the associated electric field will flatten and extend. Due to this effect, the distant collision contribution to Equation 4.5 will increase as  $\ln(\beta\gamma)$  but the polarization of the media truncates this rise. At high energies, the correction is given by

2825      Equation 4.7

$$(4.7) \quad \delta/2 \longrightarrow \ln(\hbar\omega_p/I) + \ln(\beta\gamma) - 1/2$$

2826      where  $\hbar\omega_p$  represents the plasma energy that depends on the electron density of the media and  
 2827      the electron mass and can be calculated as  $\sqrt{\rho\langle Z/A\rangle} \times 28.816$  eV. The introduction of this cor-  
 2828      rection term reduces the increase of the mean stopping power at higher energies as can be seen in  
 2829      Figure 4.23. Moreover, due to poorer electron density, the effect is less visible on gases than on  
 2830      liquids and solids has can be seen from Figure 4.24.

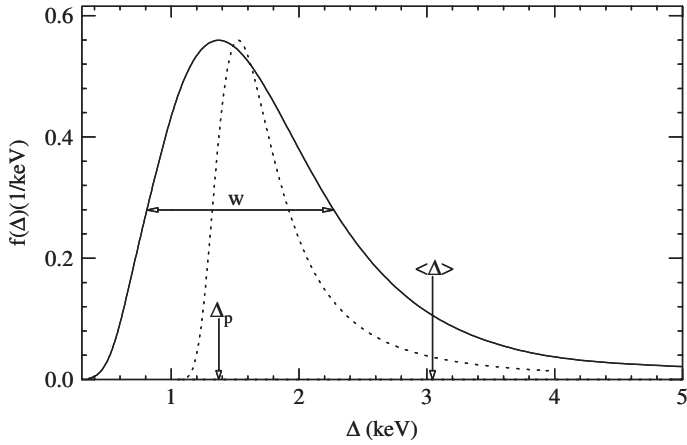


Figure 4.27: Example of straggling function  $f(\Delta)$  of particles passing through 1.2 cm of Argon gas with a  $\beta\gamma$  of 3.6 and represented with a solid line. The original Landau distribution is showed with a dashed line [243].

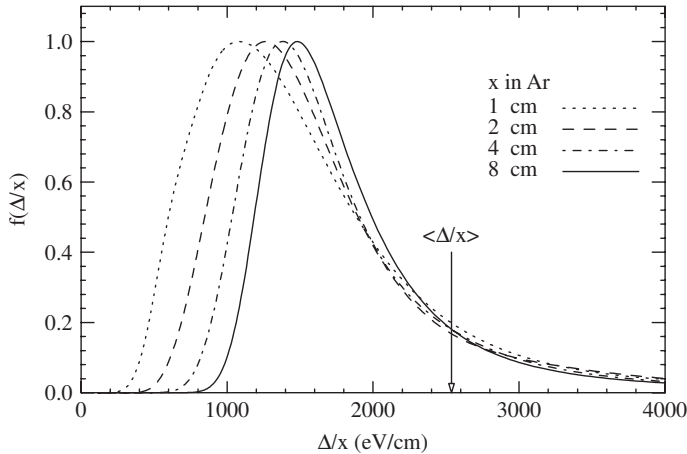


Figure 4.28: Evolution of straggling functions  $f(\Delta)$  of particles passing through a volume of Argon gas with a  $\beta\gamma$  of 3.6 with increasing thickness  $x$  [243].

2831      The mean energy loss per collision can be difficult to measure for low data samples but is not  
 2832      always representative of the energy loss distribution for a given incident particle energy. Hence, it is

2833 easier to access the most probable energy loss which is a lower value than than the average loss due  
 2834 to the distribution of the energy transfer. This value is well described by a highly skewed Landau  
 2835 distribution for detectors with "moderate" thickness  $x$ , expressed in g mol<sup>-1</sup>. But for gas volumes,  
 2836 a Landau distribution greatly underestimates the width  $w$  of the distribution and only succeeds to  
 2837 provide with a correct value for the most probable energy loss, as showed in Figure 4.27. Thus,  
 2838 the energy loss distribution is better represented by its most probable energy loss  $\Delta_p$  and its full-  
 2839 width-at-half-maximum (FWHM)  $w$ . As showed by Figure 4.28, the distribution is affected by  
 2840 the thickness of the gas volume and the most probable energy loss normalized to the thickness is  
 2841 increased and the width decreased, converging towards the Landau distribution, whereas the mean  
 2842 energy loss is unchanged. Corrections are brought to the original Landau equation in order to account  
 2843 better for the number of collisions leading to an increased width of the energy loss distribution [243].

2844 In the case of gas mixtures, composed of several elements, using Bragg additivity it can be  
 2845 understood that the mean energy loss of the mixture is the sum of the mean energy losses in each  
 2846 individual element  $j$  layer of weight  $w_j$ .

$$(4.8) \quad \left\langle \frac{dE}{dx} \right\rangle = \sum w_j \left\langle \frac{dE}{dx} \right\rangle_j$$

### 2847 4.3.2 Primary ionization

2848 Using Bethe formula to understand the mean energy transfer of charged particles when traveling  
 2849 through a gas volume give an intuition of the physics that affect the particle but doesn't provide a  
 2850 detailed enough information about the individual ionizations along its tracks at a microscopic level.  
 2851 In order to simulate efficiently an RPC and hence understand the processes governing avalanches  
 2852 creation and growth, knowledge on the ionization process is necessary.

2853 To convert the energy loss rate into a number of primary ionizations was developed in 1980 the  
 2854 Photo-Absorption Ionisation (PAI) model [244] based on the cross section of ionization of gas atoms  
 2855 to real photons and the dielectric constant of the medium through which the charged particles are  
 2856 going. Indeed, the interaction of charged particles with the gas molecules being of electromagnetic  
 2857 nature, it is mediated by quasi-real photons and, hence, the cross section to photon ionization is  
 2858 important to understand. This approach is nevertheless semi-classical as it relies on classical elec-  
 2859 trodynamics and it only gives access to the energy transfer to the gas atoms and no information on  
 2860 the energy dissipation and secondary emissions is available on the output of the model. The energy  
 2861 transferred to the medium is not all used for ionization. For an energy deposition  $\Delta$ , the number of  
 2862 electron-ion pairs produced is:

$$(4.9) \quad \Delta = n_i W$$

2863  $W$  corresponds to the mean work per pair production that depends on the medium and is greater  
 2864 than the ionization potential leading to the conclusion that part of the transferred energy is dissipated  
 2865 through other processes [239, 245]. In order to understand the energy dissipation and the secondary  
 2866 emissions, the fine structure of each atom is taken into account. Through the PAI model, the incident  
 2867 charged particle interacts is assumed to interact with the full atom rather than with a single electron.

2868 Although, considering that the particle interacts with a single electron, leads to the possibility to  
 2869 study the excited state of the atom once the photo-electron has been emitted with an energy corre-  
 2870 sponding to the transferred energy minus the binding energy of the electronic shell. The resulting

vacancies in the electronic shell will be filled through emission of photons or Auger electrons and can contribute to further ionization or excitation in the gas volume. Fluorescence photons are usually not considered as they only constitute a very small fraction of secondary emissions [246]. Assuming that the transferred energy is absorbed in its totality by a single electronic shell, the PAI model was modified to include relaxations and constitute the new Photo-Absorption Ionisation with Relaxation (PAIR) model [246]. In this model, the cross section corresponding to the whole atom is re-expressed using a sum of partial cross sections corresponding to the different electronic shells. When one or more electrons are knocked out of the atom, the vacancies are filled by electrons of the shell above with relaxation by Auger electron emission. These processes happen in cascade from the inner shell to the outer one until all the vacancies are filled and the energy has been released.

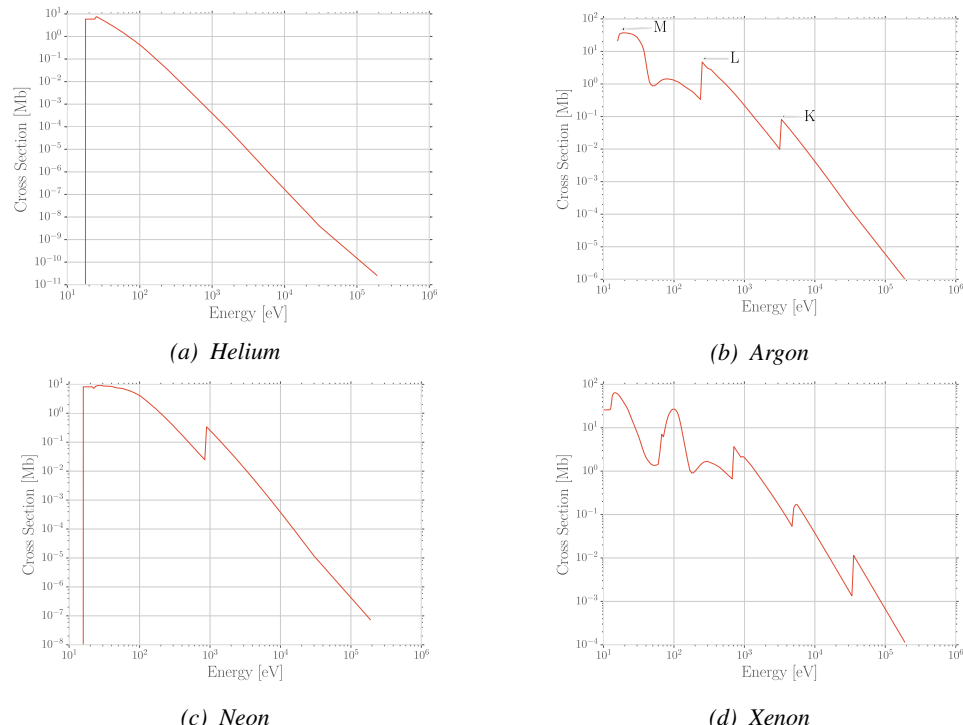


*Figure 4.29: Photoabsorption cross section as computed by HEED for noble gases with different electric shell numbers [239].*

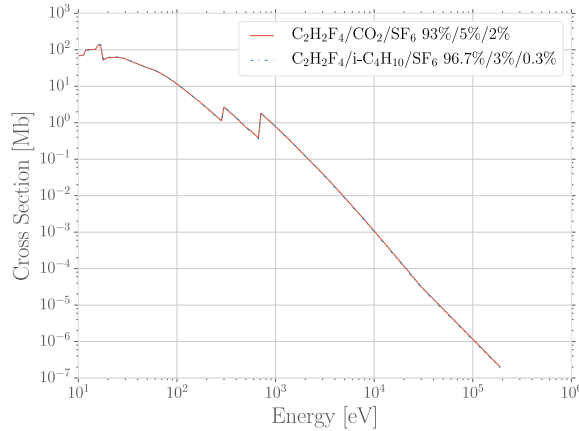


*Figure 4.30: Photoabsorption cross section as computed by HEED for typical RPC gas mixtures [239]. The RPC mixture with  $CO_2$  corresponds to the mixture used by CALICE SDHCAL [247] while the other one was foreseen for the experiment ATLAS [248] but has been changed since then.*

This model is included in the program HEED developed at CERN [249] and called by Garfield, a program developed for the simulation of gaseous detectors. The results for the cross section for a few noble gases are given in Figure 4.29. It can be seen that for each shell, the cross section is increased. More complex patterns are seen with bigger atoms such as Xenon on Figure 4.29d. For gas mixtures, like the typical RPC mixtures, the cross section is showed in Figure 4.30. Both mixtures being mainly composed of  $C_2H_2F_4$ , the variations in between the 2 cross section profiles are very subtle and depends on the concentration of the other compounds.

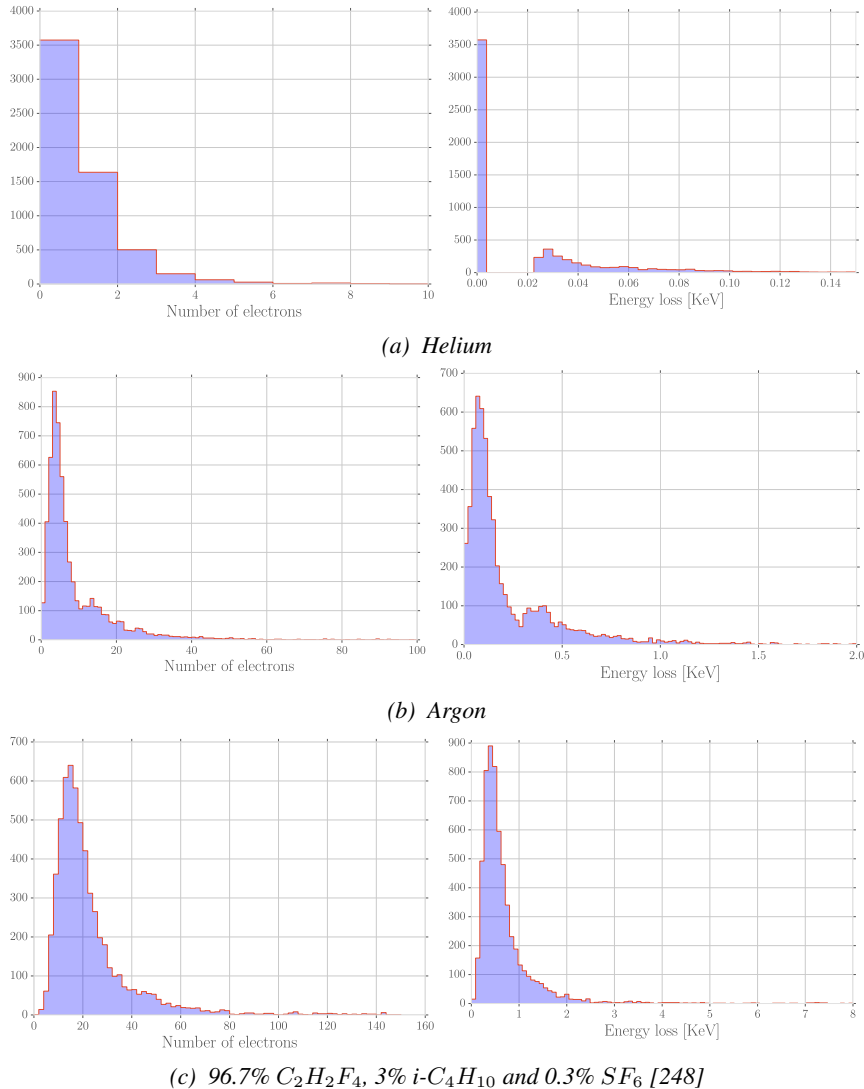


Figure 4.31: Distributions of number of electrons (left) and energy loss (right) for a 5 GeV/c muon passing through 1.2 mm of Helium (Figure 4.31a), Argon (Figure 4.31b) or a typical RPC gas mixture (Figure 4.31c) [239].

Once the cross section of interaction is known, it is possible to extract the distribution of energy loss and of the number of produced electrons, as showed in Figure 4.31 for Helium, Argon, which is used in gaseous detectors, and for a typical RPC mixture [239]. The distributions are computed using HEED and show typical straggling function profiles with some complex structures that can be related to interaction of the incoming particle with the different electronic shells. Helium does not have a great photoabsorption cross-section according to Figure 4.29a and a muon will not be likely to lose a lot of energy and to create a lot of electrons whereas in a more complex atom like Argon, the cross-section is greater and will lead to a greater energy loss of muons and more electron produced. Finally, a complex gas mixture used in RPCs will offer an even greater cross-section, a wider energy loss distribution and will be able to produce more electrons. The same information is seen by looking

at the evolution of the mean number of clusters as a function of the lorentz factor associated to muons showed in Figure 4.32a. Indeed, the greater photoabsorption cross-section of RPC mixtures allows for a much greater number of clusters to be created by charged particles. The size of these clusters is studied through Figure 4.32b which shows that, in most of the cases ( $\approx 80\%$ ), the clusters only are composed of a single electron which is consistent with minimum ionizing particles.

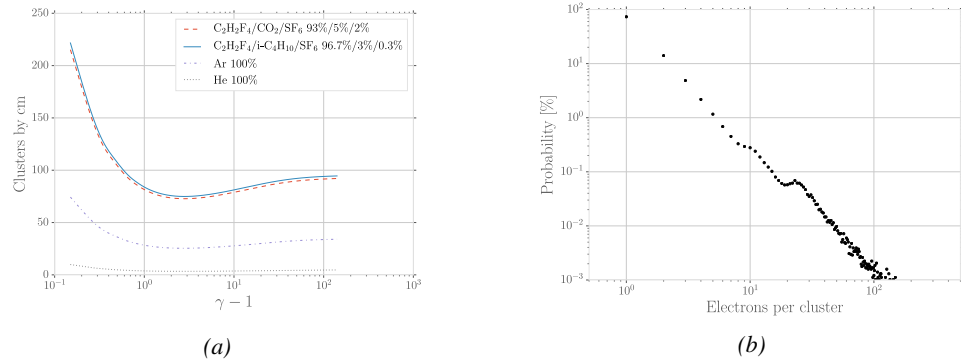


Figure 4.32: Figure 4.32a: Mean cluster density for muons through different gas volumes [239]. Figure 4.32b: Distribution of the number of electrons per cluster for a 5 GeV/c muon traveling through a mixture of 96.7%  $C_2H_2F_4$ , 3%  $i-C_4H_{10}$  and 0.3%  $SF_6$  [239, 248].

### 4.3.3 Development and propagation of avalanches

From the clusters released in the gas volume by the charged particles, free electrons will start drifting due to the electric applied in between the electrodes of the RPC. Gaining velocity and energy, these electrons in their turn will be able to ionize the gas. This process being repeated by all the produced electrons will trigger an avalanche to develop.

The growth of the avalanche can be intuitively understood as a competition between two effects. Due to their increasing energy, electrons have a probability to trigger new ionizations by interacting with gas molecules. On the other hand, before the minimal amount of energy is reached, the electrons can get attached to a gas molecule instead. These two effects can be described using a simple model in which the multiplication and attachment processes are given by the Townsend coefficient  $\alpha$  and the attachment coefficient  $\eta$ , assuming that the history of previous interactions in the gas does not influence new interactions. This model simply takes into account probabilities to have at the gas depth  $z$ , for a given number  $n$  of free electrons in the gas,  $n+1$  or  $n-1$  electrons at the depth  $z+dz$  (respectively  $n\alpha dz$  and  $n\eta dz$ ). Then, the mean number of electrons  $\bar{n}$  and cations  $\bar{p}$  can be written for single compound gases as

$$(4.10) \quad \frac{d\bar{n}}{dz} = (\alpha - \eta)\bar{n}, \quad \frac{d\bar{p}}{dz} = \alpha\bar{n}$$

which, assuming the initial conditions  $\bar{n}(0) = 1$  and  $\bar{p}(0) = 0$ , lead to the mean number of electrons and cations at a depth  $z$

$$(4.11) \quad \bar{n}(z) = e^{(\alpha-\eta)z}, \quad \bar{p}(z) = \frac{\alpha}{\alpha-\eta} \left( e^{(\alpha-\eta)z} - 1 \right)$$

2920     The Townsend and attachment coefficient as a function of the applied electric field are given in  
 2921     Figure 4.33 for a standard RPC gas mixture using Magboltz [250].

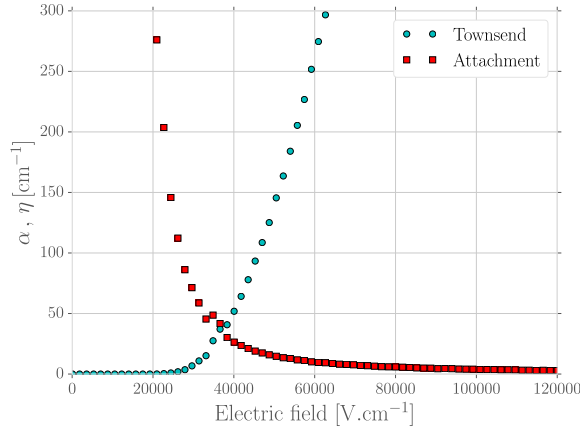


Figure 4.33: Townsend and attachment coefficient for a typical 96.7/3/0.3 mixture of  $C_2H_2F_4/i-C_4H_{10}/SF_6$ , at a temperature  $T = 296.15\text{ K}$  and a pressure  $P = 1013\text{ hPa}$  [239, 248].

2922     Nevertheless, there are more to the avalanche growth than simply these two factors. Throughout  
 2923     the 20<sup>th</sup> century, models have been developed to better understand the physics of discharges in gas.  
 2924     In 1937, Furry developed a model to describe electromagnetic cascades [251] that would be used for  
 2925     electron avalanches in gas during the 1950s. Furry realized that the use of a Poisson law to describe  
 2926     the distribution of shower sizes could not be accurate as he understood that the events occurring in  
 2927     the development of a cascade are not independent from each other, as a Poisson law would suggest.  
 2928     Indeed, part of the particles produce others and this process depends on both their original energy  
 2929     and energy lost. Experimental results showed excess of small showers and an under estimate of very  
 2930     large ones. To solve this problem, Furry proposed a distribution of sizes of following the likelihood  
 2931     described in Equation 4.12, in which  $\bar{n} = e^{\alpha z}$ , compared with a Poisson law in Figure 4.34.

$$(4.12) \quad P(n, \bar{n}) = \bar{n}^{-1}(1 - \bar{n}^{-1})^{n-1}$$

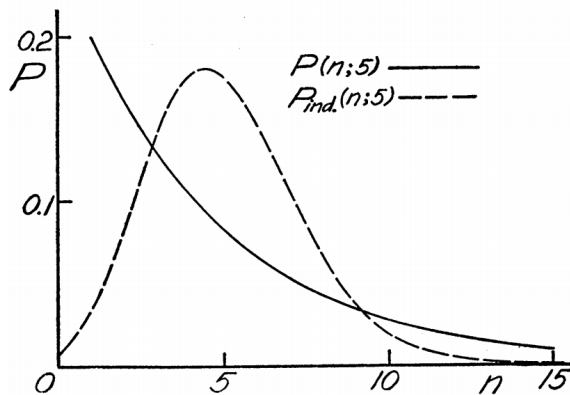


Figure 4.34: Comparison of the distribution law of Furry and the Poisson law for  $\bar{n} = 5$  [251].

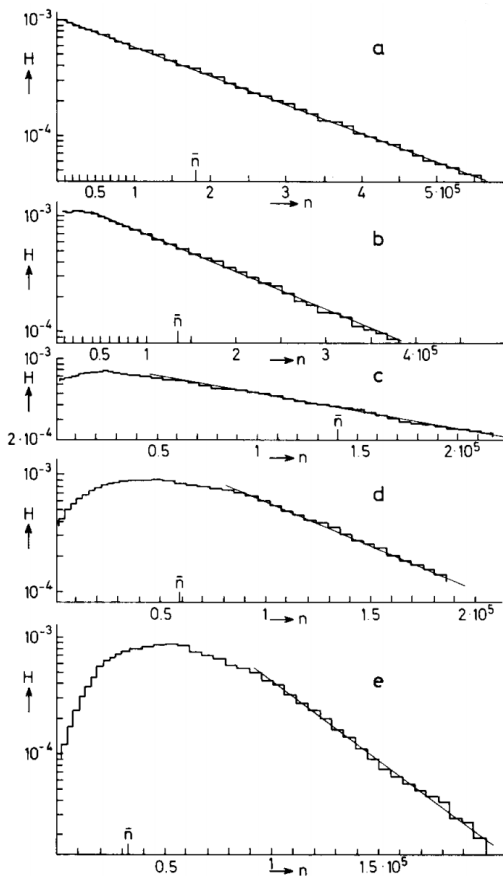


Figure 4.35: Single-electron avalanche size distribution in a proportional counter filled with methylal at different  $E/p$  values. (a) 70, (b) 76.5, (c) 105, (d) 186.5, (e) 426V/cm torr [252].

In this model, no extra energy is brought to the electrons in the showers, contrary to the case of a gaseous detector such as an RPC where an electric field accelerates them. Using the Furry model, Genz studied the fluctuations in electron avalanches in gaseous detectors [252]. Collisions leading to ionizations leave electrons with an energy much smaller than the ionization energy  $eU_i$ , where  $U_i$  is the ionization potential of a gas molecule. Hence, the electrons need to travel a distance  $s = U_i/E$  along the electric field  $E$  to acquire a high enough energy to trigger a new ionization. For the probability of a new ionization to be independent from the path followed by the electrons since the previous ionization, the mean free path  $1/\alpha$  of electrons in the gas has to be large compared to  $s$  and thus  $E/\alpha \gg U_i$ . The Townsend coefficient is related to the gas pressure leading to conditions on the value of  $E/p$ . Avalanches in gas are large compared to the showers Furry has studied in his original paper. For very large avalanche sizes, Equation 4.12 can be written as an exponential, as showed in Equation 4.13.

$$(4.13) \quad P(n, \bar{n}) = \bar{n}^{-1} e^{-n/\bar{n}}$$

This exponential behaviour is showed through Figure 4.35. In practice, to fully understand the avalanche growth, taking into account the path followed by electrons from one ionization to another

will become necessary. In the same paper, Genz then discusses models using Polya distributions to estimate the multiplication by looking at the size of the avalanche it self. Indeed, the number of charge carriers in the avalanche might become important enough to have an effect on the multiplication process. To account for this, it was proposed to use a varying Townsend coefficient such as described by Equation 4.14 depending on the position  $x$  in which  $\theta$  is an empirical parameter leading to the probability distribution of Equation 4.15. In the limit case where  $\theta$  goes to 0, the formula describes again the Furry model. But the data deviates from this model as well at large  $n$  values. Moreover, the introduction of an empirical parameter makes the model hard to interpret physically.

$$(4.14) \quad \alpha(n, x) = \alpha(x) \left(1 + \frac{\theta}{n}\right), \quad n > 0$$

$$(4.15) \quad P(n, x) = \frac{1 + \theta}{\bar{n}} \frac{1}{\theta!} \left(\frac{n(1 + \theta)}{\bar{n}}\right)^{\theta} e^{-\frac{n(1 + \theta)}{\bar{n}}}$$

In order to have a model that describes reality better, the introduction of the attachment into the model is an important step. Despite its limitations, the Furry model had the advantage to well describe avalanches occurring when the attachment could be ignored. This is only natural that this model was then extended to included attachment. This was done by Riegler, Lippmann and Veenhof [248] which showed that what was important was to consider both the Townsend coefficient describing the multiplication *and* the attachment coefficient, not only the effective multiplication coefficient  $\bar{\alpha} = \alpha - \eta$ . The probability to see an avalanche started by a single electron grow to a size  $n$  after having traveled a distance  $z$  through the gas is given by Equation 4.16.

$$(4.16) \quad \begin{aligned} P(n, z) = & P(n-1, z) (n-1)\alpha dz (1 - (n-1)\eta dz) \\ & + P(n, z) (1 - n\alpha dz) (1 - n\eta dz) \\ & + P(n, z) n\alpha dz n\eta dz \\ & + P(n+1, z) (1 - (n+1)\alpha dz) (n+1)\eta dz \end{aligned}$$

The first term of this probability that from a state with  $n-1$  electrons, only 1 multiplies while the others don't get attached. Both the second and third terms describes the probability that from a state with already  $n$  electrons the total number of electrons stay the same. On the second term, no electron gets attached nor multiplies while on the third term, 1 electron gets multiplied and 1 gets attached to compensate. Finally, the fourth term describes the probability to fall from a state with  $n+1$  to a state with  $n$  electrons due to the attachment of a single electron. At the first order, the evaluation of the previous expression leads to Equation 4.17 which general solution is given in Equation 4.18 in which are introduced the variables  $\bar{n}(z)$ , defined as in Equation 4.11, and  $k = \eta/\alpha$  making explicit the fact that the distribution does not depend on the effective Townsend coefficient only.

$$(4.17) \quad \frac{dP(n, z)}{dz} = -P(n, z)n(\alpha + \eta) + P(n-1, z)(n-1)\alpha + P(n+1, z)(n+1)\eta$$

$$(4.18) \quad P(n, z) = \begin{cases} k^{\frac{\bar{n}(z)-1}{\bar{n}(z)-k}}, & n = 0 \\ \bar{n}(z) \left(\frac{1-k}{\bar{n}(z)-k}\right)^2 \left(\frac{\bar{n}(z)-1}{\bar{n}(z)-k}\right)^{n-1}, & n > 0 \end{cases}$$

The example given through Figure 4.36 shows the importance of each individual process in the growth of avalanches and the fluctuation of their size. The values of  $\alpha$  and  $\eta$  will influence the probability distribution, as can be seen from Figure 4.36a. Then, Figure 4.36b shows that the fluctuation really takes place within the very first interactions. Indeed, when the avalanche contains a large enough number of charge carriers (a few hundreds), its size then increases like  $e^{z(\alpha-\eta)}$ .

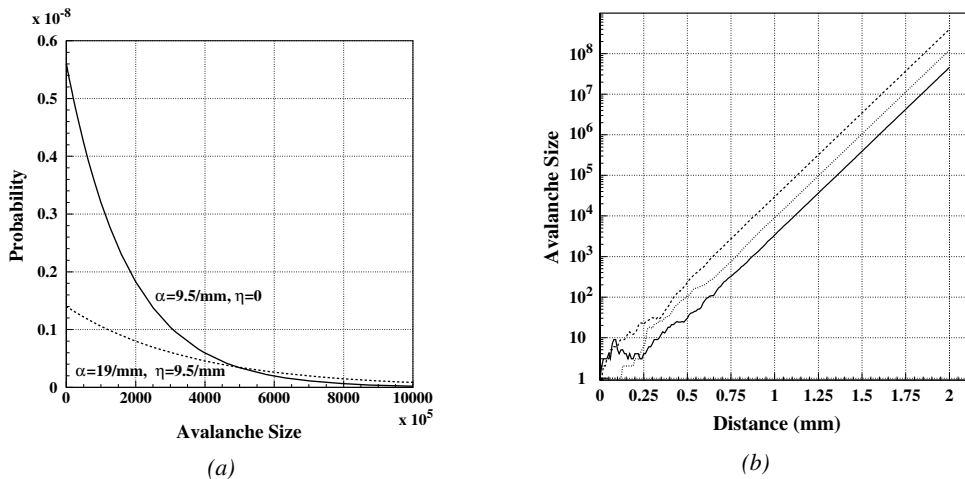


Figure 4.36: Figure 4.36a: Comparison of avalanche size distributions for different values of Townsend and attachment coefficients. The effective Townsend coefficient is the same for both distributions. Figure 4.36b: Fluctuation in avalanches size for avalanche started by a single electron with  $\alpha = 13 \text{ mm}^{-1}$  and  $\eta = 3.5 \text{ mm}^{-1}$  [248].

#### 4.3.4 Drift and diffusion of the electron cloud

During the growth of avalanches, an electron cloud drifting along the electric field through the gas will undergo thermal diffusion due to random collisions with the gas molecules. This phenomenon can be studied using Maxwell-Boltzmann distribution whose mean is defined by the thermal energy of the cloud  $\langle E \rangle = 3/2kT$  with an extra component coming from the constant drift motion. The drift of electrons along the field lines is usually observed on a macroscopic scale through which the speed can be assimilated to a constant  $v_D$  which corresponds to the mean drift speed over a large number of collisions in the gas.

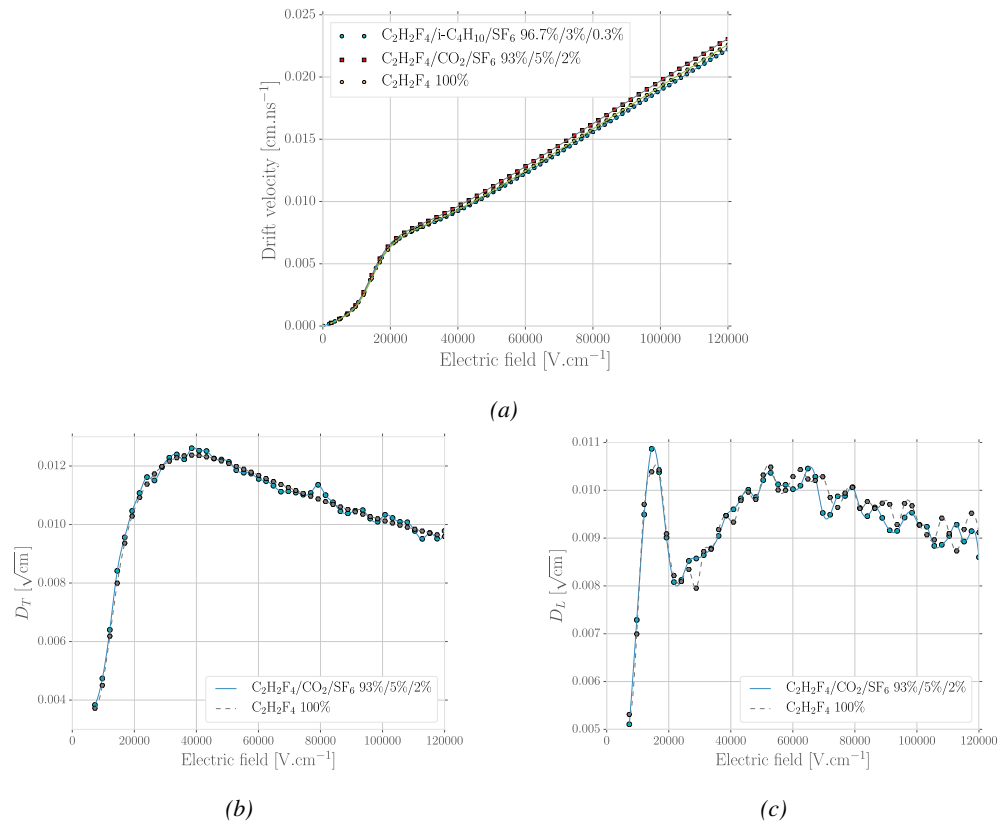


Figure 4.37: Figure 4.37a: Electrons mean drift velocity  $v_D$  in pure  $C_2H_2F_4$  and typical RPC gas mixtures. Figure 4.37b: Transverse diffusion coefficient in pure  $C_2H_2F_4$  and a typical RPC gas mixture. Figure 4.37c: Longitudinal diffusion coefficient in pure  $C_2H_2F_4$  and a typical RPC gas mixture. All results are given with a pressure  $P = 760$  Torr and a temperature  $T = 296.15$  K [239].

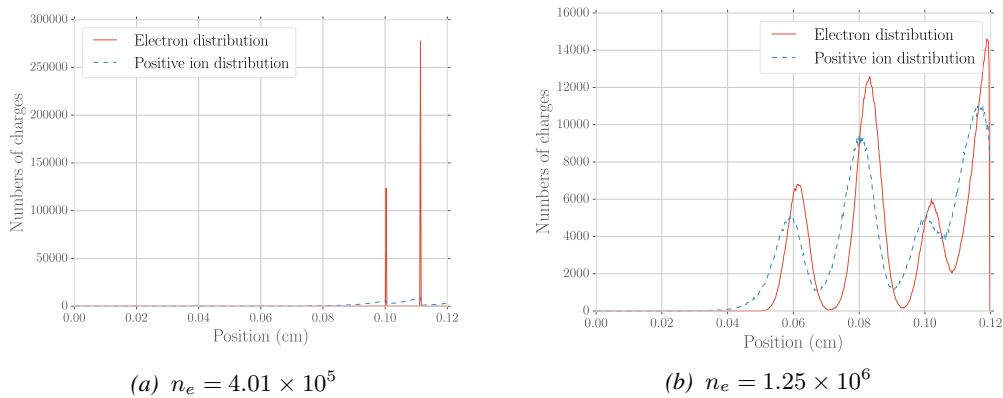


Figure 4.38: Comparison of the free charge carriers in the gas after a time  $t = 7.90$  ns in the case where no diffusion is taken into account to simulate the avalanche (Figure 4.38a) and in the case where the diffusion is implemented (Figure 4.38b) [239].

Indeed, at the microscopic scale, the electrons are drifting over a distance  $\delta z$  while acquiring the corresponding kinetic energy  $T = e_0 |\vec{E}| \delta z$  until they are slowed down by a collision in which they lose part of their energy. This process is repeated as long as electrons are free carriers. Starting from a point-like electron cloud, the Gaussian density distribution at  $\vec{r}_0$  will be described by Formula 4.19 in which the width of the isotropic distribution is  $\sigma = 2\bar{D}t$ , with  $\bar{D}$  being a diffusion coefficient expressed in  $\text{m}^2/\text{s}$  [221].

$$(4.19) \quad \varphi(\vec{r}, t) = \frac{1}{(\sqrt{2\pi}\sigma(t))^3} \exp\left(-\frac{(\vec{r} - \vec{r}_0)^2}{2\sigma^2(t)}\right)$$

Now, if the constant drifting motion is added, the distribution is anisotropic and can be divided onto transversal (Formula 4.20) and longitudinal (Formula 4.21) terms,  $\varphi(r, z, t) = \varphi_T(r, t)\varphi_L(z, t)$ , with a cylindrical symmetry around the field axis [221]. The variables  $t$  and  $\sigma_{T,L}(t)$  can be hidden to the profit of the diffusion coefficients by using the relations  $v_D = l/t$  and  $\sigma_{T,L}^2(t) = 2\bar{D}_{T,L}l/v_D$  and introducing new diffusion coefficients  $D_{T,L} = \sqrt{2\bar{D}_{T,L}/v_D}$  in order to explicitly show the dependence of the Gaussian width in drifted distance  $l$ .

$$(4.20) \quad \varphi_T(r, t) = \frac{1}{D_T^2 l} \exp\left(-\frac{(r - r_0)^2}{2D_T^2 l}\right)$$

$$(4.21) \quad \varphi_L(z, t) = \frac{1}{\sqrt{2\pi l} D_L} \exp\left(-\frac{(z - z_0)^2}{2D_L^2 l}\right)$$

These coefficients, as well as the drift velocity of the electrons, can be calculated thanks to Magboltz as showed in Figure 4.37. The influence of the diffusion on the distribution of charge carriers throughout the gas volume is depicted in Figure 4.38. From very localised electron clusters in the gas in Figure 4.38a, a Gaussian diffusion is then visible in Figure 4.38b. Due to the interactions with gas molecules during the drift, diffusions can occur in the forward and backward direction. Electrons diffused backward will effectively drift over a longer distance and multiply more than electrons diffused forward that will see a shorter drift length. As an effect, the avalanche develops over a longer time and extends over a greater gas volume than in the case the electron cloud is considered as point like and without diffusion. Moreover, as a side effect to the longer growth of the avalanche due to backward longitudinal diffusion, the total production of electrons is increased.

### 4.3.5 Space charge effect & streamers

Now that has been considered the basic processes that influence the development of avalanches in a gaseous detector in the previous sections, it is now important to consider the influence of the charge carriers present in the avalanche on the electric field seen by the avalanche. Indeed, each charged particle induces an electric field and it is only natural that the increasing density of electrons and ions in the detector volume will affect the electric field. Thus, parameters such as the Townsend and attachment coefficients, drift velocity or diffusion coefficients will find themselves to be modified along the gas gap length due to this effect referred to as *space charge effect*. Figure 4.39 is a more detailed version of Figure 4.1 (b) in which three electric regions are distinguished [221]. When compared to the linear electric field of strength  $E_0$  that is developed in between the detector's electrodes, the

3016 accumulation of negative charges (electrons) on the front of the avalanche will reinforce the effective  
 3017 electric field in between the anode and the avalanche front. Deeper in the gas volume, the positive  
 3018 charges (cations) slowly drift towards the cathode and can induce together with the avalanche front  
 3019 opposite electric field loops. Finally, due to the density of positive charges, the electric field seen in  
 3020 between the ions tails and the cathode charged with negative charges is on average stronger than  $E_0$   
 3021 and compensate for the locally reversed field  $E_2$ . Lippmann roughly estimated by considering that  
 3022  $10^6$  charges were contained in a sphere of radius  $r_d = 0.1$  mm that the space charge effect could  
 3023 change the electric field by 3% and the Townsend and attachment coefficient up to 14% [221, 239].

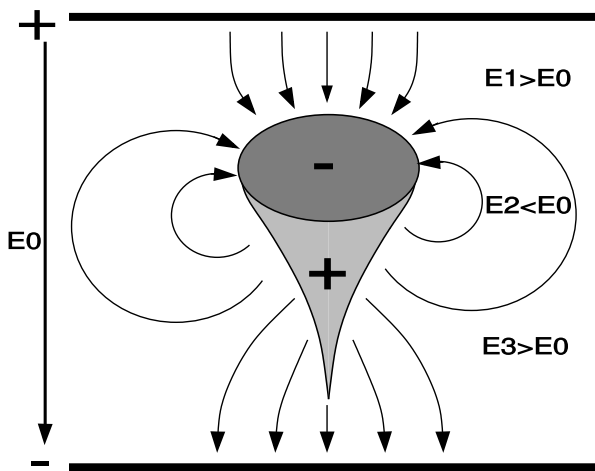
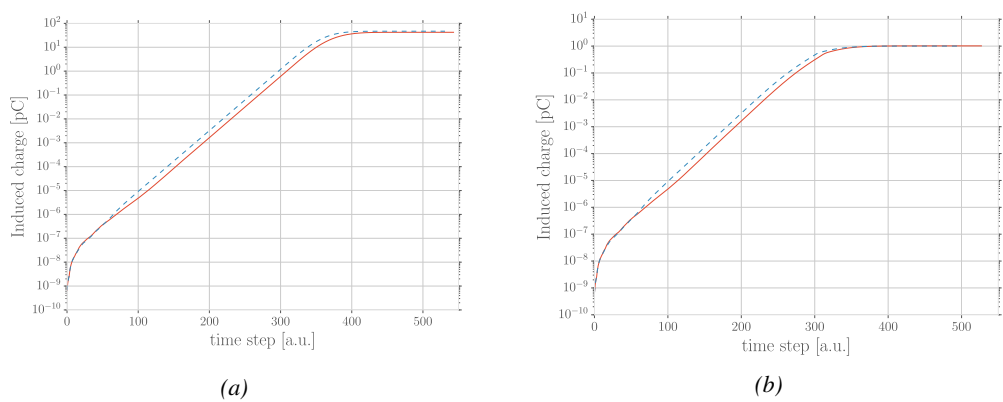


Figure 4.39: Schematic representation of an avalanche and of the electric field deformation it causes due to the local concentration of charge carriers [221].

3024 To account for the space charge effect, the electric potential and field of free charges are solved  
 3025 and applied to each charge in the avalanche [221, 239]. As discussed by Français who has been  
 3026 working on simulating RPCs similar to that used by the SDHCAL project of ILC, the computation  
 3027 of these equations for each individual charge carrier to dynamically know the space charge field at  
 3028 every stage of an avalanche development is a difficult task and would require far too much computa-  
 3029 tion time and a solution is to pre-compute an interpolation table keeping an adequately large number  
 3030 of values of the space charge field for each position in space thanks to which the values stored in the  
 3031 interpolation table become very close to the analytic solution and allow for a much faster simulation.  
 3032

3033 The study of space charge effect through simulation shows that it can lead to a saturation of  
 3034 the avalanche growth due to the deformation of the electric field, as showed through Figure 4.40.  
 3035 Additionally, a more precise understanding of the space charge effect is given through Figure 4.41  
 3036 which looks at the distribution of charges and the distortion of the electric field at different steps of  
 3037 the evolution of an avalanche in a RPC. At the moment a 5 GeV muon ionizes the gas, electron-ion  
 3038 pairs are created in the gas in different clusters (Figure 4.41a). Later, the first clusters have reached  
 3039 the anode while the clusters that were created closest to the cathode are now big enough to start  
 3040 influencing the electric field in the gap (Figure 4.41b). When a cluster is big enough, the electric  
 3041 field in front of it locally increases a lot and contributes to a stronger but very localised multipli-  
 3042 cation. At the same moment, the positive ions right behind the cluster avalanche front decrease the  
 3043 electric field, saturating the electron multiplication on the tail of the electron cloud (Figure 4.41c).

3044 Finally, when all the electrons have reached the anode and are relaxing, the electric field still is very  
 3045 deformed by the distribution of both positive and negative ions in the gas volume closest to the anode  
 3046 (Figure 4.41d).



*Figure 4.40: Evolution of the charge induced by an avalanche started by a single electron in a 1.2 mm thick RPC with an applied electric field of 54 kV/cm in the case space charge is not taken into account (Figure 4.40a) and in the case it is implemented into the simulation (Figure 4.40b). The total induced charge is correlated to the size of the avalanche [239].*

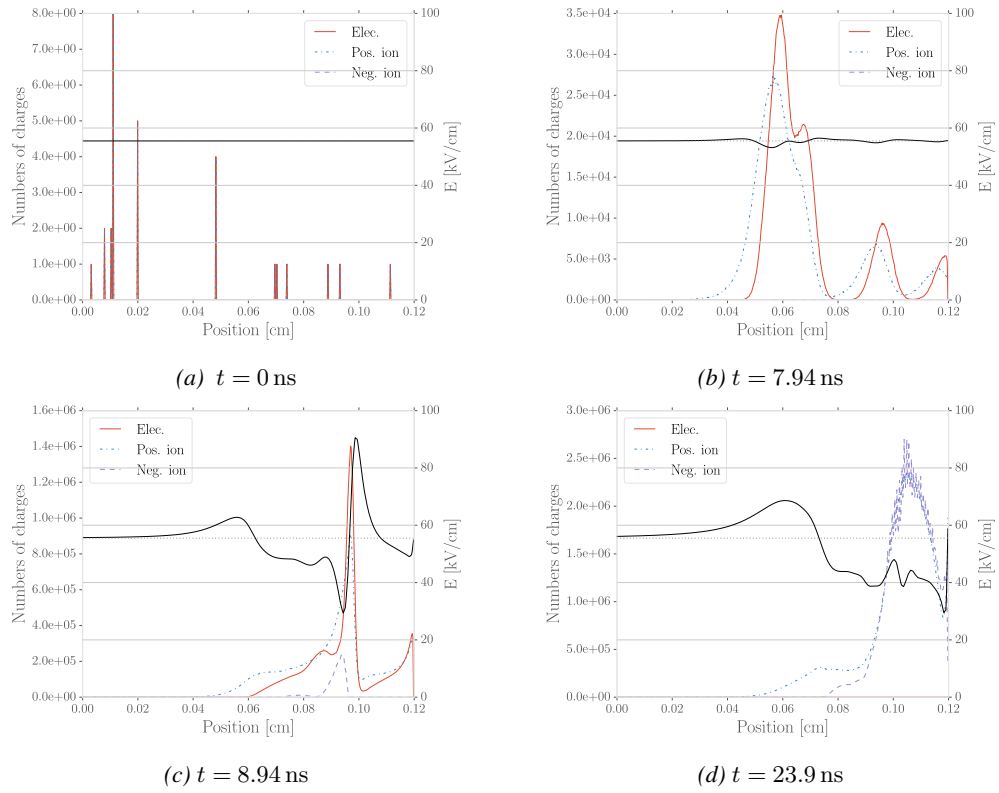


Figure 4.41: Distributions of charge carriers within the gas volume of a 1.2 mm thick RPC and the corresponding deformation of the electric field at different time steps with an applied electric field of 55.5 kV/cm [239].

3047     The electric field following the development of an avalanche can stay perturbed for a long time  
 3048     with respect to the avalanche development due to the slow drift of the much heavier ions. This can  
 3049     result in powerful secondary avalanches triggered by the fluctuation of the electric field together with  
 3050     the emission of UV-photons leading to emission of electrons at the surface of the electrode. This is  
 3051     a slow phenomenon compared to the development of avalanches. Experimentally, it is observed that  
 3052     the stronger the electric field applied over the gap, the sooner after the avalanche, referred to as *pre-*  
 3053     *cursor signal* in this context, and the stronger will the secondary avalanche be, possibly reaching the  
 3054     streamer regime. This could be due to the amount of UV-photons emitted by the growing precursor.  
 3055     These photons will be able to trigger new avalanches in a radius of a few mm around the precursor  
 3056     by knocking electrons from the cathode by photoelectric effect. The strong distortions of the electric  
 3057     field due to a large avalanche will be more likely to emit UV-photons as the electric field at the front  
 3058     of the precursor avalanche will be large, providing the electrons with a larger energy. Eventually, the  
 3059     new avalanches can grow to form streamers.

## 3060 4.4 Effect of atmospherical conditions on the detector's performance

3061

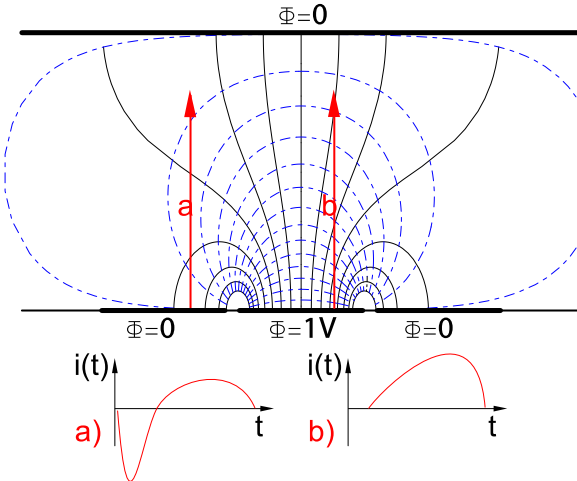


Figure 4.42: Representation of the weighting field in the volume of an RPC and the resulting induced current in the strip placed at 1 V and its neighbour connected to the ground. The induced current corresponds, as can be understood from Formula 4.22 [221].

3062 Accordingly to Ramo's theorem, the movement of charge carriers, and in particular, the movement  
 3063 of a dense electron cloud toward the anode induces a current signal on one or more of the readout  
 3064 electrodes (strips or pads). The ions on the other hand induce only a very small current as their  
 3065 movement is much slower than which of the electrons. The current induced by  $n_C l$  clusters of  $N_j(t)$   
 3066 charge carriers drifting at velocities  $\vec{v}_{Dj}(t) = \vec{x}_j(t)$  at a time  $t$  is given by Formula 4.22 in which  $e_0$   
 3067 is the unit charge and  $\vec{E}_w$  is the weighting field.

$$(4.22) \quad i(t) = \sum_{j=1}^{n_C l} \vec{E}_{wj}(\vec{x}_j(t)) \cdot \vec{v}_{Dj}(t) e_0 N_j(t)$$

3068 The weighting field, that has been schematized in Figure 4.42, corresponds to the electric field  
 3069 that would be observed in the gas gap if a readout electrode is placed at a potential of 1 V while  
 3070 keeping all the other electrodes grounded. Then the induced charge in the readout can be simply  
 3071 obtained by integrating Formula 4.22 over the duration  $T$  of the signal, as given by Formula 4.23.

$$(4.23) \quad Q(t) = \int_0^T \sum_{j=1}^{n_C l} \vec{E}_{wj}(\vec{x}_j(t)) \cdot \vec{v}_{Dj}(t) e_0 N_j(t)$$

3072 The signal induced in the readout of RPCs operated in avalanche mode is then sent into Front-  
 3073 End Electronics in which they will be pre-amplified and discriminated. The discrimination and  
 3074 digitization of signals in CMS FEE are described through Figure 4.43. On a first stage, analogic  
 3075 signals are amplified, following the curve given on Figure 4.44, and then sent to the Constant Frac-  
 3076 tion Discriminator (CFD) described in Figure 4.45. At the end of the chain, 100 ns long pulses are

3077 sent in the LVDS output. The digital signals are both used as trigger for CMS and to evaluate the  
 3078 performance of the detectors. The performance will depend on the applied HV, i.e. on the electric  
 3079 field inside of the gas volume, but also on the threshold applied on the CFDs. Indeed, in order to  
 3080 reduce the probability to measure noise, the threshold is set to a level where the noise is strongly  
 3081 suppressed while the signals are not too affected. Typically, CMS FEEs are set to a threshold of  
 3082 215 mV after pre-amplification, corresponding to an input charge of about 140 fC.

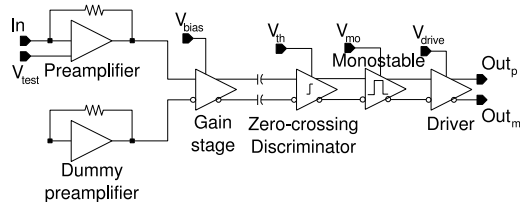


Figure 4.43: Schematics of CMS RPC FEE logic.

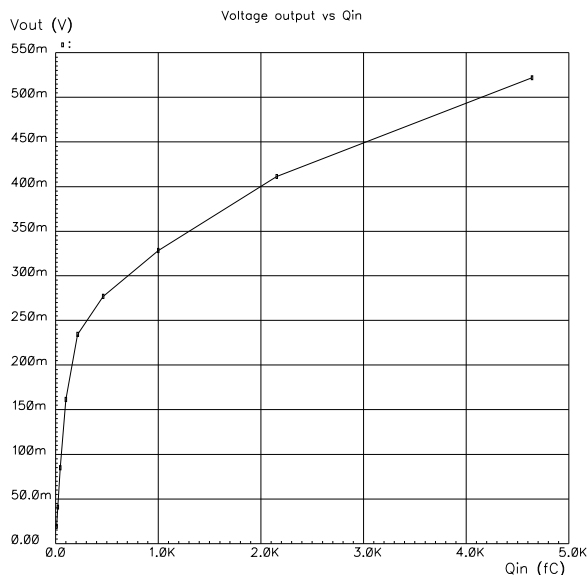
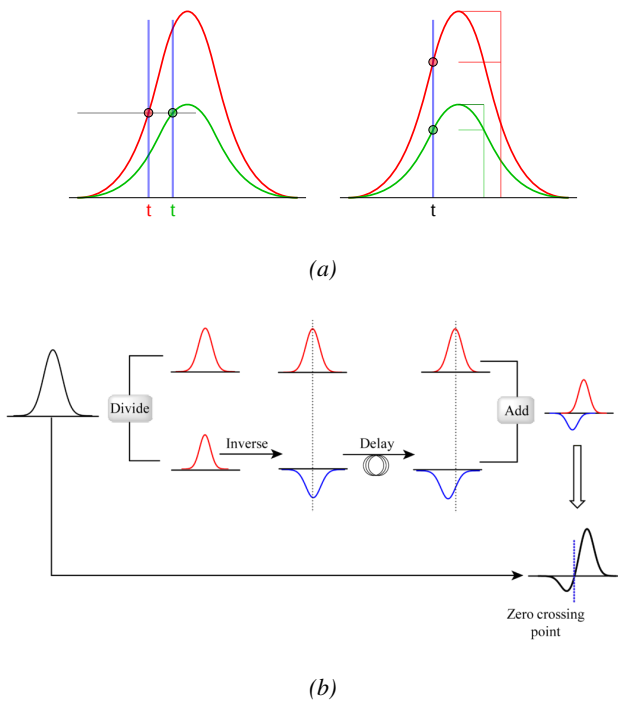


Figure 4.44: Equivalence in between the charge of the induced signal in input of the CMS FEE and the signal strength on the output of the pre-amplifier.



*Figure 4.45: Description of the principle of a CFD. A comparison of threshold triggering (left) and constant fraction triggering (right) is shown in Figure 4.45a. Constant fraction triggering is obtained thanks to zero-crossing technique as explained in Figure 4.45b. The signal arriving at the input of the CFD is split into three components. A first one is delayed and connected to the inverting input of a first comparator. A second component is connected to the noninverting input of this first comparator. A third component is connected to the noninverting input of another comparator along with a threshold value connected to the inverting input. Finally, the output of both comparators is fed through an AND gate.*

The performance of a detector is then simply measured relatively to which of a reference detector used as trigger as the ratio in between the number of events recorded in coincidence in the detector and the reference and the total number of trigger events,  $\epsilon = n_{events}/n_{triggers}$ . An example of efficiency measured as a function of the effective voltage  $HV_{eff}$  is given in Figure 4.46 and can be fitted thanks to a sigmoidal function described as in Formula 4.24 and where  $\epsilon_{max}$  is the maximal efficiency of the detector,  $\lambda$  is proportional to the slope at half maximum and  $HV_{50}$  is the value of the voltage when the efficiency reaches half of the maximum.

$$(4.24) \quad \epsilon(HV_{eff}) = \frac{\epsilon_{max}}{1 + e^{-\lambda(HV_{eff} - HV_{50})}}$$

CMS RPC also define two points on this sigmoid that called *knee* and *working point*. The corresponding voltages  $HV_{knee}$  is defined as the voltage at 95% of the maximum efficiency, and  $HV_{WP}$  is defined as in Formula 4.25.

$$(4.25) \quad HV_{WP} = HV_{knee} + \begin{cases} 100V & (\text{barrel}) \\ 150V & (\text{endcap}) \end{cases}$$

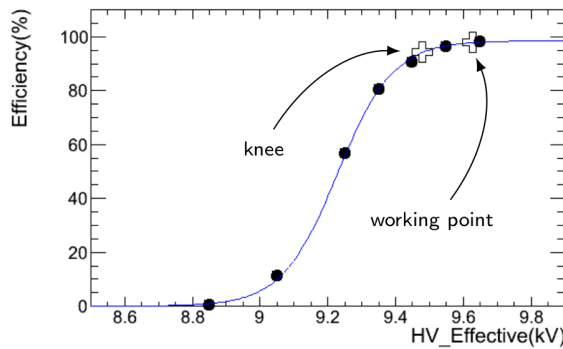
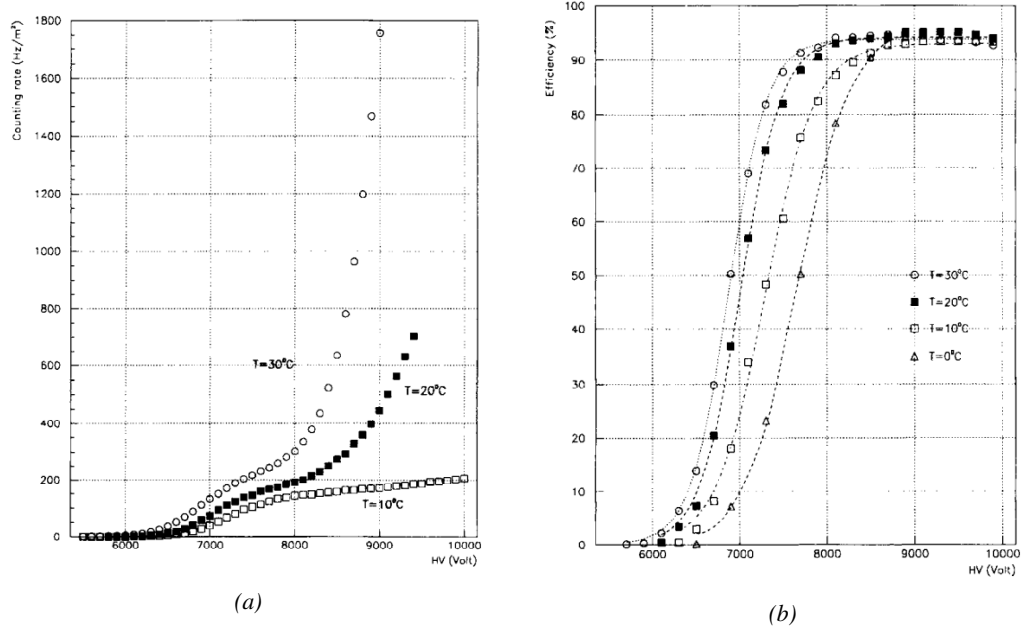


Figure 4.46: Typical efficiency sigmoid of a CMS RPC detector. The black dots correspond to the data, the blue line to the sigmoid fit and the opened cross to the knee and working extracted from the fit line.

Nevertheless, the voltage applied on a detector may vary due to a change in environmental conditions. Indeed, the variation of temperature and/or pressure will have effect on the gas density and the electrodes' resistivity which can be overcome by changing the electric field accordingly. The variation in temperature and pressure are depicted respectively in Figure 4.47 and Figure 4.48. A standard procedure to correct for temperature and pressure variations is to keep the factor  $HV \cdot T/P$  constant using Formula 4.26 [253, 254] with reference values for  $T_0$  and  $P_0$ . For example, CMS uses  $T_0 = 293.15$  K and  $P_0 = 965$  hPa.

$$(4.26) \quad HV_{app} = HV_{eff} \frac{P_0}{P} \frac{T}{T_0}$$



*Figure 4.47: Effect of the temperature variation on the rate (Figure 4.47a) and the efficiency (Figure 4.47b) of an RPC [253].*

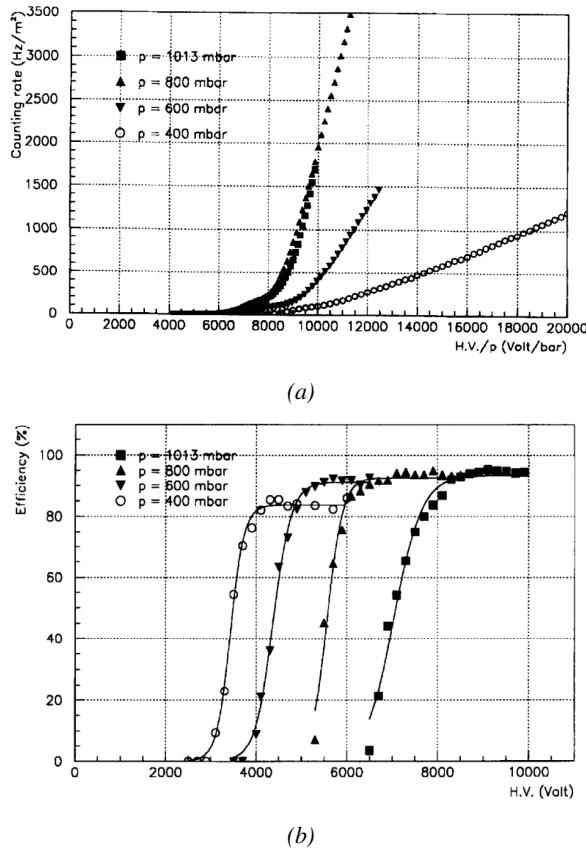


*Figure 4.48: Effect of the pressure variation on the rate (Figure 4.48a) and the efficiency (Figure 4.48b) of an RPC [254].*

It was actually found that such a simple procedure would overcorrect the applied voltage in the case the variations of temperature or pressure were too important [255–258]. CMS, considering that the temperature variations in the detector cavern were very small, decided only to improve the pressure correction, giving rise to Formula 4.27 [255] while on the other hand, ATLAS decided to have a more robust correction for both parameters and uses Formula 4.28 instead [258]. The coefficients  $\alpha$ , in the case of CMS, and  $\alpha, \beta$ , in the case of ATLAS, are extracted from fit on available dataset obtained during the operation of the detectors.

$$(4.27) \quad HV_{app} = HV_{eff} \left( 1 - \alpha + \alpha \frac{P_0}{P} \right) \frac{T}{T_0}, \quad \alpha = 0.8$$

$$(4.28) \quad HV_{eff} = HV_{app} \left( 1 + \alpha \frac{\Delta T}{T_0} \right) \left( 1 - \beta \frac{\Delta P}{P_0} \right), \quad \alpha = 0.5, \beta = 0.71$$



# 5

3107

3108

3109

## Longevity studies and Consolidation of the present CMS RPC subsystem

3110 The RPC system, located in both barrel and endcap regions, provides a fast, independent muon trigger  
3111 with a looser  $p_T$  threshold over a large portion of the pseudo-rapidity range ( $|\eta| < 1.6$ ). During  
3112 HL-LHC operations the expected conditions in terms of background and pile-up will make the iden-  
3113 tification and correct  $p_T$  assignment a challenge for the muon system. The goal of RPC upgrade is to  
3114 provide additional hits to the Muon System with more precise timing. All this information will be  
3115 elaborated by the Trigger System in a global way enhancing the performance of the trigger in terms  
3116 of efficiency and rate control. The RPC Upgrade is based on two projects: an improved Link Board  
3117 System and the extension of the RPC coverage up to  $|\eta| = 2.4$ .

3118 The Link Board System is responsible for the processing, the synchronization and the zero-  
3119 suppression the signals coming from the RPC FEBs. The Link Board components have been pro-  
3120 duced between 2006 and 2007 and will be subjected to ageing and failure on a long term scale. An  
3121 upgraded Link Board System will overcome the ageing problems and will allow for a more precise  
3122 timing information to the RPC hits from 25 to 1.5 ns.

3123 In order to develop an improved RPC that fulfills CMS requirements, an extensive R&D program is  
3124 being conducted. The benefits of adding two new RPC layers in the innermost ring of stations 3 and  
3125 4 will be mainly observed in the neutron-induced background reduction and efficiency improvement  
3126 for both trigger and offline reconstruction.

3127 The coverage of the RPC System up to higher pseudo-rapidity  $|\eta| = 2.1$  was part of the original  
3128 CMS TDR. Nevertheless, the expected background rates being higher than the certified rate capabili-  
3129 ty of the present CMS RPCs in that region and the budget being limited, RPCs were restricted to a  
3130 shorter range. Even though the iRPC technology that will equip the extension of the Muon System  
3131 will be different than the current CMS RPC technology, it is necessary to certify the rate capability  
3132 and longevity of the existing detectors as the radiation level will increase together with the increase  
3133 of instantaneous luminosity of the LHC. For this purpose, spare RPC detectors built but not installed  
3134 in CMS have been installed in different irradiation facilities, first of all, to certify the detectors to the

new levels of irradiation they will be subjected to and, finally, to study their ageing and certify their good operation throughout the HL-LHC program.

## 5.1 Testing detectors under extreme conditions

The upgrade from LHC to HL-LHC will increase the peak luminosity from  $10^{34} \text{ cm}^{-2} \text{ s}^{-1}$  to reach  $5 \times 10^{34} \text{ cm}^{-2} \text{ s}^{-1}$ , increasing in the same way the total expected background to which the RPC System will be subjected to. Mainly composed of low energy gammas, neutrons, and electrons and positrons from  $p$ - $p$  collisions, but also of low momentum primary and secondary muons, punch-through hadrons from calorimeters, and particles produced in the interaction of the beams with collimators, the background will mostly affect the regions of CMS that are the closest to the beam line, i.e. the RPC detectors located in the endcaps.

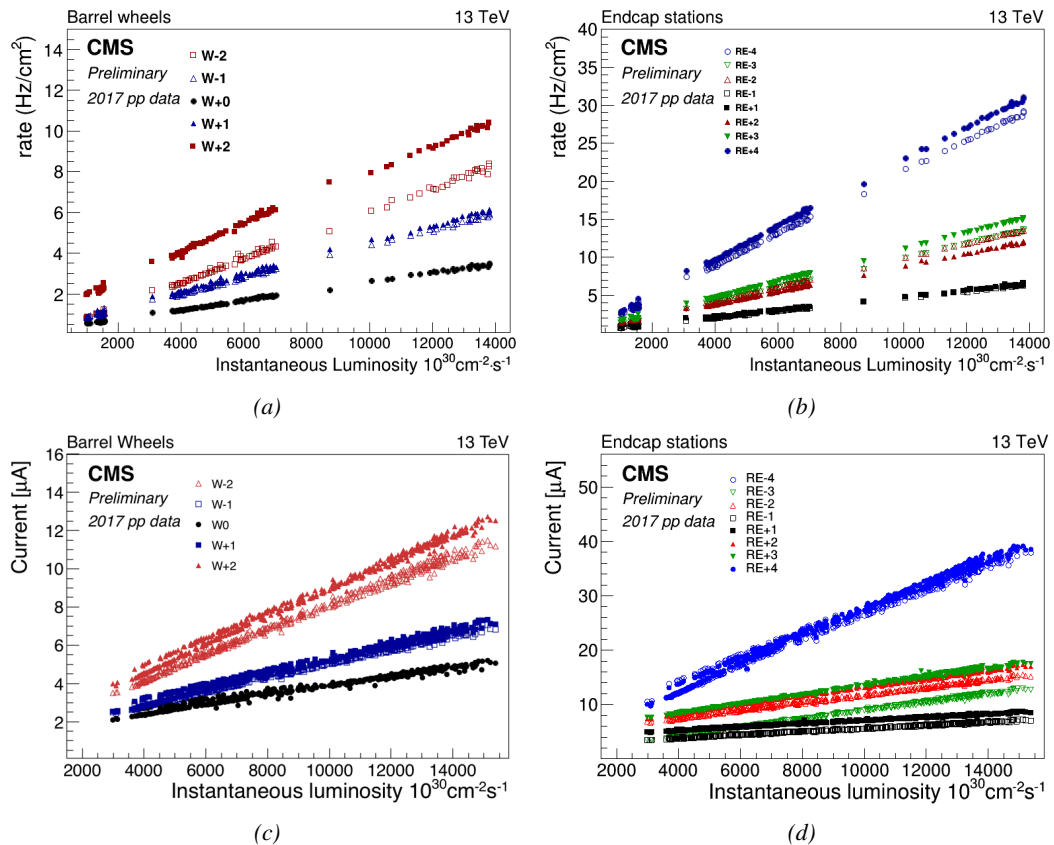


Figure 5.1: Mean RPC Barrel (left column) and Endcap (right column) rate (top row) and current (bottom row) as a function of the instantaneous luminosity as measured in 2017  $p$ - $p$  collision data.

Data collected over 2017, presented through Figure 5.1, allows to study the values of the background rate in all the RPC System. This was achieved thanks to a monitoring of the rates in each RPC rolls, where rolls correspond to the pseudo-rapidity partitioning of the readout electronics, and of the current in each HV channel. A linear dependence is between the mean rate or current with

instantaneous luminosity is showed in selected runs with identical LHC running parameters. In Figure 5.2, a linear extrapolation of the distribution of the background hit rate per unit area as well as the integrated charge is showed at a HL-LHC condition. The maximum rate per unit area in the endcap detectors at HL-LHC conditions is expected to be of the order of  $600 \text{ Hz/cm}^2$  while the charge deposition should exceed  $800 \text{ mC/cm}^2$ . The detectors will then be certified up to an irradiation of  $840 \text{ mC/cm}^2$ . These extrapolations are provided with a required safety factor 3 for the certification study.

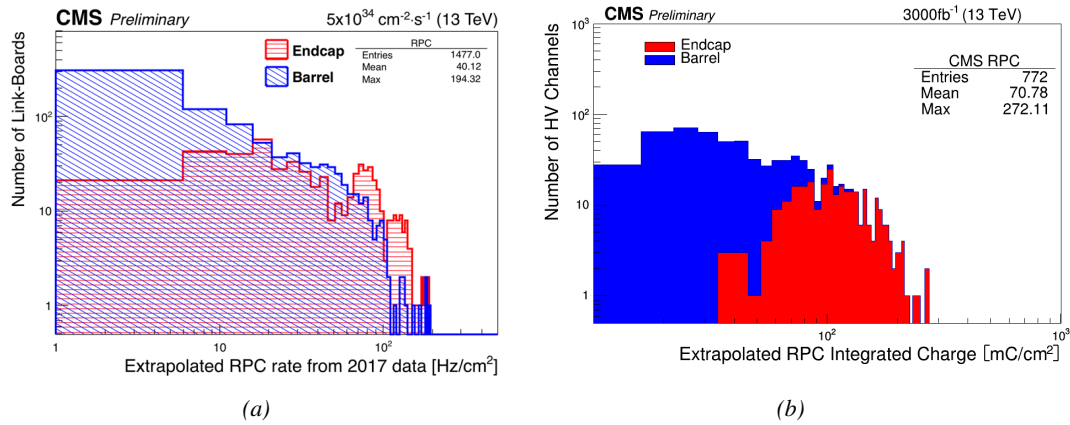


Figure 5.2: Figure 5.2a: The hit rate per region (Barrel, Endcap) is linearly extrapolated to HL-LHC highest instantaneous luminosity ( $5 \times 10^{34} \text{ cm}^{-2} \text{ s}^{-1}$ ) using the rate as a function of instantaneous luminosity recorded by RPCs in 2017 showing a linear dependence. Figure 5.2b: The integrated charge per region (Barrel, Endcap) is extrapolated to HL-LHC integrated luminosity ( $3000 \text{ fb}^{-1}$ ) using the data accumulated in 2016 in every HV channel.

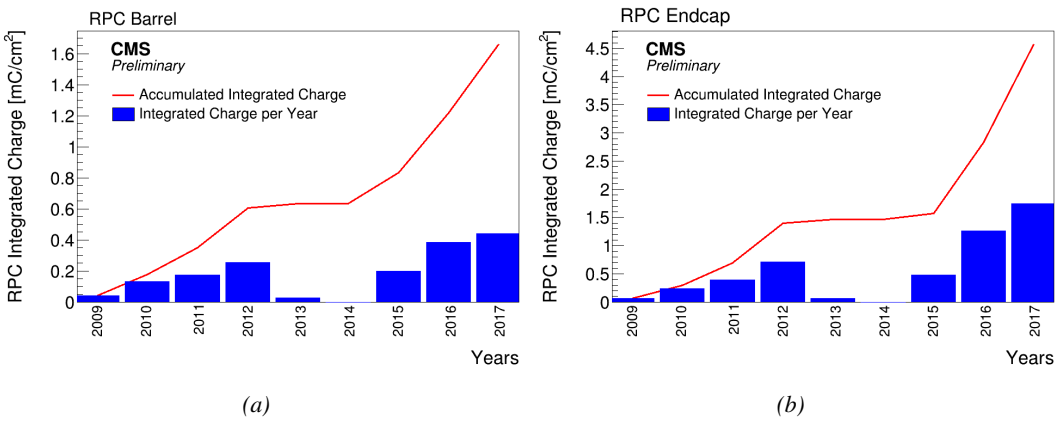


Figure 5.3: CMS RPC mean integrated charge in the Barrel region (Figure 5.3a) and the Endcap region (Figure 5.3b). The integrated charge per year is shown in blue. The red curve shows the evolution of the accumulated integrated charge through time. The blank period in 2013 and 2014 corresponds to LS1. The total integrated charge for the entire operation period (Oct.2009 - Dec.2017) is estimated to be about  $1.66 \text{ mC/cm}^2$  in the Barrel and  $4.58 \text{ mC/cm}^2$  in the Endcap.

In the past, extensive long-term tests were carried out at several gamma and neutron facilities

certifying the detector performance. Both full size and small prototype RPCs have been irradiated with photons up to an integrated charge of  $\sim 0.05 \text{ C/cm}^2$  and  $\sim 0.4 \text{ C/cm}^2$  respectively and were certified for rates reaching  $200 \text{ Hz/cm}^2$  [259, 260]. Since the beginning of Run-I until December 2017, the RPC system provided stable operation and excellent performance and did not show any ageing effects for a maximum integrated charge in a detector of the order of  $0.01 \text{ C/cm}^2$  - the average being of the order of  $2 \text{ mC/cm}^2$  in the Barrel and  $5 \text{ mC/cm}^2$  in the Endcap, closer to the beam line, as can be seen from Figure 5.3 - and a peak luminosity reaching  $1.4 \times 10^{34} \text{ cm}^{-2} \text{ s}^{-1}$  during 2017 data taking period.

To perform the necessary studies on the present CMS RPC detectors, facilities offering the possibility to irradiate the chambers are necessary in order to recreate HL-LHC conditions or stronger and study their performance through time. Such facilities exist at CERN and were exploited to conduct this study. A first series of preliminary studies was conducted in the former gamma facility of CERN (GIF) before its dismantlement. This preliminary study was used as a stepping stone towards the building of a more powerful irradiation fully dedicated to longevity studies of CMS and ATLAS subsystems in the perspective of HL-LHC. The period of preliminary work has also been a key moment in the elaboration and improvement of data acquisition, offline analysis and online monitoring tools that are extensively used in the new gamma irradiation facility.

### 5.1.1 GIF

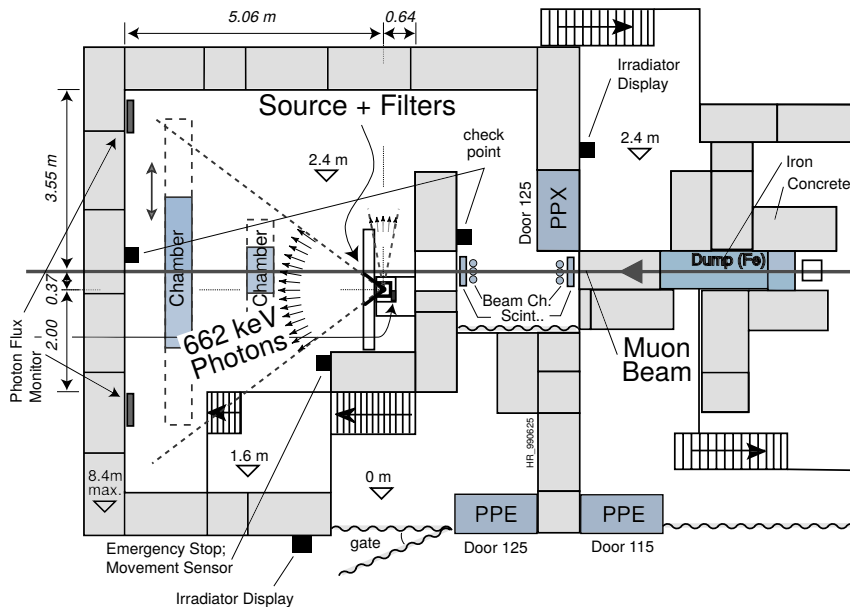


*Figure 5.4: Layout of the test beam zone called X5c GIF at CERN. Photons from the radioactive source produce a sustained high rate of random hits over the whole area. The zone is surrounded by 8 m high and 80 cm thick concrete walls. Access is possible through three entry points. Two access doors for personnel and one large gate for material. A crane allows installation of heavy equipment in the area.*

Located in the SPS West Area at the downstream end of the X5 test beam, the Gamma Irradiation Facility (GIF) was a test area in which particle detectors were exposed to a particle beam in presence of an adjustable gamma background [261]. Its goal was to reproduce background conditions these

detectors would suffer in their operating environment at LHC. GIF layout is showed in Figure 5.4. Gamma photons are produced by a strong  $^{137}\text{Cs}$  source installed in the upstream part of the zone inside a lead container. The source container includes a collimator, designed to irradiate a  $6 \times 6 \text{ m}^2$  area at 5 m maximum to the source. A thin lens-shaped lead filter helps providing with a uniform out-coming flux in a vertical plane, orthogonal to the beam direction. The photon rate is controlled by further lead filters allowing the maximum rate to be limited and to vary within a range of four orders of magnitude. Particle detectors under test are then placed within the pyramidal volume in front of the source, perpendicularly to the beam line in order to profit from the homogeneous photon flux. Adjusting the background flux of photons can then be done by using the filters and choosing the position of the detectors with respect to the source.

As described on Figure 5.5, the  $^{137}\text{Cs}$  source emits a 662 keV photon in 85% of the decays. An activity of 740 GBq was measured on the 5<sup>th</sup> of March 1997. To estimate the strength of the flux in 2014, was considered the nuclear decay through time associated to the Cesium source whose half-life is well known ( $t_{1/2} = (30.05 \pm 0.08) \text{ y}$ ). The GIF tests were done in between the 20<sup>th</sup> and the 31<sup>st</sup> of August 2014, i.e. at a time  $t = (17.47 \pm 0.02) \text{ y}$  resulting in an attenuation of the activity from 740 GBq in 1997 to 494 GBq in 2014.

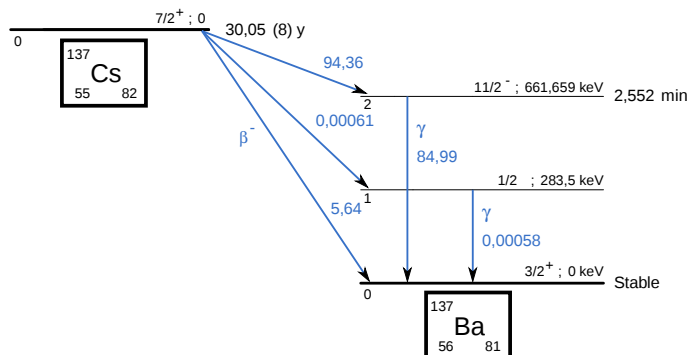


Figure 5.5:  $^{137}\text{Cs}$  decays by  $\beta^-$  emission to the ground state of  $^{137}\text{Ba}$  (BR = 5.64%) and via the 662 keV isomeric level of  $^{137}\text{Ba}$  (BR = 94.36%) whose half-life is 2.55 min.

### 5.1.2 GIF++

The new Gamma Irradiation Facility (GIF++), located in the SPS North Area at the downstream end of the H4 test beam, has replaced its predecessor during LS1 and has been operational since spring 2015 [262]. Like GIF, GIF++ features a  $^{137}\text{Cs}$  source of 662 keV gamma photons, their fluence being controlled with a set of filters of various attenuation factors. The source provides two separated large irradiation areas for testing several full-size muon detectors with homogeneous irradiation, as presented in Figure 5.6.

The source activity was measured to be about 13.5 TBq in March 2016. The photon flux being far greater than HL-LHC expectations, GIF++ provides an excellent facility for accelerated ageing tests of muon detectors. The source is situated in a bunker designed to perform irradiation test along a muon beam line, the muon beam being available during selected periods throughout the year. The H4 beam, providing the area with muons with a maximum momentum of about 150 GeV/c, passes through the GIF++ zone and is used to periodically study the performance of the detectors placed under long term irradiation. Its flux is of  $104 \text{ particles/s/cm}^2$  focused in an area similar to

3208  $10 \times 10 \text{ cm}^2$ . Therefore, with properly adjusted filters, one can simulate the background expected at  
 3209 HL-LHC and study the performance and ageing of muon detectors in HL-LHC environment.

3210

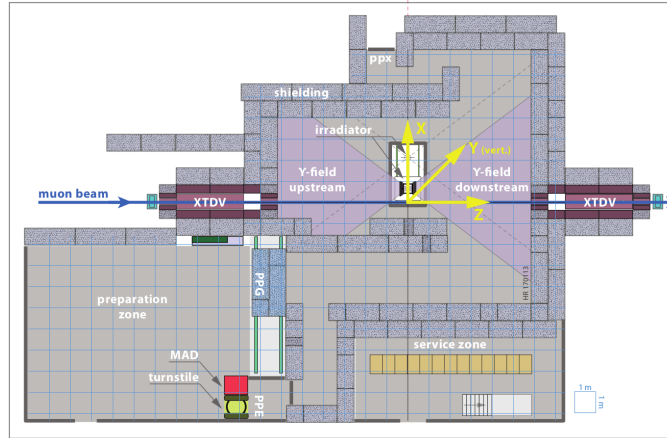


Figure 5.6: Floor plan of the *GIF++* facility. When the facility downstream of the *GIF++* takes electron beam, a beam pipe is installed along the beam line ( $z$ -axis). The irradiator can be displaced laterally (its center moves from  $x = 0.65 \text{ m}$  to  $2.15 \text{ m}$ ), to increase the distance to the beam pipe.

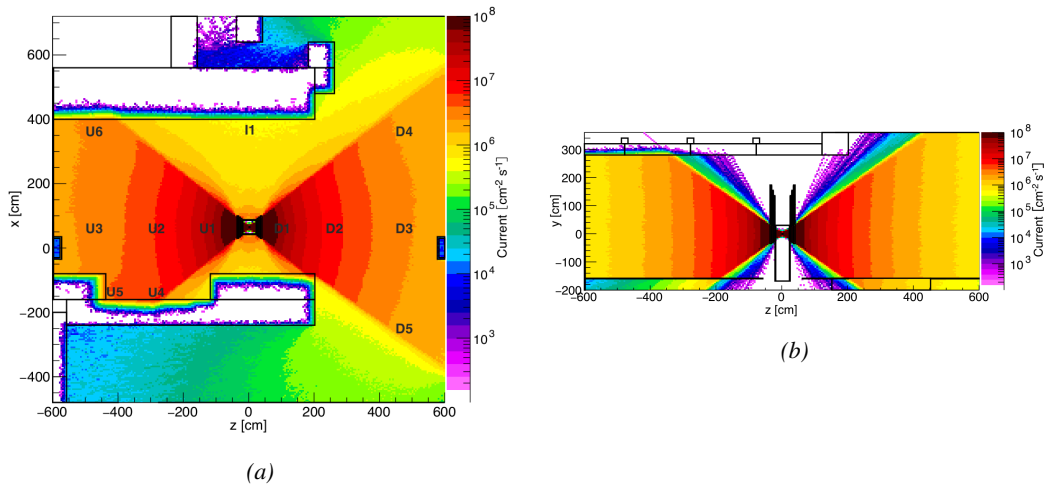


Figure 5.7: Simulated unattenuated current of photons in the  $xz$  plane (Figure 5.7a) and  $yz$  plane (Figure 5.7b) through the source at  $x = 0.65 \text{ m}$  and  $y = 0 \text{ m}$  [263]. With angular correction filters, the current of 662 keV photons is made uniform in  $xy$  planes.

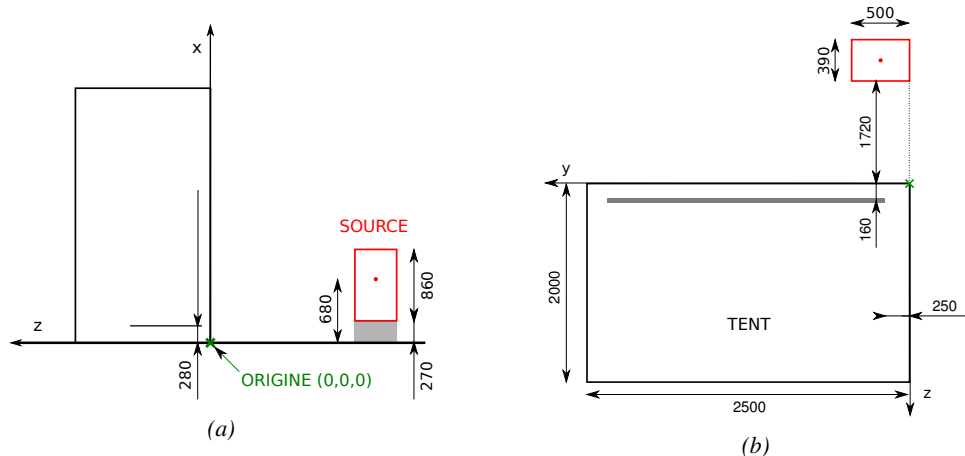
3211 The gamma current as simulated with GEANT4 is presented in Figure 5.7 in which the labels  
 3212 UN, DN, with  $N \in [1 : 5]$  and I1 correspond to the position of different Radiation Monitoring  
 3213 (RADMON) sensors dedicated to measuring the irradiation in the bunker area [263]. According to  
 3214 the simulation results, that agree within 12% to the doses measured with the RADMONs, the RPCs  
 3215 that will be tested in *GIF++* can expect a maximal gamma current of the order of  $2$  to  $5 \times 10^6$

3216  $\text{cm}^{-2} \text{s}^{-1}$  assuming they will always stay in a region in between sensor U5 and the back wall of the  
 3217 upstream area.

## 3218 5.2 Preliminary studies at GIF

### 3219 5.2.1 RPC test setup

3220 During summer 2014, preliminary tests have been conducted in the GIF area on an endcap chamber  
 3221 of type RE4/2 and labeled RE-4-2-BARC-161 produced for the extension of the endcap with a  
 3222 fourth disk in 2013. This chamber has been placed into a trolley covered with a tent. The positions  
 3223 of the RPC inside the tent and of the tent with respect to the source in the bunker are described in  
 3224 Figure 5.8. The goal of the study was to have a preliminary understanding of the rate capability  
 3225 of the present technology used in CMS. It was decided to measure the efficiency of the RPC under  
 3226 irradiation at detecting cosmic muons as, at the time of the tests, the beam not operational anymore.  
 3227 Three different absorber settings were used and compared to the case where the detector was not ir-  
 3228 radiated in order to study the evolution of the performance of the detector with increasing exposition  
 3229 to gamma radiation. First of all, measurements were done with the fully opened source. To complete  
 3230 this preliminary study, the gamma flux has been attenuated by a factor 2, a factor 5 and finally the  
 3231 source was shut down. The efficiency of the RPC at detecting the cosmic muons in coincidence with  
 3232 a cosmic trigger as well as the background rate as seen by the detectors were measured.



3233 *Figure 5.8: Description of the RPC setup. Dimensions are given in mm. A tent containing RPCs is placed  
 3234 at 1720 mm from the source container. The source is situated in the center of the container. RE-4-2-BARC-  
 3235 161 chamber is 160 mm inside the tent. This way, the distance between the source and the chambers plan is  
 3236 2060 mm. Figure 5.8a provides a side view of the setup in the xz plane while Figure 5.8b shows a top view in  
 3237 the yz plane.*

3238 The trigger system was composed of two plastic scintillators and was placed in front of the setup  
 3239 with an inclination of  $10^\circ$  with respect to the detector plane in order to look at cosmic muons. Using  
 3240 this particular trigger layout, showed in Figure 5.9, leads to a cosmic muon hit distribution into the  
 3241 chamber similar to the one of Figure 5.10. Measured without gamma irradiation, two peaks can  
 3242 be seen on the profile of readout partition B, centered on strips 52 and 59. Section 5.2.2 will help  
 3243 us understand that these two peaks are due respectively to forward and backward coming cosmic  
 3244

3239 particles where forward coming particles are first detected by the scintillators and then the RPC  
 3240 while the backward coming muons are first detected in the RPC.



*Figure 5.9: RE-4-2-BARC-161 chamber is inside the tent as described in Figure 5.8. In the top right, the two scintillators used as trigger can be seen. This trigger system has an inclination of 10° relative to horizontal and is placed above half-partition B2 of the RPCs. PMT electronics are shielded thanks to lead blocks placed in order to protect them without stopping photons from going through the scintillators and the chamber.*

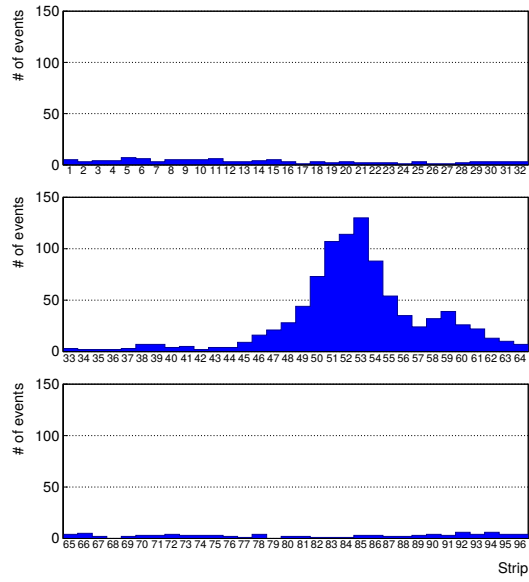


*Figure 5.10: Hit distributions over all three partitions of RE-4-2-BARC-161 chamber is showed. Top, middle and bottom figures respectively correspond to partitions A, B, and C. The profiles show that some events still occur in other half-partitions than B2, which corresponds to strips 49 to 64, in front of which the trigger is placed, contributing to the inefficiency of detection of cosmic muons. In the case of partitions A and C, the very low amount of data can be interpreted as noise. On the other hand, it is clear that a little portion of muons reach the half-partition B1, corresponding to strips 33 to 48.*

3241 The data taking is then performed thanks to a CEAN TDC module of type V1190A [264] to  
 3242 which is connected the digitized output of the RPC Front-End Board, as described in Figure 5.11a  
 3243 and the trigger signal from the telescope. The communication with the computer is performed thanks  
 3244 to a CAEN communication module of type V1718 [265]. In order to control the rates recorded by  
 3245 the detector, the digitized RPC signals are also sent to scalers as described in Figure 5.11b. The  
 3246 C++ DAQ software used in GIF was developed as an early attempt towards the understanding of  
 3247 the CAEN libraries and the data collected by the TDCs was saved into .dat files is analysed with  
 3248 an algorithm computing parameters such as efficiency, hit profile, cluster size, or gamma and noise  
 3249 rates which was developed with C++ as well. Finally, histograms and curves are produced using  
 3250 ROOT.

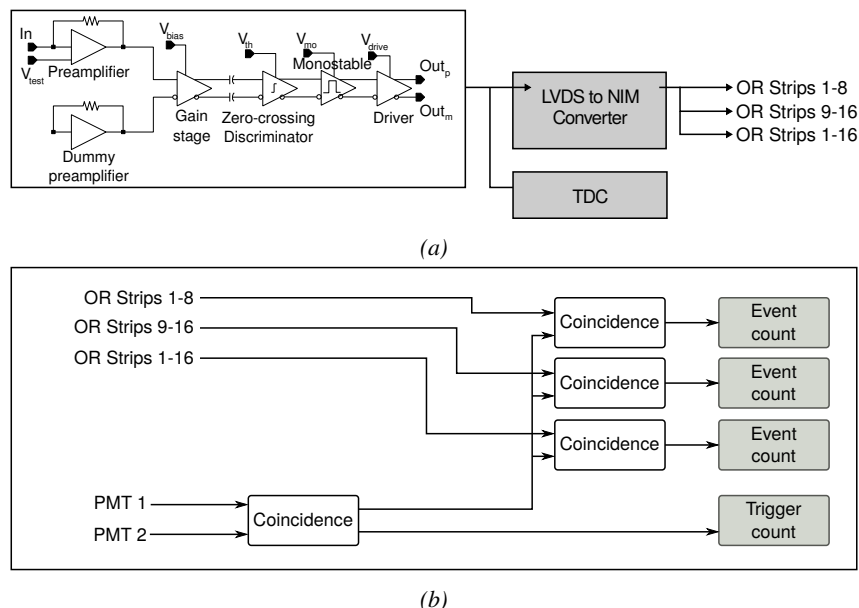


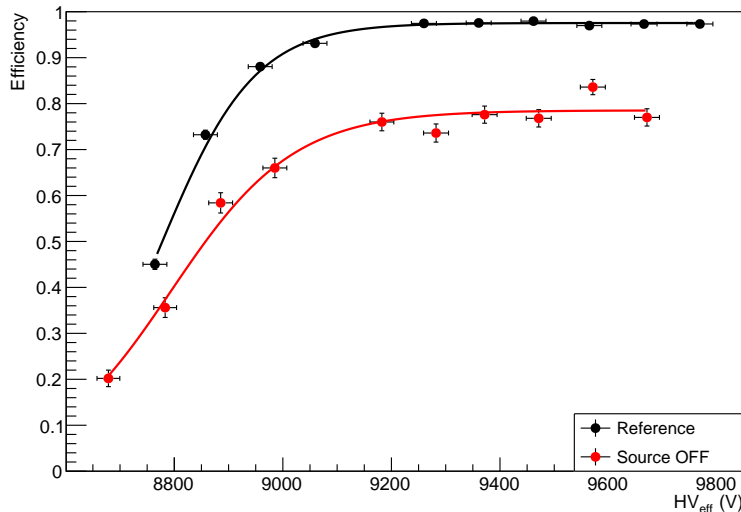
Figure 5.11: Signals from the RPC strips are shaped by the FEE described on Figure 5.11a. Output LVDS signals are then read-out by a TDC module connected to a computer or converted into NIM and sent to scalers. Figure 5.11b describes how these converted signals are put in coincidence with the trigger.

### 3251 5.2.2 Geometrical acceptance of the setup layout to cosmic muons

3252 In order to profit from a constant gamma irradiation, the detectors inside of the GIF bunker need  
 3253 to be placed in a plane orthogonal to the beam line. The muon beam that used to be available was  
 3254 meant to test the performance of detectors under test. This beam being not active anymore, another  
 3255 solution to test detector performance had to be used. Thus, it has been decided to use cosmic muons  
 3256 detected through a telescope composed of two scintillators. Lead blocks were used as shielding to  
 3257 protect the photomultipliers from gammas as can be seen from Figure 5.9.

3258 An inclination of  $\sim 10^\circ$  has been given to the cosmic telescope to maximize the muon flux. A  
 3259 good compromise had to be found between good enough muon flux and narrow enough hit distribution  
 3260 to be sure to contain all the events into only one half partitions as required from the limited  
 3261 available readout hardware. It was then foreseen to detect muons and read them out only from  
 3262 half-partition B2, the last 16 channels of readout partition B (i.e. strips 49 to 64). Nevertheless,

3263 a consequence of the misplaced trigger, that can be seen as a loss of events in half-partition B1  
 3264 (strips 33 to 48) in Figure 5.10, is an inefficiency. The observed inefficiency of approximately 20%  
 3265 highlighted in Figure 5.12 by comparing the performance of chamber RE-4-2-BARC-161 as mea-  
 3266 sured prior to the study at GIF and at GIF without irradiation seems too important, compared to the  
 3267 12.7% of data contained into the first 16 strips observed on Figure 5.10, to only be explained by the  
 3268 geometrical acceptance of the setup itself. Simulations have been conducted to show how the setup  
 3269 brings inefficiency.



3270 *Figure 5.12: Results are derived from data taken on half-partition B2 only. On the 18<sup>th</sup> of June 2014, data  
 has been taken on chamber RE-4-2-BARC-161 at CERN building 904 (Prevessin Site) with cosmic muons  
 providing us a reference efficiency plateau of  $(97.54 \pm 0.15)\%$  represented by a black curve. A similar  
 measurement has been done at GIF on the 21<sup>st</sup> of July with the same chamber giving a plateau of  $(78.52 \pm 0.94)\%$   
 represented by a red curve.*

### 3270 5.2.2.1 Description of the simulation layout

3271 The layout of GIF setup has been reproduced, only roughly using Figure 5.9 due to the lack of  
 3272 measures, and incorporated into a C++ Monte Carlo (MC) simulation to study the geometrical ac-  
 3273 ceptance of the telescope projected onto the readout strips [266]. A 3D view of the simulated layout  
 3274 is given into Figure 5.13. Muons are generated randomly in a horizontal plane located at a height  
 3275 corresponding to the lowest point of the PMTs. This way, the needed size of the plane in order to  
 3276 simulate events happening at very large azimuthal angles (i.e.  $\theta \approx \pi$ ) can be kept relatively small  
 3277 while the total number of muon tracks to propagate is kept relatively small. The muon flux is de-  
 3278 signed to follow the usual  $\cos^2\theta$  distribution for cosmic particles. The goal of the simulation is to  
 3279 look at muons that pass through the telescope composed of the two scintillators and define their dis-  
 3280 tribution onto the RPC read-out plane. During the reconstruction, the read-out plane is then divided  
 3281 into read-out strips and each muon track is assigned to a strip.

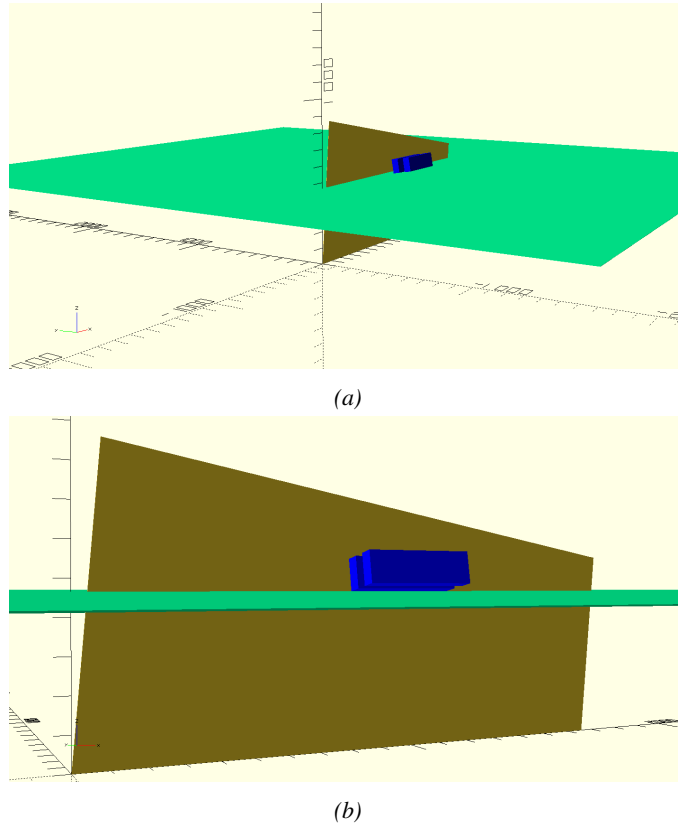


Figure 5.13: Representation of the layout used for the simulations of the test setup. The RPC read-out plane is represented as a yellow trapezoid while the two scintillators as blue cuboids looking at the sky. The green plane corresponds to the muon generation plane within the simulation. Figure 5.8a shows a global view of the simulated setup. Figure 5.8b shows a zoomed view that allows to see the two scintillators as well as the full RPC plane.

### 5.2.2.2 Simulation procedure

*N<sub>μ</sub>* = 10<sup>8</sup> muons are randomly generated inside the muon plane with an azimuthal angle  $\theta$  chosen to follow a  $\cos^2\theta$  distribution. Infinite planes are associated to each surface of the scintillators. Knowing the muon position into the muon generation plane and its direction allows, by assuming that muons travel in a straight line, to compute the intersection of the muon track with these planes. Applying conditions to the limits on the contours of the scintillators' faces then gives an answer to whether or not the muon passed through the scintillators. In the case the muon was not *detected* into both scintillators, the simulation discards the muon and generates a new one.

On the contrary, if the muon is labeled as good, its position within the RPC read-out plane is computed and the corresponding strip, determined through geometrical tests, gets a *hit*. Muon hits fill different histograms whether they are associated to forward or backward coming muons. A discrimination is performed according to their direction components. An ( $x, y, z$ ) position into the generation plane as well as a ( $\theta; \phi$ ) pair are associated to each generated muon providing with information on the direction the track follows. This way, muons satisfying the condition  $0 \leq \phi < \pi$  are labeled as *backward* coming muons while muons satisfying  $\pi \leq \phi < 2\pi$  as *forward* coming

3297 muons.

### 3298 5.2.2.3 Results and limitations

3299 The output from the simulation is given in Figure 5.14 in which the distribution is showed for all  
 3300 muons but also for the separate contributions of forward and backward coming muons. The strip  
 3301 number is here given in a range of 1 to 32 corresponding to the 32 strips contained in each RPC  
 3302 read-out partition, without taking into account the fact that partition B of an RPC correponds, by  
 3303 convention, to strips 33 to 64. Comparing the number of muons recorded respectively in the first 16  
 3304 strips and the in all of the 32 strips of the RPC read-out panel, it can be established than, out of the  
 3305 total amount of muons that have passed through the telescope and reached the RPC, 16.8% where to  
 3306 be detected in the 16 first strip of the read-out plane corresponding to half partition B1. This brings  
 3307 a geometrical inefficiency of the same amount that can then be used to correct the data by scaling up  
 3308 by a factor  $c_{geo} = 1/(1 - 0.168)$  the maximum efficiency measured during data taking.

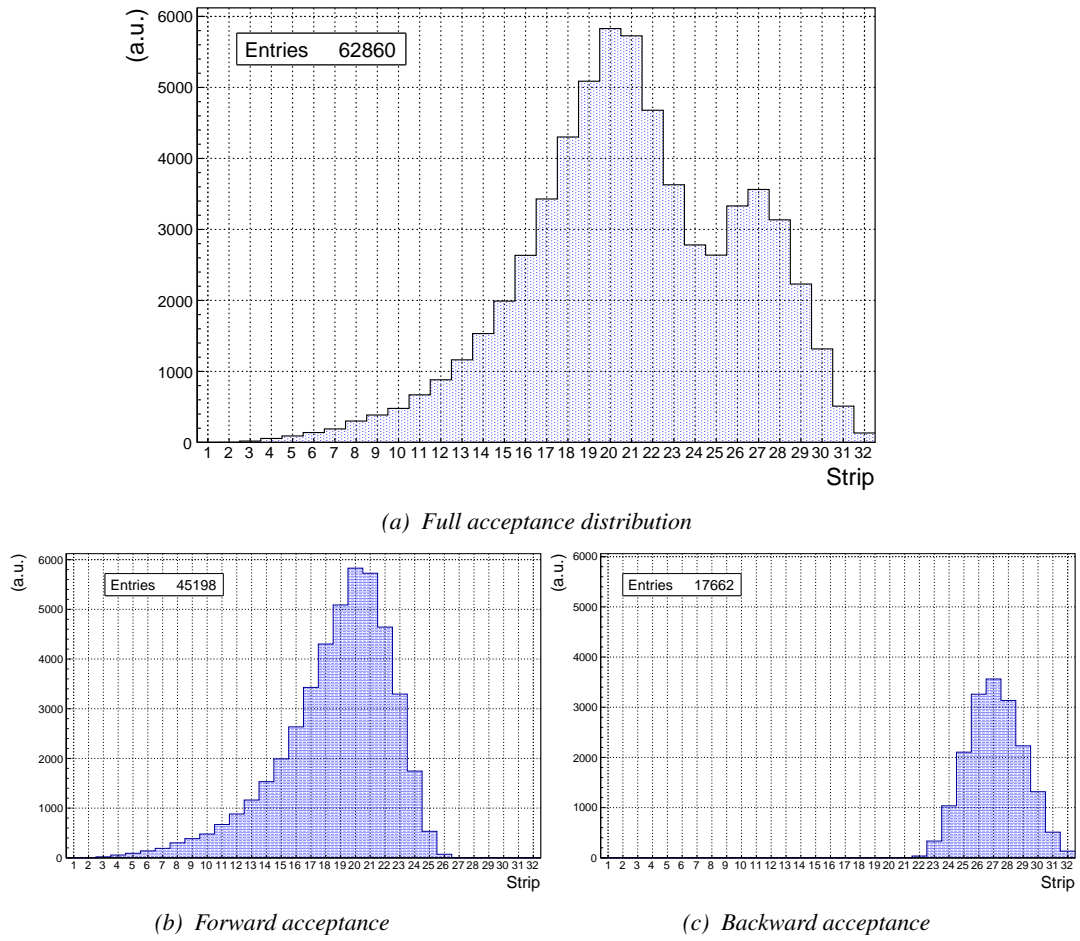


Figure 5.14: Geometrical acceptance distribution as provided by the Monte Carlo simulation.

3309 Nevertheless, it is difficult to evaluate a systematic uncertainty on this geometrical correction for

3310 different reasons. First of all, even though the dimensions of the scintillators and of the RPC are well  
 3311 known, the position of each element of the setup with respect to one another was not measured. It was  
 3312 then necessary, using known dimensions, to extract the positions of each element from Figure 5.9  
 3313 with unknown uncertainty. The inclination is also roughly measured to be  $10^\circ$  and even if the  
 3314 position of each peak, distant in the simulation of 7 strips, tends to confirm this assumption, the  
 3315 geometrical inefficiency would be affected by a variation of the inclination angle. Introducing in the  
 3316 simulation an error of  $\pm 2^\circ$  would lead to a correction factor  $c_{geo} = 1.20^{+0.04}_{-0.03}$  that allows for a good  
 3317 improvement of the efficiency measured in GIF, as can be seen from Figure 5.15. GIF measurement  
 3318 is in agreement with the reference curve within statistical errors.

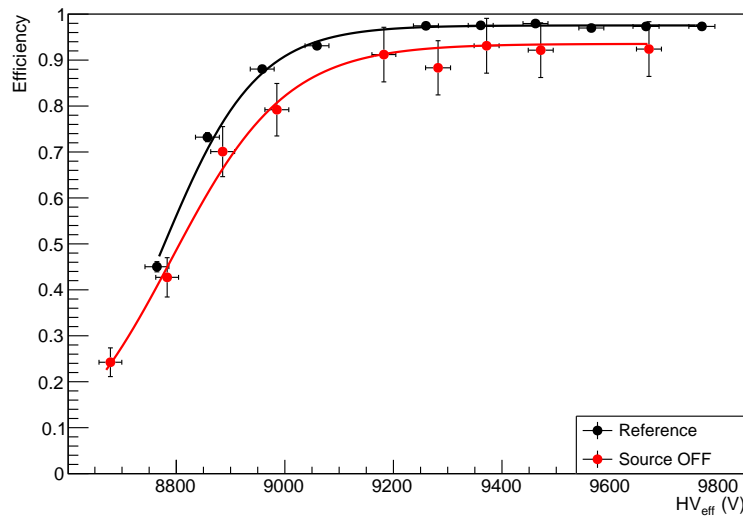
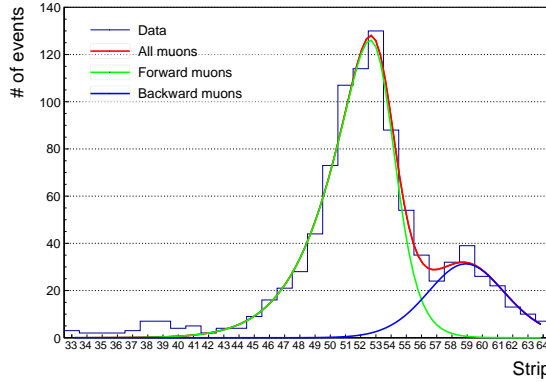


Figure 5.15: Correction of the efficiency without source. The efficiency after correction gets much closer to the Reference measurement performed before the study in GIF by reaching a plateau of  $(93.52 \pm 2.64)\%$ .

3319 Further corrections could be also be brought as it can easily be understood that the distribution  
 3320 showed through Figure 5.14a differs from the measured hit profile showed in Figure 5.10. The  
 3321 contributions of forward and backward muon indicate that 28.1% of the total geometrical acceptance  
 3322 should contribute to detecting backward muons whereas it is measured that the hit profile contains  
 3323 22.0% of backward data only. This estimation of the backward versus forward content in the data was  
 3324 done through a fit using a sum of two skew distribution, one acting on the forward muon peak while  
 3325 the other acts on the backward muon fit, as showed in Figure 5.16. Although a skew distribution  
 3326 lacks physical interpretation, it allows fitting easily such kind of data. A description of a skew  
 3327 distribution, as the product of a gaussian and a sigmoid (Formula 5.1), is given through Formula 5.2.

$$(5.1) \quad g(x) = A_g e^{\frac{-(x-\bar{x})^2}{2\sigma^2}}, \quad s(x) = \frac{A_s}{1 + e^{-\lambda(x-x_i)}}$$

$$(5.2) \quad sk(x) = g(x) \times s(x) = A_{sk} \frac{e^{\frac{-(x-\bar{x})^2}{2\sigma^2}}}{1 + e^{-\lambda(x-x_i)}}$$



*Figure 5.16: Hit distributions over read-out partition B of RE-4-2-BARC-161 chamber together with skew distribution fits corresponding to forward and backward coming muons.*

From the obvious difference in between geometrical simulation and data, it is necessary to realize that the geometrical acceptance and the hit profile are two distinct information. When the geometrical acceptance only provides with the information about what the detector can expect to see in a perfect world where all muons are detected in the exact same way independently from their energy, angle of incidence, fluctuation of the detector gain due to complex avalanche development, thresholds applied on the scintillators and on the RPC FEEs to reduce the noise, the cross-talk and corresponding spread of the induced charge observed on the read-out strips, the hit profile provides the final product of all the previously mentioned contributions and can greatly differ from purely geometrical considerations. A full physics analysis involving softwares such as GEANT would be required to further refine the correction on the measured efficiency at GIF.

### 5.2.3 Photon flux at GIF

In order to understand and evaluate the  $\gamma$  flux in the GIF area, simulations had been conducted at the time GIF was opened for research purposes [261]. Table 5.1 presented in this article gives the  $\gamma$  flux for different distances  $D$  to the source. The simulation was done using GEANT and a Monte Carlo N-Particle (MCNP) transport code, and the flux  $F$  is given with the estimated error from these packages expressed in %.

Nominal ABS	Photon flux $F$ [ $\text{cm}^{-2} \text{s}^{-1}$ ]			
	at $D = 50 \text{ cm}$	at $D = 155 \text{ cm}$	at $D = 300 \text{ cm}$	at $D = 400 \text{ cm}$
1	$0.12 \times 10^8 \pm 0.2\%$	$0.14 \times 10^7 \pm 0.5\%$	$0.45 \times 10^6 \pm 0.5\%$	$0.28 \times 10^6 \pm 0.5\%$
2	$0.68 \times 10^7 \pm 0.3\%$	$0.80 \times 10^6 \pm 0.8\%$	$0.25 \times 10^6 \pm 0.8\%$	$0.16 \times 10^6 \pm 0.6\%$
5	$0.31 \times 10^7 \pm 0.4\%$	$0.36 \times 10^6 \pm 1.2\%$	$0.11 \times 10^6 \pm 1.2\%$	$0.70 \times 10^5 \pm 0.9\%$

*Table 5.1: Total photon flux ( $E\gamma \leq 662 \text{ keV}$ ) with statistical error predicted considering a  $^{137}\text{Cs}$  activity of 740 GBq at different values of the distance  $D$  to the source along the x-axis of irradiation field [261].*

The simulation does not provide with an estimated flux at the level of the RPC under test. First of all, it is necessary to extract the value of the flux from the available data contained in the original paper and then to estimate the flux in 2014 at the time the experimentation took place. In the case of a pointlike source emitting isotropic and homogeneous gamma radiations, the gamma flux  $F$  at a

3348 distance  $D$  from the source with respect to a reference point situated at  $D_0$  where a known flux  $F_0$   
 3349 is measured will be expressed like in Formula 5.3, assuming that the flux decreases as  $1/D^2$ , where  
 3350  $c$  is a fitting factor that can be written from Formula 5.3 as Formula 5.4. Finally, using Equation 5.4  
 3351 and the data of Table 5.1, with  $D_0 = 50$  cm as reference point, Table 5.2 can be built. It is interesting  
 3352 to note that  $c$  for each value of  $D$  doesn't depend on the absorption factor.

$$(5.3) \quad F^{ABS} = F_0^{ABS} \times \left( \frac{cD_0}{D} \right)^2$$

$$(5.4) \quad c = \frac{D}{D_0} \sqrt{\frac{F^{ABS}}{F_0^{ABS}}} , \quad \Delta c = \frac{c}{2} \left( \frac{\Delta F^{ABS}}{F^{ABS}} + \frac{\Delta F_0^{ABS}}{F_0^{ABS}} \right)$$

Nominal ABS	Correction factor $c$		
	at $D = 155$ cm	at $D = 300$ cm	at $D = 400$ cm
1	$1.059 \pm 0.70\%$	$1.162 \pm 0.70\%$	$1.222 \pm 0.70\%$
2	$1.063 \pm 1.10\%$	$1.150 \pm 1.10\%$	$1.227 \pm 0.90\%$
5	$1.056 \pm 1.60\%$	$1.130 \pm 1.60\%$	$1.202 \pm 1.30\%$

Table 5.2: Correction factor  $c$  is computed thanks to Formula 5.4 taking as reference  $D_0 = 50$  cm and the associated flux  $F_0^{ABS}$  for each absorption factor available in table 5.1.

3353 For the range of  $D/D_0$  values available, it is possible to use a simple linear fit to get the evolution  
 3354 of  $c$  that can be expressed as  $c(D/D_0) = aD/D_0 + b$ . Using Formula 5.5, but neglecting the  
 3355 uncertainty on  $D$  that will only be used when extrapolating the values for the position of the RPC  
 3356 under test whose position is not perfectly known, the results showed in Figure 5.17 is obtained.  
 3357 Figure 5.17b confirms that using only a linear fit to extract  $c$  is enough as the evolution of the rate  
 3358 that can be obtained superimposes well on the simulation points.

$$(5.5) \quad F^{ABS} = F_0^{ABS} \left( a + \frac{bD_0}{D} \right)^2 , \quad \Delta F^{ABS} = F^{ABS} \left[ \frac{\Delta F_0^{ABS}}{F_0^{ABS}} + 2 \frac{\Delta a + \Delta b \frac{D_0}{D} + \Delta D \frac{bD_0}{D^2}}{a + \frac{bD_0}{D}} \right]$$

3359 In the context of the 2014 GIF tests, the RPC read-out plane is located at a distance  $D = 206$  cm  
 3360 from the source. Moreover, to estimate the strength of the flux in 2014, it is necessary to consider the  
 3361 nuclear decay through time associated to the Cesium source whose half-life is well known ( $t_{1/2} =$   
 3362  $(30.05 \pm 0.08)$  y). The very first source activity measurement has been done on the 5<sup>th</sup> of March  
 3363 1997 while the GIF tests were done in between the 20<sup>th</sup> and the 31<sup>th</sup> of August 2014, i.e. at a time  
 3364  $t = (17.47 \pm 0.02)$  y resulting in an attenuation of the activity from 740 GBq in 1997 to 494 GBq in  
 3365 2014. All the needed information to extrapolate the expected flux through the detector at the moment  
 3366 of GIF preliminary tests has now been assembled, leading to Table 5.3. By assuming a sensitivity of  
 3367 the RPC to  $\gamma$  of  $2 \times 10^{-3}$ , the order of magnitude of the expected hit rate per unit area would be of  
 3368 the order of the kHz for the fully opened source, as reported in the last column of the table.

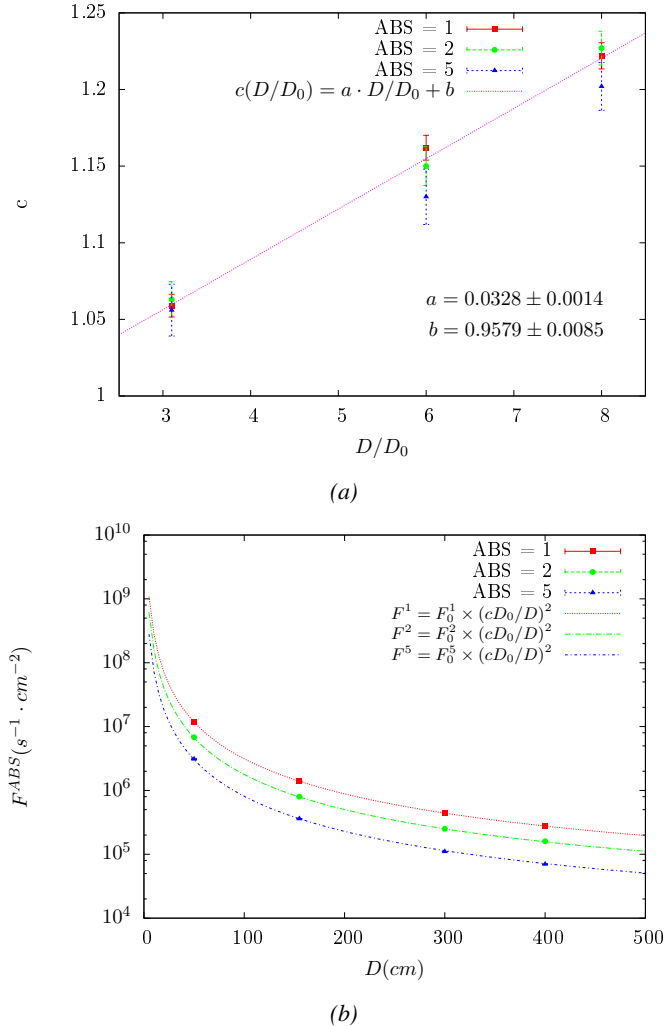


Figure 5.17: Figure 5.17a shows the linear approximation fit performed on data extracted from table 5.2. Figure 5.17b shows a comparison of Formula 5.5 with the simulated flux using  $a$  and  $b$  given in figure 5.17a in formulae 5.3 and the reference value  $D_0 = 50\text{ cm}$  and the associated flux for each absorption factor  $F_0^{ABS}$  from table 5.1.

Nominal ABS	Photon flux $F$ [ $\text{cm}^{-2} \text{s}^{-1}$ ]			Rate [ $\text{Hz}/\text{cm}^2$ ] at $D^{2014} = 206\text{ cm}$
	at $D_0^{97} = 50\text{ cm}$	at $D^{97} = 206\text{ cm}$	at $D^{2014} = 206\text{ cm}$	
1	$0.12 \times 10^8 \pm 0.2\%$	$0.84 \times 10^6 \pm 1.2\%$	$0.56 \times 10^6 \pm 1.2\%$	$1129 \pm 14$
2	$0.68 \times 10^7 \pm 0.3\%$	$0.48 \times 10^6 \pm 1.2\%$	$0.32 \times 10^6 \pm 1.2\%$	$640 \pm 8$
5	$0.31 \times 10^7 \pm 0.4\%$	$0.22 \times 10^6 \pm 1.2\%$	$0.15 \times 10^6 \pm 1.2\%$	$292 \pm 4$

Table 5.3: The data at  $D_0$  in 1997 is taken from [261]. Using Formula 5.5, the flux at  $D$ , including an error of 1 cm, can be estimated in 1997. Then, taking into account the attenuation of the source activity, the flux at  $D$  can be estimated at the time of the tests in GIF in 2014. Assuming a sensitivity of the RPC to  $\gamma$  s =  $2 \times 10^{-3}$ , an estimation of the hit rate per unit area is obtained.

3369 The goal of the study will be to have a good measurement of the intrinsic performance without  
 3370 source irradiation. Then, taking profit of the two working absorbers, at absorption factors 5 (300 Hz)  
 3371 and 2 ( $\sim 600$  Hz) the goal will be to show that the detectors fulfill the performance certification of  
 3372 CMS RPCs. Finally, a first idea of the performance of the detectors at higher backgrounds will be  
 3373 provided with absorption factor 1 (no absorption and  $>1$  kHz)).

### 3374 5.2.4 Results and discussions

3375 The data taking at GIF has been conducted in between the 21<sup>st</sup> and the 31<sup>st</sup> of August, 2014. Data  
 3376 has been collected with source both ON and OFF using three different absorber settings (ABS 5, 2  
 3377 and 1) in order to vary the irradiation on the RPC. For each source setting, two HV scans have been  
 3378 performed with two different trigger settings. During a first scan the trigger sent to the TDC module  
 3379 was the coincidence of the two scintillators composing the telescope while during a second scan the  
 3380 trigger was a pulse coming from a pulse generator in order to measure the noise or gamma rate seen  
 3381 by the chamber. Indeed, using a pulse allows to trigger at moments not linked to any physical event  
 3382 and, hence, to obtain a *RANDOM* trigger on noise and gamma events to measure the associated rates,  
 3383 the probability to have a pulse in coincidence with a cosmic muon being negligible.

3384 From the cosmic trigger scans, a summary of the efficiencies and corresponding cluster sizes is  
 3385 showed in Figure 5.18. The efficiency curves with Source ON show a shift with respect to the case  
 3386 without irradiation. With ABS 5, the general shape of the efficiency curve stays unchanged whereas  
 3387 a clear alteration of the performance is observed at ABS 2 and ABS 1. From the cluster size results,  
 3388 a reduction of the cluster size under irradiation can be observed at equivalent efficiency. This effect  
 3389 can be due to the perturbation of the electric field by the strong rate of gamma particles starting  
 3390 avalanches in the gas volume of the detector.

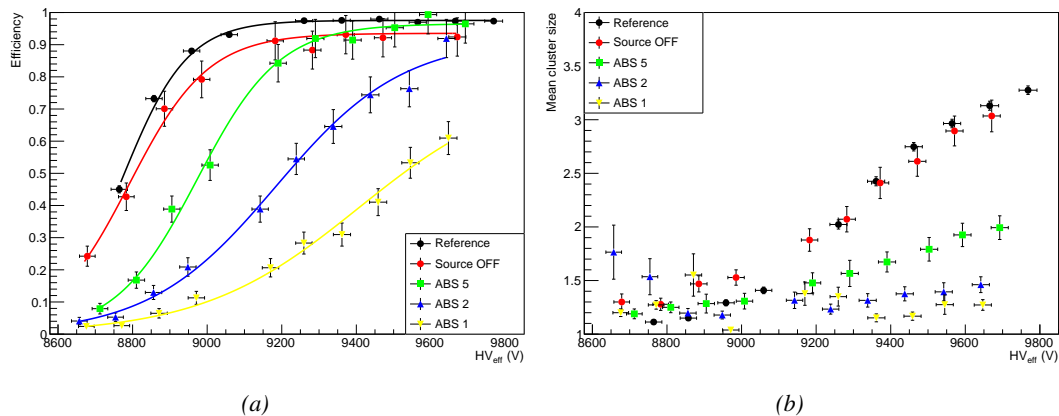
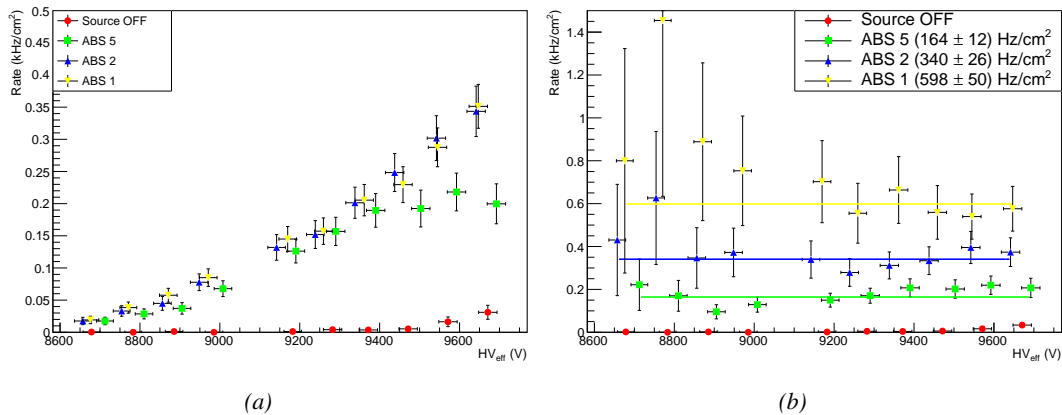


Figure 5.18: Efficiency (Figure 5.18a) and cluster size (Figure 5.18b) of chamber RE-4-2-BARC-161 measured at GIF with Source OFF (red) and Source ON using different absorber settings: ABS 5 (green), ABS 2 (blue) and ABS 1 (yellow). The results are compared to the Reference values obtained with cosmics.

3391 It is necessary to study the evolution of the performance of the chamber with the increasing rate.  
 3392 In Figure 5.19a, the noise rate when the source is OFF stays low but increases at voltages above  
 3393 9500 V. The rise of the noise rate in the detector can be related to the increased streamer probability  
 3394 observed with such a large electric field. The rates with source ON measured at GIF all show a

similar behaviour until a high voltage of approximately 9400 V at which the rate of ABS 5 saturates, corresponding to the chamber reaching full efficiency. It is important to note that, even though the rates look similar independently from the gamma flux, relatively to the efficiency of the chamber, the rate actually increases with increasing flux at equivalent efficiency. A rough way to measure the rate effectively observed by the detector for each source setting would be to normalize the measured rates to the efficiency of the detector. This exercise was done with Figure 5.19b from which constant fits where done on Source ON data in order to extract the rate the chamber was subjected to.



*Figure 5.19: Rates in chamber RE-4-2-BARC-161 measured at GIF with Source OFF (red) and Source ON using different absorber settings: ABS 5 (green), ABS 2 (blue) and ABS 1 (yellow). On Figure 5.19b, the rates of Figure 5.19a were normalized to the measured efficiency, and constant fits are performed on Source ON data showing the gamma rate in the chamber.*

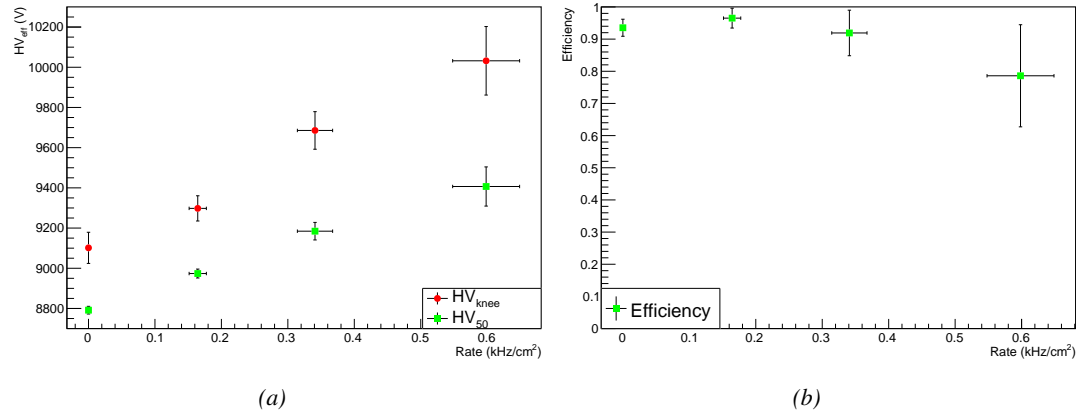


*Figure 5.20: Evolution of the voltages at half maximum and at 95% of the maximum efficiency (Figure 5.20a), and of the maximum efficiency (Figure 5.20b) as a function of the rate in chamber RE-4-2-BARC-161. The data is extracted from the fits in Figures 5.18a and 5.19b.*

The results need to be taken with care as a better estimation of the rate would have been to push the detector towards higher voltages to reach the efficiency plateau for each absorber configuration

and only then extract the measured rate at working voltage, defined as in Formula 4.25. Nevertheless, using this method to estimate the rate to which the chamber is subjected, it is possible to look at the evolution of the  $HV_{50}$  and  $HV_{knee}$  (the working voltage being defined to be 150 V above the knee in the endcap) as a function of the increasing rate as showed in Figure 5.20. The results from GIF suggest that at a rate of 600 Hz/cm<sup>2</sup> the working voltage of the chamber is increased by a thousand V while the efficiency is reduced to approximately 80%, although the result still is consistent with an efficiency better than 90% due to the large error on the measurement. Moreover, it is likely that the rates obtained through fitting on normalized values is underestimated. Indeed, monitoring the current in the three gaps composing a CMS endcap RPC (Figure 5.21) while knowing the rate, the charge deposition per avalanche  $q_\gamma$  can be computed.

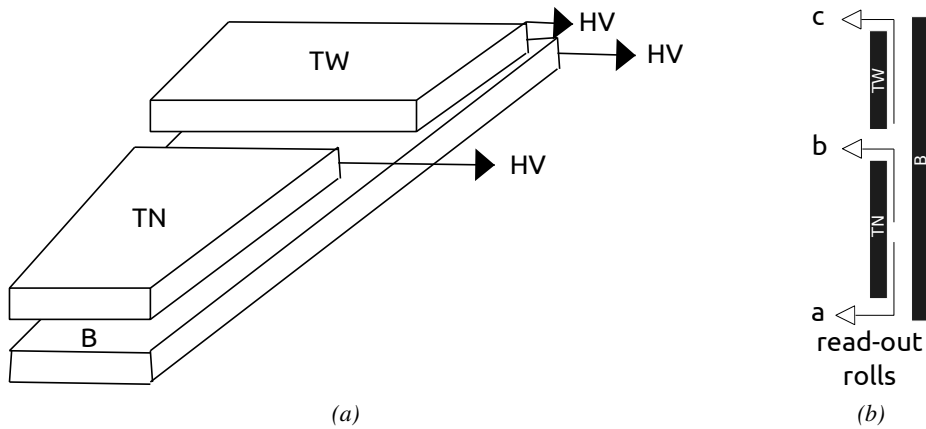
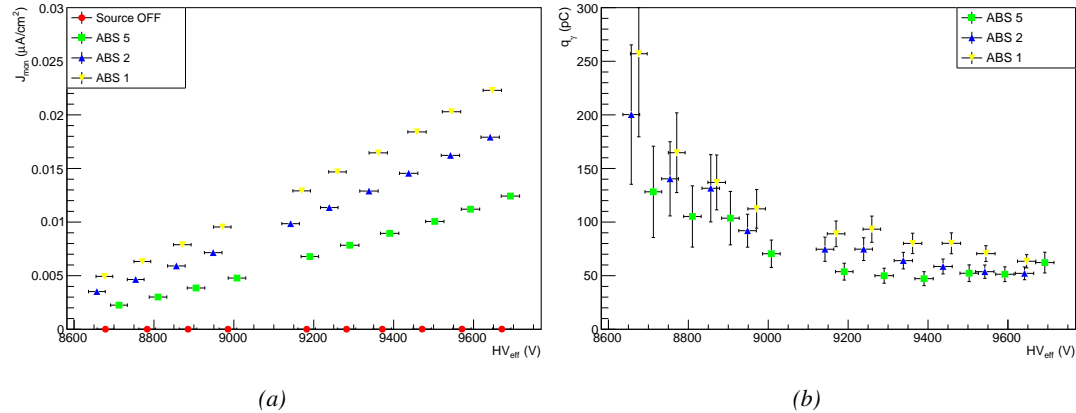


Figure 5.21: Presentation of a double-gap endcap RPC with its three RPC gaps. Due to the partitioning of the read-out strips into three rolls, the TOP layer of gap is divided into two gaps: TOP NARROW (TN) and TOP WIDE (TW). The BOTTOM (B) only consists in one gap.

A charge is expressed in C which is consistent with a current density, expressed in A/cm<sup>2</sup>, divided by a rate per unit area, expressed in Hz/cm<sup>2</sup>. The current driven by the RPC is assumed to be due to the irradiation, hence, to the avalanches developing in the gas volume due to the photons of the Cesium source. On the other hand, the rate is supposed to be a measure of the number of photons interacting with the detector. This way, it comes that the charge deposition per avalanche is expressed like  $q_\gamma = J_{mon}/R_\gamma$ ,  $J_{mon}$  being the monitored current density and  $R_\gamma$  the measured  $\gamma$  rate. The current density is computed as the sum of the current density measured on the top gap layer and of which measured in the bottom gap layer,  $J_{mon} = (I_{mon}^{TW} + I_{mon}^{TN})/(A_{TW} + A_{TN}) + I_{mon}^B/A_B$ ,  $A_{B,TN,TW}$  being the active area and  $I_{mon}^{B,TN,TW}$  the monitored currents of the gaps. According to Figure 5.22, the charge deposition per avalanche consistently converges to a value of the order of 50 pC for each absorber setting which corresponds to a value more than twice greater than what reported in literature for CMS detectors [267, 268] indicating that the rates could have been wrongly evaluated during the short study performed at GIF. An increase of the  $\gamma$  rate by a factor 2 would be consistent with the expected rates calculated in Table 5.3, assuming the sensitivity to  $\gamma$  to be of the order of  $2 \times 10^{-3}$ .



*Figure 5.22: Current density and charge deposition per gamma avalanche, defined as the current density normalized to the measured rate taken from Figure 5.19a as a function of the effective high voltage in chamber RE-4-2-BARC-161 measured at GIF with Source ON using different absorber settings: ABS 5 (green), ABS 2 (blue) and ABS 1 (yellow).*

Overall, working at GIF has been a rewarding experience as it offered CMS RPC R&D team the possibility to start developing the necessary skills and tools that would become the core of GIF++ experiment. The quality of the results can be argued both due to the little robustness of the experimental setup and the lack of available statistics to draw conclusions from, bringing large errors on the final result. The confrontation of the data to known results pointed to a failure in correctly measuring the  $\gamma$  rate at working voltage and, hence, to an overestimation of the charge per avalanche and of the drift of working voltage with increasing rate. Nevertheless, the prototypes of DAQ and offline analysis tools proved to be reliable.

### 5.3 Longevity tests at GIF++

#### 5.3.1 Selection and characterization of CMS RPCs for longevity at GIF++

First proposed in 2009 [269], the new Gamma Irradiation Facility of CERN was thought in the perspective of future upgrades of LHC that would bring detectors to be operated in a high irradiation environment. GIF++ would thus provide all LHC R&D teams working on behalf of the different LHC experiment with a facility to perform longevity studies using a very intense Cesium gamma source.

In the specific case of CMS RPC, the longevity studies imply a constant irradiation of selected detectors in order to accumulate a charge equivalent to what is expected during HL-LHC, i.e. a charge of  $0.8 \text{ C}/\text{cm}^2$  according to Figure 5.2 including a safety factor 3, while other detectors are left non-irradiated to be used as references. Throughout the irradiation campaign, the performance of the irradiated and reference detectors will be periodically probed using the high intensity H4 muon beam. Dedicated test beam periods will be used to measure the efficiency and  $\gamma$  rate at the level of the detectors with different source absorber settings to have access to the rate capability of CMS RPCs, that needs to be certified above  $600 \text{ Hz}/\text{cm}^2$ , and to identify signs of ageing in the case the performance of the irradiated detectors diverges from those of the reference detectors with increasing accumulated charge. Other than the performance of the detectors, signs of ageing

3454 could come from increasing dark current that would be related to local ageing of the electrodes  
 3455 triggered by the hydrofluoric acid ( $HF$ ) production in an irradiated environment.  $HF$  is produced  
 3456 by the decomposition of  $C_2H_2F_4$  molecules during the charge multiplication process and leads to  
 3457 increased dark current and noise in Bakelite RPCs treated with linseed oil. This effect is strongly  
 3458 reinforced by the presence of UV photons [270, 271]. A close monitoring of the current driven by  
 3459 the detectors will then be necessary as well as dedicated periodical electrode resistivity measurement  
 3460 and chromatography measurement on the gas exhaust.

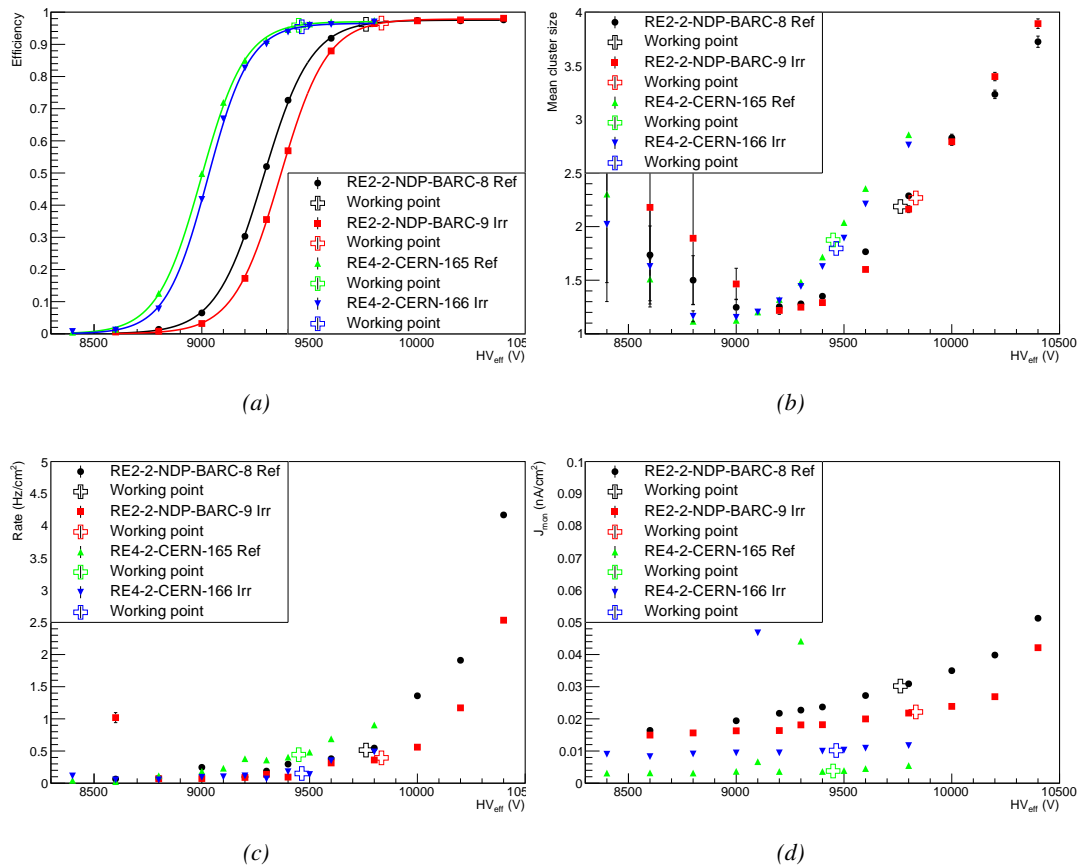


Figure 5.23: Characterization of CMS RPC detectors foreseen to be used at Gif++ for longevity studies of the present system. Using cosmic muons, efficiency (Figure 5.23a) and cluster size (Figure 5.23b) were measured as well as noise rate (Figure 5.23c) and current density (Figure 5.23d). For each detector, the working voltage, defined as in Formula 4.25, was extracted from sigmoid fits performed in Figure 5.23a and the values of efficiency, cluster size, noise rate and current density at this voltage are reported using open crosses.

3461 As the maximum background is found in the endcap, the choice naturally was made to focus  
 3462 the Gif++ longevity studies on endcap chambers. Most of the RPC system was installed in 2007.  
 3463 Nevertheless, the large chambers in the fourth endcap (RE4/2 and RE4/3) have been installed during  
 3464 LS1 in 2014. The Bakelite of these two different productions having different properties, four spare  
 3465 chambers of the present system were selected. From the original CMS RPC system, two RE2/2  
 3466 spares were selected along two RE4/2 spares from the newest detectors. Having two chambers of

3467 each type allows to always keep one of them non-irradiated as reference. Due to the limited gas  
 3468 flow in GIF++, the RE4 chamber remained non-irradiated until end of November 2016 where the  
 3469 longevity studies could finally be started on those chambers.

3470 The performance of the chambers prior to the start of the longevity campaign has been char-  
 3471 acterized in Ghent before being shipped to CERN to be installed in GIF++. The results of the  
 3472 characterization are showed in Figure 5.23 and summarized in Table 5.4. A clear difference in per-  
 3473 formance for both types of chambers is observed as the working voltages of the newest chambers,  
 3474 of type RE4, are 300 to 400 V lower to the older chambers indicating that the gap thickness of RE4  
 3475 detectors could be thinner. This conclusion could as well be supported by the lower cluster size at  
 3476 working voltages that also are smaller in RE4 chambers. Even though the measured currents are  
 3477 low, RE4 detectors draw less current without irradiation than RE2 detectors pointing to a difference  
 3478 in electrode resistivity that were produced at different moments. Efficiency and noise rate levels are  
 3479 of the same order of magnitude for both type of RPCs.

RPC	RE2-2-NPD-BARC-08	RE2-2-NPD-BARC-09	RE4-2-CERN-165	RE4-2-CERN-166
Used as	Reference	Irradiation	Reference	Irradiation
$HV_{WP}$ [V]	(9762 ± 6)	(9833 ± 6)	(9449 ± 5)	(9464 ± 5)
Efficiency at WP	(96.2 ± 0.3)	(96.6 ± 0.3)	(95.9 ± 0.3)	(95.5 ± 0.3)
Cluster size at WP	(2.19 ± 0.04)	(2.27 ± 0.05)	(1.88 ± 0.04)	(1.80 ± 0.04)
Noise at WP [Hz/cm <sup>2</sup> ]	(0.51 ± 0.01)	(0.39 ± 0.01)	(0.44 ± 0.00)	(0.15 ± 0.01)
$J^{WP}$ [pA/cm <sup>2</sup> ]	(30.1 ± 0.1)	(22.2 ± 0.1)	(3.8 ± 0.0)	(10.2 ± 0.0)

Table 5.4: Summary of the characterization measurement performed in Ghent on CMS RPC detectors foreseen to be used at GIF++ for longevity studies of the present system. For each detector, the working voltage, defined as in Formula 4.25, was extracted from sigmoid fits performed in Figure 5.23a and the values of efficiency, cluster size, noise rate and current density at this voltage are reported.

### 5.3.2 RPC test setup

3481 For an easy manipulation of the detectors, a trolley with a structure containing slots in which the  
 3482 RPCs can be slid vertically and referred to as T1 was used. In this position, each chamber is in a  
 3483 plane perpendicular to the beam line and the source flux as can be seen through Figure 5.24, receiving  
 3484 a uniform irradiation. Moreover the trolley allows for easy movement of the system. Indeed, the  
 3485 position of the trolley varies according to the period of the year.

3486 During the dedicated test beam periods during which GIF++ longevity experiments are in control  
 3487 of the muon beam, the trolley is placed in the upstream region of the bunker, in the beam line, as  
 3488 described through Figure 5.24a. The CMS RPC detectors are the ones being farther away from the  
 3489 source on this side of the source as other detectors need to be certified at higher background rates. An  
 3490 additional trolley, reffered to as T3, containing iRPCs and tracking RPCs is placed in between the  
 3491 source and the trolley containing present CMS RPCs. Indeed, iRPCs need to be certified at higher  
 3492 rates and thus need to be placed closer to the source to receive a stronger irradiation using the same  
 3493 absorber settings. The space on T1 being limited, the tracking RPCs used for extra offline informa-  
 3494 tion during the analysis are placed on the same trolley than iRPCs and are kept at full efficiency at  
 3495 all time to reconstruct muon tracks in correlate them with hits recorded in T1 chambers. The beam  
 3496 trigger system is composed of 2 scintillators placed outside on each side of the bunker and of a third  
 3497 scintillator placed in between T1 and the wall of the bunker along the beam line.

3498 However, most of the year, T1 is placed in the so called *ageing position* corresponding to the

furthest position from the source outside of the beam line, which needs to stay clear during periods where GIF++ doesn't have the control of the beam so that a beam tube can be installed through the bunker, as can be seen in Figure 5.24b. The reason for placing the chambers as far as possible from the source comes from the too high irradiation delivered by the source during the irradiation periods where all the other experiment having placed detectors into the bunker requires to integrate as much charge as possible. Hence, the source is operated with any absorbers. On the contrary, during the test beam periods, all the groups working in GIF++ are interested in operating the source using various absorber settings to study the performance of their detectors under different irradiation conditions. The time spent with a source fully opened and during which the RPCs of T1 are kept at a standby voltage of 6500 V much lower than what necessary to grow avalanches in the gas is then small compared to the time spent with other source settings and during which data can be taken.

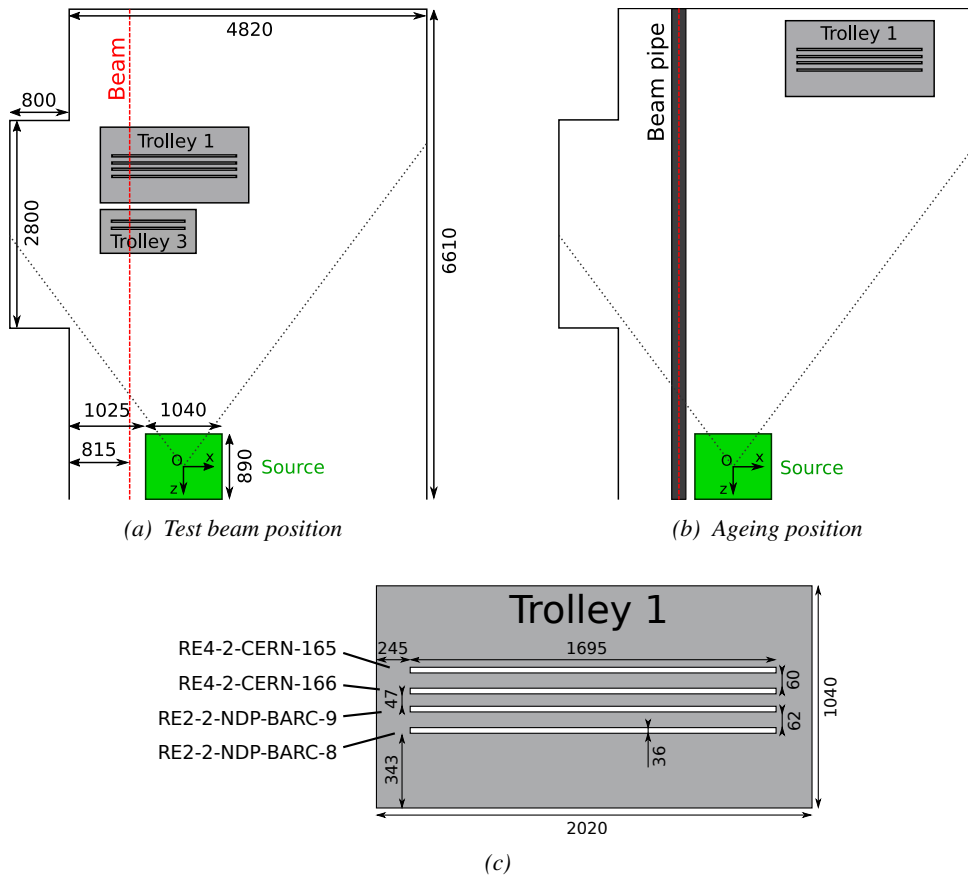


Figure 5.24: CMS RPC setup inside of GIF++ bunker during test beam (Figure 5.24a) and ageing periods (Figure 5.24b). The space in between the RPCs and the source is usually used by other detectors while the space in between T1 and the upstream wall is not filled. Due to the presence of the beam pipe, the trolley is moved away from the beam line during irradiation periods and placed farther away from the source for less intense irradiation. The position of the trolley can vary due to the use of the space by other setups and is then not exact. In the contrary, the position of the chambers in the trolley is fixed and given in Figure 5.24c.

From the bunker area, the detectors are connected to the service area, visible in Figure 5.6, through the wooden floor thanks to long cable. The service area hosts all the high and low voltage

power supplies, the TDCs and computers used for data acquisition and preliminary offline analysis used to fill the Detector Control Software (DCS) webpage, referred to as WebDCS, with Data Quality Monitoring (DQM) histograms useful for the shifters on duty in the control room located farther in the building, away from the beam lines, as well as the gas system required for the gaseous detectors installed in GIF++ [272]. The detectors read-out is, as in the case of GIF, connected to V1190A VME TDCs communicating with the DAQ computer thanks to a V1718 VME bridge manufactured by CAEN. Moreover, a constant monitoring of all the environmental parameters, in different points of the bunker area, gas parameters, to control its composition, temperature and pressure, and of the voltages and currents delivered by the power supplies is performed and displayed on the homepage of the WebDCS interface.

### 5.3.3 GIF++ data flow

At GIF++, the CMS RPC R&D experiment collects different types of data coming from the detectors monitored parameters, such as voltage and currents, the gas, source, and environmental parameters, and, of course, the TDC data in which are collected the actual muon and gamma physics. These different data sources compose three different data flows as presented in Figure 5.25.

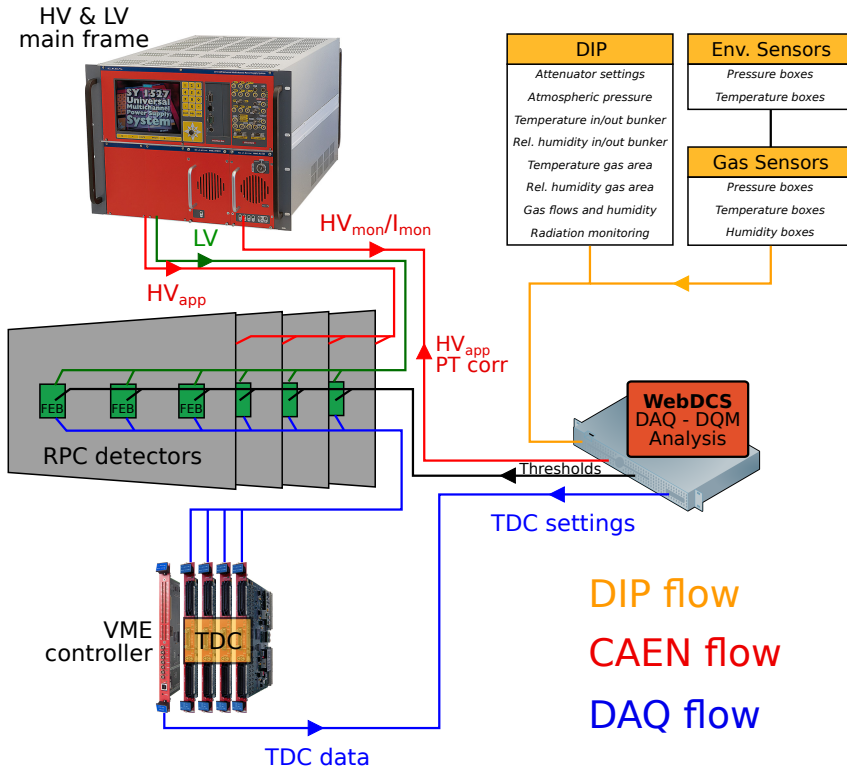


Figure 5.25: Visualisation of the main data flows in GIF++. The yellow flow lines correspond to the DIP flow used for source, environmental and gas information. The red flow lines are for the CAEN flow through which the WebDCS communicates the voltages to be applied on the detectors using pressure and temperature information and retrieves the monitored voltages and currents. Finally, the blue flow lines correspond to the DAQ flow through which the RPC data is collected from the TDCs by the computer.

3527     The *DIP flow*, DIP being a communication system allowing for exchange of real-time information  
 3528     between systems, concerns all the data coming from the gas composition, temperature and  
 3529     humidity, the environmental temperature and pressure, the source settings and the radiation monitoring  
 3530     sensors. The experimental area is in charge of measuring, storing and distributing the data  
 3531     of interest for all of the users of the facility (source settings, radiation monitoring, gas composition  
 3532     at the exit of the gas mixer and general environmental information). Retrieving this data is done by  
 3533     accessing to the database of the experimental hall in which GIF++ is located through DIP communica-  
 3534     tion. More specific data such as gas flow, temperature and humidity at the level of the detectors  
 3535     (upstream and downstream of the detectors) as well as environmental parameters are at the charge  
 3536     of the users. For this reason, several pressure, temperature and humidity sensors were installed on  
 3537     the gas distribution system of the RPC trolleys. The corresponding data flow, although not related  
 3538     to DIP itself, is saved together with the DIP data into the local CMS RPC database and displayed  
 3539     on the front page of the WebDCS together with alerts in the case the values measured are out of  
 3540     optimal working range. The data is particularly important to perform the PT correction described in  
 3541     Section 4.4 of Chapter 4 and keep stable the effective voltage of the detectors. Monitoring history  
 3542     plots are made using JavaScript are also displayed for an easy access to past information, as  
 3543     showed in Figure 5.26.

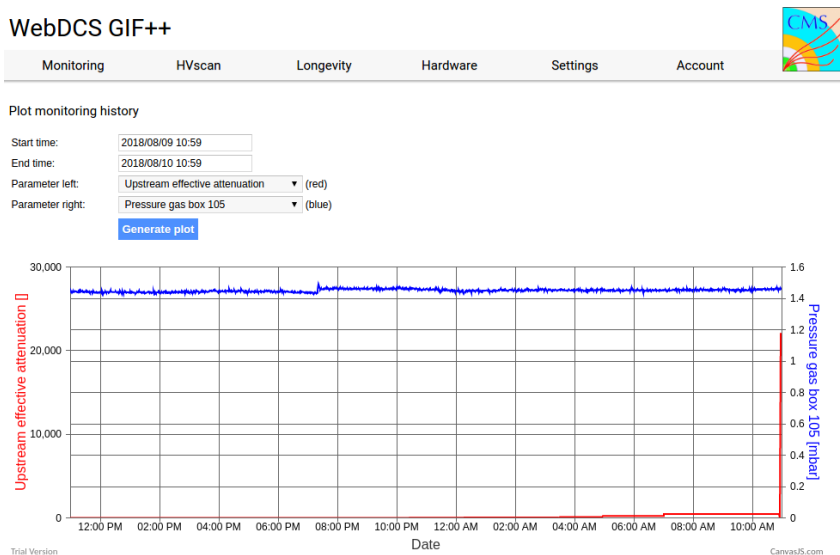


Figure 5.26: *DIP monitoring history accessed through GIF++ WebDCS interface.*

3544     The data flow related to the monitoring of the detector high voltages and currents, referred to  
 3545     as *CAEN flow* as a reference to the manufacturer of power supplies, is retrieved thanks to computer  
 3546     to main frame communications. Indeed, during the operations (irradiation or beam period), these  
 3547     values can be accessed directly through the bus of the main frame hosting the high voltage supplies.  
 3548     Finally, the DAQ flow concerns all data acquired through the use of the TDCs, i.e. all the muon or  
 3549     gamma data recorded by the detectors under test at GIF++.

### 3550 5.3.4 Measurements performed during beam periods

3551 As previously described, two types of measurement are performed on the chambers during beam  
 3552 periods. On one hand, it is interesting to measure the efficiency of the RPCs with increasing voltage  
 3553 with different source absorber settings but on the other hand, it is important to correlate the efficiency  
 3554 information to the gamma rate seen by the chambers at the voltages that were scanned for efficiency.  
 3555 The choice was made to separate efficiency measurements from rate measurements to better manage  
 3556 time and data volume. In both cases, TDC data recorded during so called *HV scans* is divided into  
 3557 *runs*, one for each high voltage point, whose data is stored into ROOT files. The TDC settings  
 3558 used during both these scans as well as the ROOT data structure are detailed in Section A.4.2 of  
 3559 Appendix A.

3560 The goal of both efficiency and rate scans is to measure the rate capability of the detectors but  
 3561 also to monitor any degradation of the performance due to ageing. This way, during test beam  
 3562 periods the efficiency and corresponding gamma background are measured to correlate the evolution  
 3563 of rate capability at different stages of irradiation. In the absence of other signs of ageing, a reduction  
 3564 of the rate capability could be related to an increase of the electrodes resistivity.

#### 3565 5.3.4.1 Efficiency scans

3566 The HV scans performed to specifically measure the muon detection efficiency under different ir-  
 3567 radiation conditions follow a standardized procedure. Data using the DAQ is taken at the same 12  
 3568 HV points for all chambers, ranging from 9 kV to 10.1 kV by steps of 100 V. For each HV run,  
 3569 a minimum of 5000 muon beam triggers, provided by the coincidence of the three scintillators, is  
 3570 required in order to accumulate enough statistics for a reliable computation of the efficiency of the  
 3571 detectors. In addition to the four RPCs held on T1, two tracking RPCs installed on T3 are kept at  
 3572 a fixed voltage of 9.7 kV to provide the analysis software [273] with beam position information to  
 3573 exclude off-track signals. The tracking RPCs, whose design is based on which of CMS RPCs, are  
 3574 double gap detectors featuring 2 mm HPL electrodes and 2 mm gas gaps. Finally, the monitored  
 3575 currents and voltages are recorded in histograms along the TDC data in a different ROOT file for  
 3576 each run.

3577 HV scans are taken for different source settings as the goal is to irradiate all the detectors with a  
 3578 minimal rate of 600 Hz/cm<sup>2</sup>. Usually, a full study of the performance of the detectors is performed  
 3579 with Source OFF, and then with nine absorber settings that attenuate the nominal gamma flux by  
 3580 factors from more than 200 to only 3, settings with fully opened source being avoided with RPCs  
 3581 in test beam position. Adjusting the gamma flux is possible thanks to the three layers of absorbers  
 3582 featured on the Cesium source [274].

#### 3583 5.3.4.2 Rate scans

3584 These background measurements are performed using a similar HV scan procedure than in the case  
 3585 of efficiency measurements. The HV scan in test beam period will be taken fewer HV points than  
 3586 for the efficiency scans as the region of interest is located around the knee and efficiency plateau  
 3587 of the detectors in order to extract through linear interpolation the value of the rate at the working  
 3588 voltage deduced from the efficiency scan. Thus, these scans are performed only on six HV points  
 3589 ranging from 9.5 kV to 10 kV. Rate scans are substantially heavier than efficiency scans. Indeed, a  
 3590 good estimation of the rate requires a long enough integrated time worth of data. The way data is  
 3591 collected, detailed in Appendix A, makes the DAQ search for data stored in the TDC buffers prior to

3592 the trigger signal. The time window from which the data is collected ranges in between only 25 ns  
 3593 to more than 50  $\mu$ s. The Cesium source delivering a consistent gamma flux, it was decided than a  
 3594 total integrated time of 0.2 s would be enough to have a reliable calculation of the  $\gamma$  rate. This is  
 3595 achieved by taking 20,000 random trigger pulses delivered by a pulse generator at a frequency of  
 3596 300 Hz while extracting 10  $\mu$ s of data from the buffers for each trigger.

3597 Separating rate measurements from efficiency measurement was motivated by the inconsistency  
 3598 of the muon beam provided in GIF++. Using periods without beam to measure rates with a good  
 3599 statistics allows for faster study programs. Moreover, depending on the muon strength that can  
 3600 strongly vary due to users placed upstream of GIF++ and using magnets, the number of muon de-  
 3601 livered per beam spill can make the accumulation of 20,000 events too long for the other users of  
 3602 GIF++. Hence, efficiency scans are performed with lower statistics, and the time window from which  
 3603 the data is extracted is strongly reduced (400ns for efficiency scans versus 10  $\mu$ s for rate scans) to  
 3604 keep the data size to its bare minimum.

### 3605 5.3.4.3 Offline analysis and Data Quality Monitoring

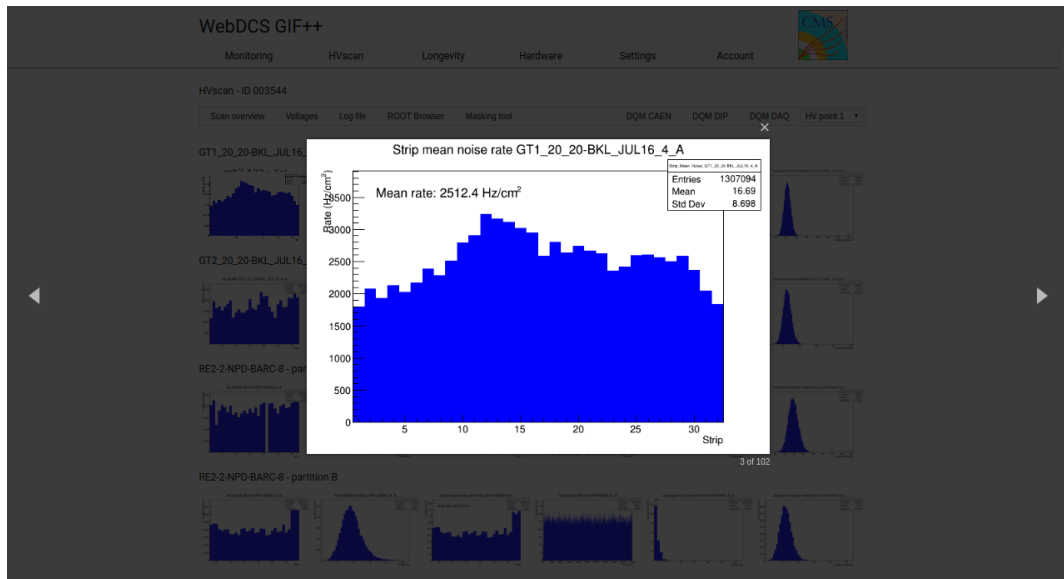
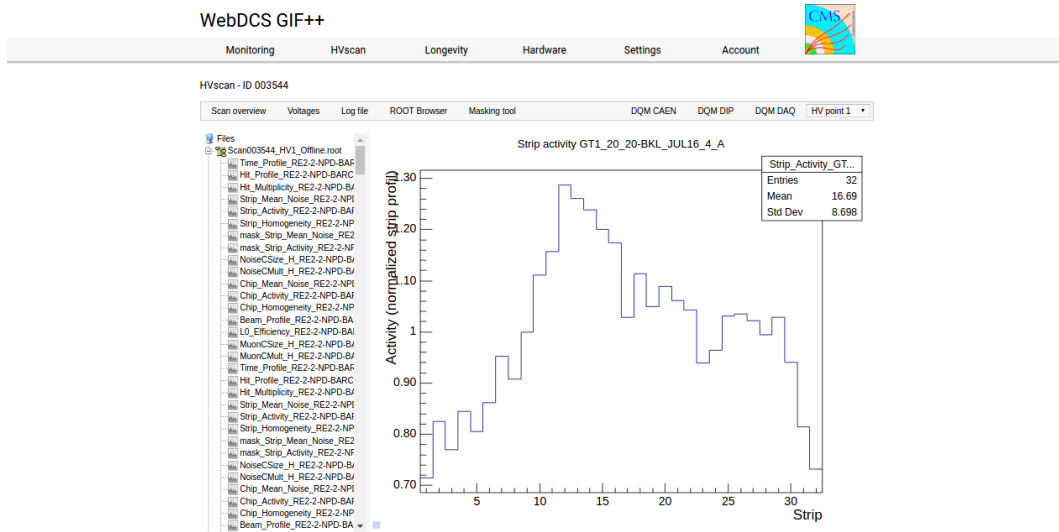


Figure 5.27: Example of DQM page available on CMS RPC WebDCS in GIF++. The rate measured in one of the tracking chambers, namely GT1\_20\_20-BKL\_JUL16\_4, is presented here. The DQM page allows clicking on each histogram to extend its view and to navigate through the histograms thanks to the left and right arrows.

3606 The data recorded during efficiency and rate scans always consist in two ROOT files per run, a run  
 3607 corresponding to a HV point. One of the files corresponds to the TDC data, a collection of hits  
 3608 per active channel on the read-out of the RPCs, while the second is the CAEN main frame data,  
 3609 offering a monitoring of the currents and high voltages. This data is systematically analysed at the  
 3610 end of each scan thanks to the Offline Analysis tool of GIF++, detailed in Appendix B, that produces  
 3611 histograms such as hit, rate and time profiles, hit multiplicities, gamma cluster sizes or multiplicities  
 3612 for the DQM display of the WebDCS, as showed in Figure 5.27. More histograms can be accessed  
 3613 through the ROOT browser included in the WebDCS, as showed in Figure 5.28. Moreover, the

analysis performed thanks to the Offline tool is definitive in the case of evaluating the rates from rate scans. On the contrary, the algorithm for efficiency calculation is kept simple and approximative in the tool as including tracking into the analysis requires manual adjustment for each individual scan.



*Figure 5.28:* Example of DQM ROOT Browser page available on CMS RPC WebDCS in GIF++. The strip activity profile, defined as the rate profile normalized to the mean rate, in one of the tracking chambers, namely GT1\_20\_20-BKL\_JUL16\_4, is presented here. Available ROOT files and histograms can be browsed thanks to the left panel showing the directory and files structures.

### 5.3.5 Measurements performed during irradiation periods

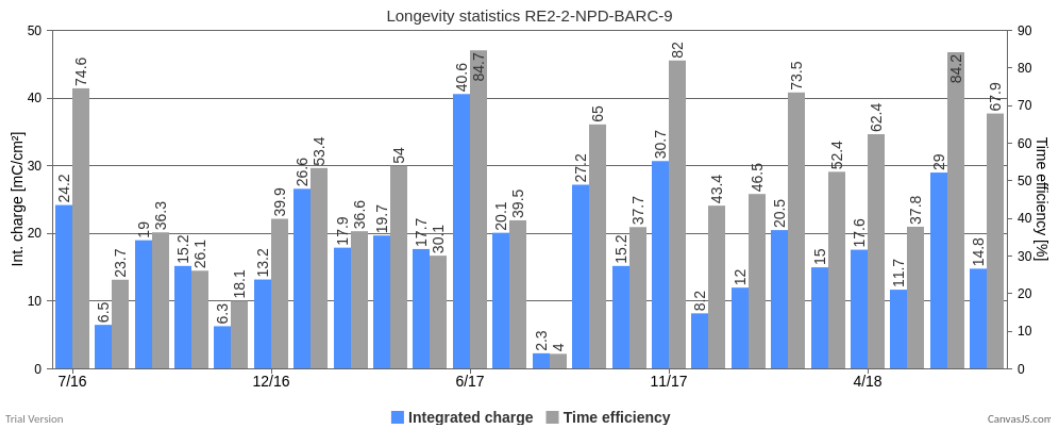


*Figure 5.29:* Longevity statistics of chamber RE2-2-NPD-BARC-9 in GIF++. For each month since July 2017, the integrated charge (in blue) as well as the time efficiency of irradiation (in gray) is reported.

Even though test beam periods are stressful times has an extensive data taking planing needs to be finalized in a short amount of time, the biggest amount of data comes from irradiation periods. Indeed, when T1 is moved back to its ageing position in between each test beam periods, data is recorded at any time the source can be switched ON for irradiation. Indeed, other experiments in the area might prevent the source from staying opened continuously. As an example, the time efficiency of irradiation of CMS RPC detectors in GIF++ is presented in Figure 5.29.

Several types of measurement are performed throughout the irradiation period. Indeed, as long as the detectors are being irradiated, a monitoring of the currents is performed to evaluate the corresponding integrated charge considering the irradiation time. Moreover, the corresponding gamma rates need to be measured on a regular basis. Ageing signs can be understood through an increase of the detector noise correlated with an increased dark current. For this purpose, HV scans are performed to measure the noise with increasing voltage and the dark currents. Another way to highlight ageing is through the loss of rate capability of the detectors. During irradiation periods this can be looked through thanks to HV scans performed at various source settings, which are referred to as *source scans*. The loss in rate capability could be understood by a saturation of the measured at higher gamma flux. This effect could be correlated with an increase of the electrodes resistivity. The resistivity is then measure periodically during the year, generally before or after test beam periods by the use of Argon breakdown technic.

### 5.3.5.1 Longevity scans

The main activity of irradiation periods consists in the *longevity scans* during which the currents of the irradiated chambers are continuously monitored. The two irradiated chambers, RE2–2–NPD–BARC–09 and RE4–2–CERN–166, are both brought to a voltage of 9.8 kV while the source flux can vary depending on the need of experiments using the facility. The currents are recorded on each active gas volume and each gap contribution is then translated into the mean chamber integrated charge as can be seen from Figure 5.30. At the end of each longevity scan the integrated charge accumulated in each chamber is used to update the summary plots providing the collaboration with official results to be spread.

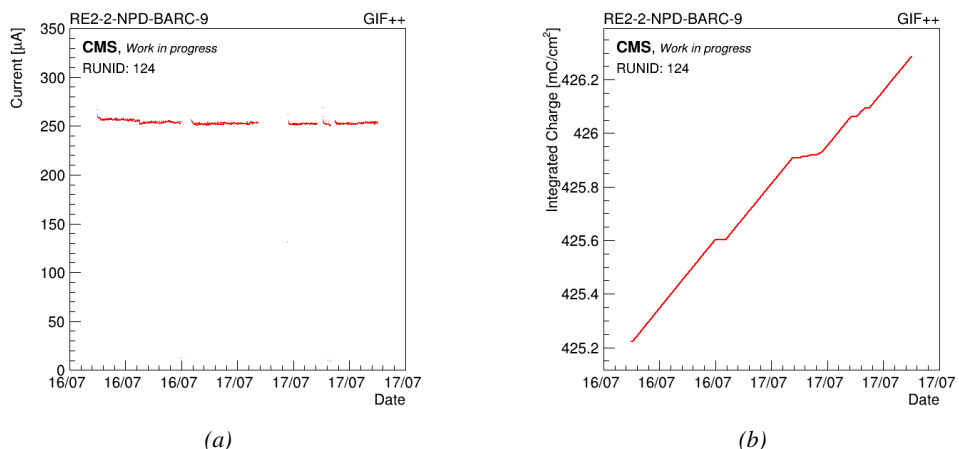


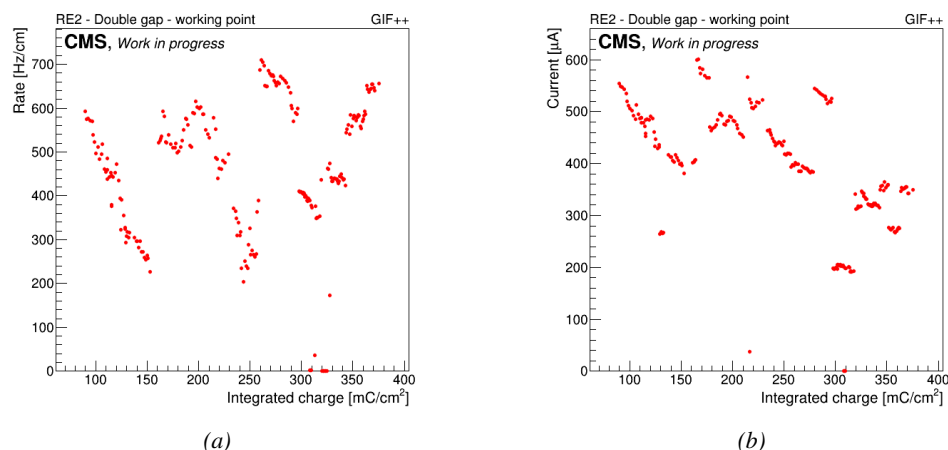
*Figure 5.30: Example of current monitoring (Figure 5.30a) and of corresponding integrated charge (Figure 5.30b) of chamber RE2–2–NPD–BARC–09. The decrease of current is related to a decrease of the voltage due to the daily rate scan procedure or to periods during which the source was turned OFF.*

### 3645 5.3.5.2 Daily rate monitoring scans

3646 Every night during longevity scans, the DAQ is used to perform *daily rate scans*. These scans aim  
 3647 at keeping track of the gamma rate measured in the irradiated RPCs during longevity but is also  
 3648 measured the noise rate at standby voltage and this, for each gap individually. The procedure for  
 3649 these HV scans consist in 9 runs for which 50,000 random triggers are requested, corresponding to  
 3650 0.5 s of total integrated time.

- 3651 1- All gaps are first left at the irradiation voltage of 9.8 kV to measure the  $\gamma$  rate.
- 3652 2- Then all gaps are brought to the standby voltage of 6.5 kV to measure the noise rate of the full  
 detectors.
- 3654 3- Both top gaps (TW and TN) are brought to a voltage equivalent to an OFF status, i.e. 1 kV so  
 3655 that the noise contribution of only the bottom gap at standby voltage can be measured.
- 3656 4- The bottom gaps are ramped up toward the working voltage of 9.8 kV to measure their contri-  
 3657 bution to the gamma rate estimation.
- 3658 5-8 The steps 3 and 4 are repeated on TN and then on TW, keeping the bottom and the top gap  
 3659 which is not of interest at a voltage of 1 kV. This way, the individual contribution to the noise  
 3660 and gamma rates are known.
- 3661 9- Finally, both TW and TN are brought to working voltage while the bottom gap is left at 1 kV  
 3662 to measure the gamma rate for the full top layer at once.

3663 Finally, the voltages of all gaps are brought back to working voltage for the longevity program  
 3664 to continue until the next daily scan.



3663 *Figure 5.31: Example of rate (Figure 5.31a) and current (Figure 5.31b) monitoring of chamber  
 3664 RE2-2-NPD-BARC-09 with increasing integrated charge. The variations of the rate and current are cor-  
 3665 related and corresponds to change of source irradiation, gas flow, gas humidity, or environmental conditions.*

3665 Naturally, as this data is taken using GIF++ DAQ, two ROOT files containing the DAQ data and  
 3666 CAEN data are created for each runs in the exact same way than for efficiency or rate scans taken  
 3667 during test beam periods but while the currents are still monitored by the longevity scan and saved

3668 into GIF++ database for an easy evaluation of the currents to the integrated charge. The Offline  
 3669 Analysis tool provides then the DQM page with histograms and daily values can be assembled in  
 3670 long term monitoring plots to study the variations of rate and current with increasing integrated  
 3671 charge, as presented in Figure 5.31. The rates on every single read-out channel are also tracked to  
 3672 control their activity with increasing integrated charge and, this way, understand the appearance of  
 3673 hot spots through noisy channels, as showed in Figure 5.32.

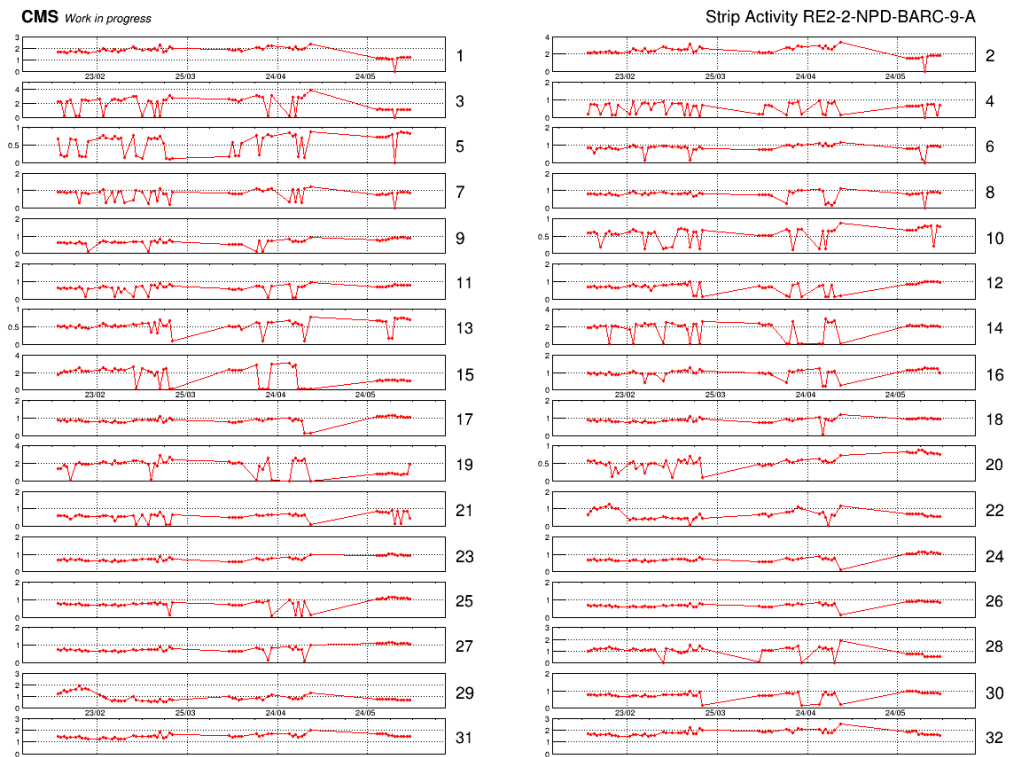


Figure 5.32: Example of strip activity of chamber RE2-2-NPD-BARC-09 monitoring through time. The activity of a strip is defined as the rate of the individual channel normalized to the mean rate measured in the corresponding read-out partition.

### 3674 5.3.5.3 Weekly noise monitoring scans

3675 Once a week, the source is turned OFF for the CMS RPC to make a noise scan, which consist  
 3676 into a HV scan composed of seven runs and involving both the irradiated but also the reference  
 3677 chambers, providing with a weekly monitoring of the evolution of the irradiated chambers noise and  
 3678 dark current. The first run is taken at standby voltage for all chambers while the next 6 runs are taken  
 3679 with voltages ranging from 9.4 to 9.9 kV in order to have for both type of chambers, RE2 and RE4, a  
 3680 coverage of the noise rate in the voltage region in which the efficiency rises and reaches the plateau.

### 3681 5.3.5.4 Weekly source scans

3682 Directly following the weekly noise scans, HV rate scans are organised at three different source set-  
 3683 tings, usually corresponding to ABS 6.8, 4.6 and 3.3. The procedure of these HV scans is strictly

3684 similar to which of weekly noise scans, involving the four RPCs in order to have a weekly com-  
3685 parison of the values recorded in every chamber. Measuring with all detectors at the same time  
3686 allows getting rid of potential systematics that might make the rates (noise or gamma) vary from one  
3687 measurement to another. If such systematic effect occurs, it will be observed in all detectors.

3688 **5.3.5.5 Weekly current scans**

3689 The previously detailed daily rate scans, but also the weekly noise and source scans are interesting  
3690 tools to look at an increase of noise rates and dark currents or at a loss of rate capability and point  
3691 to an increase of surface resistivity of the electrodes through the absorption of hydrofluoric acid.  
3692 Nevertheless, periodically measuring the currents on wider high voltage ranges allows to have access  
3693 to the ohmic part of the current driven by the detectors related to the electrodes resistance. This is  
3694 why precise current scans, consisting only in measuring the current driven through the four detectors,  
3695 are performed each week. The scan procedure consists in 131 high voltage steps in between 500 V  
3696 and 10 kV by steps of 100 V until the standby voltage of 6.5 kV is reached and then by steps of  
3697 50 V. The current increase in between 500 V and the voltage where charge multiplication starts to  
3698 occur is only driven by the resistance of the detector to current and thus increases linearly. A fit on  
3699 this linear increase of the currents in the range before charge multiplication occurs gives access to  
3700 the resistance of the system electrodes/gas. If any variation of the electrode resistance occurs, the  
3701 global resistance will increase and so will the current. Technically, these scans will record a ROOT  
3702 file per HV step that will have the same format than the CAEN ROOT file saved during other HV  
3703 scans and is also analysed using the Offline Analysis tool to provide with DQM histograms as well  
3704 as standardised  $I/V$  tables.

3705 **5.3.5.6 Resistivity measurements**

3706 Aside of the parameters monitored to spot ageing, the resistivity of the HPL planes is measured  
3707 regularly before or after test beam periods through high voltage scans of the detectors operated  
3708 with pure Argon. The electric field strength at which Argon breaks down being well known, the  
3709 breakdown voltage in the detectors is measured and gives an information about the resistance of the  
3710 electrodes, as above the breakdown voltage Argon turns into a conductive plasma and thus does not  
3711 offer electric resistance anymore, which then can be used to calculate the resistivity of the electrode  
3712 material. The Argon line in GIF++ are not kept humid and thus this measurement is not performed  
3713 too often to make sure the electrodes don't dry out, leading to an increase of the electrode resistivity.

3714 **5.3.6 Results and discussions**

3715 Since 2015, CMS RPCs have been irradiated in GIF++ with the goal to reach a total integrated  
3716 charge per irradiated detector of  $0.84 \text{ C/cm}^2$  while certifying the detectors to a rate capability of  
3717  $600 \text{ Hz/cm}^2$ . As of today, the RE2 and RE4 chambers respectively achieved 51 and 26% of the  
3718 total irradiation program. A few years of irradiation are expected before reaching the end of the  
3719 longevity study and a final answer on whether the detector will be able to live through HL-LHC or  
3720 not. A negative answer to this question would probably lead to solutions to replace the detectors  
3721 before HL-LHC or to improve the shielding of these detectors against background radiation in the  
3722 experimental cavern, which could be a more sustainable solution.

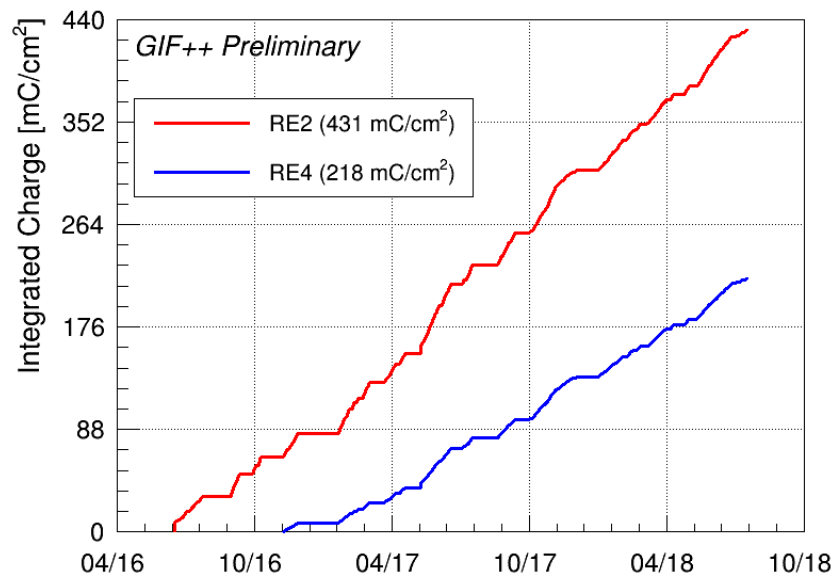


Figure 5.33: Total integrated charge in the irradiated RPCs, RE2–2–NPD–BARC–9 and RE4–2–CERN–165, before starting August 2018 test beam period. The irradiation of the RE2 chamber started in June 2016 while the RE4 chamber couldn't be irradiated before November 2016.



# 6

3723

3724

3725

## Improved RPC investigation and preliminary electronics studies

3726 The extension in the endcap of the RPC sub-system towards higher pseudo-rapidity will bring the  
3727 new detectors to be exposed to much more intense background radiations due to the proximity of  
3728 the detectors with the beam line (Figure 3.5). The challenge will be to produce high counting rate  
3729 detectors with limited ageing rate to ensure a stable operation of the detector over a period longer  
3730 than ten years. In Chapter 4 was discussed the influence of the detector design (number and thickness  
3731 of gas volumes, OR system, etc...) on the charge deposition and rate capability. Nevertheless, this  
3732 question can also be addressed from the electronics point of view as a better signal-to-noise ratio  
3733 would also mean the possibility to greatly lower the charge threshold on the signals to be detected,  
3734 allowing to use the detector at lower gain, hence lowering the charge deposition per avalanche in the  
3735 gas volume. Cardarelli showed that the production of low-noise fast FEEs could help decreasing the  
3736 charge deposition per avalanche at working voltage by an order of magnitude, virtually increasing  
3737 the life expectancy of such a detector in the same way [275].

### 3738 **6.1 FEE candidates for the production of iRPCs**

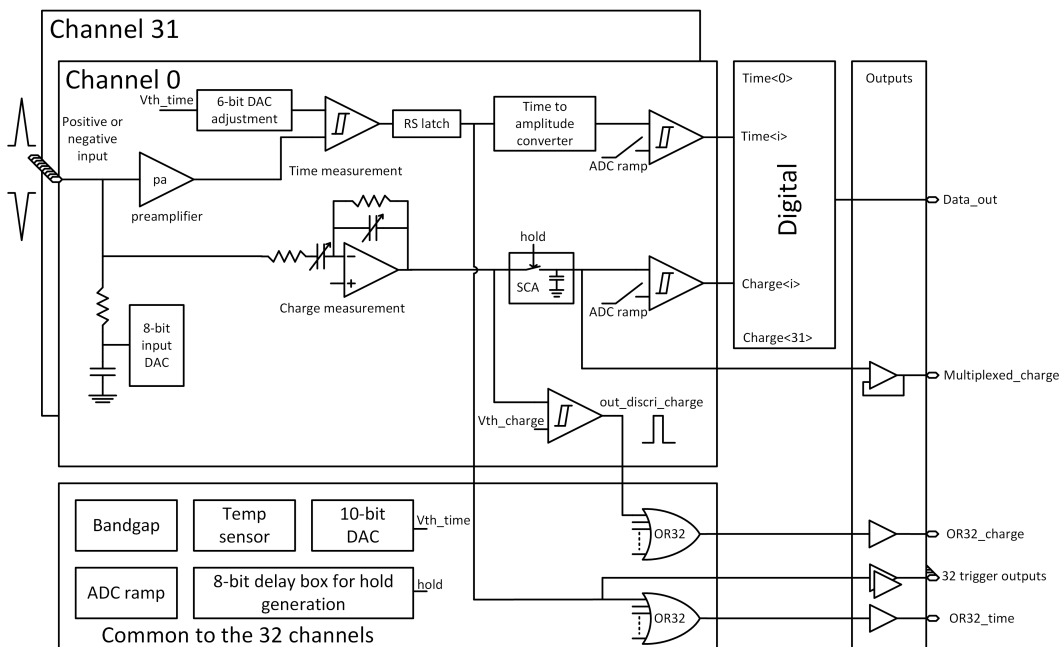
3739 The extension of the third or fourth endcap disks with improved RPCs has been presented in Chap-  
3740 ter 3 together with the expected background levels (Figure 3.23). An important piece of these iRPCs  
3741 will be the Front-End Electronics that will equip the chambers. A fast, low-jitter and low-charge  
3742 sensitive electronics will help reducing further the charge deposition in the detector by making it  
3743 possible to operate at lower gain.

3744 In the context of the CMS Muon Upgrade, two FEE solutions have been considered to equip the  
3745 iRPCs. The baseline for the RPC upgrade is based on the PETIROC ASIC, initially for Time-of-  
3746 flight (ToF) applications. A back-up solution is also under study and focusses on a new low-noise  
3747 preamplifier designed in INFN laboratories in Rome to replace the preamplification stage of the  
3748 already existing CMS RPC Front-End Board.

3749      The FEEs that are foreseen to equip the new RPCs need to be able to detect charges as small as  
 3750      10 fC. Not only the new electronics need to be fast and reliable, they also should be able to sustain  
 3751      the high radiation the detectors will be subjected to in the region closest to the beam.

### 3752    6.1.1 CMS RPCROC: the RPC upgrade baseline

3753    Designed by Weeroc, a spin-off company from the french OMEGA laboratory, the PETIROC 2A  
 3754    consists in a fast and low jitter 32-channel ASIC originally developed to read-out Silicon Photomul-  
 3755    tiplier (SiPM) in ToF applications and that allows for precise time measurements [198, 199]. The  
 3756    ASIC uses an AMS 350 ns SiGe technology. The block diagram of the ASIC is showed on Fig-  
 3757    ure 6.1. A 10-bit DAC allows to adjust the trigger level in a dynamical range spanning from 0.5 to  
 3758    a few tens of photoelectrons and a 6-bit DAC to adjust the response of each individual channel to  
 3759    similar a level.



3760    *Figure 6.1: PETIROC 2A block diagram.*

3761    Nevertheless, in order to adapt this ASIC to CMS, modifications were brought to the PETIROC [177].  
 3762    In the new CMS RPCROC, the measurement of the charge will be performed by a TimeOverTech-  
 3763    nique, taking profit of the capacity the ASIC has in measuring both the leading and trailing edges of the  
 3764    input signals. The dynamic range will be expanded towards lower values to allow for the detection  
 3765    of charges as low as 10 fC. Due to the radiation levels that are foreseen at the level of the iRPCs, the  
 3766    SiGe technology will be replaced by the Taiwan Semiconductor Manufacturing Company (TSMC)  
 3767    130 nm CMOS, to increase its radiation hardness while keeping fast pre-amplification and discrimi-  
 3768    nation with a very low jitter that can reach less than 20 ps if no internal clock is used, as can be seen  
 3769    from Figure 6.2. The ASIC is associated with an FPGA which purpose is to measure time thanks to  
 3770    a TDC with a time resolution of 50-100 ps developed by Tsinghua University and that will provide  
 a measurement of the signal position along the strip with a precision of a few cm by measuring the

<sup>3771</sup> signal timing on both ends of the strips. In order to read-out all 96 strips, 3 ASICs and 3 TDCs, each  
<sup>3772</sup> having an increased number of 64-channels, are hosted on a FEB attached to the chamber.

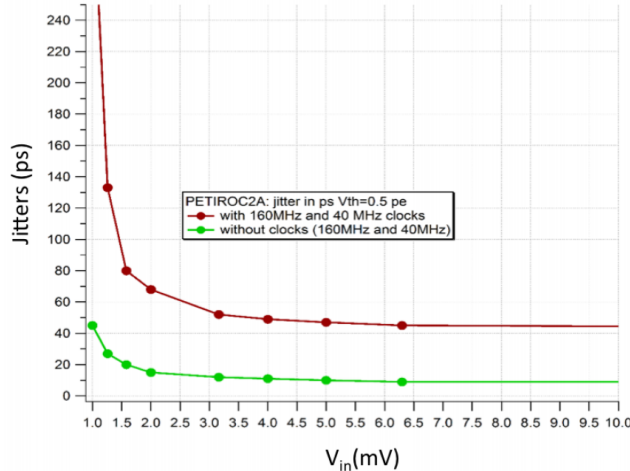


*Figure 6.2: The PETIROC time jitter as a function of the input signal amplitude, measured with and without internal clocks.*

### <sup>3773</sup> 6.1.2 INFN Front-End Electronics: a robust back-up solution

## <sup>3774</sup> 6.2 Preliminary tests at CERN

### <sup>3775</sup> 6.2.1 INFN preamplifiers

<sup>3776</sup> INFN electronics were the first ones to be tested by CMS RPC group in collaboration with colleagues  
<sup>3777</sup> from INFN Roma working in the ATLAS RPC group. Indeed, at first the electronics only consisted  
<sup>3778</sup> in a new low-noise preamplifier produced by the team of Cardarelli with the purpose of equipping the  
<sup>3779</sup> new generation of ATLAS RPCs [276]. The tests with CMS RPCs were performed in February 2013  
<sup>3780</sup> outside of the old GIF facility presented in Chapter 5.1.1. Four preamplifier channels were lended by  
<sup>3781</sup> Cardarelli to equip four CMS RPC channels as presented in Figure 6.6. They were directly connected  
<sup>3782</sup> to the strips for the signals induced by muons passing through the gas volume of the chamber to be  
<sup>3783</sup> amplified. The output was then sent to a discriminator to digitize the signals and filter out the noise  
<sup>3784</sup> by tuning the threshold level. The NIM quad discriminator 821 manufactured by LECROY used  
<sup>3785</sup> during this experiment only allows at minimum to set the threshold at a voltage of approximately  
<sup>3786</sup> 30 mV on the input signals. Thus, two values of discrimination were used ( $\sim 75$  mV and  $\sim 30$  mV).

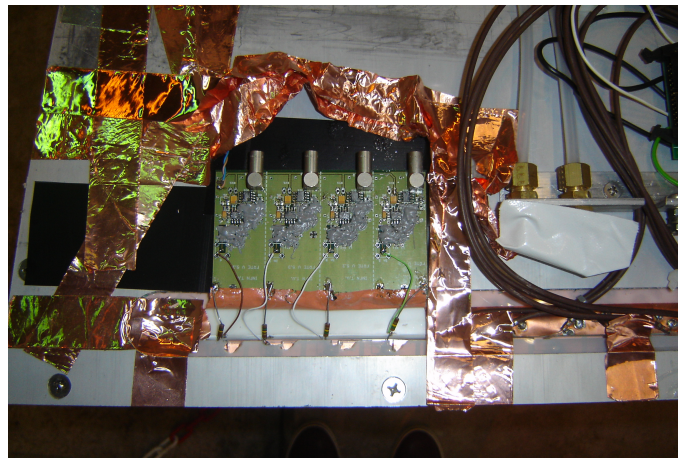
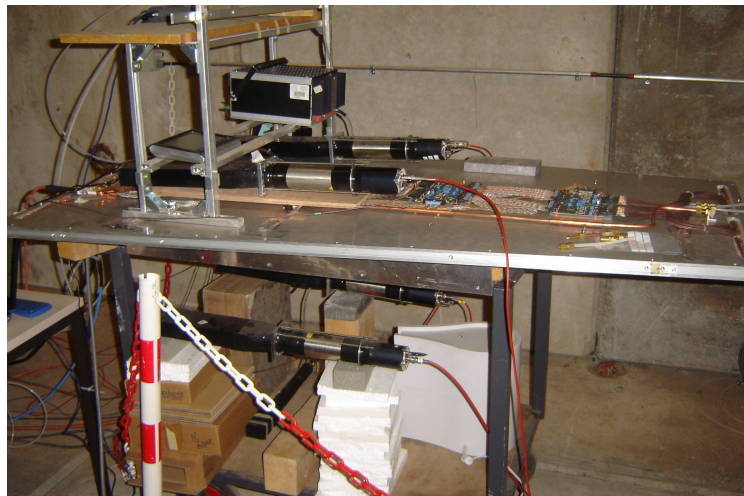


Figure 6.3: The four channels of INFN preamplifiers are mounted directly on a CMS RPC and connected to the four outermost read-out strips of the detector.

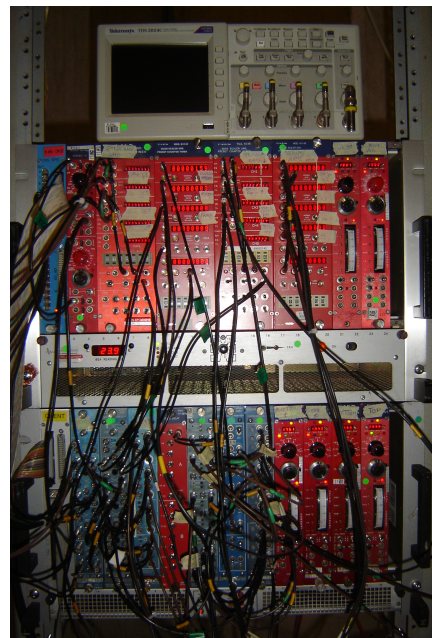
3787 The performance of the chamber equipped with these new preamplifiers was compared to the  
3788 performance of CMS FEEs. The experimental setup used is described in Figure 6.4. PMTs a little  
3789 less wide than four strips were used to trigger the data taking. Two pairs were used in coincidence  
3790 on both the strips connected to the INFN preamplifiers and to the ones connected to the CMS FEEs.  
3791 An extra PMT, placed perpendicularly to the rest of the setup at the bottom of the setup was used  
3792 to detect potential showers and send VETO signals if necessary. A last PMT was used close to the  
3793 power supplies to measure and discard signals due to electromagnetic noise and is not visible on  
3794 the pictures. Finally, after discrimination, the output of the INFN preamplifiers together with the  
3795 signals from the CMS FEEs were sent to scalers to count the detected signals versus the number of  
3796 trigger coincidences as no DAQ software was available at the time. The full pulse processing for this  
3797 experiment is shown in Figure 6.5.



(a)



(b)



(c)

Figure 6.4: Experimental setup used to test the INFN preamplifier with respect to the CMS FEEs.

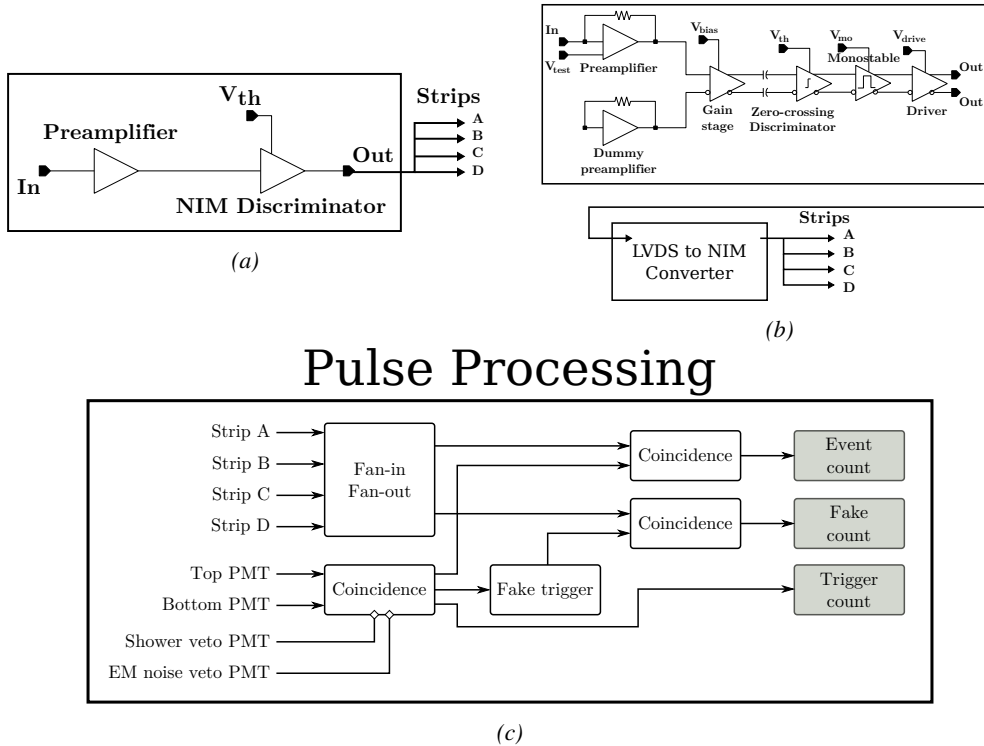


*Figure 6.5: The block diagrams corresponding to the signal treatment for both INFN preamplifier (Figure 6.5a) and CMS FEEs (Figure 6.5b) are shown. The digitized signals are then counted in coincidence with the trigger signals provided by PMTs (Figure 6.5c).*

3798 The data taking program consisted in High Voltage scans. A first point was taken at 0 V to only  
 3799 measure noise. Then the HV was increased to an applied value of 7 kV. The voltage was increased  
 3800 in steps of 500 V until 8 kV from where it was increased in steps of 100 V until an upper limit of  
 3801 10 kV. After rising the voltage over the electrodes of the RPC, a waiting period of 15 minutes was  
 3802 observed to leave time to the electrodes to charge and to the currents to stabilize. The currents were  
 3803 reported at the moment the data taking was started. At each HV step, except at 0 V, approximatively  
 3804 300 triggers were taken to estimate the efficiency of the detector by counting the number of hits in the  
 3805 system (A or B or C or D), referring to the strips. The noise rate per unit area was measured during  
 3806 the first 100 s of data taking by counting the number of hits received in each read-out strip. The  
 3807 cluster size, the average number of adjacent strips fired during a muon event, could not be measured  
 3808 due to the lack of available scalers.

3809 During the data acquisition, in addition to counting the number of signals with respect to the  
 3810 number of triggers, the current or the noise rate per unit area as a function of the increasing voltage,  
 3811 the environmental parameters were monitored. Using the information provided by a humidity and  
 3812 temperature sensor on the gas input line together with the environmental pressure given by a weather  
 3813 station, the applied voltage could be corrected following Formula 4.27. Moreover, the voltage line  
 3814 was filtered to prevent noise and higher currents in the RPC under test.

3815 The results of the preliminary tests are presented in Figure 6.6. More details on the fit performed  
 3816 on the data are provided in Table 6.1. As can be seen, being able to use electronics with a much  
 3817 higher sensitivity allows for a HV shift of up to 475 V with a threshold as low as 3 fC corresponding

3818 to the lowest threshold available on the discriminator modules. On the other hand, the higher charge  
 3819 sensitivity also brings a higher noise level. After a first series of measurement performed with a bad  
 3820 grounding leading to grounding loops and hence an artificially higher noise, it can be concluded that  
 3821 the noise rate per unit area of such electronics is approximately one of manitude higher than the noise  
 3822 measured with the CMS FEB. The noise reaches approximately  $2 \text{ Hz/cm}^2$  at the level of the  
 3823 working in the case of the INFN preamplifier while it is lower than  $0.2 \text{ Hz/cm}^2$  for the CMS FEB.  
 3824 It is likely that the higher sensitivity also brings a higher sensitivity to local discharges happening  
 3825 in the gas due to fluctuations of the electric field. The surface of the electrodes not being perfectly  
 3826 smooth, the local electric field may vary quickly. The gas molecules circulating in the gas could  
 3827 then be ionised by the fast variation of the field and trigger an avalanche that can then be detected.  
 3828 Reducing the noise rate per unit area would then come from an improvement of the detector itself  
 3829 rather than from a reduction of the electronic noise of the INFN preamplifier.

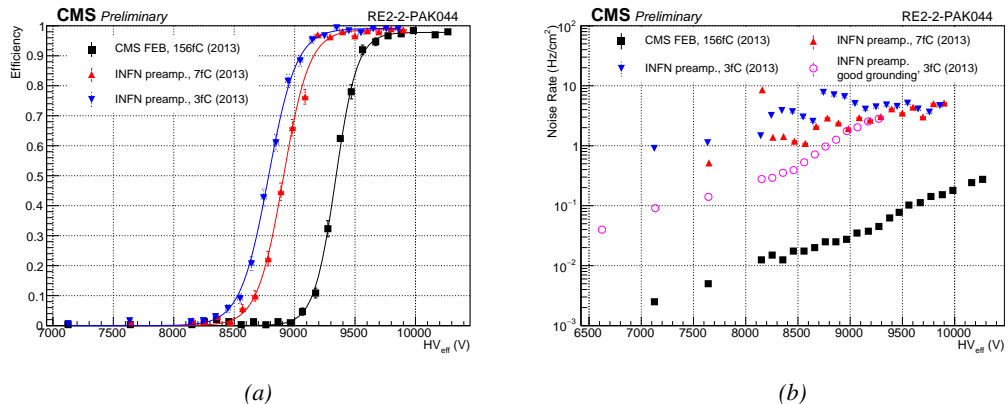


Figure 6.6: Efficiency (Figure 6.6a) and noise rate per unit area (Figure 6.6b) of the CMS RE2-2 detector tested with the standard CMS FEBs (black) and with the INFN preamplifier at different thresholds (red and blue). An extra HV scan was performed with better conditions to measure the noise with a threshold of 3 fC on the INFN preamplifiers.

Data	$\epsilon_{max}$	$\lambda (\times 10^{-2} \text{ V}^{-1})$	$\text{HV}_{50}$ (V)	$\epsilon_{WP}$	$\text{HV}_{WP}$ (V)
CMS FEB, 156fC (2013)	$(0.978 \pm 0.004)$	$(1.12 \pm 0.07)$	$(9339 \pm 11)$	$(0.97 \pm 0.01)$	$(9752 \pm 27)$
INFN preamp., 7fC (2013)	$(0.987 \pm 0.003)$	$(0.93 \pm 0.05)$	$(8907 \pm 11)$	$(0.97 \pm 0.01)$	$(9374 \pm 27)$
INFN preamp., 3fC (2013)	$(0.991 \pm 0.003)$	$(0.86 \pm 0.04)$	$(8783 \pm 11)$	$(0.98 \pm 0.01)$	$(9276 \pm 27)$

Table 6.1: Results of the sigmoid fit (Formula 4.24) performed on the data presented in Figure 6.6a. The working point and its corresponding efficiency are computed using Formulas 4.24 and 4.25.

### 6.2.2 INFN preamplifiers mounted onto CMS Front-End Board

3831 Following the first experiment performed in the experimental hall aside of the old GIF, a new se-  
 3832 ries of tests has been done in the CMS RPC assembly laboratory at CERN. For this purpose, the  
 3833 preamplifiers have been designed to be standalone single channels. To have a consistent comparison  
 3834 with the CMS FEB, a FEB prototype has been built based on the current CMS design. As shown  
 3835 in Figure 6.7, the preamplifiers are meant to be plugged in one of the available 16 channels of the  
 3836 board that produces an LVDS output with similar characteristics than the CMS FEB.

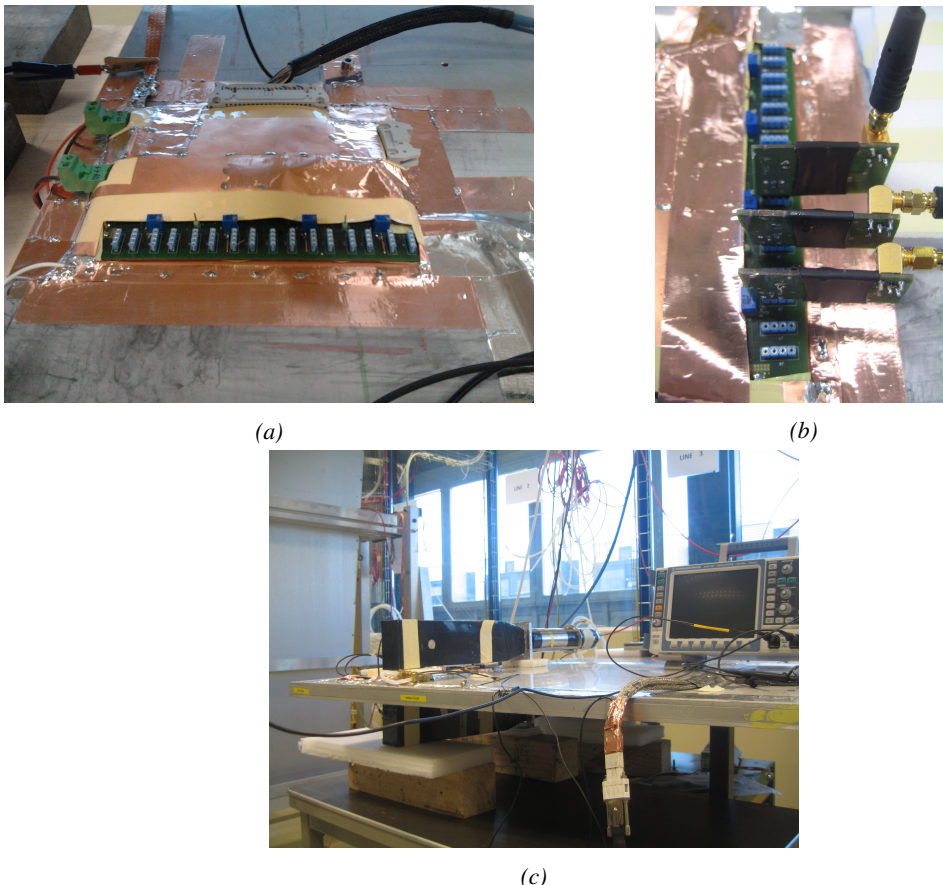


*Figure 6.7: Figure reffig:Setup-INFN-904:A: Shielded Front-End Board on which the INFN preamplifiers are to be mounted. Figure reffig:Setup-INFN-904:B: Three INFN preamplifiers connected onto the test FEB. Figure reffig:Setup-INFN-904:C: Experimental setup used to test the INFN preamplifier single mounted on a FEB similar to the CMS FEB.*

At the time of the second experiment, only three channels could be lent by the team of INFN Roma. The impedance of the preamplifiers was set to  $100\ \Omega$  at delivery. The strips are then connected to the preamplifiers using  $50\ \Omega$  coaxial cables equipped with SMC connectors, known for their good transmission. To match the impedance of the preamplifier input with the signal cable, a  $100\ \Omega$  resistor was added in parallel of the input line. In CMS endcap RPCs, the strips are left floating. For the purpose of this test, it was necessary to terminate the strips on both ends to prevent reflections in the transmission line. The impedance of the strips being approximately  $25\ \Omega$ , the strips were terminated with  $50\ \Omega$  resistors on the signal cable side, and with  $25\ \Omega$  resistors on the end side.

The threshold of the zero-crossing discriminators used on the FEB is controlled via a labview interface similar to the one used to control the threshold of the CMS FEB. Various thresholds were used in a range in between 7 and 5 fC. These values are a little higher than the minimal threshold of about 3 fC used during the first experiment due to limitations of the FEB itself.

Finally, it was decided to use the same PMTs than in the first experiment as trigger. This time, they were placed on their narrow side to only cover an area on the detector smaller than three strips. On the data acquisition side, no DAQ software was available yet at the time of experimentation and

3852 scalers were once again used. As can be seen from Figure 6.8, the pulse processing has been inspired  
 3853 by the previous scheme. Thanks to the lower number of channels to monitor, the cluster size could  
 3854 be estimated by counting the signals on single channels (A, B and C on their own) but also on groups  
 3855 of two (A and B, B and C) and three channels (A and B and C) in coincidence with the trigger.

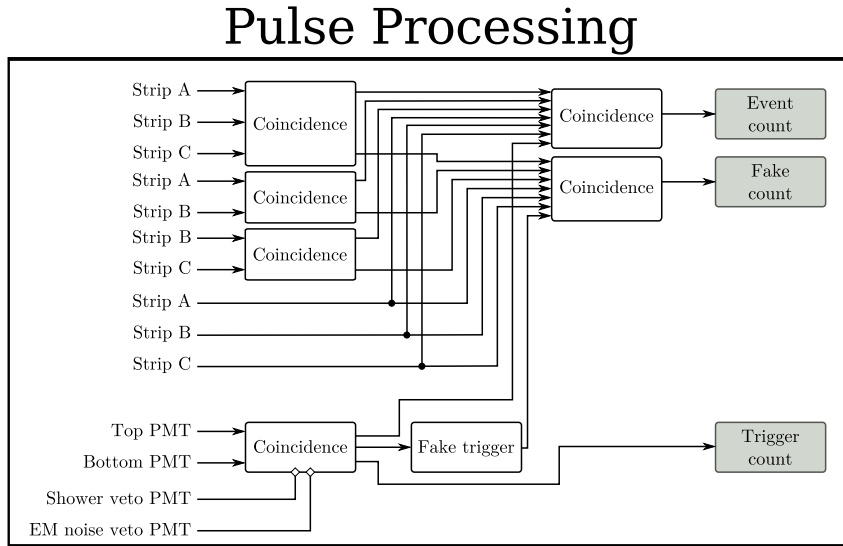


Figure 6.8: Similarly to Figure 6.5c, the signals are counted in coincidence with the trigger signals provided by PMTs. To estimate the cluster size, the channels are counted by groups of three, two but also alone.

3856 The results of the second round of tests with INFN preamplifiers are presented in Figure 6.9  
 3857 and Table 6.2. These results are consistent with what was measured with the first tested prototypes.  
 3858 The efficiency sigmoid has been measured once again with the CMS FEB, using a threshold of  
 3859 170 fC and is in agreement with the data collected in 2013. The performance of the detector with the  
 3860 preamplifiers tuned at 7.2 and 6.4 fC falls in the very same values than the setting at 7 fC according  
 3861 to the table. A maximum shift of 410 V is observed for a threshold of 5 fC.

3862 With the care placed into having a good grounding of the setup as well as a good impedance  
 3863 matching, the noise rate per unit area is this time lower than what previously measured. Nevertheless,  
 3864 it still is more than one order of magnitude higher than in the case of the CMS FEB with a threshold  
 3865 set at 170 fC. The noise rate is measured to be at lowest around 0.7 Hz/cm<sup>2</sup> when measured to be  
 3866 approximately 0.05 Hz/cm<sup>2</sup> for the CMS FEB. At such high threshold values, the noise rate per unit  
 3867 area is not expected to vary much. The data collected at the RPC assembly laboratory then displays  
 3868 much better data taking conditions with both electronics.

3869 Finally, the cluster size is measured to be similar for both electronics at the level of the working  
 3870 point and is in between 2.2 and 2.4 strips on average. The spatial resolution of both devices would  
 3871 then be the same.

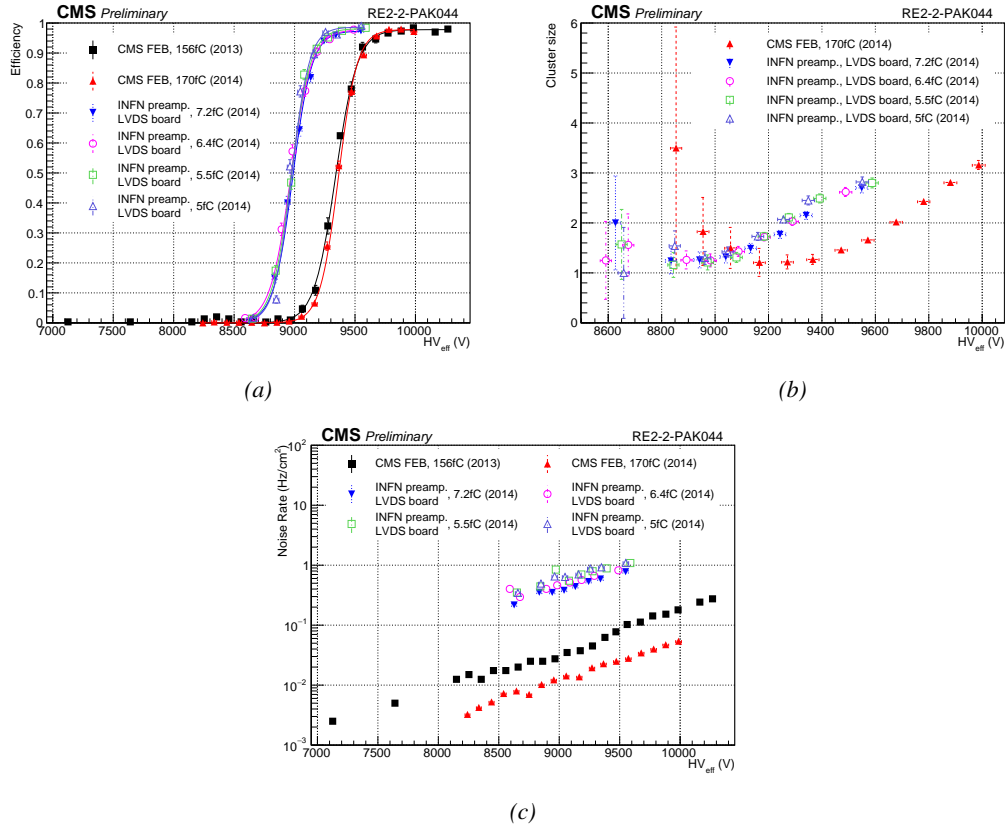


Figure 6.9: Efficiency (Figure 6.9a), cluster size (Figure 6.9b) and noise rate per unit area (Figure 6.9c) of the CMS RE2-2 detector tested with the standard CMS FEBs (black and red) and with the INFN preamplifier mounted onto the CMS FEB at different thresholds (blue, pink, green and purple).

Data	$\epsilon_{max}$	$\lambda \cdot 10^{-2} \text{ V}^{-1}$	$HV_{50}$ (V)	$\epsilon_{WP}$	$HV_{WP}$ (V)
CMS FEB, 156fC (2013)	$(0.978 \pm 0.004)$	$(1.12 \pm 0.07)$	$(9339 \pm 11)$	$(0.97 \pm 0.01)$	$(9752 \pm 27)$
CMS FEB, 170fC (2014)	$(0.978 \pm 0.003)$	$(1.30 \pm 0.06)$	$(9364 \pm 9)$	$(0.97 \pm 0.01)$	$(9740 \pm 19)$
INFN/CMS FEB, 7.2fC (2014)	$(0.973 \pm 0.006)$	$(1.26 \pm 0.09)$	$(8985 \pm 10)$	$(0.97 \pm 0.01)$	$(9368 \pm 26)$
INFN/CMS FEB, 6.4fC (2014)	$(0.978 \pm 0.007)$	$(1.16 \pm 0.08)$	$(8969 \pm 11)$	$(0.97 \pm 0.01)$	$(9372 \pm 28)$
INFN/CMS FEB, 5.5fC (2014)	$(0.981 \pm 0.005)$	$(1.26 \pm 0.09)$	$(8973 \pm 12)$	$(0.97 \pm 0.01)$	$(9357 \pm 28)$
INFN/CMS FEB, 5fC (2014)	$(0.987 \pm 0.004)$	$(1.37 \pm 0.10)$	$(8976 \pm 12)$	$(0.98 \pm 0.01)$	$(9342 \pm 28)$

Table 6.2: Results of the sigmoid fit (Formula 4.24) performed on the data presented in Figure 6.9a. The working point and its corresponding efficiency are computed using Formulas 4.24 and 4.25.

In addition to the tests performed on the electronics with the CMS RPC, the electronics also have been tested on a gRPC designed in Ghent. The gRPC used for this experiment is described in Figure 6.10. The detector, showed on Figure 6.11, uses a double-gap layout with float glass electrodes of 1.1 mm and a gas gap of 1.2 mm. The electrodes themselves are made out of four pieces of glass glued together. Such a design was studied for high-rate detection purposes and aimed to serve as a proof of concept for RPCs built using small pieces assembled together to produce a larger detection area. Indeed, in the context of R&D in the field of high-rate RPCs, most low resistivity materials are custom made doped glass or ceramics plates. These materials can't be

3880 produced in large areas as they are not manufactured on a large enough scale. Thus, building large  
 3881 detectors requires using such methods.

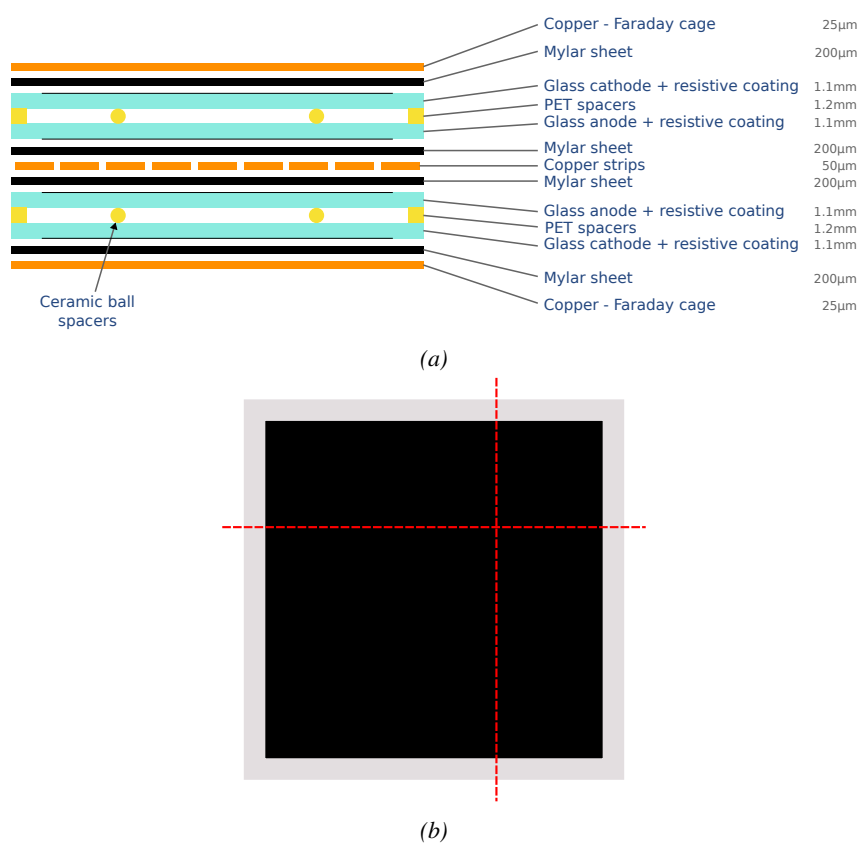


*Figure 6.10: The glass RPC developed by Ghent uses a double-gap design (Figure 6.10a). The electrodes are made of four pieces of float glass glued into a single plate (Figure 6.10b). Indeed a gluing technique has been investigated as most new low resistivity materials foreseen for RPCs of the new generation are not available in large areas.*

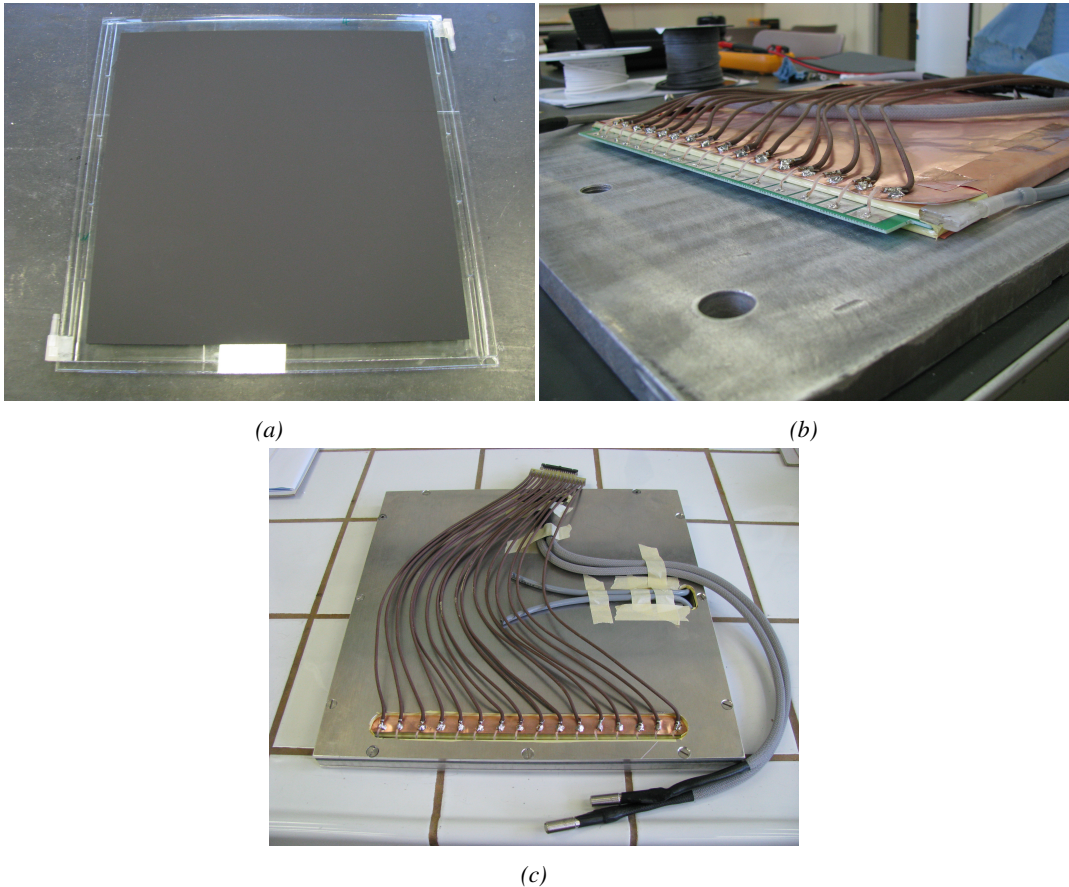


*Figure 6.11: Figure 6.11a: A gap used to conceive the gRPC tested at CERN. Figure 6.11b: Both gaps with their read-out panel are placed into a faraday made out of copper. Figure 6.11c: The faraday cage containing the double-gap gRPC is finally placed into its aluminium case.*

3882 The tests involving this detector were conducted in 2015 with the setup described by Figure 6.12.  
 3883 The photomultipliers used to trigger the data taking were a little larger than the detector and the strips  
 3884 themselves. Similarly to the case of the GIF experiment described in Section 5.2.2 of Chapter 5, it  
 3885 has been necessary to evaluate the geometrical acceptance of the setup to detect cosmic muons.  
 3886 This way, a C++ Monte Carlo simulation has been written using the dimensions of the experimental  
 3887 setup. By running 1000 simulations in which a million muons were generated in a source plane much  
 3888 larger than the experimental setup itself to reach high zenith angles, the geometrical acceptance was  
 3889 measured to be  $(0.9835 \pm 0.0014)$ . This factor has then been used to correct the measured efficiency  
 3890 of the detector.

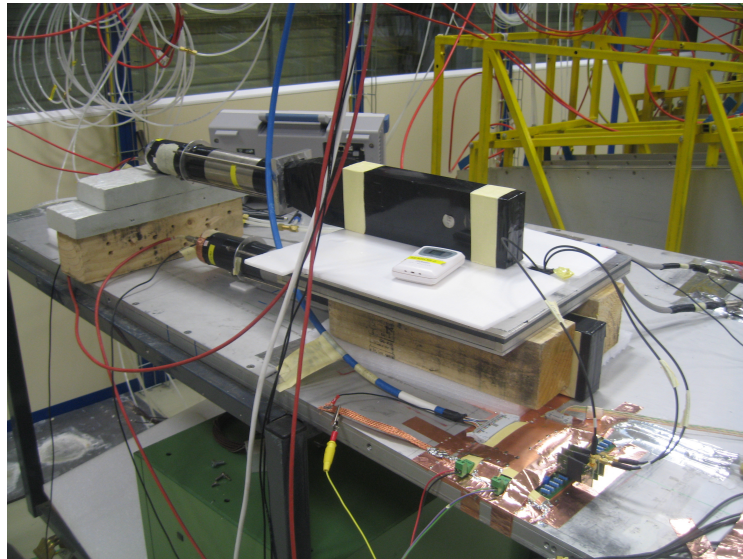


*Figure 6.12: Experimental setup used to test the INFN preamplifier mounted on the CMS like FEB with the glass RPC build by Ghent.*

3891     Thanks to the activities ongoing for the preparation of the CMS RPC experiment taking place at  
 3892     GIF++ and detailed in Chapter 5, a first prototype of DAQ software was available to automate the  
 3893     data tacking process. Thanks to this early version of the software, the pulse processing was made  
 3894     more simple. The three channels connected to the preamplifiers were sent directly into a V1190A  
 3895     TDC manufactured by CAEN. The trigger was provided by the same trigger pulse processing de-  
 3896     scribed in Figure 6.8. The output of the coincidence of both scintillators was sent into the *TRIGGER*  
 3897     input of the TDC. The communication with the computer was done thanks to a V1718 module.  
 3898     More details on the DAQ can be found in Appendix A. Contrary to the data now collected at GIF++,  
 3899     the output of the first DAQ script consisted in a simple text file using a format described in Source  
 3900     Code 6.1. The analysis is then performed using a loop through the data file.

```

Evt0      nHits
ChHit1    THit1
ChHit2    THit2
ChHit3    THit3
ChHit4    THit4
ChHit5    THit5
3901 ...
Evt1      nHits
ChHit1    THit1
ChHit2    THit2
ChHit3    THit3
...
  
```

3902     *Source Code 6.1: Description of the format used to store the data collected during the experiment aiming at  
           testing the INFN electronics with a gRPC built by Ghent. For each trigger received in the TDC module, an  
           event is created. A first line containing two columns is written in the output file with the event number EvtX  
           and the recorded number of hits nHits. This line is directly followed by the list of hits in each channel ChHitX  
           and their corresponding time stamp THitX organized into two columns.*

3903 The results of the experiment with the gRPC are provided in Figure 6.13 and Table 6.3. The  
 3904 efficiency of the detector reaches 95% at working voltage, indicating that such a detector using  
 3905 electrodes composed of several glued pieces can be an option for the future of RPC technologies.  
 3906 The benefits of the preamplifiers is once again visible through the huge efficiency shift towards lower  
 3907 voltages. The shift reaches almost 470 V for thresholds lower than 6 fC.

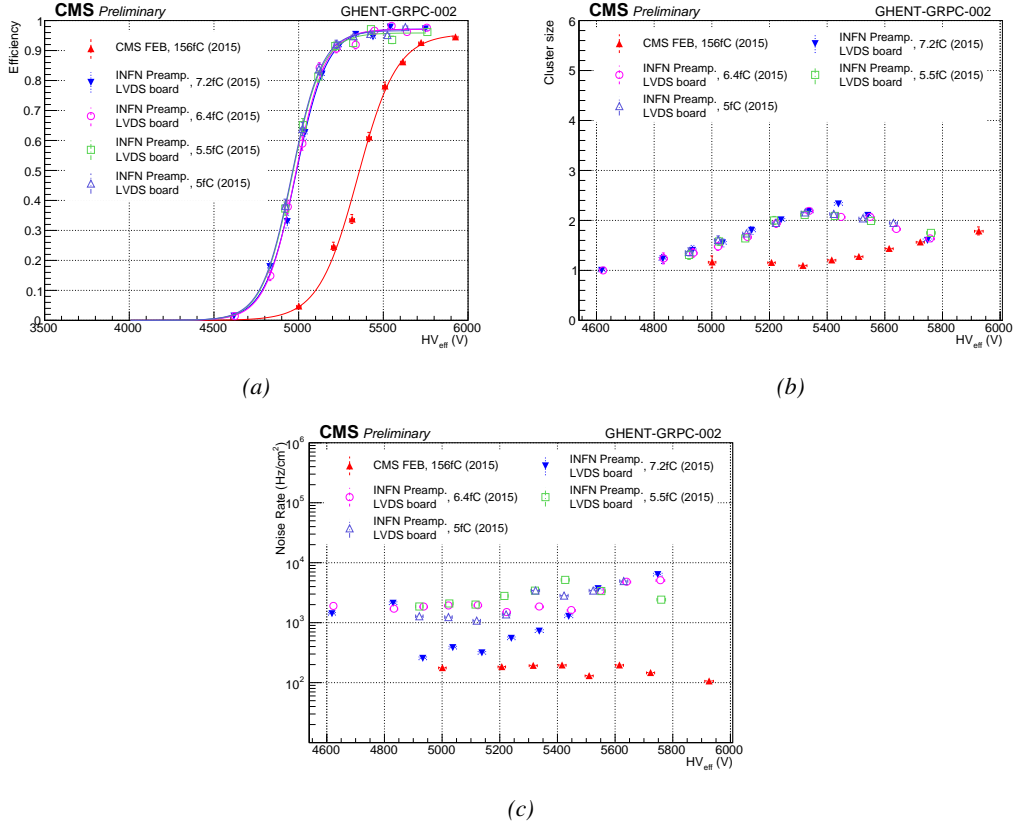


Figure 6.13: Efficiency (Figure 6.13a), cluster size (Figure 6.13b) and noise rate per unit area (Figure 6.13c) of the Ghent gRPC detector tested with the standard CMS FEBs (red) and with the INFN preamplifier mounted onto the CMS FEB at different thresholds (blue, pink, green and purple).

Data	$\epsilon_{max}$	$\lambda \cdot 10^{-2} \text{ V}^{-1}$	$HV_{50}$ (V)	$\epsilon_{WP}$	$HV_{WP}$ (V)
CMS FEB, 156fC (2015)	(0.956 ± 0.007)	(0.86 ± 0.04)	(5349 ± 8)	(0.94 ± 0.01)	(5839 ± 23)
INFN/CMS FEB, 7.2fC (2015)	(0.972 ± 0.006)	(1.09 ± 0.06)	(4983 ± 8)	(0.96 ± 0.01)	(5403 ± 22)
INFN/CMS FEB, 6.4fC (2015)	(0.971 ± 0.005)	(1.13 ± 0.06)	(4981 ± 8)	(0.96 ± 0.01)	(5391 ± 22)
INFN/CMS FEB, 5.5fC (2015)	(0.959 ± 0.006)	(1.13 ± 0.11)	(4960 ± 11)	(0.95 ± 0.02)	(5371 ± 37)
INFN/CMS FEB, 5fC (2015)	(0.967 ± 0.006)	(1.12 ± 0.11)	(4959 ± 11)	(0.96 ± 0.02)	(5371 ± 38)

Table 6.3: Results of the sigmoid fit (Formula 4.24) performed on the data presented in Figure 6.13a. The working point and its corresponding efficiency are computed using Formulas 4.24 and 4.25.

3908 The cluster size also shows a shift but its value suddenly decreases after 5.4 kV. After a rise  
 3909 above 2, the cluster size drops when the detector reaches the plateau. A first idea to explain this

phenomenon would be to check the cluster algorithm to make sure that it is not biased and does not introduce a fake split of the clusters due to arbitrarily strict selection rules. Clusters are always made of neighbour strips getting a hit within a certain time window. In the algorithm written to analyse the data, it is required for the maximum time difference between the earliest hit and the latest hit in a cluster to be smaller than 10 ns. Physically, assuming of drift velocity of the electrons in the gas of the order of 0.1 mm/ns [277], the growth of an avalanche only takes a few ns. This effect is visible in Figure 6.14a in which the maximum time difference has been artificially increased to 300 ns. The peak reveals that the avalanches are not expected to grow over a time period longer than 10 ns. No peak emerges at time differences longer than 10 ns indicating that the choice of a short time development within the algorithm was justified. This conclusion is supported by Figure 6.14b in which the evolution of the reconstructed cluster size with increasing maximum time difference shows no effect.

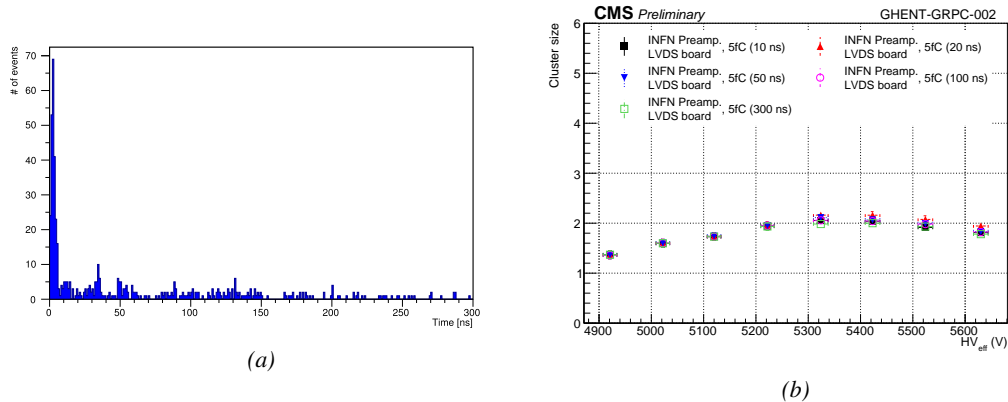


*Figure 6.14: Figure 6.14a: Time difference between the first and last hit composing a cluster in the gRPC. The maximum time difference is set to 300 ns. Figure 6.14b: Variation of the reconstructed average cluster size as a function of the time constraint used in the algorithm.*

Due to the available number of channels, the cluster size is limited to 3. It is reasonable to assume that this only is the cause of the fall of cluster size beyond 5.4 kV. Indeed looking closely at both Figure 6.15 and Figure 6.16, the link between increasing HV and decreasing cluster size can be understood. On the one hand, Figure 6.15 indicates that the cluster size features at first a maximum at 1. The maximum moves then from 1 to 3 over the points at 5120 V, 5222 V and 5324 V. Then over the last three voltage points, the bin at 2 drops to the profit of the bin at 1, the bin at 3 staying more or less stable. On the other hand, Figure 6.16 provides us more information about the localisation of the clusters among the three read-out strips. At the lowest two voltages, most of the data is contained in the central strip. At 5120 V, the highest bin is the one corresponding to the central strip with a cluster size of 1. Already at 5222 V, the balance changes towards the central strip with 3 strips in the clusters. At 5324 V, even more events happen with clusters of all 3 strips while the events with a single hit in the side strips starts to increase. The number of events with cluster made of all 3 strips will not vary much anymore while the number of events with clusters made of 2 strips will decrease and the single hits in the side strips will continue rising. This information indicates that the avalanches in the gap start to get stronger. Indeed, the increase of the events containing single hits mainly increases on the side strips points to an intensification of the avalanche gain on the strip adjacent to the three channels connected to the read-out setup. Only a single hit is read-out while

in reality this was the contribution of bigger avalanches. The events with clusters of size 2 tend to decrease due to the stronger gain that should normally be triggering wider avalanches. The cluster size distribution of Figure 6.15 gives the impression that the distribution is moving towards higher values but the geometrical limitation of the system due to the very low number of channels makes it impossible to measure.

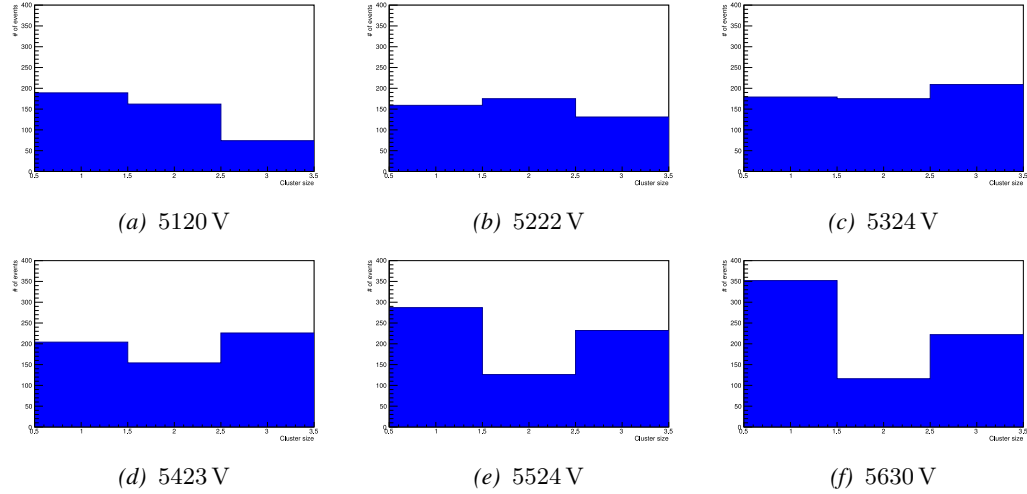


*Figure 6.15: Evolution of the cluster size distribution with increasing voltage for the gRPC tested with the INFN preamplifiers using a threshold of 5 fC.*

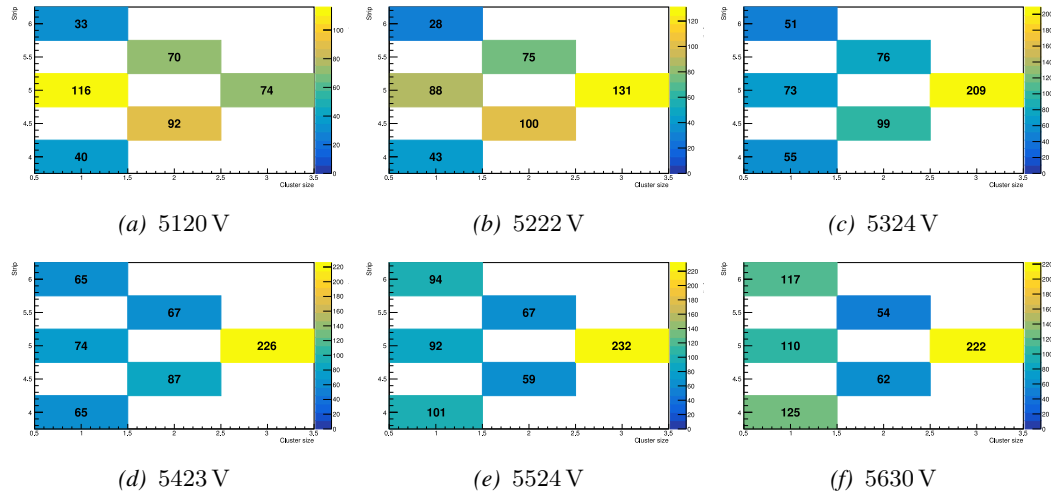


*Figure 6.16: Map of the cluster size distribution as a function of the cluster position with increasing voltage for the gRPC tested with the INFN preamplifiers using a threshold of 5 fC.*

Eventhough the performance of the detector are promising, the results concerning the noise rate per unit area seem to indicate that the detector and its combination with the electronics in the case of this experiment produces very high levels of noise, if compared to the noise measured in the RE4

3947 detector. With each type of electronics, the noise doesn't indicate a clear correlation with increasing  
 3948 voltage. The hypothesis at this stage would be that the noise is not created inside of the gas volume by  
 3949 avalanches triggered along the glueing lines, where the electric field could be abruptly perturbed.  
 3950 It would rather come from the read-out channel itself, and from its connection to the electronics.  
 3951 Indeed, looking at the noise profile measured in the detector and presented in Figure 6.17a, it is clear  
 3952 that the noise is localised in two areas corresponding to the HV connectors in the case of the HV  
 3953 scan performed with the CMS FEB. Moreover, contrary to the very careful work performed on the  
 3954 RE2 chamber to match the impedance of the strips with the read-out cables connected to the board  
 3955 on which the INFN preamplifiers are mounted, no matching was done on the gRPC due to a lack  
 3956 of time. The noise measured in the tested three channels is showed in Figure 6.17b. This region of  
 3957 the detector doesn't correspond to the HV connectors according to Figure 6.17a. Nevertheless, the  
 3958 number of hits counted in the detector is much higher than in the CMS FEB case. Looking more  
 3959 carefully to Figure 6.18 presenting the hit time profile in both cases together with the time profile of  
 3960 the CMS RE2-2 detector tested with INFN preamplifiers, it is clear that the detector is noisier. Also,  
 3961 the reflections due to the impedance mismatch is clearly visible in Figure 6.18b.

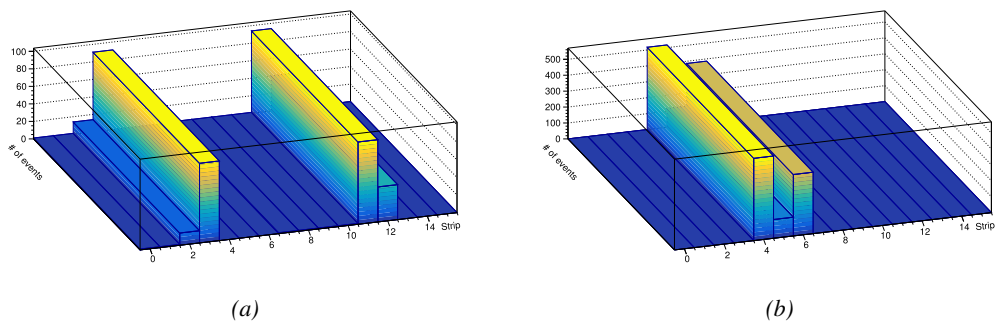


*Figure 6.17: Noise profile measured in the glass RPC built by Ghent tested with the standard CMS FEB (Figure 6.17a) and the INFN preamplifiers mounted on a CMS-like FEB (Figure 6.17b).*

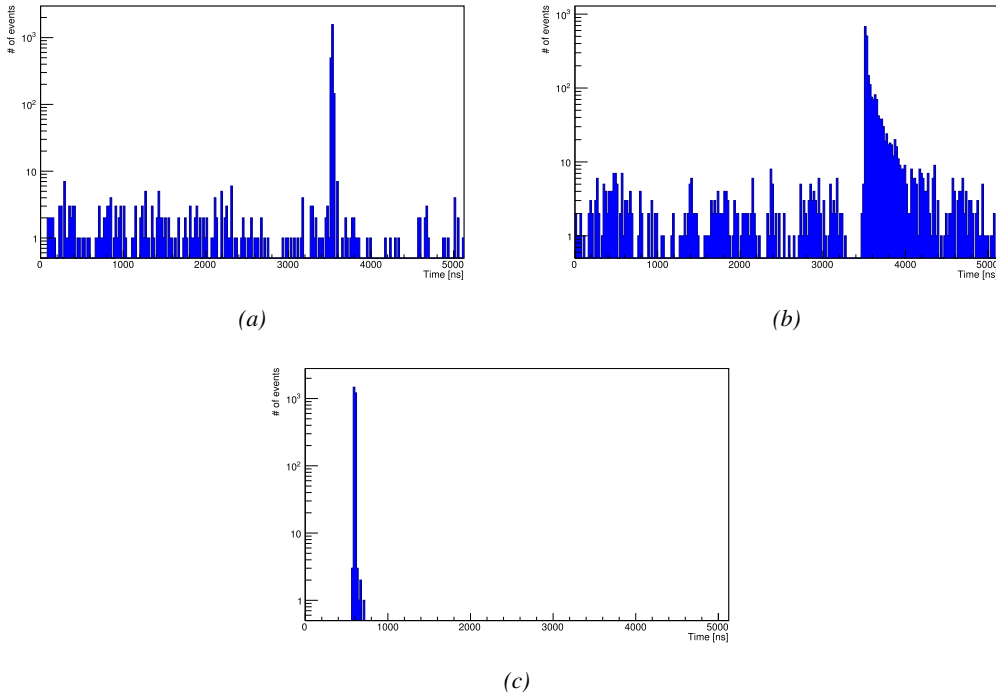


*Figure 6.18: The arrival time of the hits recorded in the gRPC tested with the CMS FEB (Figure 6.18a) and with the INFN preamplifiers (Figure 6.18b), and recorded in the CMS RE2 RPC tested with the INFN preamplifiers (Figure 6.18c).*

### 6.2.3 HARDROC 2 readout panel

The HAdronic RPC Digital Read-Out Chip (HARDROC) ASIC, as its name suggests, has been developed for RPC applications and in particular for the read-out RPCs of the Semi-Digital HCAL (SDHCAL) that is being studied in the perspective of the International Linear Collider (ILC). The SDHCAL detectors are required to have a high granularity compared to the CMS RPCs and hence, they use 1 cm<sup>2</sup> read-out pads instead of strips. This choice results in a huge number of channels. The ASIC is mounted directly on the read-out pannel for compactness as can be seen in Figure ?? and feature three thresholds to provide a semi-digital information.

The PETIROC that inspired the CMS RPCROC uses a similar technology than the one developed by the HARDROC and is manufactured by the same company. It is safe to conclude that the preliminary results obtained with the HARDROC electronics constitute a strong indication on the potential performance of a FEB developed specifically for CMS detectors. The leading institute in the development of the SDHCAL based on single-gap glass RPCs (gRPCs) is the Institut de Physique Nucléaire de Lyon (IPNL) which also played a great role in developing iRPCs for CMS.

A read-out pannel using the HARDROC 2 technology was lended by this institute and was tested onto a CMS RPC. Contrary to the tests with the INFN preamplifiers that were made using an RE2-2 CMS RPC built in 2007 for the second endcap disk of CMS, the choice was made to use an RE4-3 detector built during LS1 to equip the fourth endcap. Indeed, the pannel can't be sandwiched between two RPC gaps due to the embedded electronics and a single CMS RPC gap was used. At the time of this experiment, only RE4-3 gaps were available and the choice was made to change

3982 detector with respect to the previous series of tests conducted on the INFN preamplifiers. As for  
 3983 the INFN preamplifiers, the pannel has been tested on the gRPC built by UGent. The gRPC being  
 3984 smaller than the HARDROC read-out that was used for the experiment but thanks to the 2D read-out  
 3985 using pads, this was not a problem for the data acquisition.



(a)

(b)

*Figure 6.19: Experimental setups used to test the HARDROC2 electronics with a CMS RE4-3 gap (Figure 6.19a) and a gRPC gap built in Ghent (Figure 6.19b).*

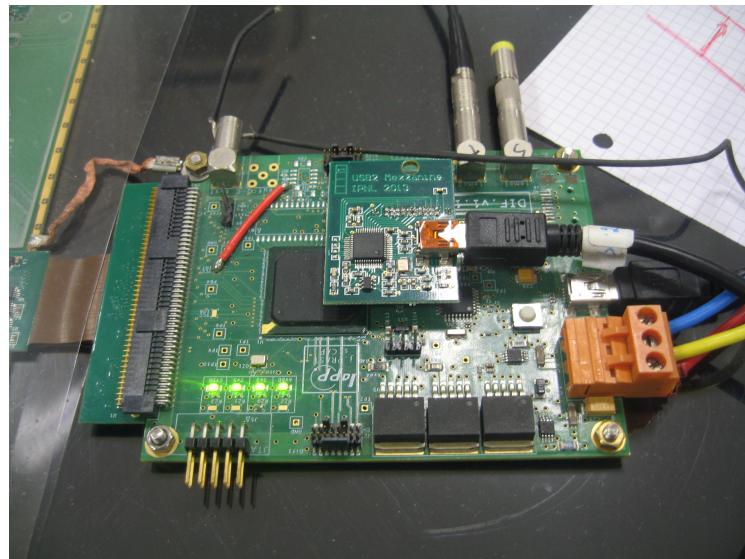


*Figure 6.20: HARDROC2 control chip with its "Mezzanine" used to collect the data from the different HARDROC ASICs and communicate with the computer. On top of the picture, the trigger is brought by a coaxial cable. The connection with the computer is assured by both the USB cables.*

3986 Once again, the experiment was conducted in the CMS RPC assembly laboratory at CERN and  
 3987 the setups are shown in Figure 6.19. The read-out panel is placed directly on top of the gaps and  
 3988 pressed against the detector surface thanks to weights. The same PMTs are used to provide a trigger

to the data acquisition. In the particular case of the HARDROC 2 electronics, the output signal does not correspond to the LVDS signals provided by the CMS FEB. Moreover, there would be more than 1500 channels to constantly monitor and unfortunately, there would not be enough VME TDC modules to use with the DAQ software designed for the experiment involving the INFN preamplifiers. Nevertheless, a custom-made DAQ software was designed by the members of IPNL's team to read-out the electronics through the chip presented in Figure 6.20. The data is stored in the buffer of the ASIC continuously and dumped into the computer when a trigger is signal is received.

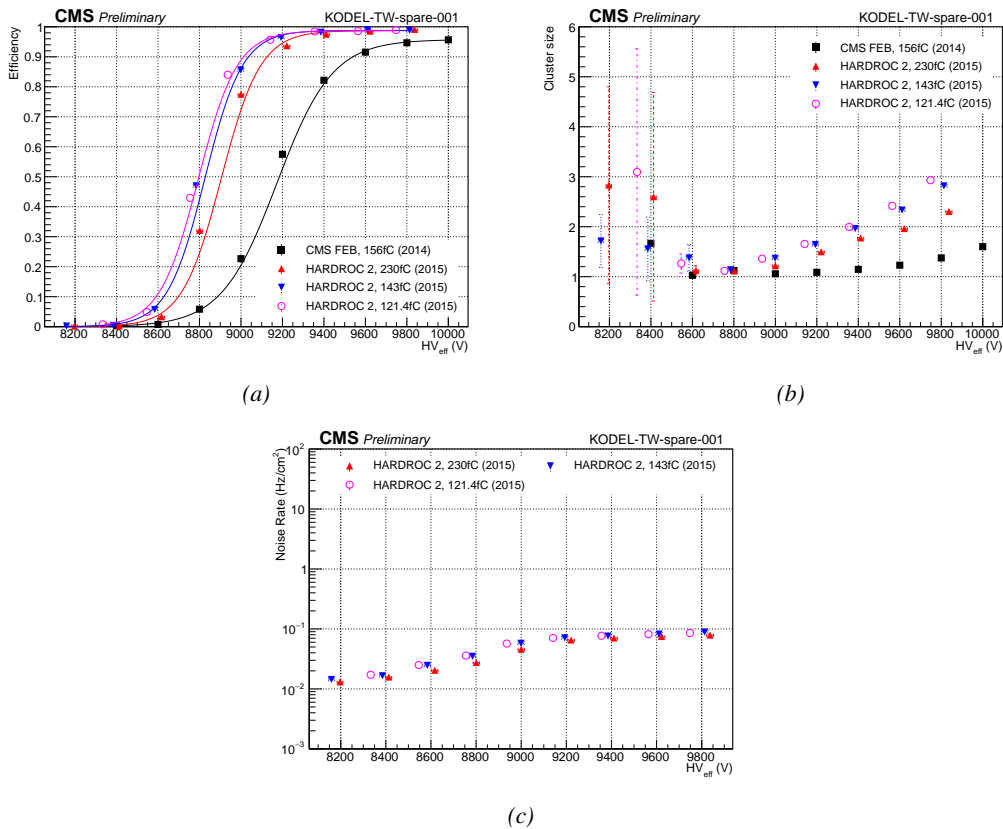


Figure 6.21: Efficiency (Figure 6.21a), cluster size (Figure 6.21b) and noise rate per unit area (Figure 6.21c) of the CMS RE4-3 detector tested in single gap mode with the standard CMS FEBs (black) and with the HARDROC 2 readout panel at different thresholds (red, blue and pink).

Data	$\epsilon_{max}$	$\lambda \cdot 10^{-2} \text{ V}^{-1}$	$HV_{50}$ (V)	$\epsilon_{WP}$	$HV_{WP}$ (V)
CMS FEB, 156fC (2014)	$(0.958 \pm 0.000)$	$(0.75 \pm 0.00)$	$(9174 \pm 1)$	$(0.94 \pm 0.00)$	$(9716 \pm 2)$
HARDROC 2, 230fC (2015)	$(0.987 \pm 0.002)$	$(1.06 \pm 0.04)$	$(8905 \pm 8)$	$(0.98 \pm 0.01)$	$(9333 \pm 17)$
HARDROC 2, 143fC (2015)	$(0.988 \pm 0.001)$	$(1.10 \pm 0.04)$	$(8826 \pm 8)$	$(0.98 \pm 0.01)$	$(9243 \pm 17)$
HARDROC 2, 121.4fC (2015)	$(0.987 \pm 0.001)$	$(1.07 \pm 0.04)$	$(8795 \pm 8)$	$(0.98 \pm 0.01)$	$(9220 \pm 17)$

Table 6.4: Results of the sigmoid fit (Formula 4.24) performed on the data presented in Figure 6.21a. The working point and its corresponding efficiency are computed using Formulas 4.24 and 4.25.

The results of the tests conducted with the HARDROC 2 on a CMS gap are presented in Fig-

ure 6.21 and Table 6.4. These results can hardly be compared to what was measured with the INFN preamplifiers as the detector was not tested using the single-gap mode. The tested thresholds are high compared to the ones displayed by the INFN preamplifiers and are of the order of magnitude of the current CMS FEB. Nevertheless, the performance of the detector equipped with this read-out pannel is measured to be better. Indeed, a shift of 400 to 500 V is observed at thresholds ranging from 230 to 121.4 fC. [Here it could be nice to bring an explanation to this observation.]

The cluster size is provided for information as a direct comparison of the cluster size measured with  $1\text{ cm}^2$  pads and long copper strips with width of a few cm is not possible. The measured cluster size at working voltage with the CMS FEB is consistent with what would be expected of a single-gap RPC. Indeed, the usage of two gaps in an OR system allows for a stronger overall gain and hence, the cluster size is greater. A more precise estimation of the charge spread inside of the gap is obtained using pads instead of strips. At working voltage, an avalanche is detected within less than two pads on average. An extra information could be used to further improve the spatial resolution of the detector. Indeed, as stated in the introduction of the Section, the HARDROC 2 is a semi-digital electronics and features three threshold levels. Tuning these thresholds would lead to an approximation of the induced charge profile over the neighbouring pads. A gaussian fit over the digitized distribution would give an estimation of the position of the avalanche center.

Finally, the noise measured in the electronics is of the same order of what had been measured in Figure 6.9c. It is safe to assume that the noise level in the case of a single-gap RPC is expected to be of the same order of magnitude than its double-gap counterpart as the noise mainly is electromagnetic. Figure 6.22 provides a clearer understanding of the position of the trigger PMTs and of the noise measured with the HARDROC. The noise of the electronics itself is very small and the read-out pannel is sensitive enough to measure the noise in the RPC gap. Indeed, except for a few visible hot spots, the observed noise profile corresponds perfectly to the spacer positions inside of the gap volume. The PET buttons used to maintain the uniformity of the gas volume cause noise at their proximity as they modify the local electric field.

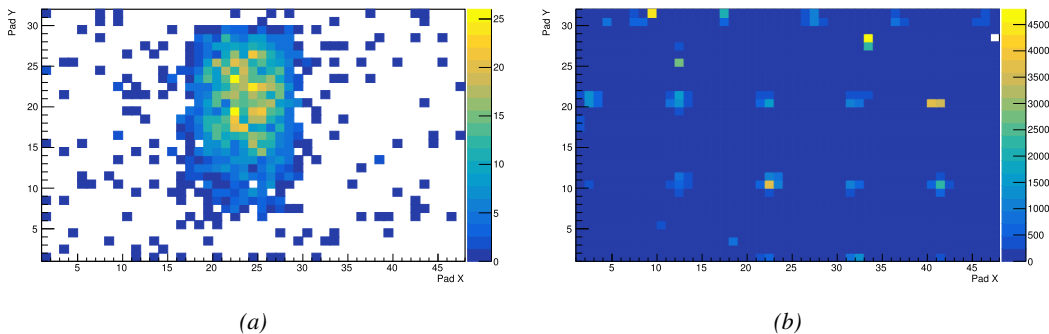


Figure 6.22: Measured muon (Figure 6.22a) and noise (Figure 6.22a) profiles in the read-out pads of the HARDROC 2 over a CMS RE4-3 gap. The inner structure of the gap and the presence of the spacers in the volume is visible.

The results of the experiment with the gRPC are provided in Figure 6.23 and Table 6.5. Unfortunately the gRPC had not been tested in single gap mode with the CMS FEB. Thus, a direct comparison is not possible as the data were not collected in similar conditions. The detector could only be tested with a single HARDROC 2 threshold setting (143 fC). As for the double-gap, the effi-

4027 ciciency of the single-gap reaches 95% at working voltage. The working voltage is consistent with the  
 4028 double-gap detector operated with the CMS FEB indicating that the HARDROC is more sensitive to  
 4029 lower charges. The difference in efficiency rising is consistent with the use of one gap versus two in  
 4030 the case of the CMS FEB.

4031 As discussed in the case of the CMS RE4-3 gap, the direct comparison of the cluster sizes is  
 4032 not possible. In this sense, the proximity of both results only is fortuitous. The cluster size of  
 4033 approximately 1.6 measured with the HARDROC 2 at working voltage is of the same order than  
 4034 what had previously been measured for the CMS gap indicating that at equivalent performance, the  
 4035 gain and hence, the induced charge could be comparable.

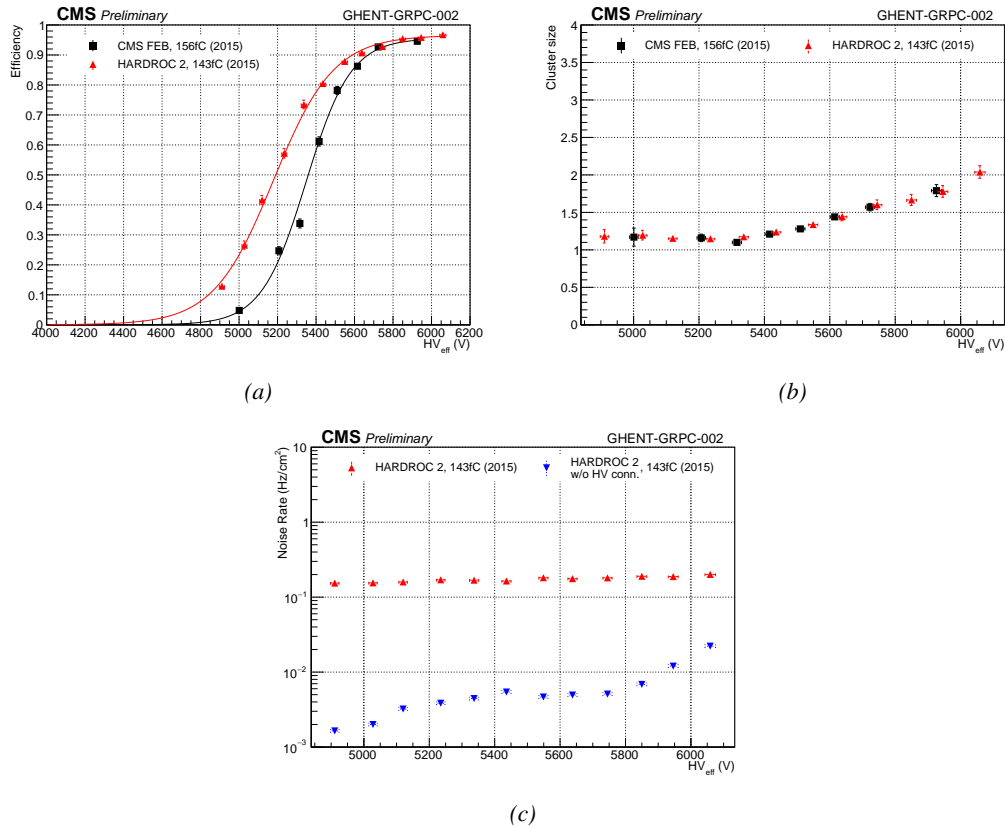


Figure 6.23: Efficiency (Figure 6.21a), cluster size (Figure 6.21b) and noise rate per unit area (Figure 6.21c) of the UGent gRPC tested in double-gap mode with the standard CMS FEBs (black) and in single-gap with the HARDROC 2 readout panel at a threshold of 143 fC (red).

Data	$\epsilon_{max}$	$\lambda \cdot 10^{-2} \text{ V}^{-1}$	$HV_{50}$ (V)	$\epsilon_{WP}$	$HV_{WP}$ (V)
CMS FEB, 156fC (2015)	$(0.956 \pm 0.007)$	$(0.86 \pm 0.04)$	$(5349 \pm 8)$	$(0.94 \pm 0.01)$	$(5839 \pm 23)$
HARDROC 2, 143fC (2015)	$(0.966 \pm 0.004)$	$(0.64 \pm 0.02)$	$(5179 \pm 7)$	$(0.95 \pm 0.01)$	$(5790 \pm 25)$

Table 6.5: Results of the sigmoid fit (Formula 4.24) performed on the data presented in Figure 6.23a. The working point and its corresponding efficiency are computed using Formulas 4.24 and 4.25.

4036 Finally, the noise measured in the electronics seemed higher than in the case of the CMS gap.

Looking closer to the noise profile provided in Figure 6.24, it can be seen that the noise measurement was affected by the HV connector. Indeed, the high noise measured in pads 41 and 42 along X and 22 to 25 along Y, corresponds exactly to the position of the HV connector on the cathode side. Contrary to the case of the CMS gap were the HV connector was far from the read-out area, the gRPC is smaller than the read-out and due to the poor grounding of the setup the electric field created by the HV connector could affect the read-out. Excluding the corresponding pads gives a much more reliable noise measurement as can be seen in Figure 6.23c. Through the noise profile, a better understanding of the gRPC uniformity can be obtained. First of all, the row corresponding to Y=16 seem consistently noisier than the neighbouring pads and could correspond to the glueing line that lies along this pad row. The noise increase along this line is not very clear though and no corresponding behaviour can be observed along the other glueing line along column X=31. But the gas volume corresponding to the largest glass plate, spreading from columns 31 to 47 along X and rows 1 to 16 clearly shows a stronger noise in its center. The detection area being small, only a few ceramic ball spacers were used to maintain the distance in between the electrodes. It is not impossible that the ball spacer located in the center of this volume popped out. Due to the absence of a spacer, the force applied by electric field onto the electrodes could have made the distance in between the electrodes smaller and artificially increased the observed electric field, also increasing the measured noise.

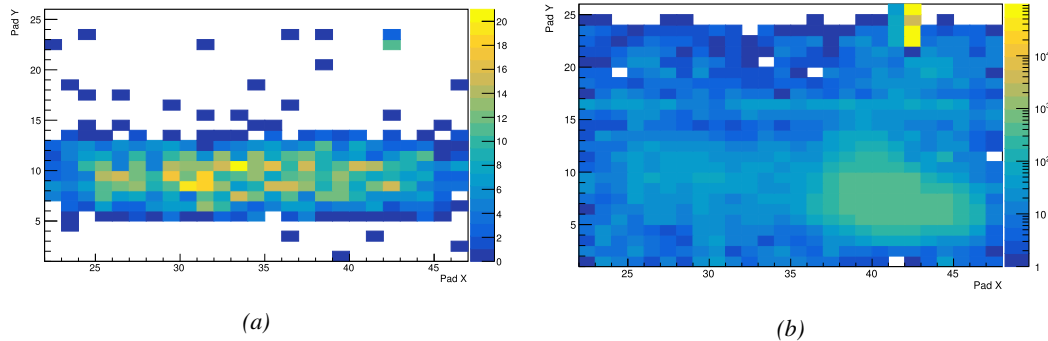


Figure 6.24: Measured muon (Figure 6.24a) and noise (Figure 6.24a) profiles in the read-out pads of the HARDROC 2 over a gRPC gap built by Ghent.



# 7

4054

4055

## Conclusions and outlooks

4056 **7.1 Conclusions**

4057 **7.2 Outlooks**



# A

4058

4059

## A data acquisition software for CAEN VME TDCs

4060

4061 Certifying detectors in the perspective of HL-LHC required to develop tools for the GIF++ experi-  
4062 ment. Among them was the C++ Data Acquisition (DAQ) software that allows to make the commu-  
4063 nications in between a computer and TDC modules in order to retrieve the RPC data [278]. In this  
4064 appendix, details about this software, as of how the software was written, how it functions and how  
4065 it can be exported to another similar setup, will be given.

### 4066 A.1 GIF++ DAQ file tree

4067 GIF++ DAQ source code is fully available on github at [https://github.com/afagot/GIF\\_](https://github.com/afagot/GIF_DAQ)  
4068 DAQ. The software requires 3 non-optional dependencies:

- 4069 • CAEN USB Driver, to mount the VME hardware,  
4070 • CAEN VME Library, to communicate with the VME hardware, and  
4071 • ROOT, to organize the collected data into a TTree.

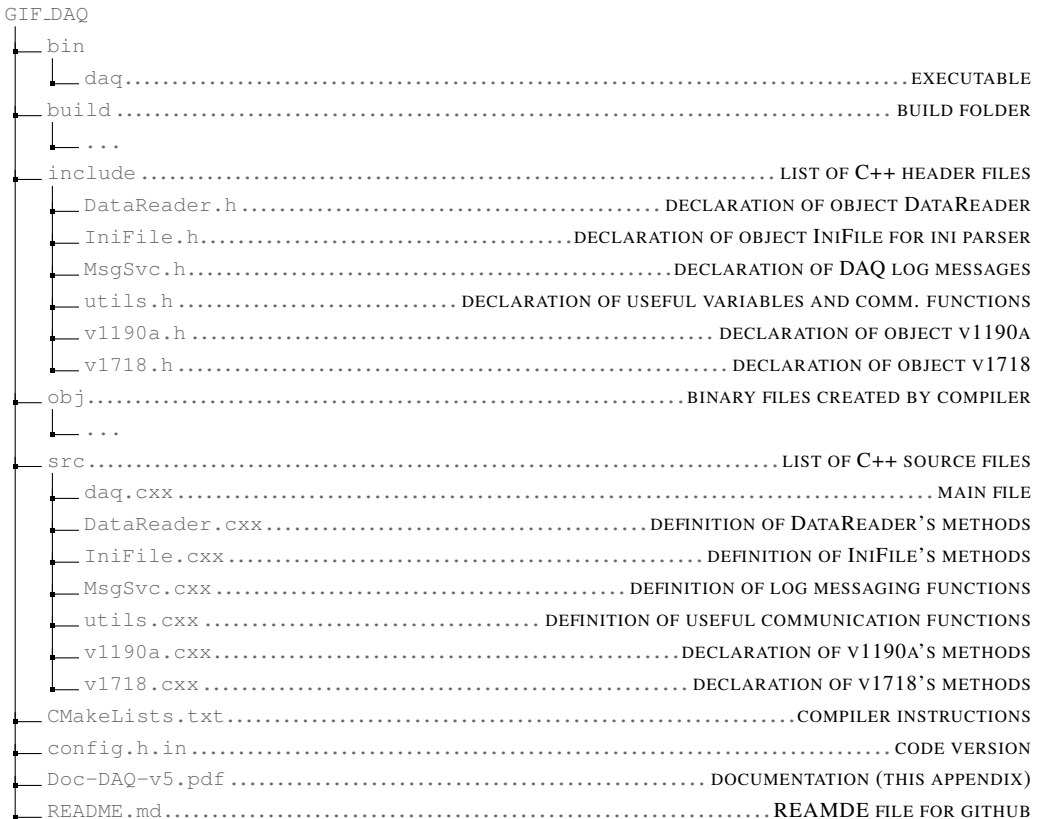
4072 The CAEN VME library will not be packaged by distributions and will need to be installed man-  
4073 ually. To compile the GIF++ DAQ project via a terminal, from the DAQ folder use the command:

```
4074 mkdir build  
4075 cd build  
cmake ..  
make install
```

4076 The source code tree is provided below along with comments to give an overview of the files' con-  
4077 tent. The different objects created for this project (`v1718`, `v1190a`, `IniFile` & `DataReader`) will be

4078 described in details in the following sections.

4079



4080

## A.2 Usage of the DAQ

4081 GIF++ DAQ, as used in GIF++, is not a standalone software. Indeed, the system being more complexe,  
 4082 the DAQ only is a sub-layer of the software architecture developped to control and monitor  
 4083 the RPCs that are placed into the bunker for performance study in an irradiated environment. The top  
 4084 layer of GIF++ is a Web Detector Control System (webDCS) application. The DAQ is only called  
 4085 by the webDCS when data needs to be acquired. The webDCS operates the DAQ through command  
 4086 line. To start the DAQ, the webDCS calls:

4087

```
4088     bin/daq /path/to/the/log/file/in/the/output/data/folder
```

4089

where `/path/to/the/log/file/in/the/output/data/folder` is the only argument required. This log file is important for the webDCS as this file contains all the content of the communication of the webDCS and the different systems monitored by the webDCS. Its content is constantly displayed during data taking for the users to be able to follow the operations. The communication messages are normally sent to the webDCS log file via the functions declared in file `MsgSvc.h`, typically `MSG_INFO(string message)`.

4090

### A.3 Description of the readout setup

The CMS RPC setup at GIF++ counts 5 V1190A Time-to-Digital Converter (TDC) manufactured by CAEN [264]. V1190A are VME units accepting 128 independent Multi-Hit/Multi-Event TDC channels whose signals are treated by 4 100 ps high performance TDC chips developed by CERN / ECP-MIC Division. The communication between the computer and the TDCs to transfer data is done via a V1718 VME master module also manufactured by CAEN and operated from a USB port [265]. These VME modules are all hosted into a 6U VME 6021 powered crate manufactured by W-Ie-Ne-R than can accommodate up to 21 VME bus cards [279]. These 3 components of the DAQ setup are shown in Figure A.1.

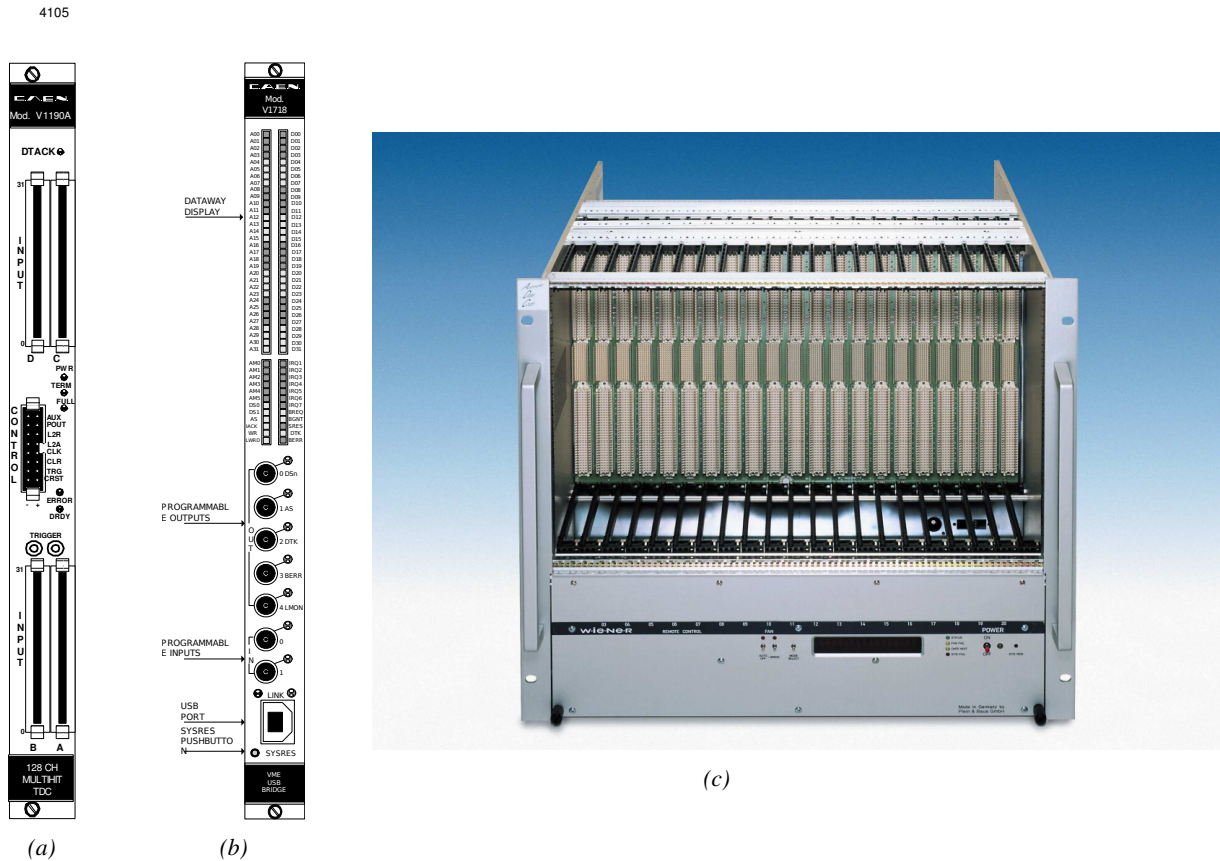


Figure A.1: (A.1a) View of the front panel of a V1190A TDC module [264]. (A.1b) View of the front panel of a V1718 Bridge module [265]. (A.1c) View of the front panel of a 6U 6021 VME crate [279].

### A.4 Data read-out

To efficiently perform a data readout algorithm, C++ objects to handle the VME modules (TDCs and VME bridge) have been created along with objects to store data and read the configuration file that comes as an input of the DAQ software.

#### A.4.1 V1190A TDCs

The DAQ used at GIF takes profit of the *Trigger Matching Mode* offered by V1190A modules. This setting is enabled through the method `v1190a::SetTrigMatching (int ntdcs)` where `ntdcs` is the total number of TDCs in the setup this setting needs to be enabled for (Source Code A.1). A trigger matching is performed in between a trigger time tag, a trigger signal sent into the TRIGGER input of the TDC visible on Figure A.1a, and the channel time measurements, signals recorded from the detectors under test in our case. Control over this data acquisition mode, explained through Figure A.2, is offered via 4 programmable parameters:

- **match window:** the matching between a trigger and a hit is done within a programmable time window. This is set via the method

```
void v1190a::SetTrigWindowWidth(UINT windowWidth, int ntdcs)
```

- **window offset:** temporal distance between the trigger tag and the start of the trigger matching window. This is set via the method

```
void v1190a::SetTrigWindowWidth(UINT windowWidth, int ntdcs)
```

- **extra search margin:** an extended time window is used to ensure that all matching hits are found. This is set via the method

```
void v1190a::SetTrigSearchMargin(UINT searchMargin, int ntdcs)
```

- **reject margin:** older hits are automatically rejected to prevent buffer overflows and to speed up the search time. This is set via the method

```
void v1190a::SetTrigRejectionMargin(UINT rejectMargin, int ntdcs)
```

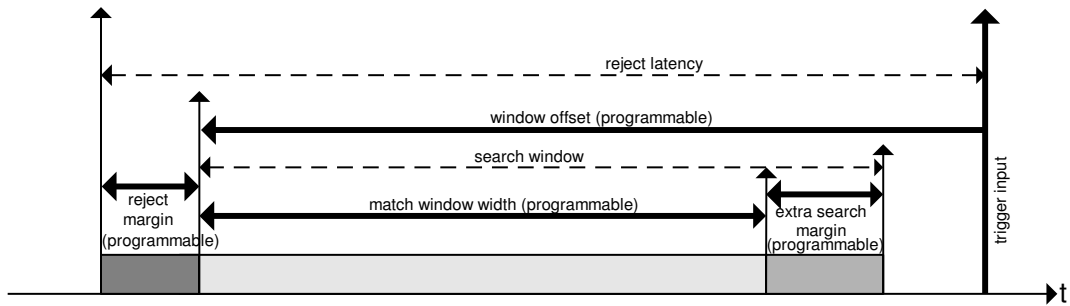


Figure A.2: Module V1190A Trigger Matching Mode timing diagram [264].

Each of these 4 parameters are given in number of clocks, 1 clock being 25 ns long. It is easy to understand at this level that there are 3 possible functioning settings:

- **1:** the match window is entirely contained after the trigger signal,
- **2:** the match window overlaps the trigger signal, or
- **3:** the match window is entirely contained before the trigger signal as displayed on Figure A.2.

In both the first and second cases, the sum of the window width and of the offset can be set to a maximum of 40 clocks, which corresponds to 1  $\mu$ s. Evidently, the offset can be negative, allowing

4138 for a longer match window, with the constraint of having the window ending at most 1  $\mu$ s after the  
4139 trigger signal. In the third case, the maximum negative offset allowed is of 2048 clocks (12 bit) cor-  
4140 responding to 51.2  $\mu$ s, the match window being strictly smaller than the offset. In the case of GIF++,  
4141 the choice has been made to use this last setting by delaying the trigger signal. During the studies  
4142 performed in GIF++, both the efficiency of the RPCs, probed using a muon beam, and the noise or  
4143 gamma background rate are monitored. The extra search and reject margins are left unused.

4144 To probe the efficiency of RPC detectors, the trigger time tag is provided by the coïncidence of  
4145 scintillators when a bunch of muons passes through GIF++ area is used to trigger the data acquisi-  
4146 tion. For this measurement, it is useful to reduce the match window width only to contain the muon  
4147 information. Indeed, the delay in between a trigger signal and the detection of the corresponding  
4148 muon in the RPC being very contant (typically a few tens of ns due to jitter and cable length), the  
4149 muon signals are very localised in time. Thus, due to a delay of approximalety 325 ns in between  
4150 the muons and the trigger, the settings were chosen to have a window width of 24 clocks (600 ns)  
4151 centered on the muon peak thanks to a negative offset of 29 clocks (725 ns).

4152 On the otherhand, monitoring the rates don't require for the DAQ to look at a specific time window.  
4153 It is important to integrate enough time to have a robust measurement of the rate as the number of  
4154 hits per time unit. The triggering signal is provided by the pulse generator integrated into the com-  
4155 munication module V1718 at a frequency of 100 Hz to ensure that the data taking occurs in a random  
4156 way, uncorrelated with beam physics, to probe only the irradiation spectrum on the detectors. The  
4157 match window is set to 400 clocks (10  $\mu$ s) and the negative offset to 401 clocks as it needs to exceed  
4158 the value of the match window.

4159  
4160 The v1190a object, defined in the DAQ software as in Source Code A.1, offers the possil-  
4161 ity to store all TDCs in the readout setup into a single object containing a list of hardware ad-  
4162 dresses (addresses to access the TDCs' buffer through the VME crate) and each constructor and  
4163 method acts on the list of TDCs to set the different acquisition parameters as describe above.  
4164 The type of trigger matching is chosen with `v1190a::SetTrigMatching()` and the time substrac-  
4165 tion, used to have a time measurement referring to the beggining of the time window, is set by  
4166 `v1190a::SetTrigTimeSubtraction()`. Then, the wiwdow width and offset are respectively set  
4167 thanks to `v1190a::SetTrigWindowWidth()` and `v1190a::SetTrigWindowOffset()`. The rejection  
4168 and extra search margin, even if left unused and hence set to a default value of 0, can be set through  
4169 `v1190a::SetTrigRejectionMargin()` and `v1190a::SetTrigSearchMargin()`. These methods are  
4170 then called in `v1190a::SetTrigConfiguration()` that uses the information contained in the config-  
4171 uration file `IniFile *iniFile` to set the different TDC parameters. A thorough explaination of the  
4172 content of the configuration file is provided in Section A.5.2.

4173  
4174 Among the other methods of class `v1190a` can be found a set of the detection mode (`v1190a::SetTDC`  
4175 `DetectionMode()`), of the TDC time resolution (`v1190a::SetTDCResolution()`), of the dead time  
4176 in between two consecutive signals recorded into a single channel (`v1190a::SetTDCDeadTime()`) or  
4177 of the maximal number of signals that can be recorded per event (`v1190a::SetTDCEventSize()`). To  
4178 help with setting these parameters, `enum` were used (`EdgeMode`, `Resolution`, `DeadTime` and `HitMax`  
4179 are defined in `include/v1190a.h`).

```

4180
class v1190a
{
    private :
        long Handle;
        vector<Data32> Address;
        CVDataWidth DataWidth;
        CVAAddressModifier AddressModifier;

    public:

        v1190a(long handle, IniFile *inifile, int ntdcs);
        ~v1190a();
        Data16 write_op_reg(Data32 address, int code, string error);
        Data16 read_op_reg(Data32 address, string error);
        void Reset(int ntdcs);
        void Clear(int ntdcs);
        void TestWR(Data16 value, int ntdcs);
        void CheckTDCStatus(int ntdcs);
        void CheckCommunication(int ntdcs);
        void SetTDCTestMode(Data16 mode, int ntdcs);
        void SetTrigMatching(int ntdcs);
        void SetTrigTimeSubtraction(Data16 mode, int ntdcs);
        void SetTrigWindowWidth(Uint windowHeight, int ntdcs);
        void SetTrigWindowOffset(Uint windowOffset, int ntdcs);
        void SetTrigSearchMargin(Uint searchMargin, int ntdcs);
        void SetTrigRejectionMargin(Uint rejectMargin, int ntdcs);
        void GetTrigConfiguration(int ntdcs);
        void SetTrigConfiguration(IniFile *inifile, int ntdcs);
        void SetTDCDetectionMode(Data16 mode, int ntdcs);
        void SetTDCResolution(Data16 lsb, int ntdcs);
        void SetTDCDeadTime(Data16 time, int ntdcs);
        void SetTDCHeadTrailer(Data16 mode, int ntdcs);
        void SetTDCEventSize(Data16 size, int ntdcs);
        void SwitchChannels(IniFile *inifile, int ntdcs);
        void SetIRQ(Data32 level, Data32 count, int ntdcs);
        void SetBlockTransferMode(Data16 mode, int ntdcs);
        void Set(IniFile *inifile, int ntdcs);
        void CheckStatus(CVErrorCodes status) const;
        int ReadBlockD32(Uint tdc, const Data16 address,
                           Data32 *data, const Uint words, bool ignore_berr);
        Uint Read(RAWData *DataList, int ntdcs);
};

4181

```

4182       *Source Code A.1: Description of C++ object v1190a.*

4183       The detection mode corresponds to the type of edge detection the TDC will be using to  
 4184       record the data. The TDCs can record the time stamp of the leading edge alone, of the trailing edge  
 4185       alone, of both or they can operate in pair mode, meaning that the leading edge is recorded together  
 4186       with the time difference in between leading and trailing edges. This last mode is not very practical  
 4187       for the case of GIF++ measurements as the information is coded into a single words in the TDC's  
 4188       buffer, putting strong constraints on the time window and duration of the input signals. Indeed,  
 4189       when recording the edges individually (single edge or both edges), a 32-bit word, of which 18 are  
 4190       used to provide the time information alone, is stored into memory for each signal edge. With the  
 4191       pair mode, instead of having one 32-bit word per edge, only a single 32-bit word is written of which  
 4192       12 are used for the leading edge time information and 6 for the width of the pulse, as described on  
 4193       p73 of reference [264]. This way, even though the pair mode is convenient to use as it automatically

4194 correlates a leading edge with the corresponding signal width in a single word, it is advised to be  
 4195 careful when using it and to be aware of the extra time constraints (for both leading time and signal  
 4196 width) that will come for choosing this setting. If it is necessary to work with large input signals,  
 4197 the mode recording both edges will be preferred to the pair mode and the association of a leading  
 4198 and trailing edges pair will then be performed offline by the user. Then, the time resolution is to be  
 4199 chosen in a range from 100 to 800 ps, the dead time in a range from 5 to 100 ns, and the maximal  
 4200 number of hits per event in a range from 0 to 128 with the possibility to choose to have no limits.

#### 4201 A.4.2 DataReader

4202 Enabled thanks to `v1190a::SetBlockTransferMode()`, the data transfer is done via Block Transfer  
 4203 (BLT). Using BLT allows to transfer a fixed number of events called a *block*. This is used together  
 4204 with an Almost Full Level (AFL) of the TDCs' output buffers, defined through `v1190a::SetIRQ()`.  
 4205 This AFL gives the maximum amount of 32735 words (16 bits, corresponding to the depth of a TDC  
 4206 output buffer) that can be written in a buffer before an Interrupt Request (IRQ) is generated and seen by  
 4207 the VME Bridge V1718, which sends a `BUSY` signal intended to stopping the data acquisition during  
 4208 the transfer of the content of each TDC buffers before resuming. For each trigger, 6 words or more  
 4209 are written into the TDC buffer:

- 4210 • **a global header** providing information of the event number since the beginning of the data  
 4211 acquisition,
- 4212 • **a TDC header** which is enabled thanks to `v1190a::SetTDCHeadTrailer()`,
- 4213 • **the TDC data (if any)**, 1 for each hit recorded during the event, providing the channel and the  
 4214 time stamp associated to the hit,
- 4215 • **a TDC error** providing error flags,
- 4216 • **a TDC trailer** which is enabled thanks to `v1190a::SetTDCHeadTrailer()`,
- 4217 • **a global trigger time tag** that provides the absolute trigger time relatively to the last reset,  
 4218 and
- 4219 • **a global trailer** providing the total word count in the event.

4220 CMS RPC FEEs provide with 100 ns long LVDS output signals that are injected into the TDCs'  
 4221 input. Any avalanche signal that gives a signal above the FEEs threshold is thus recorded by the  
 4222 TDCs as a hit within the match window. Each hit is assigned to a specific TDC channel with a time  
 4223 stamp, with a precision of 100 ps. The reference time,  $t_0 = 0$ , is provided by the beginning of the  
 4224 match window. Thus for each trigger, coming from a scintillator coincidence or the pulse generator,  
 4225 a list of hits is stored into the TDCs' buffers and will then be transferred into a ROOT Tree.  
 4226 When the BLT is used, it is easy to understand that the maximum number of words that have been set  
 4227 as AFL will not be a finite number of events or, at least, the number of events that would be recorded  
 4228 into the TDC buffers will not be a multiple of the block size. In the last BLT cycle to transfer data,  
 4229 the number of events to transfer will most probably be lower than the block size. In that case, the  
 4230 TDC can add fillers at the end of the block but this option requires to send more data to the computer  
 4231 and is thus a little slower. Another solution is to finish the transfer after the last event by sending a  
 4232 bus error that states that the BLT reached the last event in the pile. This method has been chosen in

4233   GIF++.

4234   Due to irradiation, an event in GIF++ can count up to 300 words per TDC. A limit of 4096 words  
 4235   (12 bits) has been set to generate IRQ which represent from 14 to almost 700 events depending on  
 4236   the average of hits collected per event. Then the block size has been set to 100 events with enabled  
 4237   bus errors. When an AFL is reached for one of the TDCs, the VME bridge stops the acquisition by  
 4238   sending a BUSY signal.

4239

4240   The data is then transferred one TDC at a time into a structure called `RAWData` (Source Code A.2).  
 4241   Note that the structure as presented here is used when a single edge detection is used as there is only  
 4242   one time stamp list associated to the hits. When using detection on both edges, a second time stamp  
 4243   list could be added and when using pair detection, a list with the signal width could be added instead.  
 4244

```
4245   struct RAWData {
    vector<int> *EventList;
    vector<int> *NHitsList;
    vector<int> *QFlagList;
    vector<vector<int> > *ChannelList;
    vector<vector<float> > *TimeStampList;
};
```

4246

*Source Code A.2: Description of data holding C++ structure `RAWData`.*

```
4247 class DataReader
{
    private:
        bool StopFlag;
        IniFile *iniFile;
        Data32 MaxTriggers;
        v1718 *VME;
        int nTDCs;
        v1190a *TDCs;
        RAWData TDCData;

    public:
        DataReader();
        virtual ~DataReader();
        void SetIniFile(string inifilename);
        void SetMaxTriggers();
        Data32 GetMaxTriggers();
        void SetVME();
        void SetTDC();
        int GetQFlag(Uint it);
        void Init(string inifilename);
        void FlushBuffer();
        void Update();
        string GetFileName();
        void WriteRunRegistry(string filename);
        void Run();
};
```

4248

*Source Code A.3: Description of C++ object `DataReader`.*

4249

In order to organize the data transfer and the data storage, an object called `DataReader` was  
 4250   created (Source Code A.3). On one hand, it has `v1718` and `v1190a` objects as private members for  
 4251   communication purposes, such as VME modules settings via the configuration file `*iniFile` or data

4252 read-out through `v1190a::Read()` and on the other hand, it contains the structure `RAWData` that allows  
 4253 to organise the data in vectors reproducing the tree structure of a ROOT file.  
 4254 Each event is transferred from `TDCData` and saved into branches of a ROOT `TTree` as 3 integers  
 4255 that represent the event ID (`EventCount`), the number of hits read from the TDCs (`nHits`), and the  
 4256 quality flag that provides information for any problem in the data transfer (`qflag`), and 2 lists of  
 4257 `nHits` elements containing the fired TDC channels (`TDCCh`) and their respective time stamps (`TDCTS`),  
 4258 as presented in Source Code A.4. The ROOT file file is named using information contained into  
 4259 the configuration file, presented in section A.5.2. The needed information is extracted using method  
 4260 `DataReader::GetFileName()` and allow to build the output filename format `ScanXXXXXX_HVX_DAQ.root`  
 4261 where `ScanXXXXXX` is a 6 digit number representing the scan number into GIF++ database and `HVX`  
 4262 the HV step within the scan that can be more than a single digit. An example of ROOT data file is  
 4263 provided with Figure A.3.

```
4264
  RAWData TDCData;
  TFile *outputFile = new TFile(outputFileName.c_str(), "recreate");
  TTree *RAWDataTree = new TTree("RAWData", "RAWData");

  int EventCount = -9;
  int nHits = -8;
  int qflag = -7;
  vector<int> TDCCh;
  vector<float> TDCTS;

  RAWDataTree->Branch("EventNumber", &EventCount, "EventNumber/I");
  RAWDataTree->Branch("number_of_hits", &nHits, "number_of_hits/I");
  RAWDataTree->Branch("Quality_flag", &qflag, "Quality_flag/I");
  RAWDataTree->Branch("TDC_channel", &TDCCh);
  RAWDataTree->Branch("TDC_TimeStamp", &TDCTS);

  //...
  //Here read the TDC data using v1190a::Read() and place it into
  //TDCData for as long as you didn't collect the requested amount
  //of data.
  //...

  for(Uint i=0; i<TDCData.EventList->size(); i++) {
    EventCount = TDCData.EventList->at(i);
    nHits = TDCData.NHitsList->at(i);
    qflag = TDCData.QFlagList->at(i);
    TDCCh = TDCData.ChannelList->at(i);
    TDCTS = TDCData.TimeStampList->at(i);
    RAWDataTree->Fill();
  }
}
```

4266 *Source Code A.4: Highlight of the data transfer and organisation within `DataReader::Run()` after the data  
 has been collected into `TDCData`.*

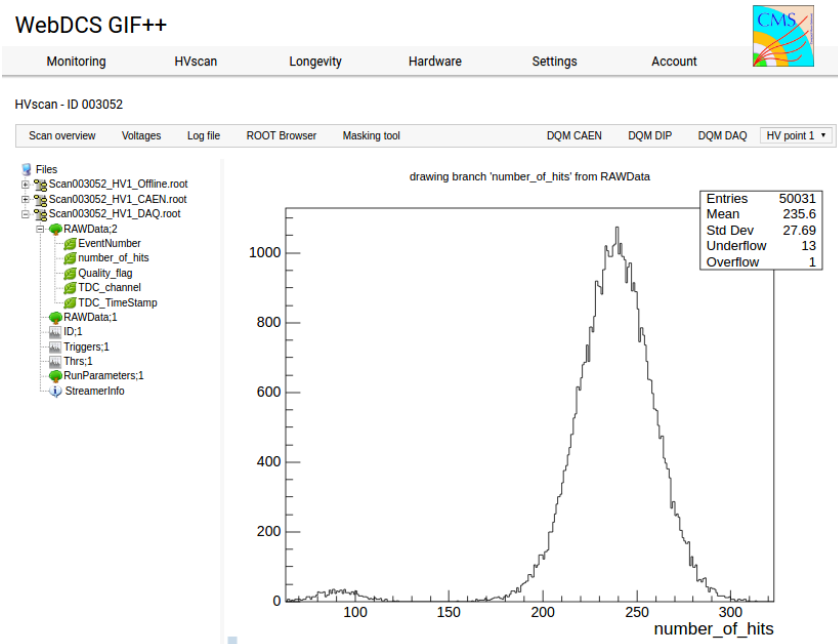


*Figure A.3: Structure of the ROOT output file generated by the DAQ. The 5 branches (EventNumber, number\_of\_hits, Quality\_flag, TDC\_channel and TDC\_TimeStamp) are visible on the left panel of the ROOT browser. On the right panel is visible the histogram corresponding to the variable nHits. In this specific example, there were approximately 50k events recorded to measure the gamma irradiation rate on the detectors. Each event is stored as a single entry in the TTree.*

#### 4267 A.4.3 Data quality flag

4268 Among the parameters that are recorded for each event, the quality flag is determined on the fly  
 4269 by checking the data recorded by every single TDC. An `enum` called `QualityFlag` was written to  
 4270 associate the key `GOOD` to the integer 1 and `CORRUPTED` to 0. From method `v1190a::Read()`, it can  
 4271 be understood that the content of each TDC buffer is readout one TDC at a time. Entries are created  
 4272 in the data list for the first TDC and then, when the second buffer is readout, events corresponding  
 4273 to entries that have already been created to store data for the previous TDC are added to the existing  
 4274 list element. On the contrary, when an event entry has not been yet created in the data list, a new  
 4275 entry is created.

4276 It is possible that each TDC buffer contains a different number of events. In cases where the first  
 4277 element in the buffer list is an event for corresponds to a new entry, the difference in between the  
 4278 entry from the buffer and the last entry in the data list is recorded and checked. If it is greater than 1,  
 4279 what should never be the case, the quality flag is set to `CORRUPTED` for this TDC and an empty entry  
 4280 is created in the place of the missing ones. Missing entries are believe to be the result of a bad hold  
 4281 on the TDC buffers at the moment of the readout. Indeed, the software hold is effective only on 1  
 4282 TDC at a time and no solution as been found yet to completely block the writting in the buffers when  
 4283 an IRQ is received.

4284 At the end of each BLT cycle, the ID of the last entry stored for each TDC buffer is not recorded.  
 4285 When starting the next cycle, if the first entry in the pile corresponds to an event already existing  
 4286 in the list, the readout will start from this list element and will not be able to check the difference

4287 in between this entry's ID and the one of the last entry that was recorded for this TDC buffer in  
 4288 the previous cycle. In the case events were missing, the flag stays at its initial value of 0, which is  
 4289 similar to CORRUPTED and it is assumed that then this TDC will not contribute to number\_of\_hits,  
 4290 TDC\_channel or TDC\_TimeStamp. Finally, since there will be 1 RAWData entry per TDC for each event  
 4291 (meaning nTDCs entries, referring to DataReader private attribute), the individual flags of each TDC  
 4292 will be added together. The final format is an integer composed nTDCs digits where each digit is the  
 4293 flag of a specific TDC. This is constructed using powers of 10 like follows:

4294        TDC 0: QFlag =  $10^0 \times \text{QualityFlag}$

4295        TDC 1: QFlag =  $10^1 \times \text{QualityFlag}$

4296        ...

4297        TDC N: QFlag =  $10^N \times \text{QualityFlag}$

4298        and the final flag to be with N digits:

4299        QFlag = n....3210

4300        each digit being 1 or 0. Below is given an example with a 4 TDCs setup.

4301        If all TDCs were good : QFlag = 1111,

4302        but if TDC 2 was corrupted : QFlag = 1011.

4303        When data taking is over and the data contained in the dynamical RAWData structure is transferred  
 4304 to the ROOT file, all the 0s are changed into 2s by calling the method DataReader::GetQFlag().  
 4305 This will help translating the flag without knowing the number of TDCs beforehand. Indeed, a flag  
 4306 111 could be due to a 3 TDC setup with 3 good individual TDC flags or to a more than 3 TDC setup  
 4307 with TDCs those ID is greater than 2 being CORRUPTED, thus giving a 0.

4308        The quality flag has been introduced quite late, in October 2017 only, to the list of GIFT++ DAQ  
 4309 parameters to be recorded into the output ROOT file. Before this addition, the missing data, corrupting  
 4310 the quality for the offline analysis, was contributing to artificially fill data with lower multiplicity.  
 4311 Looking at TBranch number\_of\_hits provides an information about the data of the full GIFT++  
 4312 setup. When a TDC is not able to transfer data for a specific event, the effect is a reduction of the  
 4313 total number of hits recorded in the full setup, this is what can be seen from Figure A.4. After offline  
 4314 reconstruction detector by detector, the effect of missing events can be seen in the artificially filled  
 4315 bin at multiplicity 0 shown in Figure A.5. Nonetheless, for data with high irradiation levels, as it is  
 4316 the case for Figure A.5a, discarding the fake multiplicity 0 data can be done easily during the offline  
 4317 analysis. At lower radiation, the missing events contribution becomes more problematic as the mul-  
 4318 tiplicity distribution overlaps the multiplicity 0 and that in the same time the proportion of missing  
 4319 events decreases. Attempts to fit the distribution with a Poisson or skew distribution function were  
 4320 not conclusive and this very problem has been at the origin of the quality flag that allows to give a  
 4321 non ambiguous information about each event quality.

4322

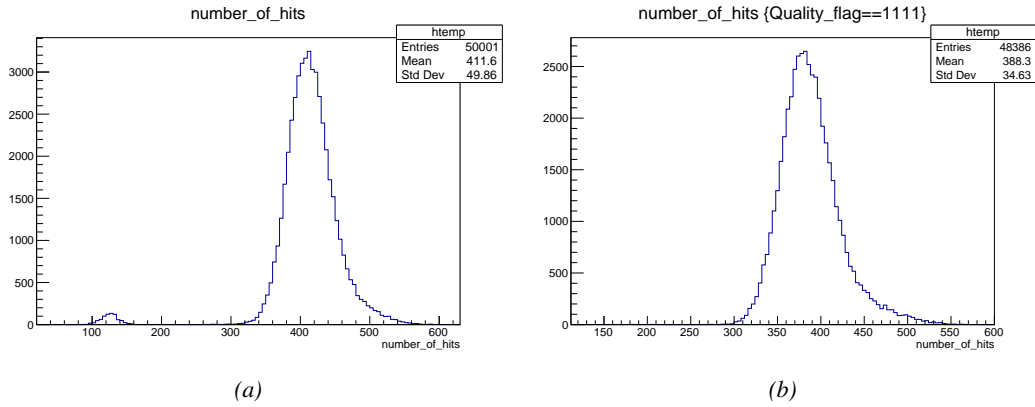


*Figure A.4: The effect of the quality flag is explained by presenting the content of TBranch `number_of_hits` of a data file without `Quality_flag` in Figure A.4a and the content of the same TBranch for data corresponding to a `Quality_flag` where all TDCs were labelled as `GOOD` in Figure A.4b taken with similar conditions. It can be noted that the number of entries in Figure A.4b is slightly lower than in Figure A.4a due to the excluded events.*

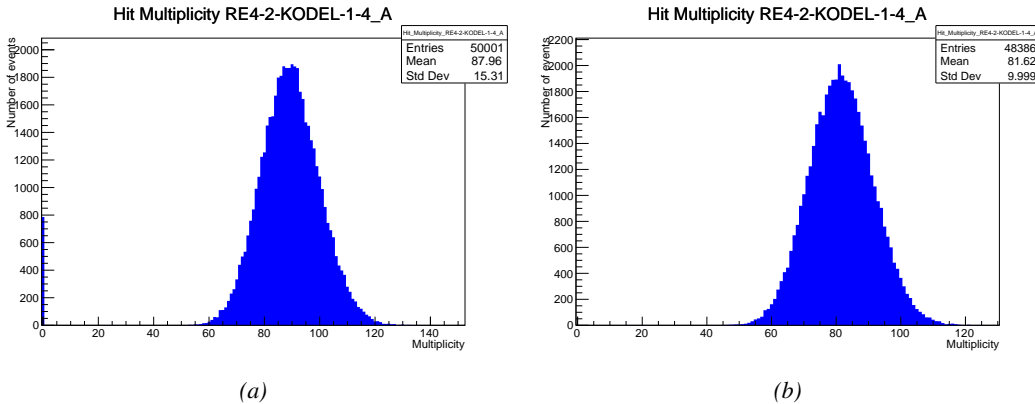


*Figure A.5: Using the same data as previously showed in Figure A.4, the effect of the quality flag is explained by presenting the reconstructed hit multiplicity of a data file without `Quality_flag` in Figure A.5a and the reconstructed content of the same RPC partition for data corresponding to a `Quality_flag` where all TDCs were labelled as `GOOD` in Figure A.5b taken with similar conditions. The artificial high content of bin 0 is completely suppressed.*

## 4323 A.5 Communications

4324 To ensure data readout and dialog in between the machine and the TDCs or in between the webDCS  
 4325 and the DAQ, different communication solutions were used. First of all, it is important to have a  
 4326 module to allow the communication in between the TDCs and the computer from which the DAQ  
 4327 operates. When this communication is effective, shifters using the webDCS to control data taking  
 4328 can thus send instructions to the DAQ.

4330 **A.5.1 V1718 USB Bridge**

4331 In the previous section, the data transfer as been discussed. The importance of the `v1718` object  
 4332 (Source Code A.5), used as private member of `DataReader`, was not explicited. VME master  
 4333 modules are used for communication purposes as they host the USB port that connects the pow-  
 4334 ered crate buffer to the computer were the DAQ is installed. From the source code point of view,  
 4335 this object is used to control the communication status, by reading the returned error codes with  
 4336 `v1718::CheckStatus()`, or to check for IRQs coming from the TDCs through `v1718::CheckIRQ()`.  
 4337 To ensure that triggers are blocked at the hardware level, a NIM pulse is sent out of one of the two  
 4338 first programmable outputs of the module (`v1718::SendBUSY()`) to the VETO of the coïndidence  
 4339 module where the trigger signals originate. As long as this signal is ON, no trigger can reach the  
 4340 TDCs anymore. Finally, used in the case of noise and background measurements in which the trig-  
 4341 ger needs not to be provided by the muon beam but by an uncorrelated source, a pulse generator  
 4342 is enabled with `v1718::RDMTriggerPulse()`. The "random" pulse is sent through the third and  
 4343 fourth outputs of the module. Both the BUSY signal and the random pulse are shaped in the method  
 4344 `v1718::SetPulsers()` where the number of pulses to be generated, their width, as well as the period  
 4345 of the pulse generator is defined.

4346

```
class v1718{
    private:
        int             Handle;
        Data32          Data;           // Data
        CVIRQLevels    Level;         // Interrupt level
        CVAddressModifier AM;          // Addressing Mode
        CVDataWidth     DataSize;      // Data Format
        Data32          BaseAddress;   // Base Address

    public:
        v1718(IniFile *inifile);
        ~v1718();
        long            GetHandle(void) const;
        int             SetData(Data16 data);
4347      Data16          GetData(void);
        int             SetLevel(CVIRQLevels level);
        CVIRQLevels    GetLevel(void);
        int             SetAM(CVAddressModifier am);
        CVAddressModifier GetAM(void);
        int             SetDatasize(CVDataWidth datasize);
        CVDataWidth     GetDataSize(void);
        int             SetBaseAddress(Data16 baseaddress);
        Data16          GetBaseAddress(void);
        void            CheckStatus(CVErrorCodes status) const;
        bool            CheckIRQ();
        void            SetPulsers(UINT RDM_Frequency);
        void            SendBUSY(PulserLevel level);
        void            RDMTriggerPulse(PulserLevel level);
};
```

4348

*Source Code A.5: Description of C++ object v1718.*

4349 **A.5.2 Configuration file**

4350 The DAQ software takes as input a configuration file written using INI standard [280]. This file is  
 4351 partly filled with the information provided by the shifters when starting data acquisition using the  
 4352 webDCS, as shown by Figure A.6. This information is written in section [**General**] and will later  
 4353 be stored in the ROOT file that contains the DAQ data as can be seen from Figure A.3. Indeed,  
 4354 another TTree called `RunParameters` as well as the 2 histograms `ID`, containing the scan number,  
 4355 start and stop time stamps, and `Triggers`, containing the number of triggers requested by the shifter,  
 4356 are available in the data files. Moreover, `ScanID` and `HV` are then used to construct the file name  
 4357 thanks to the method `DataReader::GetFileName()`.

Chamber	RE2-2-NPD-BARC-8	RE2-2-CERN-105	RE2-2-NPD-BARC-9	RE2-2-CERN-105	RE4-2-KODEL-1-4	Max triggers
HV <sub>eff</sub> 1	8600	8500	8600	8500	6500	
HV <sub>eff</sub> 2	8700	8600	8700	8600	6600	
HV <sub>eff</sub> 3	8800	8700	8800	8700	6700	
HV <sub>eff</sub> 4	8900	8800	8900	8800	6800	
HV <sub>eff</sub> 5	9000	8900	9000	8900	6900	
HV <sub>eff</sub> 6	9100	9000	9100	9000	7000	
HV <sub>eff</sub> 7	9200	9100	9200	9100	7100	
HV <sub>eff</sub> 8	9300	9200	9300	9200	7200	
HV <sub>eff</sub> 9	9400	9300	9400	9300	7300	
HV <sub>eff</sub> 10	9500	9400	9500	9400	7400	

Figure A.6: WebDCS DAQ scan page. On this page, shifters need to choose the type of scan (Rate, Efficiency or Noise Reference scan), the gamma source configuration at the moment of data taking, the beam configuration, and the trigger mode. These information will be stored in the DAQ ROOT output. Are also given the minimal measurement time and waiting time after ramping up of the detectors is over before starting the data acquisition. Then, the list of HV points to scan and the number of triggers for each run of the scan are given in the table underneath.

4358 The rest of the information is written beforehand in the configuration file template, as explicated  
 4359 in Source Code A.6, and contains the hardware addresses to the different VME modules in the  
 4360 setup as well as settings for the TDCs. As the TDC settings available in the configuration file are not  
 4361 supposed to be modified, an improvement would be to remove them from the configuration file and  
 4362 to hardcode them inside of the DAQ code itself or to place them into a different INI file that would  
 4363 host only the TDC settings to lower the probability for a bad manipulation of the configuration file  
 4364 that can be modified from one of webDCS' menus.

4365

```

[General]
TdcS=4
ScanID=$scanid
HV=$HV
RunType=$runtype
MaxTriggers=$maxtriggers
Beam=$beam
[VMEInterface]
Type=V1718
BaseAddress=0xFF0000
Name=VmeInterface
int_trig_freq=100
[TDC0]
Type=V1190A
BaseAddress=0x00000000
Name=Tdc0
StatusA00-15=1
StatusA16-31=1
StatusB00-15=1
StatusB16-31=1
StatusC00-15=1
StatusC16-31=1
StatusD00-15=1
StatusD16-31=1
[TDC1]
Type=V1190A
BaseAddress=0x11110000
Name=Tdc1
StatusA00-15=1
StatusA16-31=1
StatusB00-15=1
StatusB16-31=1
StatusC00-15=1
StatusC16-31=1
StatusD00-15=1
StatusD16-31=1
4366
[TDC2]
Type=V1190A
BaseAddress=0x22220000
Name=Tdc2
StatusA00-15=1
StatusA16-31=1
StatusB00-15=1
StatusB16-31=1
StatusC00-15=1
StatusC16-31=1
StatusD00-15=1
StatusD16-31=1
[TDC3]
Type=V1190A
BaseAddress=0x44440000
Name=Tdc3
StatusA00-15=1
StatusA16-31=1
StatusB00-15=1
StatusB16-31=1
StatusC00-15=1
StatusC16-31=1
StatusD00-15=1
StatusD16-31=1
[TDCSettings]
TriggerExtraSearchMargin=0
TriggerRejectMargin=0
TriggerTimeSubtraction=0b1
TdcDetectionMode=0b01
TdcResolution=0b10
TdcDeadTime=0b00
TdcHeadTrailer=0b1
TdcEventSize=0b1001
TdcTestMode=0b0
BLTMode=1

```

*Source Code A.6: INI configuration file template for 4 TDCs. In section [General], the number of TDCs is explicitated and information about the ongoing run is given. Then, there are sections for each and every VME modules. There buffer addresses are given and for the TDCs, the list of channels to enable is given. Finally, in section [TDCSettings], a part of the TDC settings are given.*

```

4367 typedef map< const string, string > IniFileData;

4368 class IniFile{
4369     private:
4370         bool          CheckIfComment(string line);
4371         bool          CheckIfGroup(string line, string& group);
4372         bool          CheckIfToken(string line, string& key, string& value);
4373         string        FileName;
4374         IniFileData  FileData;
4375         int           Error;
4376
4377     public:
4378         IniFile();
4379         IniFile(string filename);
4380         virtual      ~IniFile();
4381
4382         // Basic file operations
4383         void          SetFileName(string filename);
4384         int           Read();
4385         int           Write();
4386         IniFileData GetFileData();
4387
4388         // Data readout methods
4389         Data32 addressType(string groupname, string keyname, Data32 defaultvalue);
4390         long intType(string groupname, string keyname, long defaultvalue);
4391         long long longType(string groupname, string keyname, long long
4392         ↵ defaultvalue);
4393         string stringType(string groupname, string keyname, string defaultvalue);
4394         float floatType(string groupname, string keyname, float defaultvalue);
4395
4396         // Error methods
4397         string GetErrorMsg();
4398     };

```

4369       *Source Code A.7: Description of C++ object IniFile used as a parser for INI file format.*

4370       In order to retrieve the information of the configuration file, the object `IniFile` has been developed  
4371       to provide an INI parser, presented in Source Code A.7. It contains private methods returning a  
4372       boolean to check the type of line written in the file, whether a comment, a group header or a key line  
4373       (`IniFile::CheckIfComment()`, `IniFile::CheckIfGroup()` and `IniFile::CheckIfToken()`). The  
4374       key may sometimes be referred to as *token* in the source code. Moreover, the private element  
4375       `FileData` is a map of `const` string to string that allows to store the data contained inside the  
4376       configuration file via the public method `IniFile::GetFileData()` following the formatting (see  
4377       method `IniFile::Read()`):

```

4378
4379     string group, token, value;
4380     // Get the field values for the 3 strings.
4381     // Then concatenate group and token together as a single string
4382     // with a dot separation.
4383     token = group + "." + token;
4384     FileData[token] = value;

```

4380 More methods have been written to translate the different keys into the right variable format  
 4381 when used by the DAQ. For example, to get a **float** value out of the configuration file data, knowing  
 4382 the group and the key needed, the method `IniFile::floatType()` can be used. It takes 3 arguments  
 4383 being the group name and key name (both `string`), and a default **float** value used as exception in  
 4384 the case the expected combination of group and key cannot be found in the configuration file. This  
 4385 default value is then used and the DAQ continues on working after sending an alert in the log file for  
 4386 further debugging.

4387

### 4388 A.5.3 WebDCS/DAQ intercommunication

4389 When shifters send instructions to the DAQ via the configuration file, it is the webDCS itself that  
 4390 gives the start command to the DAQ and then the 2 softwares use inter-process communication  
 4391 through file to synchronise themselves. This communication file is represented by the variable `const`  
 4392 `string __runstatuspath`.

4393 On one side, the webDCS sends commands or status that are readout by the DAQ:

- 4394 • INIT, status sent when launching a scan and read via function `CtrlRunStatus(...)`,
- 4395 • START, command to start data taking and read via function `CheckSTART()`,
- 4396 • STOP, command to stop data taking at the end of the scan and read via function `CheckSTOP()`,  
 4397 and
- 4398 • KILL, command to kill data taking sent by user and read via function `CheckKILL()`. Note that  
 4399 the DAQ doesn't stop before the current ROOT file is safely written and saved.

4400 and on the other, the DAQ sends status that are controled by the webDCS:

- 4401 • DAQ\_RDY, sent with `SendDAQReady()` to signify that the DAQ is ready to receive commands  
 4402 from the webDCS,
- 4403 • RUNNING, sent with `SendDAQRunning()` to signify that the DAQ is taking data,
- 4404 • DAQ\_ERR, sent with `SendDAQError()` to signify that the DAQ didn't receive the expected com-  
 4405 mand from the webDCS or that the launch command didn't have the right number of argu-  
 4406 ments,
- 4407 • RD\_ERR, sent when the DAQ wasn't able to read the communication file, and
- 4408 • WR\_ERR, sent when the DAQ wasn't able to write into the communication file.

### 4409 A.5.4 Example of inter-process communication cycle

4410 Under normal conditions, the webDCS and the DAQ processes exchange commands and status via  
 4411 the file hosted at the address `__runstatuspath`, as explained in subsection A.5.3. An example of  
 4412 cycle is given in Table A.1. In this example, the steps 3 to 5 are repeated as long as the webDCS tells  
 4413 the DAQ to take data. A data taking cycle is the equivalent as what is called a *Scan* in GIFT++ jargon,

4414 referring to a set a runs with several HV steps. Each repetition of steps 3 to 5 is then equivalent to a  
 4415 single *Run*.

4416 At any moment during the data taking, for any reason, the shifter can decide that the data taking  
 4417 needs to be stopped before it reached the end of the scheduled cycle. Thus at any moment on the  
 4418 cycle, the content of the inter-process communication file will be changed to `KILL` and the DAQ will  
 4419 shut down right away. The DAQ checks for `KILL` signals every 5s after the TDCs configuration is  
 4420 over. So far, the function `CheckKILL()` has been used only inside of the data taking loop of method  
 4421 `DataReader::Run()` and thus, if the shifter decides to KILL the data taking during the TDC con-  
 4422 figuration phase or the HV ramping in between 2 HV steps, the DAQ will not be stopped smoothly  
 4423 and a *force kill* command will be sent to stop the DAQ process that is still awake on the computer.  
 4424 Improvements can be brought on this part of the software to make sure that the DAQ can safely  
 4425 shutdown at any moment.

4426

step	actions of webDCS	status of DAQ	<code>__runstatuspath</code>
1	launch DAQ ramp voltages ramping over wait for currents stabilization	readout of IniFile configuration of TDCs	INIT
2		configuration done send DAQ ready wait for <code>START</code> signal	DAQ_RDY
3	waiting time over send <code>START</code>		START
4	wait for run to end monitor DAQ run status	data taking ongoing check for <code>KILL</code> signal	RUNNING
5		run over send <code>DAQ_RDY</code> wait for next DCS signal	DAQ_RDY
6	ramp voltages ramping over wait for currents stabilization		DAQ_RDY
3	waiting time over send <code>START</code>		START
4	wait for run to end monitor DAQ run status	update IniFile information data taking ongoing check for <code>KILL</code> signal	RUNNING
5		run over send <code>DAQ_RDY</code> wait for next DCS signal	DAQ_RDY
7	send command <code>STOP</code>	DAQ shuts down	STOP

Table A.1: Inter-process communication cycles in between the webDCS and the DAQ through file string signals.

## A.6 Software export

4427 In section A.2 was discussed the fact that the DAQ as written in its last version is not a standalone  
 4428 software. It is possible to make it a standalone program that could be adapted to any VME setup

4430 using V1190A and V1718 modules by creating a GUI for the software or by printing the log messages  
4431 that are normally printed in the webDCS through the log file, directly into the terminal. This  
4432 method was used by the DAQ up to version 3.0 moment where the webDCS was completed. Also, it  
4433 is possible to check branches of DAQ v2.X to have example of communication through a terminal.  
4434 DAQ v2.X is nonetheless limited in its possibilities and requires a lot of offline manual interventions  
4435 from the users. Indeed, there is no communication of the software with the detectors' power  
4436 supply system that would allow for a user a predefine a list of voltages to operate the detectors at  
4437 and loop over to take data without any further manual intervention. In v2.X, the data is taken for a  
4438 single detector setting and at the end of each run, the softwares asks the user if he intends on taking  
4439 more runs. If so, the software invites the user to set the operating voltages accordingly to what is  
4440 necessary and to manual update the configuration file in consequence. This working mode can be a  
4441 very first approach before an evolution and has been successfully used by colleagues from different  
4442 collaborations.

4443 For a more robust operation, it is recommended to develop a GUI or a web application to interface  
4444 the DAQ. Moreover, to limit the amount of manual interventions, and thus the probability to make  
4445 mistakes, it is also recommended to add an extra feature into the DAQ by installing the HV Wrapper  
4446 library provided by CAEN of which an example of use in a similar DAQ software developped by a  
4447 master student of UGent, and called TinyDAQ, is provided on UGent's github. Then, this HV Wrapper  
4448 will help you communicating with and give instructions to a CAEN HV powered crate and can  
4449 be added into the DAQ at the same level where the communication with the user was made in DAQ  
4450 v2.X. In case you are using another kind of power system for your detectors, it is stringly adviced to  
4451 use HV modules or crates that can be remotely controloled via a using C++ libraries.

4452



# B

4453

4454

## Details on the offline analysis package

4455 The data collected in GIF++ thanks to the DAQ described in Appendix A is difficult to interpret by  
4456 a human user that doesn't have a clear idea of the raw data architecture of the ROOT data files. In  
4457 order to render the data human readable, a C++ offline analysis tool was designed to provide users  
4458 with detector by detector histograms that give a clear overview of the parameters monitored during  
4459 the data acquisition [273]. In this appendix, details about this software in the context of GIF++, as  
4460 of how the software was written and how it functions will be given.

### 4461 B.1 GIF++ Offline Analysis file tree

4462 GIF++ Offline Analysis source code is fully available on github at [https://github.com/afagot/GIF\\_OfflineAnalysis](https://github.com/afagot/GIF_OfflineAnalysis). The software requires ROOT as non-optionnal dependency  
4463 as it takes ROOT files in input and write an output ROOT file containing histograms. To compile the  
4464 GIF++ Offline Analysis project is compiled with cmake. To compile, first a build/ directory must  
4465 be created to compile from there:

```
4467 mkdir build
4468 cd build
4469 cmake ..
4470 make
4471 make install
```

4469 To clean the directory and create a new build directory, the bash script cleandir.sh can be used:

```
4470
4471 ./cleandir.sh
```

4472 The source code tree is provided below along with comments to give an overview of the files' con-  
4473 tent. The different objects created for this project (`Infrastructure`, `Trolley`, `RPC`, `Mapping`, `RPCHit`,  
4474 `RPCCluster` and `Inifile`) will be described in details in the following sections.

4475

```

GIF_OfflineAnalysis
├── bin
│   └── offlineanalysis ..... EXECUTABLE
├── build..... CMAKE COMPILATION DIRECTORY
└── ...
    ├── include..... LIST OF C++ HEADER FILES
    │   ├── Cluster.h..... DECLARATION OF OBJECT RPCCLUSTER
    │   ├── Current.h..... DECLARATION OF GETCURRENT ANALYSIS MACRO
    │   ├── GIFTrolley.h..... DECLARATION OF OBJECT TROLLEY
    │   ├── Infrastructure.h..... DECLARATION OF OBJECT INFRASTRUCTURE
    │   ├── IniFile.h..... DECLARATION OF OBJECT INI FILE FORINI PARSER
    │   ├── Mapping.h..... DECLARATION OF OBJECT MAPPING
    │   ├── MsgSvc.h..... DECLARATION OF OFFLINE LOG MESSAGES
    │   ├── OfflineAnalysis.h..... DECLARATION OF DATA ANALYSIS MACRO
    │   ├── RPCTracker.h..... DECLARATION OF OBJECT RPC
    │   ├── RPCHit.h..... DECLARATION OF OBJECT RPCHIT
    │   ├── types.h..... DEFINITION OF USEFUL VARIABLE TYPES
    │   └── utils.h..... DECLARATION OF USEFUL FUNCTIONS
    ├── obj..... BINARY FILES CREATED BY COMPILER
    └── ...
        ├── src..... LIST OF C++ SOURCE FILES
        │   ├── Cluster.cc..... DEFINITION OF OBJECT RPCCLUSTER
        │   ├── Current.cc .....

```

## 4476 B.2 Usage of the Offline Analysis

4477 In order to use the Offline Analysis tool, it is necessary to know the Scan number and the HV Step  
 4478 of the run that needs to be analysed. This information needs to be written in the following format:

4479

4480 Scan00XXXX\_HVY

4481 where XXXX is the scan ID and y is the high voltage step (in case of a high voltage scan, data will be  
 4482 taken for several HV steps). This format corresponds to the base name of data files in the database

4483 of the Gif++ webDCS. Usually, the offline analysis tool is automatically called by the webDCS at  
 4484 the end of data taking or by a user from the webDCS panel if an update of the tool was brought.  
 4485 Nonetheless, an expert can locally launch the analysis for tests on the Gif++ computer, or a user can  
 4486 get the code on its local machine from github and download data from the webDCS for its own anal-  
 4487 ysis. To launch the code, the following command can be used from the `GIF_OfflineAnalysis` folder:

4488  
 4489     `bin/offlineanalysis /path/to/Scan00XXXX_HVY`

4490 where, `/path/to/Scan00XXXX_HVY` refers to the local data files. Then, the offline tool will by itself  
 4491 take care of finding all available ROOT data files present in the folder, as listed below:

- 4492     ● `Scan00XXXX_HVY_DAQ.root` containing the TDC data as described in Appendix A.4.2 (events,  
 4493       hit and timestamp lists), and
- 4494     ● `Scan00XXXX_HVY_CAEN.root` containing the CAEN mainframe data recorded by the monitor-  
 4495       ing tool webDCS during data taking (HVs and currents of every HV channels). This file is  
 4496       created independently of the DAQ.

## 4497     **B.2.1 Output of the offline tool**

### 4498       **B.2.1.1 ROOT file**

4499 The analysis gives output ROOT datafiles that are saved into the data folder and called using the  
 4500 naming convention `Scan00XXXX_HVY_Offline.root`. Inside those, a list of `TH1` histograms can be  
 4501 found. Its size will vary as a function of the number of detectors in the setup as each set of histograms  
 4502 is produced detector by detector. For each partition of each chamber, can be found:

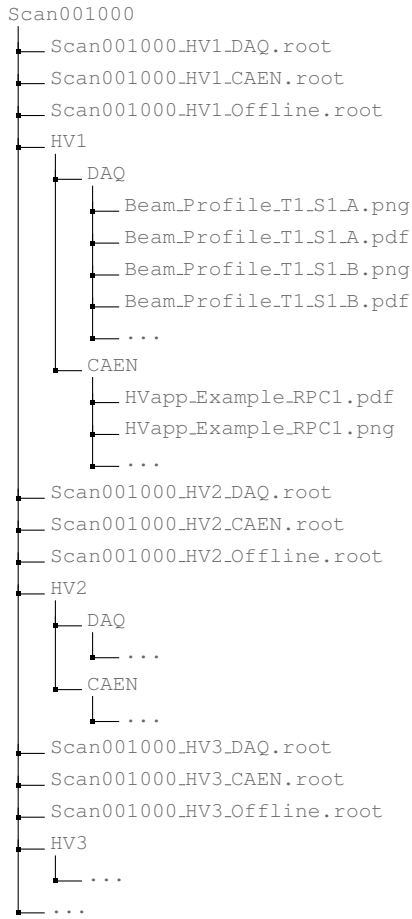
- 4503     ● `Time_Profile_Tt_Sc_p` shows the time profile of all recorded events (number of events per  
 4504       time bin),
- 4505     ● `Hit_Profile_Tt_Sc_p` shows the hit profile of all recorded events (number of events per chan-  
 4506       nel),
- 4507     ● `Hit_Multiplicity_Tt_Sc_p` shows the hit multiplicity (number of hits per event) of all recorded  
 4508       events (number of occurrences per multiplicity bin),
- 4509     ● `Time_vs_Strip_Profile_Tt_Sc_p` shows the 2D time vs strip profile of all recorded events  
 4510       (number of events per time bin per strip),
- 4511     ● `Strip_Mean_Noise_Tt_Sc_p` shows noise/gamma rate per unit area for each strip in a se-  
 4512       lected time range. After filters are applied on `Time_Profile_Tt_Sc_p`, the filtered version  
 4513       of `Hit_Profile_Tt_Sc_p` is normalised to the total integrated time and active detection area  
 4514       of a single channel,
- 4515     ● `Strip_Activity_Tt_Sc_p` shows noise/gamma activity for each strip (normalised version of  
 4516       previous histogram - strip activity = strip rate / average partition rate),
- 4517     ● `Strip_Homogeneity_Tt_Sc_p` shows the *homogeneity* of a given partition ( $\text{homogeneity} = \exp(-\text{strip rates standard deviation}(\text{strip rates in partition}/\text{average partition rate}))$ ),

- `mask_Strip_Mean_Noise_Tt_Sc_p` shows noise/gamma rate per unit area for each masked strip in a selected time range. Offline, the user can control the noise/gamma rate and decide to mask the strips that are judged to be noisy or dead. This is done via the *Masking Tool* provided by the webDCS,
- `mask_Strip_Activity_Tt_Sc_p` shows noise/gamma activity per unit area for each masked strip with respect to the average rate of active strips,
- `NoiseCSize_H_Tt_Sc_p` shows noise/gamma cluster size, a cluster being constructed out of adjacent strips giving a signal at the *same time* (hits within a time window of 25 ns),
- `NoiseCMult_H_Tt_Sc_p` shows noise/gamma cluster multiplicity (number of reconstructed clusters per event),
- `Chip_Mean_Noise_Tt_Sc_p` shows the same information than `strip_Mean_Noise_Tt_Scp` using a different binning (1 chip corresponds to 8 strips),
- `Chip_Activity_Tt_Sc_p` shows the same information than `strip_Activity_Tt_Scp` using chip binning,
- `Chip_Homogeneity_Tt_Sc_p` shows the homogeneity of a given partition using chip binning,
- `Beam_Profile_Tt_Sc_p` shows the estimated beam profile when taking efficiency scan. This is obtained by filtering `Time_Profile_Tt_Sc_p` to only consider the muon peak where the noise/gamma background has been subtracted. The resulting hit profile corresponds to the beam profile on the detector channels,
- `Efficiency_Fake_Tt_Ss_p` shows the efficiency given by fake hits by probing outside the peak in an uncorrelated window as wide as the peak window,
- `Efficiency_Peak_Tt_Ss_p` shows the efficiency given by hits contained in the peak window,
- `PeakCSize_H_Tt_Sc_p` shows the cluster size that was estimated using all the hits in the peak window,
- `PeakCMult_H_Tt_Sc_p` shows the cluster multiplicity that was estimated using all the hits in the peak window,
- `L0_Efficiency_Tt_Sc_p` shows the level 0 muon efficiency that was estimated **without** muon tracking after correction,
- `MuonCSize_H_Tt_Sc_p` shows the level 0 muon cluster size that was estimated **without** muon tracking after correction, and
- `MuonCMult_H_Tt_Sc_p` shows the level 0 muon cluster multiplicity that was estimated **without** muon tracking after correction.

In the histogram labels, `t` stands for the trolley number (1 or 3), `c` for the chamber slot label in trolley `t` and `p` for the partition label (A, B, C or D depending on the chamber layout) as explained in Chapter 5.3.

4555     In the context of GIF++, an extra script called by the webDCS is called to extract the histograms  
 4556     from the ROOT files. The histograms are then stored in PNG and PDF formats into the correspond-  
 4557     ing folder (a single folder per HV step, so per ROOT file). An example of histogram organisation is  
 4558     given bellow for an hypothetical scan 001000 with at least 3 HV steps and whose chamber located in  
 4559     slot 1 of trolley 1 is called *Example\_RPC1* and has at least 2 read-out partitions A and B. The goal is  
 4560     to then display the histograms graphs on the Data Quality Monitoring (DQM) page of the webDCS,  
 4561     as presented in Figure 5.27, in order for the users to control the quality of the data taking at the end  
 4562     of data taking.

4563



4564

### B.2.1.2 CSV files

4565     Moreover, up to 4 CSV files can be created depending on which ones of the 3 input files were in the  
 4566     data folder:

4567     • Offline-Corrupted.csv , is used to keep track of the amount of data that was corrupted and  
 4568       removed from old data format files that don't contain any data quality flag.

- 4569     ● `Offline-Current.csv`, contains the summary of the currents and voltages applied on each  
 4570       RPC HV channel.
- 4571     ● `Offline-L0-EffCl.csv`, is used to write the efficiencies, cluster size and cluster multiplicity  
 4572       of efficiency runs. Note that `L0` refers here to *Level 0* and means that the results of efficiency and  
 4573       clusterization are a first approximation calculated without performing any muon tracking in  
 4574       between the different detectors. This offline tool provides the user with a preliminar calcula-  
 4575       tion of the efficiency and of the muon event parameters. Another analysis software especially  
 4576       dedicated to muon tracking is called on selected data to retrieve the results of efficiency and  
 4577       muon clusterization using a tracking algorithm to discriminate noise or gamma from muons  
 4578       as muons are the only particles that pass through the full setup, leaving hits than can be used  
 4579       to reconstruct their tracks.
- 4580     ● `Offline-Rate.csv`, is used to write the noise or gamma rates measured in the detector readout  
 4581       partitions.

4582     Note that these 4 CSV files are created along with their *headers* (`Offline-[...]-Header.csv`  
 4583       containing the names of each data columns) and are automatically merged together when the offline  
 4584       analysis tool is called from the webDCS, contrary to the case where the tool is runned locally from  
 4585       the terminal as the merging bash script is then not called. Thus, the resulting files, used to make  
 4586       official plots, are:

- 4587     ● `Corrupted.csv`,
- 4588     ● `Current.csv`,
- 4589     ● `L0-EffCl.csv`.
- 4590     ● `Rate.csv`.

### 4591     **B.3 Analysis inputs and information handling**

4592     The usage of the Offline Analysis tool as well as its output have been presented in the previous sec-  
 4593       tion. It is now important to dig further and start looking at the source code and the inputs necessary  
 4594       for the tool to work. Indeed, other than the raw ROOT data files that are analysed, more information  
 4595       needs to be imported inside of the program to perform the analysis such as the description of the  
 4596       setup inside of GIFT++ at the time of data taking (number of trolleys, of RPCs, dimensions of the  
 4597       detectors, etc...) or the mapping that links the TDC channels to the coresponding RPC channels in  
 4598       order to translate the TDC information into human readable data. Two files are used to transmit all  
 4599       this information:

4600

- 4601     ● `Dimensions.ini`, that provides the necessary setup and RPC information, and
- 4602     ● `ChannelsMapping.csv`, that gives the link between the TDC and RPC channels as well as the  
 4603       *mask* for each channel (masked or not?).

### 4604 B.3.1 Dimensions file and IniFile parser

4605 GIF++ CMS RPC setup consists in detectors held into trolleys inside of the GIF++ bunker. Each of  
 4606 these detector may have a read-out segmented to cover different pseudo-rapidity range once intalled  
 4607 in CMS. The segmentation of the read-out is referred to as "partitions". This input file, present in  
 4608 every data folder, allows the analysis tool to know of the number of active trolleys, the number of  
 4609 active RPCs in those trolleys, and the details about each RPCs such as the number of RPC gaps, the  
 4610 number of pseudo-rapidity partitions, the number of strips per partion or the dimensions. To do so,  
 4611 there are 3 types of groups in the INI file architecture. Groups are sections of the INI file content  
 4612 starting with a title encapsulated in between square brackets. A first general group, appearing only  
 4613 once at the head of the document, gives information about the number of active trolleys as well  
 4614 as their IDs, as presented in Source Code B.1. For each active trolley, a group similar to Source  
 4615 Code B.2 can be found containing information about the number of active detectors in the trolley  
 4616 and their IDs. Each trolley group as a `Tt` name format, where `t` is the trolley ID. Finally, for each  
 4617 detector stored in slots of an active trolley, there is a group providing information about their names  
 4618 and dimensions, as shown in Source Code B.3. Each slot group as a `TtSs` name format, where `s` is  
 4619 the slot ID of trolley `t` where the active RPC is hosted.

```
4620 [General]
4621 nTrolleys=2
4621 TrolleysID=13
```

4622 *Source Code B.1: Example of `[General]` group as might be found in `Dimensions.ini`. In GIF++, only 2 trolleys are available to hold RPCs and place them inside of the bunker for irradiation. The IDs of the trolleys are written in a single string as "13" and then read character by character by the program.*

```
4623 [T1]
4623 nSlots=4
4623 SlotsID=1234
```

4624 *Source Code B.2: Example of trolley group as might be found in `Dimensions.ini`. In this example, the file tells that there are 4 detectors placed in the holding slots of the trolley T1 and that their IDs, written as a single string variable, are 1, 2, 3 and 4.*

```
4625 [T1S1]
Name=RE2-2-NPD-BARC-8
Partitions=3
Gaps=3
Gap1=BOT
Gap2=TN
Gap3=TW
AreaGap1=11694.25
AreaGap2=6432
AreaGap3=4582.82
Strips=32
ActiveArea-A=157.8
ActiveArea-B=121.69
ActiveArea-C=93.03
```

4626 *Source Code B.3: Example of slot group as might be found in `Dimensions.ini`. In this example, the file provides information about a detector named RE2-2-NPD-BARC-8, having 3 pseudo-rapidity readout partitions and stored in slot S1 of trolley T1. This is a CMS RE2-2 type of detector. This information will then be used for example to compute the rate per unit area calculation.*

4627     This information is read-out and stored in a C++ object called `IniFile`, that parses the information  
 4628     of the INI input file and stores it into a local buffer for later use. This INI parser is the exact  
 4629     same one that was previously developed for the GIF++ DAQ and described in Appendix A.5.2.

### 4630     **B.3.2 TDC to RPC link file and Mapping**

4631     The same way the INI dimension file information is stored using `map`, the channel mapping and  
 4632     mask information making the link in between TDC channels and RPC strips is stored and accessed  
 4633     through `map`. First of all, the mapping CSV file is organised into 3 columns separated by tabulations:

4635     RPC_channel	4635     TDC_channel	4635     mask
----------------------	----------------------	---------------

4636         using as formatting for each field:

4637     TSCCC	4637     TCCC	4637     M
----------------	---------------	------------

4639     `TSCCC` is a 5-digit integer where `T` is the trolley ID, `s` the slot ID in which the RPC is held inside  
 4640     the trolley `T` and `ccc` is the RPC channel number, or *strip* number, that can take values up to  
 4641     3-digits depending on the detector,

4642     `TCCC` is a 4 digit integer where `T` is the TDC ID to which the RPC is connected, `ccc` is the TDC  
 4643     channel number linked to the RPC strip that can take values in between 0 and 127, and

4644     `M` is a 1-digit integer indicating if the channel should be considered (`M = 1`) or discarded (`M = 0`)  
 4645     during analysis. Note that the absence of a third column is interpreted by the mapping file  
 4646     parser as `M = 1` by default.

4647     This mapping and masking information is readout and stored thanks to the object `Mapping`, presented in Source Code B.4. Similarly to `IniFile` objects, this class has private methods to provide with parser rules. The first one, `Mapping::CheckIfNewLine()` is used to find the newline character '`\n`' or return character '`\r`' (depending on which kind of operating system interacted with the file). Finding and identifying a newline or return character is used for the simple reason that the masking information has been introduced only during the year 2017 but the channel mapping files exist since 2015 and the very beginning of data taking at GIF++. This means that in the older data folders, before the upgrade, the channel mapping file only had 2 columns, the RPC channel and the TDC channel. For compatibility reasons, this method helps controlling the character following the readout of the 2 first fields of a line. In case any end of line character is found, no mask information is present in the file and the default `M = 1` is used. On the contrary, if the next character was a tabulation or a space, the mask information is present.

4659     Once the 3 fields have been readout, the second private method `Mapping::CheckIfTDCCh()` is used to control that the TDC channel is an existing TDC channel by checking its format. Finally, the information is stored into 3 different maps (`Link`, `ReverseLink` and `Mask`) thanks to the public method `Mapping::Read()`. `Link` allows to get the RPC channel by knowing the TDC channel while `ReverseLink` does the opposite by returning the TDC channel by knowing the RPC channel. Finally, `Mask` returns the mask associated to a given RPC channel.

```

4665 typedef map<Uint,Uint> MappingData;

4666 class Mapping {
    private:
        bool          CheckIfNewLine(char next);
        bool          CheckIfTDCCh(Uint channel);
        string         FileName;
        MappingData   Link;
        MappingData   ReverseLink;
        MappingData   Mask;
        int           Error;

4667     public:
        Mapping();
        Mapping(string baseName);
        ~Mapping();

        void SetFileName(const string filename);
        int Read();
        Uint GetLink(Uint tdcchannel);
        Uint GetReverse(Uint rpcchannel);
        Uint GetMask(Uint rpcchannel);
    };
}

```

4667 *Source Code B.4: Description of C++ object Mapping used as a parser for the channel mapping and mask file.*

## 4668 B.4 Description of GIF++ setup within the Offline Analysis tool

4669 In the previous section, the tool input files have been discussed. The dimension file information is  
 4670 stored in a map hosted by the `IniFile` object. But this information is then used to create a series of  
 4671 new objects that helps defining the GIF++ infrastructure directly into the Offline Analysis. Indeed,  
 4672 from the `RPC`, to the more general `Infrastructure`, every element of the GIF++ infrastrucutre is  
 4673 recreated for each data analysis based on the information provided in input. All this information  
 4674 about the infrastructure will be used to assign each hit signal to a specific strip channel of a specific  
 4675 detector, and having a specific active area. This way, rate per unit area calculation is possible.  
 4676

### 4677 B.4.1 RPC objects

4678 `RPC` objects have been developped to represent physical active detectors in GIF++ at the moment  
 4679 of data taking. Thus, there are as many `RPC` objects created during the analysis than there were  
 4680 active `RPCs` tested during a run. Each `RPC` hosts the information present in the corresponding INI  
 4681 slot group, as showed in B.3, and organises it using a similar architecture. This can be seen from  
 4682 *Source Code B.5*.

4683 To make the object more compact, the lists of gap labels, of gap active areas and strip active  
 4684 areas are stored into `vector` dynamical containers. `RPC` objects are always contructed thanks to the  
 4685 dimension file information stored into the `IniFILE` and their ID, using the format `TtSs`. Using the  
 4686 `RPC` ID, the constructor calls the methods of `IniFILE` to initialise the `RPC`. The other constructors  
 4687 are not used but exist in case of need. Finally, some getters have been written to access the different  
 4688 private parameters storing the detector information.

4689

### 4690 B.4.2 Trolley objects

4691 Trolley objects have been developed to represent physical active trolleys in GIF++ at the moment  
4692 of data taking. Thus, there are as many trolley objects created during the analysis than there were  
4693 active trolleys hosting RPCs under test during a run. Each Trolley hosts the information present in  
4694 the corresponding INI trolley group, as shown in B.2, and organises it using a similar architecture.  
4695 In addition to the information hosted in the INI file, these objects have a dynamical container of RPC  
4696 objects, representing the active detectors the active trolley was hosting at the time of data taking.  
4697 This can be seen from Source Code B.6.

4698 Trolley objects are always constructed thanks to the dimension file information stored into the  
4699 IniFILE and their ID, using the format `Tt`. Using the Trolley ID, the constructor calls the methods  
4700 of `IniFile` to initialise the Trolley. Retrieving the information of the RPC IDs via `SlotsID`, a new  
4701 RPC is constructed and added to the container `RPCs` for each character in the ID string. The other  
4702 constructors are not used but exist in case of need. Finally, some getters have been written to access  
4703 the different private parameters storing the trolley and detectors information.

4704

### 4705 B.4.3 Infrastructure object

4706 The Infrastructure object has been developed to represent the GIF++ bunker area dedicated to  
4707 CMS RPC experiments. With this very specific object, all the information about the CMS RPC  
4708 setup within GIF++ at the moment of data taking is stored. It hosts the information present in the  
4709 corresponding INI general group, as shown in B.1, and organises it using a similar architecture. In  
4710 addition to the information hosted in the INI file, this object has a dynamical container of Trolley  
4711 objects representing the active trolleys in GIF++ area, themselves containing RPC objects. This can  
4712 be seen from Source Code B.7.

4713 The Infrastructure object is always constructed thanks to the dimension file information stored  
4714 into the `IniFILE`. Retrieving the information of the trolley IDs via `TrolleysID`, a new Trolley is  
4715 constructed and added to the container `Trolleys` for each character in the ID string. By extension,  
4716 it is easy to understand that the process described in Section B.4.2 for the construction of RPCs  
4717 takes place when a trolley is constructed. The other constructors are not used but exist in case of  
4718 need. Finally, some getters have been written to access the different private parameters storing the  
4719 infrastructure, trolleys and detectors information.

```

4720
class RPC{
    private:
        string      name;           //RPC name as in webDCS database
        UInt       nGaps;          //Number of gaps in the RPC
        UInt       nPartitions;    //Number of partitions in the RPC
        UInt       nStrips;         //Number of strips per partition
        vector<string> gaps;      //List of gap labels (BOT, TOP, etc...)
        vector<float>  gapGeo;        //List of gap active areas
        vector<float>  stripGeo;      //List of strip active areas

    public:
        RPC();
        RPC(string ID, IniFile* geofile);
        RPC(const RPC& other);
        ~RPC();
        RPC& operator=(const RPC& other);

        string GetName();
        UInt   GetNGaps();
        UInt   GetNPartitions();
        UInt   GetNStrips();
        string GetGap(UInt g);
        float  GetGapGeo(UInt g);
        float  GetStripGeo(UInt p);
};

4721

```

4722 *Source Code B.5: Description of C++ objects RPC that describe each active detectors used during data taking.*

```

class Trolley{
    private:
        UInt       nSlots;        //Number of active RPCs in the considered trolley
        string     SlotsID;       //Active RPC IDs written into a string
        vector<RPC*> RPCs;      //List of active RPCs

    public:
        Trolley();
        Trolley(string ID, IniFile* geofile);
        Trolley(const Trolley& other);
        ~Trolley();
        Trolley& operator=(const Trolley& other);

        UInt   GetNSlots();
        string GetSlotsID();
        UInt   GetSlotID(UInt s);
        RPC*   GetRPC(UInt r);
        void   DeleteRPC(UInt r);

        //Methods to get members of RPC objects stored in RPCs
        string GetName(UInt r);
        UInt   GetNGaps(UInt r);
        UInt   GetNPartitions(UInt r);
        UInt   GetNStrips(UInt r);
        string GetGap(UInt r, UInt g);
        float  GetGapGeo(UInt r, UInt g);
        float  GetStripGeo(UInt r, UInt p);
};

4723

```

4724 *Source Code B.6: Description of C++ objects Trolley that describe each active trolley used during data taking.*

```

class Infrastructure {
    private:
        Uint             nTrolleys;   //Number of active Trolleys in the run
        string          TrolleysID;  //Active trolley IDs written into a string
        vector<Trolley*> Trolleys;  //List of active Trolleys (struct)

    public:
        Infrastructure();
        Infrastructure(IniFile* geofile);
        Infrastructure(const Infrastructure& other);
        ~Infrastructure();
        Infrastructure& operator=(const Infrastructure& other);

        Uint    GetNTrolleys();
        string GetTrolleysID();
        Uint    GetTrolleyID(Uint t);

4725        Trolley* GetTrolley(Uint t);
        void    DeleteTrolley(Uint t);

        //Methods to get members of GIFTrolley objects stored in Trolleys
        Uint    GetNSlots(Uint t);
        string GetSlotsID(Uint t);
        Uint    GetSlotID(Uint t, Uint s);
        RPC*   GetRPC(Uint t, Uint r);

        //Methods to get members of RPC objects stored in RPCs
        string GetName(Uint t, Uint r);
        Uint    GetNGaps(Uint t, Uint r);
        Uint    GetNPartitions(Uint t, Uint r);
        Uint    GetNStrips(Uint t, Uint r);
        string GetGap(Uint t, Uint r, Uint g);
        float  GetGapGeo(Uint t, Uint r, Uint g);
        float  GetStripGeo(Uint t, Uint r, Uint p);
    };

```

*Source Code B.7: Description of C++ object Infrastructure that contains the full information about CMS RPC experiment in GIF++.*

## **4727 B.5 Handeling of data**

**4728** As discussed in Appendix A.4.2, the raw data uses a `TTree` architecture where every entry is related  
**4729** to a trigger signal provided by a muon or a random pulse, whether the goal of the data taking was to  
**4730** measure the performance of the detector or the noise/gamma background respectively. Each of these  
**4731** entries, referred also as events, contain a more or less full list of hits in the TDC channels to which  
**4732** the detectors are connected. To this list of hits corresponds a list of time stamps, marking the arrival  
**4733** of the hits within the TDC channel.

**4734** The infrastructure of the CMS RPC experiment within `GIF++` being defined, combining the raw  
**4735** data information with the information provided by both the mapping/mask file and the dimension  
**4736** file allows to build new physical objects that will help in computing efficiency or rates.

### 4737 B.5.1 RPC hits

4738 The raw data stored in the ROOT file as output of the GIFT++ DAQ, is readout by the analysis tool  
 4739 using the structure `RAWData` presented in Source Code B.9 that differs from the structure presented  
 4740 in Appendix A.4.2 as it is not meant to hold all of the data contained in the ROOT file. In this sense,  
 4741 this structure is in the case of the offline analysis tool not a dynamical object and will only be storing  
 4742 a single event contained in a single entry of the `TTree`.

4743

```
class RPCHit {
    private:
        Uint Channel;      //RPC channel according to mapping (5 digits)
        Uint Trolley;     //0, 1 or 3 (1st digit of the RPC channel)
        Uint Station;     //Slot where is held the RPC in Trolley (2nd digit)
        Uint Strip;       //RPC strip where the hit occurred (last 3 digits)
        Uint Partition;   //Readout partition along eta segmentation
        float TimeStamp; //Time stamp of the arrival in TDC

    public:
        RPCHit();
        RPCHit(Uint channel, float time, Infrastructure* Infra);
        RPCHit(const RPCHit& other);
        ~RPCHit();
        RPCHit& operator=(const RPCHit& other);

        Uint GetChannel();
        Uint GetTrolley();
        Uint GetStation();
        Uint GetStrip();
        Uint GetPartition();
        float GetTime();
};

typedef vector<RPCHit> HitList;
typedef struct GIFHitList {HitList rpc[NTROLLEYS][NSLOTS][NPARTITIONS];}
    ↪ GIFHitList;

bool SortHitbyStrip(RPCHit h1, RPCHit h2);
bool SortHitbyTime(RPCHit h1, RPCHit h2);
```

4744

Source Code B.8: Description of C++ object `RPCHit`.

4745

```
struct RAWData{
    int iEvent;           //Event i
    int TDCHits;         //Number of hits in event i
    int QFlag;           //Quality flag list (1 flag digit per TDC)
    vector<Uint> *TDCCh; //List of channels giving hits per event
    vector<float> *TDCTS; //List of the corresponding time stamps
};
```

4746

Source Code B.9: Description of C++ structure `RAWData`.

4748 Each member of the structure is then linked to the corresponding branch of the ROOT data tree,  
 4749 as shown in the example of Source Code B.10, and using the method `GetEntry(int i)` of the ROOT  
 4750 class `TTree` will update the state of the members of `RAWData`.

4751 The data is then analysed entry by entry and to each element of the TDC channel list, a `RPCHit` is  
 4752 constructed by linking each TDC channel to the corresponding RPC channel thanks to the Mapping

4753 object. The information carried by the RPC channel format allows to easily retrieve the trolley and  
 4754 slot from which the hit was recorded (see section B.3.2). Using these 2 values, the readout partition  
 4755 can be found by knowing the strip channel and comparing it with the number of partitions and strips  
 4756 per partition stored into the `Infrastructure` object.

```
4757
4758   TTree* dataTree = (TTree*)dataFile.Get("RAWData");
      RAWData data;
      dataTree->SetBranchAddress("EventNumber", &data.iEvent);
      dataTree->SetBranchAddress("number_of_hits", &data.TDCNHits);
      dataTree->SetBranchAddress("Quality_flag", &data.QFlag);
      dataTree->SetBranchAddress("TDC_channel", &data.TDCCh);
      dataTree->SetBranchAddress("TDC_TimeStamp", &data.TDCTS);
```

4759 *Source Code B.10: Example of link in between RAWData and TTree.*

4760 Thus `RPCHit` objects are then stored into 3D dynamical list called `GIFHitList` (Source Code B.8)  
 4761 where the 3 dimensions refer to the 3 layers of the readout in `GIF++`: in the bunker there are *trolleys*  
 4762 ( $\tau$ ) holding detectors in *slots* ( $s$ ) and each detector readout is divided into 1 or more pseudo-rapidity  
 4763 *partitions* ( $p$ ). Using these 3 information allows to assign an address to each readout partition and  
 4764 this address will point to a specific hit list.

4765

### 4766 B.5.2 Clusters of hits

4767 All the hits contained in the ROOT file have been sorted into the different hit lists through the  
 4768 `GIFHitList`. At this point, it is possible to start looking for clusters. A cluster is a group of adjacent  
 4769 strips getting hits within a time window of 25 ns. These strips are then assumed to be part of the same  
 4770 physical avalanche signal generated by a muon passing through the chamber or by the interaction of  
 4771 a gamma stopping into the electrodes of the RPCs.

4772 To keep the cluster information, `RPCCluster` objects have been defined as shown in Source  
 4773 Code B.11. Using the information of each individual `RPCHit` taken out of the hit list, it stores  
 4774 the cluster size (number of adjacent strips composing the cluster), the first and last hit, the center for  
 4775 spatial reconstruction and finally the start and stop time stamps as well as te time spread in between  
 4776 the first and last hit.

4777

4778 To investigate the hit list of a given detector partition, the function `Clusterization()` defined  
 4779 in `include/Cluster.h` needs the hits in the list to be time sorted. This is achieved by calling func-  
 4780 tion `sort()` of library `<algorithm>` using the comparator `SortHitbyTime(RPCHit h1, RPCHit h2)`  
 4781 defined in `include/RPCHit.h` that returns `true` if the time stamp of hit `h1` is lower than that of `h2`.  
 4782 A first isolation of strips is made only based on time information. All the hits within the 25 ns win-  
 4783 dow are taken separately from the rest. Then, this sub-list of hits is sorted this time by ascending  
 4784 strip number, using this time the comparator `SortHitbyStrip(RPCHit h1, RPCHit h2)`. Finally, the  
 4785 groups of adjacent strips are used to construct `RPCCluster` objects that are then stored in a temporary  
 4786 list of clusters that is at the end of the process used to know how many clusters were reconstructed  
 4787 and to fill their sizes into an histogram that will allows to know the mean size of muon or gamma  
 4788 clusters. This method to group hits together into clusters is limited as no systematic study of the  
 4789 average avalanche time development into TDC hits was performed and that there is no correlation

4790 of both spatial and time information to make the first selection of hits. Due to this, two clusters  
 4791 developping consecutively next to each other during a total time longer to 25 ns could be wrongly  
 4792 grouped as a cluster composed of the first developed cluster plus a part of the second cluster while  
 4793 the rest of the second cluster would be placed in a second truncated cluster. This kind of event  
 4794 is not likely but needs to be taken into account nonetheless. A possible improvement would be to  
 4795 identify clusters in a 2D space whose dimensions are time and strip. In this 2D space, the cluster  
 4796 could be geometrically identified as isolated groups of adjacent strips receiving a hit at a similar time.  
 4797

```

4798
  class RPCCluster{
    private:
      Uint ClusterSize; //Size of cluster #ID
      Uint FirstStrip; //First strip of cluster #ID
      Uint LastStrip; //Last strip of cluster #ID
      float Center; //Center of cluster #ID ((first+last)/2)
      float StartStamp; //Time stamp of the earliest hit of cluster #ID
      float StopStamp; //Time stamp of the latest hit of cluster #ID
      float TimeSpread; //Time difference between earliest and latest hits
                         //of cluster #ID
    public:
      RPCCluster();
      RPCCluster(HitList List, Uint cID, Uint cSize, Uint first, Uint firstID);
      RPCCluster(const RPCCluster& other);
      ~RPCCluster();
      RPCCluster& operator=(const RPCCluster& other);

      Uint GetID();
      Uint GetSize();
      Uint GetFirstStrip();
      Uint GetLastStrip();
      float GetCenter();
      float GetStart();
      float GetStop();
      float GetSpread();
    };

    typedef vector<RPCCluster> ClusterList;

    //Other functions to build cluster lists out of hit lists
    void BuildClusters(HitList &cluster, ClusterList &clusterList);
    void Clusterization(HitList &hits, TH1 *hcSize, TH1 *hcMult);
  
```

4799

*Source Code B.11: Description of C++ object Cluster.*

## 4800 B.6 DAQ data Analysis

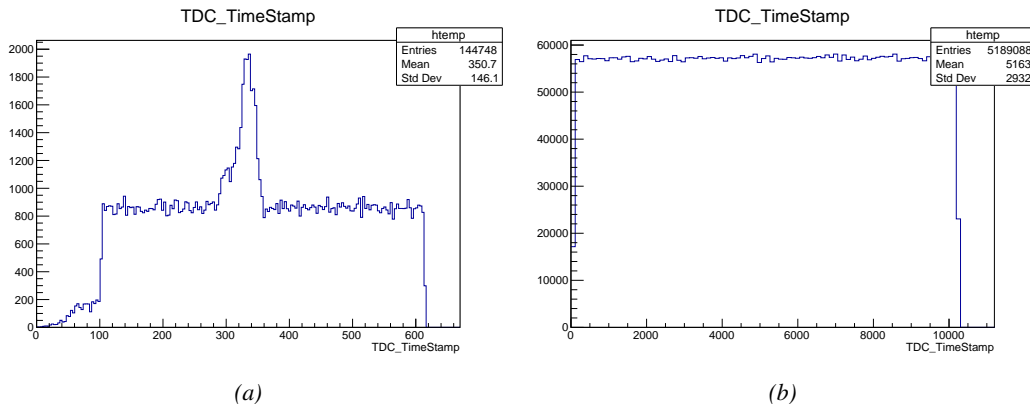
4801 All the ingredients to analyse GIFT++ data have been introduced. This section will focus on the  
 4802 different part of the analysis performed on the data, from determining the type of data the tool is  
 4803 dealing with to calculate the hit and cluster rate per unit area in each detector or reconstructing  
 4804 muon or gamma clusters.

### 4805 B.6.1 Determination of the run type

4806 In GIF++, both the performance of the detectors in detecting muons in an irradiated environment  
 4807 and the gamma or noise background can be independantly measured. These correspond to different  
 4808 run types and hence, to different TDC settings giving different data to look at.

4809 In the case of performance measurements, the trigger for data taking is provided by the coin-  
 4810 cidence of several scintillators when muons from the beam passing through the area are detected.  
 4811 Data is collected in a 600 ns wide window centered around the arrival of muons in the RPCs. The  
 4812 expected time distribution of hits is shown in Figure B.1a. The muon peak is clearly visible in the  
 4813 center of the distribution and is to be extracted from the gamma background that composes the flat  
 4814 part of the distribution.

4815 On the other hand, gamma background or noise measurements are focussed on the non muon  
 4816 related physics and the trigger needs to be independant from the muons to give a good measurement  
 4817 of the gamma/noise distribution as seen by the detectors. The trigger is then provided by a pulse  
 4818 generated by the DAQ at a frequency of 100 Hz whose pulse is not likely to be on time with a muon.  
 4819 In order to increase the integrated time without increasing proportionnaly the acquisition time, the  
 4820 width of the acquisition windows are increased to 10  $\mu$ s. The time distribution of the hits is expected  
 4821 to be flat, as shown by Figure B.1b.



4822 *Figure B.1: Example of expected hit time distributions in the cases of efficiency (Figure B.1a) and noise/gamma*  
 4823 *rate per unit area (Figure B.1b) measurements as extracted from the raw ROOT files. The unit along the x-axis*  
 4824 *corresponds to ns. The fact that "the" muon peak is not well defined in Figure B.1a is due to the contribution*  
 4825 *of all the RPCs being tested at the same time that don't necessarily have the same signal arrival time. Each*  
*individual peak can have an offset with the ones of other detectors. The inconsistancy in the first 100 ns of both*  
*time distributions is an artefact of the TDCs and are systematically rejected during the analysis.*

4826 The ROOT files include a `TTree` called `RunParameters` containing, among other things, the infor-  
 4827 mation related to the run type. The run type can then be accessed as described by Source Code B.12  
 4828 and the function `IsEfficiencyRun()` is then used to determine if the run file is an efficiency run or,  
 4829 on the contrary, another type of run (noise or gamma measurement).

4830 Finally, the data files will have a slightly different content whether it was collected before or after  
 4831 October 2017 and the upgrade of the DAQ software that brought a new information into the ROOT  
 4832 output. This is discussed in Appendix A.4.3 and implies that the analysis will differ a little depending  
 4833 on the data format. Indeed, as no information on the data quality is stored, in older data files, the cor-  
 4834 rections for missing events has to be done at the end of the analysis. The information about the type

4831 of data format is stored in the variable **bool** `isNewFormat` by checking the list of branches contained  
 4832 in the data tree via the methods `TTree::GetListOfBranches()` and `TCollection::Contains()`.

```
4833
4834     TTree* RunParameters = (TTree*)dataFile.Get("RunParameters");
4835     TString* RunType = new TString();
4836     RunParameters->SetBranchAddress("RunType", &RunType);
4837     RunParameters->GetEntry(0);
```

4835       *Source Code B.12: Access to the run type contained in `TTree* RunParameters`.*

## 4836       **B.6.2 Beam time window calculation for efficiency runs**

4837 Knowing the run type is important first of all to know the width of the acquisition window to be used  
 4838 for the rate calculation and finally to be able to seek for muons. Indeed, the peak that appears in the  
 4839 time distribution for each detectors is then fitted to extract the most probable time window in which  
 4840 the tool should look for muon hits. The data outside of this time window is then used to evaluate the  
 4841 noise or gamma background the detector was subjected to during the data taking. Computing the  
 4842 position of the peak is done calling the function `SetBeamWindow()` defined in file `src/RPCHit.cc` that  
 4843 loops a first time on the data. The data is first sorted in a 3D array of 1D histograms (`GIFH1Array`, see  
 4844 `include/types.h`). Then the location of the highest bin is determined using `TH1::GetMaximumBin()`  
 4845 and is used to define a window in which a gaussian fit will be applied to compute the peak width.  
 4846 This window is a 80 ns defined by Formula B.1 around the central bin.

$$(B.1a) \quad t_{center}(ns) = bin \times width_{bin}(ns)$$

$$(B.1b) \quad [t_{low}; t_{high}] = [t_{center} - 40; t_{center} + 40]$$

4847 Before the fit is performed, the average number of noise/gamma hits per bin is evaluated using  
 4848 the data outside of the fit window. Excluding the first 100 ns, the average number of hits per bin  
 4849 due to the noise or gamma is defined by Formula B.2 after extracting the amount of hits in the time  
 4850 windows  $[100; t_{low}]$  and  $[t_{high}; 600]$  thanks to the method `TH1::Integral()`. This average number  
 4851 of hits is then subtracted to every bin of the 1D histogram, in order to *clean* it from the noise or  
 4852 gamma contribution as much as possible to improve the fit quality. Bins where  $\langle n_{hits} \rangle$  is greater  
 4853 than the actual bin content are set to 0.

$$(B.2a) \quad \Delta t_{noise}(ns) = 600 \overbrace{-t_{high} + t_{low}}^{-80ns} - 100 = 420ns$$

$$(B.2b) \quad \langle n_{hits} \rangle = width_{bin}(ns) \times \frac{\sum_{t=100}^{t_{low}} + \sum_{t=t_{high}}^{600}}{\Delta t_{noise}(ns)}$$

4854 Finally, the fit parameters are extracted and saved for each detector in 3D arrays of **float**  
 4855 (`muonPeak`, see `include/types.h`), a first one for the mean arrival time of the muons, `PeakTime`,  
 4856 a second for the height or strength of the peak, `PeakHeight`, and a third one for the width of the  
 4857 peak, `PeakWidth`. The width is on purpose chosen to be wider than the peak and defined as  $6\sigma$  of the  
 4858 gaussian fit, for a peak range being as given by Formula B.3.

$$(B.3) \quad [t_{low}^{peak}; t_{high}^{peak}] = [t_{center}^{peak} - 3\sigma; t_{center}^{peak} + 3\sigma]$$

4859 For a finer analysis, it is advised to determine more precisely the width of the peak to exclude  
 4860 as much noise or background hits as possible. The same settings are applied to every partitions of  
 4861 the same detector. To determine which one of the detector's partitions is directly illuminated by the  
 4862 beam, the peak height of each partition is compared and the highest one is then used to define the  
 4863 peak settings.

4864 It is not possible to identify the particles causing the hits, hence muons, background gamma  
 4865 particles or even noise could be responsible of hits within the time window. To be able to account  
 4866 for this effect, the peak width extracted from the fit on the peak will also be used to define a fake  
 4867 time window, uncorrelated to the muon peak and in which a fake efficiency, contribution from both  
 4868 background and noise, will be measured. This window corresponds to the time range described in  
 4869 Formula B.4.

$$(B.4) \quad [t_{low}^{fake}; t_{high}^{fake}] = [600 - 6\sigma; 600]$$

### 4870 B.6.3 Data loop and histogram filling

4871 3D arrays of histogram are created to store the data and display it on the DQM of GIF++ webDCS  
 4872 for the use of shifters. The dimensions correspond to the different layers held into the GIF++ infras-  
 4873 tructure (trolleys `T` containing RPCs or *slots* `s` each being divided into read-out partitions `p`). These  
 4874 histograms, presented in section B.2.1.1, are filled while looping on the data. Before starting the  
 4875 analysis loop, it is necessary to control the entry quality for the new file formats featuring `QFlag`. If  
 4876 the `QFlag` value for this entry shows that 1 TDC or more have a `CORRUPTED` flag, then this event is  
 4877 discarded. The loss of statistics is low enough to be neglected. `QFlag` is controlled using the func-  
 4878 tion `IsCorruptedEvent()` defined in `src/utils.cc`. As explained in Appendix A.4.3, each digit of  
 4879 this integer represent a TDC flag that can be either 1 or 2. Each 2 is the sign of a `CORRUPTED` state.  
 4880 Then, the data is accessed entry by entry in the ROOT `TTree` using `RAWData` and each hit in the hit  
 4881 list is assigned to a detector channel and saved in the corresponding histograms. As described in  
 4882 Source Code B.13, in the first part of the analysis, in which the loop over the ROOT file's content is  
 4883 performed, the different steps are:

4884 **1- RPC channel assignment and control:** a check is done on the RPC channel extracted thanks  
 4885 to the mapping via the method `Mapping::GetLink()`. If the channel is not initialised and is 0, or if  
 4886 the TDC channel is not contained in a range in between X000 and X127, X being the TDC ID, the  
 4887 hit is discarded. This means there was a problem in the mapping. Often a mapping problem leads to  
 4888 the failure of the offline tool.

4889 **2- Creation of a `RPCHit` object:** to easily get the trolley, slot and partition in which the hit has  
 4890 been assigned, this object is particularly helpful.

4891 **3- General histograms are filled:** the hit is filled into the time distribution, global hit distribution  
 4892 and time versus strip histograms, and if the arrival time is within the first 100 ns, it is discarded and  
 4893 nothing else happens and the loop proceeds with the next hit in the list, going back to step 1.

4894

```

for(int h = 0; h < data.TDCCh->size(); h++) {
    UInt tdcchannel = data.TDCCh->at(h);
    UInt rpcchannel = RPCChMap->GetLink(tdcchannel);
    float timestamp = data.TDCTS->at(h);
    //Get rid of the hits in channels not considered in the mapping
    if(rpcchannel != NOCHANNELLINK) {
        RPCHit hit(rpcchannel, timestamp, GIFInfra);
        UInt T = hit.GetTrolley();
        UInt S = hit.GetStation()-1;
        UInt P = hit.GetPartition()-1;
        //Fill the time and hit profiles
        TimeProfile_H.rpc[T][S][P]->Fill(hit.GetTime());
        HitProfile_H.rpc[T][S][P]->Fill(hit.GetStrip());
        TimeVSChanProfile_H.rpc[T][S][P]->Fill(hit.GetStrip(),hit.GetTime());
        //Reject the 100 first ns due to inhomogeneity of data
        if(hit.GetTime() >= TIMEREJECT) {
            Multiplicity.rpc[T][S][P]++;
            if(IsEfficiencyRun(RunType)) {
                //Define peak time range for efficiency calculation
                float lowlimit_eff = PeakTime.rpc[T][S][P]
                    - PeakWidth.rpc[T][S][P];
                float highlimit_eff = PeakTime.rpc[T][S][P]
                    + PeakWidth.rpc[T][S][P];
                bool peakrange = (hit.GetTime() >= lowlimit_eff
                    && hit.GetTime() < highlimit_eff);
                //Fill hits inside of the defined peak and noise range
                if(peakrange) {
                    BeamProfile_H.rpc[T][S][P]->Fill(hit.GetStrip());
                    PeakHitList.rpc[T][S][P].push_back(hit);
                } else {
                    StripNoiseProfile_H.rpc[T][S][P]->Fill(hit.GetStrip());
                    NoiseHitList.rpc[T][S][P].push_back(hit);
                }
                //Then define time range for fake efficiency
                float highlimit_fake = BMTDCWINDOW;
                float lowlimit_fake = highlimit_fake
                    - (highlimit_eff-lowlimit_eff);
                bool fakerange = (hit.GetTime() >= lowlimit_fake
                    && hit.GetTime() < highlimit_fake);
                //Fill the hits inside of the fake window
                if(fakerange) {
                    FakeHitList.rpc[T][S][P].push_back(hit);
                }
            } else {
                //Fill the hits inside of the defined noise range
                StripNoiseProfile_H.rpc[T][S][P]->Fill(hit.GetStrip());
                NoiseHitList.rpc[T][S][P].push_back(hit);
            }
        }
    }
}

```

4895

4896

*Source Code B.13: For each entry of the raw ROOT data file, the code loops over the list of channels and corresponding time stamps contained in branches `TDC_channel` and `TDC_TimeStamp` and constructs `RPCHit` objects that are filled in the peak, noise and fake hit lists and also fills the time, hit, beam and noise profiles.*

4897

**4- Multiplicity counter:** the hit multiplicity counter of the corresponding detectors is incremented.

4898 **5-a-1 Efficiency runs - Is the hit within the peak window? :** if the hit is contained in the peak  
 4899 window previously defined by Formula B.3, it is filled into the beam hit profile histogram of the  
 4900 corresponding chamber, added into the list of peak hits and increments the counter of *in time* hits.  
 4901 The term *in time* here refers to the hits that are likely to be muons by arriving in the expected time  
 4902 window. If the hit is outside of the peak window, it is filled into the noise profile histogram of  
 4903 the corresponding detector, added into the list of noise/gamma hits and increments the counter of  
 4904 noise/gamma hits.

4905 **5-a-2 Efficiency runs - Is the hit within the fake window? :** if the hit is contained in the fake  
 4906 window previously defined by Formula B.4, it is added into the list of fake hits. Counting the fake  
 4907 hits outside the peak window allows to estimate the probability to detect in time background or noise.

4908 **5-b- Noise/gamma rate runs - Noise histograms are filled:** the hit is filled into the noise profile  
 4909 histogram of the corresponding detector, added into the list of noise/gamma hits and increments the  
 4910 counter of noise/gamma hits.

```
4911
  for(UInt tr = 0; tr < GIFInfra->GetNTrolleys(); tr++) {
    UInt T = GIFInfra->GetTrolleyID(tr);
    for(UInt sl = 0; sl < GIFInfra->GetNSlots(tr); sl++) {
      UInt S = GIFInfra->GetSlotID(tr,sl) - 1;
      UInt nStripsPart = GIFInfra->GetNStrips(tr,sl);
      string rpcID = GIFInfra->GetName(tr,sl);
      for (UInt p = 0; p < GIFInfra->GetNPartitions(tr,sl); p++) {
        //Clusterize noise/gamma data
        sort(NoiseHitList.rpc[T][S][p].begin(),
              NoiseHitList.rpc[T][S][p].end(),SortHitbyTime);
        Clusterization(NoiseHitList.rpc[T][S][p],
                       NoiseCSize_H.rpc[T][S][p],NoiseCMult_H.rpc[T][S][p]);
        //Clusterize muon data and fill efficiency histograms based on
        //the content of peak and fake hit vectors if efficiency run
        if(IsEfficiencyRun(RunType)){
          //Peak data
          sort(PeakHitList.rpc[T][S][p].begin(),
                PeakHitList.rpc[T][S][p].end(),SortHitbyTime);
          Clusterization(PeakHitList.rpc[T][S][p],
                         PeakCSize_H.rpc[T][S][p],PeakCMult_H.rpc[T][S][p]);
          if(PeakHitList.rpc[T][S][p].size() > 0)
            EfficiencyPeak_H.rpc[T][S][p]->Fill(DETECTED);
          else EfficiencyPeak_H.rpc[T][S][p]->Fill(MISSED);

          //Fake data
          if(FakeHitList.rpc[T][S][p].size() > 0)
            EfficiencyFake_H.rpc[T][S][p]->Fill(DETECTED);
          else EfficiencyFake_H.rpc[T][S][p]->Fill(MISSED);
        }
        //Save and reinitialise the hit multiplicity
        HitMultiplicity_H.rpc[T][S][p]->Fill(Multiplicity.rpc[T][S][p]);
        Multiplicity.rpc[T][S][p] = 0;
      }
    }
  }
```

4913      *Source Code B.14: Loops to clusterize the hit lists and fill efficiency and multiplicity histograms.*

4914      After the loop on the hit list of the entry is over, the next step is to clusterize the 3D lists filled

4915 in the previous steps, as displayed in Source Code B.14. A 3D loop is then started over the active  
 4916 trolley, slot and RPC partitions to access these objects. Each `NoiseHitList` and `PeakHitList`, in  
 4917 case of efficiency run, are clusterized as described in section B.5.2. There corresponding cluster size  
 4918 and multiplicity histograms are filled at the end of the clustering process.

4919 Then, the peak and fake efficiency histograms are filled in case of efficiency run. The selection is  
 4920 simply made by checking whether the RPC detected signals in the peak window or/and fake window  
 4921 during this event. In the case a hit is recorded in either of both time windows, the histogram is  
 4922 filled with 1. On the contrary, the histogram is filled with 0. Finally, it is useful to remind that  
 4923 at this level, it is not possible yet to discriminate in between a muon hit and noise or gamma hit.  
 4924 the histograms `PeakCSize_H`, `PeakCMult_H` and `EfficiencyPeak_H` are then subjected to noise and  
 4925 background contamination. This contamination is estimated thanks to the fake efficiency histogram  
 4926 `EfficiencyFake_H` and corrected at the moment the results will be written into output CSV files and  
 4927 the histograms `MuonCSize_H`, `MuonCMult_H` and `Efficiency0_H` will be filled. The correction will be  
 4928 explained in Section B.6.4.3.

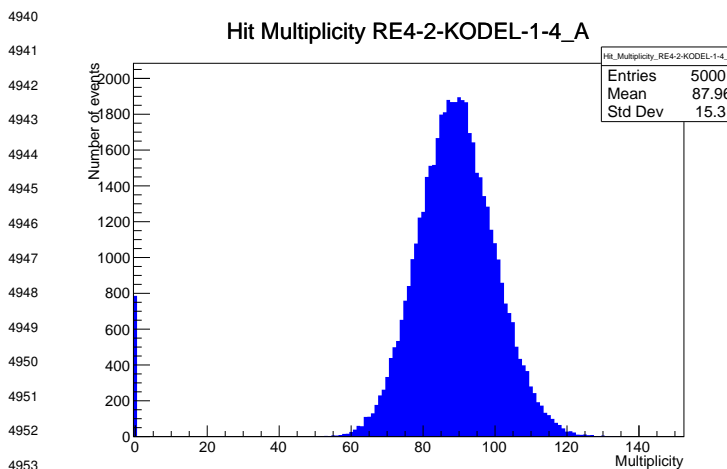
4929 Finally, the loop ends on the filling of the general hit multiplicity histogram of each detector  
 4930 partitions.

#### 4931 **B.6.4 Results calculation**

4932 As mentioned in section B.2.1, the analysis of DAQ data provides the user with 3 CSV files and  
 4933 a ROOT file associated to each and every ROOT data file. The fourth CSV file is provided by the  
 4934 extraction of the CEAN main frame data monitored during data taking and will be discussed later.  
 4935 After looping on the data in the previous part of the analysis macro, the output files are created and a  
 4936 3D loop on each RPC readout partitions is started to extract the histograms parameters and compute  
 4937 the final results.

4938

##### 4939 **B.6.4.1 Rate normalisation**



4959 *Figure B.2: The effect of the quality flag is explained by presenting the  
 4960 reconstructed hit multiplicity of a data file without `Quality_flag`. The  
 4961 artificial high content of bin 0 is the effect of corrupted data.*

The hit rate normalization corresponds to translating a number of hits recorded during the full duration of data taking into a rate per unit area value. In order to achieve such result, it is first needed to know the total integrated time and the active area of the read-out partition on which the hits are counted. The total integrated is simply the noise window used for each event multiplied by the total number of events stored in the data file.

Nevertheless, to analyse old data format files, not containing any quality flag, it is

needed to estimate the amount of corrupted data via a fit as the corrupted data will always fill events with a fake "0 multiplicity". Indeed, as no hits were stored in the DAQ ROOT files, these events artificially contribute to fill the bin corresponding to a null multiplicity, as shown in Figure B.2. In the case the mean of the hit multiplicity distribution is high, the contribution of the corrupted data can easily be evaluated for later correction by comparing the level of the bin at multiplicity 0 and of a skew fit curve that should indicate a value consistent with 0. A skew fit has been chosen over a Poisson fit as it was giving better results for lower mean multiplicity values. Nevertheless, for low irradiation cases, as explained in Appendix A.4.3, the hit multiplicity distribution mean is, on the contrary, rather small and the probability to record events without hits can't be considered small anymore, leading to a difficult and non-reliable estimation of the corruption.

```

4958
4959     needed to estimate the amount of corrupted data via a fit as the corrupted data will always fill events
4960     with a fake "0 multiplicity". Indeed, as no hits were stored in the DAQ ROOT files, these events
4961     artificially contribute to fill the bin corresponding to a null multiplicity, as shown in Figure B.2. In
4962     the case the mean of the hit multiplicity distribution is high, the contribution of the corrupted data
4963     can easily be evaluated for later correction by comparing the level of the bin at multiplicity 0 and
4964     of a skew fit curve that should indicate a value consistent with 0. A skew fit has been chosen over
4965     a Poisson fit as it was giving better results for lower mean multiplicity values. Nevertheless, for
4966     low irradiation cases, as explained in Appendix A.4.3, the hit multiplicity distribution mean is, on
4967     the contrary, rather small and the probability to record events without hits can't be considered small
4968     anymore, leading to a difficult and non-reliable estimation of the corruption.

4968
4969     if(!isNewFormat) {
5000         TF1* GaussFit = new TF1("gaussfit","[0]*exp(-0.5*((x-[1])/[2])**2)",0,Xmax);
5001         GaussFit->SetParameter(0,100);
5002         GaussFit->SetParameter(1,10);
5003         GaussFit->SetParameter(2,1);
5004         HitMultiplicity_H.rpc[T][S][p]->Fit(GaussFit,"LIQR","","0.5,Xmax");

5005         TF1* SkewFit = new TF1("skewfit","[0]*exp(-0.5*((x-[1])/[2])**2) / (1 +
5006         <- exp(-[3]*(x-[4])))",0,Xmax);
5007         SkewFit->SetParameter(0,GaussFit->GetParameter(0));
5008         SkewFit->SetParameter(1,GaussFit->GetParameter(1));
5009         SkewFit->SetParameter(2,GaussFit->GetParameter(2));
5010         SkewFit->SetParameter(3,1);
5011         SkewFit->SetParameter(4,1);
5012         HitMultiplicity_H.rpc[T][S][p]->Fit(SkewFit,"LIQR","","0.5,Xmax");

5013         double fitValue = SkewFit->Eval(1,0,0,0);
5014         double dataValue = (double)HitMultiplicity_H.rpc[T][S][p]->GetBinContent(2);
5015         double difference = TMath::Abs(dataValue - fitValue);
5016         double fitTOdataVSentries_ratio = difference / (double)nEntries;
5017         bool isFitGOOD = fitTOdataVSentries_ratio < 0.01;
5018         double nSinglehit = (double)HitMultiplicity_H.rpc[T][S][p]->GetBinContent(1);
5019         double lowMultRatio = nSinglehit / (double)nEntries;
5020         bool isMultLOW = lowMultRatio > 0.4;
5021         if(isFitGOOD && !isMultLOW){
5022             nEmptyEvent = HitMultiplicity_H.rpc[T][S][p]->GetBinContent(1);
5023             nPhysics = (int)SkewFit->Eval(0,0,0,0);
5024             if(nPhysics < nEmptyEvent)
5025                 nEmptyEvent = nEmptyEvent-nPhysics;
5026         }
5027     }
5028     double corrupt_ratio = 100.*(double)nEmptyEvent / (double)nEntries;
5029     outputCorrCSV << corrupt_ratio << '\t';
5030     float rate_norm = 0.;
5031     float stripArea = GIFInfra->GetStripGeo(tr,sl,p);

5032     if(IsEfficiencyRun(RunType)){
5033         float noiseWindow = BMTDCWINDOW - TIMEREJECT - 2*PeakWidth.rpc[T][S][p];
5034         rate_norm = (nEntries-nEmptyEvent)*noiseWindow*1e-9*stripArea;
5035     } else
5036         rate_norm = (nEntries-nEmptyEvent)*RDMNOISEWDW*1e-9*stripArea;

```

*Source Code B.15: Definition of the rate normalisation variable. It takes into account the number of non corrupted entries and the time window used for noise and background calculation, to estimate the total integrated time, and the strip active area to express the result as rate per unit area.*

4971 As can be seen in Source Code B.15, conditions have been applied to prevent bad fits and wrong  
 4972 corruption estimation in cases where :

- 4973     • The difference in between the data for multiplicity 1 and the corresponding fit value should be  
 4974       lower than 1% of the total amount of data :  $\frac{|n_{m=1} - sk(1)|}{N_{tot}} < 0.01$  where  $n_{m=1}$  is the number  
 4975       of entries with multiplicity 1,  $sk(1)$  the value of the skew fit, as defined by Formula 5.2, for  
 4976       multiplicity 1 and  $N_{tot}$  the total number of entries.
- 4977     • The amount of data contained in the multiplicity 0 bin should not exceed 40% of the total  
 4978       data content:  $\frac{n_{m=0}}{N_{tot}} \leq 0.4$  where  $n_{m=0}$  is the number of entries with multiplicity 0. This  
 4979       number has been determined to be the maximum to be able to separate the excess of data due  
 4980       to corruption from the hit multiplicity distribution.

4981 Those 2 conditions need to be fulfilled to estimate the corruption of old data format files. If the  
 4982 fit was successful, the level of corruption is written in `Offline-Corrupted.csv` and the number of  
 4983 corrupted entries, refered as the integer `nEmptyEvent`, is subtracted from the total number of entries  
 4984 when the rate normalisation factor is computed as explicitated in Source Code B.15. Note that for new  
 4985 data format files, the number of corrupted entries being set to 0, the definition of `rate_norm` stays  
 4986 valid.

#### 4987     B.6.4.2 Rate and activity

```
int nNoise = StripNoiseProfile_H.rpc[T][S][p]->GetEntries();
float averageNhit = (nNoise>0) ? (float)(nNoise/nStripsPart) : 1.;

for(Uint st = 1; st <= nStripsPart; st++){
    float stripRate =
        StripNoiseProfile_H.rpc[T][S][p]->GetBinContent(st)/rate_norm;
    float stripAct =
        StripNoiseProfile_H.rpc[T][S][p]->GetBinContent(st)/averageNhit;

    StripNoiseProfile_H.rpc[T][S][p]->SetBinContent(st,stripRate);
    StripActivity_H.rpc[T][S][p]->SetBinContent(st,stripAct);
}
```

4989     *Source Code B.16: Description of the loop that allows to set the content of each strip rate and strip activity  
 channel for each detector partition.*

4990     At this point, the strip rate histograms, `StripNoiseProfile_H.rpc[T][S][p]`, only contain an  
 4991 information about the total number of noise or background rate hits each channel received during the  
 4992 data taking. As described in Source Code B.16, a loop on the strip channels will be used to normalise  
 4993 the content of the rate distribution histogram for each detector partitions. The initial number of hits  
 4994 recorded for a given bin will be extracted and 2 values are computed.

- 4995     • The strip hit rate, defined as the number of hits recorded in the bin normalised like described  
 4996       in the previous section, using the variable `rate_norm` and the corresponding bin in histogram  
 4997       `StripNoiseProfile_H.rpc[T][S][p]` is updated, and
- 4998     • the strip activity, defined as the number of hits recorded in the bin normalised to the average  
 4999       number of hits per bin contained in the partition histogram, using the variable `averageNhit`.  
 5000       This value provides an information on the homogeneity of the detector response to the gamma

5001 background or of the detector noise. An activity of 1 corresponds to an average response.  
 5002 Above 1, the channel is more active than the average and bellow 1, the channel is less active.  
 5003 This value is filled in the histograms `StripActivity_H.rpc[T][S][p]`.

5004 On each detector partitions, which are read-out by a single FEE, all the channels are not pro-  
 5005 cessed by the same chip. Each chip can give a different noise response and hence, histograms using  
 5006 a chip binning are used to investigate chip related noise behaviours. The average values of the strip  
 5007 rate or activity grouped into a given chip are extracted using the using the function `GetChipBin()`  
 5008 and stored in dedicated histograms as described in Source Codes B.17 and B.18 respectively.

```
5009 float GetChipBin(TH1* H, Uint chip){  

  5010   Uint start = 1 + chip*NSTRIPSCHIP;  

   int nActive = NSTRIPSCHIP;  

   float mean = 0.;  

   for(Uint b = start; b <= (chip+1)*NSTRIPSCHIP; b++) {  

     float value = H->GetBinContent(b);  

     mean += value;  

     if(value == 0.) nActive--;  

   }  

   if(nActive != 0) mean /= (float)nActive;  

   else mean = 0.;  

   return mean;  

}
```

5011 *Source Code B.17: Function used to compute the content of a bin for an histogram using chip binning.*

```
5012   for(Uint ch = 0; ch < (nStripsPart/NSTRIPSCHIP); ch++) {  

    ChipMeanNoiseProf_H.rpc[T][S][p]->  

      SetBinContent(ch+1,GetChipBin(StripNoiseProfile_H.rpc[T][S][p],ch));  

    ChipActivity_H.rpc[T][S][p]->  

      SetBinContent(ch+1,GetChipBin(StripActivity_H.rpc[T][S][p],ch));  

  }
```

5013 *Source Code B.18: Description of the loop that allows to set the content of each chip rate and chip activi-  
 tity bins for each detector partition knowing the information contained in the corresponding strip distribution  
 histograms.*

5014 The activity variable is then used to evaluate the homogeneity of the detector response to back-  
 5015 ground or of the detector noise. The homogeneity  $h_p$  of each detector partition can be evaluated  
 5016 using the formula  $h_p = \exp(-\sigma_p^R/\langle R \rangle_p)$ , where  $\langle R \rangle_p$  is the partition mean rate and  $\sigma_p^R$  is the  
 5017 rate standard deviation calculated over the partition channels. The more homogeneously the rates  
 5018 are distributed and the smaller will  $\sigma_p^R$  be, and the closer to 1 will  $h_p$  get. On the contrary, if the  
 5019 standard deviation of the channel's rates is large,  $h_p$  will rapidly get to 0. This value is saved into  
 5020 histograms as shown in Source Code B.19 and could in the future be used to monitor through time,  
 5021 once extracted, the evolution of every partition homogeneity. This could be of great help to under-  
 5022 stand the apparition of eventual hot spots due to ageing of the chambers subjected to high radiation  
 5023 levels. The monitored homogeneity information could then be combined with a monitoring of the  
 5024 activity of each individual channel in order to have a finer information. Monitoring tools have been  
 5025 suggested and need to be developed for this purpose.

```

5026
float MeanPartSDev = GetTH1StdDev(StripNoiseProfile_H.rpc[T][S][p]);
float strip_homog = (MeanPartRate==0)
    ? 0.
    : exp(-MeanPartSDev/MeanPartRate);
StripHomogeneity_H.rpc[T][S][p]->Fill("exp -#left(#frac{\#sigma_{Strip}
    → Rate}}{\#mu_{Strip Rate}}\#right)",strip_homog);
StripHomogeneity_H.rpc[T][S][p]->GetYaxis()->SetRangeUser(0.,1.);

5027
float ChipStDevMean = GetTH1StdDev(ChipMeanNoiseProf_H.rpc[T][S][p]);
float chip_homog = (MeanPartRate==0)
    ? 0.
    : exp(-ChipStDevMean/MeanPartRate);
ChipHomogeneity_H.rpc[T][S][p]->Fill("exp -#left(#frac{\#sigma_{Chip}
    → Rate}}{\#mu_{Chip Rate}}\#right)",chip_homog);
ChipHomogeneity_H.rpc[T][S][p]->GetYaxis()->SetRangeUser(0.,1.);
```

5028       *Source Code B.19: Storage of the homogeneity into dedicated histograms.*

5029     **B.6.4.3 Correction of muon performance parameters**

5030 By previously filling the peak and fake efficiency histograms as well as the peak and noise cluster  
 5031 size and cluster multiplicity it is possible to compute the efficiency of muon detection, the muon  
 5032 cluster size, as well as the muon cluster multiplicity. This calculation is based on independant  
 5033 event probabilities. The independant events that can be measured in the data are, " $\mu$ : A muon was  
 5034 detected" and " $\gamma$ : noise or background was detected". It is trivial to realize that the data in the peak  
 5035 window corresponds to the intersection of both events, " $\mu \cup \gamma$ : a muon or noise or background was  
 5036 detected". This way, the efficiency measured in the peak window is actually the probability of the  
 5037 event  $\mu \cup \gamma$  while the efficiency in the fake window is then the probability of the event  $\gamma$  alone.  
 5038 Assuming that  $\mu$  and  $\gamma$  are independant, the probability of their intersection can be written as in  
 5039 Formula B.5.

$$(B.5) \quad P(\mu \cup \gamma) = P(\mu) + P(\gamma) - P(\mu)P(\gamma)$$

5040 Isolating the probability of the event  $\mu$  alone, actually corresponding to the muon detection  
 5041 efficiency, can be then calculated with the quantities that are contained in the peak and fake histogram  
 5042 as in Formula B.6.

$$(B.6) \quad P(\mu) = \frac{P(\mu \cup \gamma) - P(\gamma)}{1 - P(\gamma)} \quad \Leftrightarrow \quad \epsilon_\mu = \frac{\epsilon_{peak} - \epsilon_{fake}}{1 - \epsilon_{fake}}$$

5043 When it comes to the computation of the muon cluster size, a similar reasoning than for the muon  
 5044 detection efficiency computation can be used. Indeed, using Formula B.5, out of the total number of  
 5045 events where a muon or noise or background can be expressed as a sum of fractions of events  $\mu$ ,  $\gamma$   
 5046 and  $\mu \cap \gamma$ , the later being the event corresponding to the detection of both events simultaneously, as  
 5047 showed in Formula B.7. The fractions can be expressed as a ratio of the probabilities already known,  
 5048 using this time the notation  $P(\mu \cap \gamma)$  instead of  $P(\mu)P(\gamma)$ . This choice was made to make the code  
 5049 a little clearer.

$$(B.7) \quad 1 = F_\mu + F_\gamma + F_{\mu \cap \gamma} = \frac{P(\mu) - P(\mu \cap \gamma)}{P(\mu \cup \gamma)} + \frac{P(\gamma) - P(\mu \cap \gamma)}{P(\mu \cup \gamma)} + \frac{P(\mu \cap \gamma)}{P(\mu \cup \gamma)}$$

```

if(IsEfficiencyRun(RunType)){  

    //Evaluate the probabilities for each detection case with errors  

    float P_peak = EfficiencyPeak_H.rpc[T][S][p]->GetMean();  

    float P_fake = EfficiencyFake_H.rpc[T][S][p]->GetMean();  

    float P_muon = (P_peak-P_fake)/(1-P_fake);  

    float P_both = P_muon*P_fake;  

    float P_peak_err = sqrt(P_peak*(1.-P_peak)/nEntries);  

    float P_fake_err = sqrt(P_fake*(1.-P_fake)/nEntries);  

    float P_muon_err = sqrt(P_muon*(1.-P_muon)/nEntries);  

    float P_both_err = sqrt(P_both*(1.-P_both)/nEntries);  

    Efficiency0_H.rpc[T][S][p]->Fill("muon efficiency",P_muon);  

    Efficiency0_H.rpc[T][S][p]->Fill("muon efficiency error",P_muon_err);  

    //For each case get the fraction of events it represents  

    float F_both = P_both/P_peak;  

    float F_muon = (P_muon-P_both)/P_peak;  

    float F_fake = (P_fake-P_both)/P_peak;  

    float F_both_err = F_both*(P_both_err/P_both+P_peak_err/P_peak);  

    float F_muon_err = (P_muon_err+F_both_err+F_muon*P_peak_err)/P_peak;  

    float F_fake_err = (P_fake_err+F_both_err+F_fake*P_peak_err)/P_peak;  

    //Get the measured cluster sizes correcting using the fractions  

    float CS_peak = PeakCSIZE_H.rpc[T][S][p]->GetMean();  

    float CS_fake = NoiseCSIZE_H.rpc[T][S][p]->GetMean();  

    float CS_peak_err = 2*PeakCSIZE_H.rpc[T][S][p]->GetStdDev()  

        /sqrt(PeakCSIZE_H.rpc[T][S][p]->GetEntries());  

    float CS_fake_err = 2*NoiseCSIZE_H.rpc[T][S][p]->GetStdDev()  

        /sqrt(NoiseCSIZE_H.rpc[T][S][p]->GetEntries());  

    float CS_muon = (CS_peak-CS_fake*(F_fake+F_both/2.))/(F_muon+F_both/2.);  

    float CS_muon_err = (CS_peak_err  

        +(F_fake+F_both/2.)*CS_fake_err  

        +CS_muon*F_muon_err  

        +CS_fake*(F_fake_err+F_both_err/2.))  

        /(F_muon+F_both/2.);  

    MuonCSIZE_H.rpc[T][S][p]->Fill("muon cluster size",CS_muon);  

    MuonCSIZE_H.rpc[T][S][p]->Fill("muon cluster size error",CS_muon_err);  

    //Finally get the muon cluster multiplicity as peak-fake  

    float noiseWindow = BMTDCWINDOW - TIMEREJECT - 2*PeakWidth.rpc[T][S][p];  

    float peakWindow = 2*PeakWidth.rpc[T][S][p];  

    float CM_peak = PeakCMult_H.rpc[T][S][p]->GetMean();  

    float CM_fake = NoiseCMult_H.rpc[T][S][p]->GetMean()*peakWindow/noiseWindow;  

    float CM_muon = CM_peak-CM_fake;  

    float CM_peak_err = 2*PeakCMult_H.rpc[T][S][p]->GetStdDev()  

        /sqrt(PeakCMult_H.rpc[T][S][p]->GetEntries());  

    float CM_fake_err = 2*NoiseCMult_H.rpc[T][S][p]->GetStdDev()  

        /sqrt(NoiseCMult_H.rpc[T][S][p]->GetEntries())  

        * peakWindow/noiseWindow;  

    float CM_muon_err = CM_peak_err + CM_fake_err;  

    MuonCMult_H.rpc[T][S][p]->Fill("muon cluster multiplicity",CM_muon);  

    MuonCMult_H.rpc[T][S][p]->Fill("muon cluster multiplicity  

    ↳ error",CM_muon_err);  

    //Write in the output CSV file  

    outputEffCSV << P_muon << '\t' << P_muon_err << '\t'  

        << CS_muon << '\t' << CS_muon_err << '\t'  

        << CM_peak << '\t' << CM_peak_err << '\t';
}

```

Source Code B.20: Analysis algorithm to compute muon efficiency, cluster size and multiplicity knowing the peak and fake efficiency, cluster size and multiplicity.

5052     Each ones of these events have an associated cluster size. The cluster size of the noise or back-  
 5053     ground already is measured thanks to the clusterization of the noise hit list. In the same way, the  
 5054     peak cluster size corresponds to the cluster measured for the event  $\mu \cup \gamma$ . Nevertheless, the cluster  
 5055     of the event  $\mu \cap \gamma$  is not known but it can be assumed that the probability of having more than 1  
 5056     noise or background cluster contained in the peak window is very low if the peak wondow duration  
 5057     is compared to the background rate that rarely seen to go beyond 2000 Hz/cm<sup>2</sup> [to be confirmed].  
 5058     Hence, the cluster size that is likely to be measured in such kind of event where both a muon and a  
 5059     background or noise cluster was recorded is the average of the muon cluster size and the background  
 5060     cluster size. The cluster size  $C_{\mu \cup \gamma}$  probed in the peak can then be written as in Formula B.8 and  
 5061     leads to the expression for the muon cluster size  $C_\mu$  written in Formula B.9.

$$(B.8) \quad C_{\mu \cup \gamma} = C_\mu F_\mu + C_\gamma F_\gamma + \frac{C_\mu + C_\gamma}{2} \times F_{\mu \cap \gamma}$$

$$(B.9) \quad C_\mu = \frac{C_{\mu \cup \gamma} - C_\gamma \times (F_\gamma + F_{\mu \cap \gamma}/2)}{F_\mu + F_{\mu \cap \gamma}/2}$$

5062     Finally, the computation of the muon cluster multiplicity comes quite naturally as the cluster  
 5063     multiplicity measured in the peak to which is subtracted the background cluster multiplpicity taken  
 5064     in a window of similar width. These calculations, as well as the error propagation that was not  
 5065     explicated here, can be seen going through Source Code B.20.

#### 5066     B.6.4.4 Strip masking tool

5067     The offline tool is automatically called at the end of each data taking to analyse the data and offer  
 5068     the shifter DQM histograms to control the data quality. After the histograms have been published  
 5069     online in the DQM page, the shifter can decide to mask noisy or dead channels that will contribute  
 5070     to bias the final rate calculation by editing the mask column of `ChannelsMapping.csv` as can be seen  
 5071     in Figure B.3.

5072     From the code point of view, the function `GetTH1Mean()` is used to retrieve the mean rate par-  
 5073     tition by partition after the rates have been calculated strip by strip and filled into the histograms  
 5074     `StripNoiseProfile_H.rpc[T][S][p]`, as described through Source Code B.21.

5075     Once the mask for each rejected channel has been updated, the shifter can manually run the  
 5076     offline tool again to update the DQM plots, now including the masked strips, as well the rate results  
 5077     written in the output CSV file `Offline-Rate.csv`. If not done during the shifts, the strip masking  
 5078     procedure needs to be carefully done by the person in charge of data analysis on the scans that were  
 5079     selected to produce the final results.

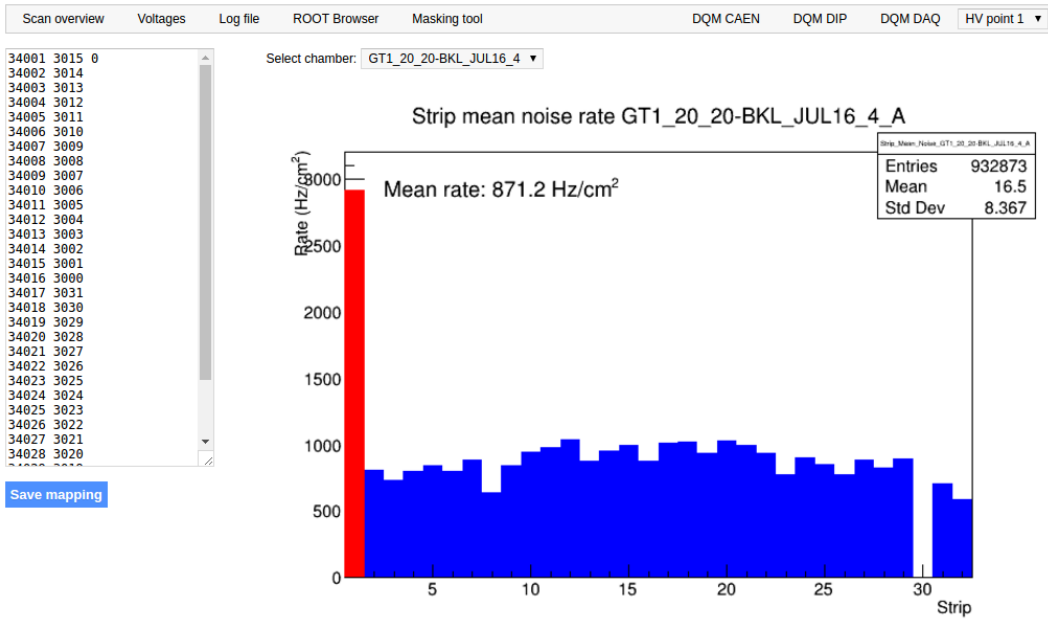


*Figure B.3: Display of the masking tool page on the webDCS. The window on the left allows the shifter to edit ChannelsMapping.csv. To mask a channel, it only is needed to set the 3rd field corresponding to the strip to mask to 0. It is not necessary for older mapping file formats to add a 1 for each strip that is not masked as the code is versatile and the default behaviour is to consider missing mask fields as active strips. The effect of the mask is directly visible for noisy channels as the corresponding bin turns red. The global effect of masking strips will be an update of the rate value showed on the histogram that will take into consideration the rejected channels.*

```

float GetTH1Mean (TH1* H){
    int nBins = H->GetNbinsX();
    int nActive = nBins;
    float mean = 0.;

    for(int b = 1; b <= nBins; b++){
        float value = H->GetBinContent (b);
        mean += value;
        if(value == 0.) nActive--;
    }

    if(nActive != 0) mean /= (float)nActive;
    else mean = 0.;

    return mean;
}

```

*Source Code B.21: The function GetTH1Mean() is used to return the mean along the y-axis of TH1 histograms containing rate information. In order to take into account masked strips whose rate is set to 0, the function looks for masked channels and decrement the number of active channels for each null value found.*

5082 **B.6.4.5 Output CSV files filling**

```

for (UInt tr = 0; tr < GIFInfra->GetNTrolleys(); tr++) {
    UInt T = GIFInfra->GetTrolleyID(tr);
    for (UInt sl = 0; sl < GIFInfra->GetNSlots(tr); sl++) {
        UInt S = GIFInfra->GetSlotID(tr,sl) - 1;
        float MeanNoiseRate = 0.;
        float ClusterRate = 0.;
        float ClusterSDev = 0.;

        for (UInt p = 0; p < GIFInfra->GetNPartitions(tr,sl); p++) {
            float MeanPartRate = GetTH1Mean(StripNoiseProfile_H.rpc[T][S][p]);
            float cSizePart = NoiseCSize_H.rpc[T][S][p]->GetMean();
            float cSizePartErr = (NoiseCSize_H.rpc[T][S][p]->GetEntries()==0)
                ? 0.
                : 2*NoiseCSize_H.rpc[T][S][p]->GetStdDev() /
                    sqrt(NoiseCSize_H.rpc[T][S][p]->GetEntries());
            float cMultPart = NoiseCMult_H.rpc[T][S][p]->GetMean();
            float cMultPartErr = (NoiseCMult_H.rpc[T][S][p]->GetEntries()==0)
                ? 0.
                : 2*NoiseCMult_H.rpc[T][S][p]->GetStdDev() /
                    sqrt(NoiseCMult_H.rpc[T][S][p]->GetEntries());
            float ClustPartRate = (cSizePart==0) ? 0.
                : MeanPartRate/cSizePart;
            float ClustPartRateErr = (cSizePart==0) ? 0.
                : ClustPartRate * cSizePartErr/cSizePart;

            outputRateCSV << MeanPartRate << '\t'
                << cSizePart << '\t' << cSizePartErr << '\t'
                << cMultPart << '\t' << cMultPartErr << '\t'
                << ClustPartRate << '\t' << ClustPartRateErr << '\t';

            RPCArea += stripArea * nStripsPart;
            MeanNoiseRate += MeanPartRate * stripArea * nStripsPart;
            ClusterRate += ClustPartRate * stripArea * nStripsPart;
            ClusterSDev += (cSizePart==0)
                ? 0.
                : ClusterRate*cSizePartErr/cSizePart;
        }
        MeanNoiseRate /= RPCArea;
        ClusterRate /= RPCArea;
        ClusterSDev /= RPCArea;
        outputRateCSV << MeanNoiseRate << '\t' << ClusterRate << '\t'
            << ClusterSDev << '\t';
    }
}

```

5084 *Source Code B.22: Description of rate result calculation and writing into the CSV output Offline-Rate.csv. Are saved into the file for each detector, the mean partition rate, cluster size and cluster mutiplicity, along with their errors, for each partition and as well as a detector average.*

5085 All the histograms have been filled. Parameters will then be extracted from them to compute the  
 5086 final results that will later be used to produce plots. Once the results have been computed, the very  
 5087 last step of the offline macro is to write these values into the corresponding CSV outputs. Aside of  
 5088 the file Offline-Corrupted.csv, 2 CSV files are being written by the macro OfflineAnalysis(),  
 5089 Offline-Rates.csv and Offline-L0-EffCl.csv that respectively contain information about noise  
 5090 or gamma rates, cluster size and multiplicity, and about level 0 reconstruction of the detector effi-  
 5091 ciency, muon cluster size and multiplicity. Details on the computation and file writing are respec-

5092 tively given in Sources Codes B.22 and B.20.

5093 **Noise/gamma background variables** are computed and written in the output file for each detector  
 5094 partitions. A detector average of the hit and cluster rate is also provided, as shown through Sources  
 5095 Code B.22. The variables that are written for each partition are:

- 5096 • The mean partition hit rate per unit area, `MeanPartRate`, that is extracted from the histogram  
`StripNoiseProfile_H` as the mean value along the y-axis, as described in section B.6.4.4. No  
 5097 error is recorded for the hit rate as this is considered a single measurement. No statistical error  
 5098 can be associated to it and the systematics are unknown.
- 5100 • The mean cluster size, `cSizePart`, is extracted from the histogram `NoiseCSize_H` and it's  
 5101 statistical error, `cSizePartErr`, is taken to be  $2\sigma$  of the total distribution.
- 5102 • The mean cluster multiplicity per trigger, `cMultPart`, is extracted from the histogram `NoiseCMult_H`  
 5103 and it's statistical error, `cMultPartErr`, is taken to be  $2\sigma$  of the total distribution. It is impor-  
 5104 tant to point to the fact that this variable gives an information that is dependent on the buffer  
 5105 window width used for each trigger for the calculation.
- 5106 • The mean cluster rate per unit area, `ClustPartRate`, is defined as the mean hit rate normalised  
 5107 to the mean cluster size and it's statistical error, `ClustPartRateErr`, is then obtained using the  
 5108 relative statistical error on the mean cluster size.

5109 **Muon performance variables** are computed as discussed in the Section B.6.4.3 and written in  
 5110 the output file for each detector partitions as shown through Sources Code B.20. It is reminded that  
 5111 this offline tool doesn't include any tracking algorithm to identify muons from the beam and only  
 5112 relies on the hits arriving in the time window corresponding to the beam time and is corrected thanks  
 5113 to the estimation of the contribution of the background and noise to the efficiency of the detector.  
 5114 Assuming that the detection of background and muons were independent events, a probabilistic  
 5115 approach was then used to correct efficiency, muon cluster size and muon cluster multiplicity. The  
 5116 variables that are written for each partition are:

- 5117 • The muon efficiency, referred to as the probability to detect a muon in the peak window  
`P_muon`, also filled in histogram `Efficiency0_H`. The statistical error related to the efficiency,  
 5118 `P_muon_err`, is computed using a binomial distribution, as the efficiency measures the proba-  
 5119 bility of "success" and "failure" to detect muons.
- 5121 • The mean muon cluster size, `CS_muon`, and its related statistical error, `CS_muon_err`, also filled  
 5122 in the histogram `MuonCSize_H`.
- 5123 • The mean muon cluster multiplicity, `CM_muon`, and its related statistical error, `CM_muon_err`,  
 5124 also filled in the histogram `MuonCMult_H`.

5125 In addition to these 2 CSV files, the histograms are saved in ROOT file `Scan00XXXX_HVY_Offline.root`  
 5126 as explained in section B.2.1.1.

## 5127 B.7 Current information extraction

5128 Detectors under test at GIF++ are connected both to a CAEN HV power supply and to a CAEN  
5129 ADC that reads the currents inside of the RPC gaps bypassing the supply cable. During data tak-  
5130 ing, the webDCS records into a ROOT file called `Scan00XXXX_HVY_CAEN.root` histograms with the  
5131 monitored parameters of both CAEN devices. Are recorded for each RPC channels (in most cases,  
5132 a channel corresponds to an RPC gap):

- 5133 • the effective voltage,  $HV_{eff}$ , set by the webDCS using the PT correction on the CAEN power  
5134 supply,
- 5135 • the applied voltage,  $HV_{app}$ , monitored by the CAEN power supply, and the statistical error  
5136 related to the variations of this value through time to follow the variation of the environmental  
5137 parameters defined as the RMS of the histogram divided by the square root of the number of  
5138 recorded points,
- 5139 • the monitored current,  $I_{mon}$ , monitored by the CAEN power supply, and the statistical error  
5140 related to the variations of this value through time to follow the variation of the environmental  
5141 parameters defined as the RMS of the histogram divided by the square root of the number of  
5142 recorded points,
- 5143 • the corresponding current density,  $J_{mon}$ , defined as the monitored current per unit area,  
5144  $J_{mon} = I_{mon}/A$ , where  $A$  is the active area of the corresponding gap,
- 5145 • the ADC current,  $I_{ADC}$ , recorded through the CAEN ADC module that monitors the dark  
5146 current in the gap itself. First of all, the resolution of such a module is better than that of  
5147 CAEN power supplies and moreover, the current is not read-out through the HV supply line  
5148 but directly at the chamber level giving the real current inside of the detector. The statistical  
5149 error is defined as the RMS of the histogram distribution divided by the square root of the  
5150 number of recorded points.

5151 Once extracted through a loop over the element of GIF++ infrastructure via the C++ macro  
5152 `GetCurrent()`, these parameters, organised in 9 columns per detector HV supply line, are written in  
5153 the output CSV file `Offline-Current.csv`. The macro can be found in the file `Current.cc`.

## References

- 5155 [1] K. Ruedenberg and W.H.E. Schwarz. "Three Millennia of Atoms and Molecules". In: *Pio-*  
5156 *neers of Quantum Chemistry*. Ed. by E. Thomas Strom and Angela K. Wilson. Vol. 1122.  
5157 ACS Symposium Series, 2013, pp. 1–45.
- 5158 [2] A. Lavoisier. *Traité élémentaire de chimie*. Éditions la Bibliothèque Digitale, 2014 (first  
5159 published 1789).
- 5160 [3] J. Dalton. *A New System of Chemical Philosophy*. William Dawson and Sons, 1808.
- 5161 [4] J. von Fraunhofer. "Bestimmung des Brechungs- und des Farben-Zerstreuungs - Vermögens  
5162 verschiedener Glasarten, in Bezug auf die Vervollkommnung achromatischer Fernröhre". In:  
5163 *Denkschriften der Königlichen Akademie der Wissenschaften zu München*. Die Akademie,  
5164 1817, pp. 193–226.
- 5165 [5] J.J. Thomson. "XL. Cathode Rays". In: *The London, Edinburgh, and Dublin Philosophical  
5166 Magazine and Journal of Science* 44:269 (1897), pp. 293–316.
- 5167 [6] J.B. Perrin. "Nouvelles propriétés des rayons cathodiques". In: *Comptes Rendus Hebdo-*  
5168 *madiques des Séances de L'Académie des Sciences*. Vol. 121. Académie des Sciences, 1895,  
5169 pp. 1130–1134.
- 5170 [7] H. Becquerel. "Déviation du rayonnement du radium dans un champ électrique". In: *Comptes  
5171 Rendus Hebdomadaires des Séances de L'Académie des Sciences*. Vol. 130. Académie des  
5172 Sciences, 1900, p. 809.
- 5173 [8] J.J. Thomson. "XXIV. On the structure of the atom: an investigation of the stability and  
5174 periods of oscillation of a number of corpuscles arranged at equal intervals around the cir-  
5175 cumference of a circle; with application of the results to the theory of atomic structure". In:  
5176 *The London, Edinburgh, and Dublin Philosophical Magazine and Journal of Science* 7:39  
5177 (1904), pp. 237–265.
- 5178 [9] E. Rutherford and T. Royds. "XXIV. Spectrum of the radium emanation". In: *The Lon-*  
5179 *don, Edinburgh, and Dublin Philosophical Magazine and Journal of Science* 16:92 (1904),  
5180 pp. 313–317.
- 5181 [10] H. Geiger. "On the scattering of the  $\alpha$ -particles by matter". In: *Proceedings of the Royal  
5182 Society A* 81 (1908), pp. 174–177.
- 5183 [11] H. Geiger and E. Marsden. "On a diffuse reflection of the  $\alpha$ -particles". In: *Proceedings of  
5184 the Royal Society A* 82 (1909), pp. 495–500.
- 5185 [12] H. Geiger. "The scattering of  $\alpha$ -particles by matter". In: *Proceedings of the Royal Society A*  
5186 83 (1910), pp. 492–504.
- 5187 [13] H. Geiger and E. Marsden. "LXI. The laws of deflexion of a particles through large angles".  
5188 In: *The London, Edinburgh, and Dublin Philosophical Magazine and Journal of Science*  
5189 25:148 (1913), pp. 604–623.

- 5190 [14] E. Rutherford. "LXXIX. The Scattering of  $\alpha$  and  $\beta$  Particles by Matter and the Structure of  
5191 the Atom". In: *The London, Edinburgh, and Dublin Philosophical Magazine and Journal of*  
5192 *Science* 21:125 (1911), pp. 669–688.
- 5193 [15] E. Rutherford. "LIV. Collision of  $\alpha$  particles with light atoms. IV. An anomalous effect in  
5194 nitrogen". In: *The London, Edinburgh, and Dublin Philosophical Magazine and Journal of*  
5195 *Science* 37:222 (1919), pp. 581–587.
- 5196 [16] O. Masson. "XXIV. The constitution of atoms". In: *The London, Edinburgh, and Dublin*  
5197 *Philosophical Magazine and Journal of Science* 41:242 (1921), pp. 281–285.
- 5198 [17] W. Prout. "On the Relation between the Specific Gravities of Bodies in their Gaseous State  
5199 and the Weights of their Atoms." In: *Annals of Philosophy* 6 (1815), pp. 321–330.
- 5200 [18] W. Prout. "Correction of a Mistake in the Essay on the Relation between the Specific Gravities  
5201 of Bodies in their Gaseous State and the Weights of their Atoms". In: *Annals of Philoso-*  
5202 *phy* 7 (1816), pp. 111–113.
- 5203 [19] E. Rutherford. "Bakerian Lecture: Nuclear constitution of atoms". In: *Proceedings of the*  
5204 *Royal Society A* 97 (1920), pp. 374–400.
- 5205 [20] W. Bothe and H. Becker. "Künstliche Erregung von Kern- $\gamma$ -Strahlen". In: *Zeitschrift für*  
5206 *Physik* 66 (1930), pp. 289–306.
- 5207 [21] H. Becker and W. Bothe. "Die in Bor und Beryllium erregten  $\gamma$ -Strahlen". In: *Zeitschrift für*  
5208 *Physik* 76 (1932), pp. 421–438.
- 5209 [22] I. Curie and F. Joliot. "Émission de protons de grande vitesse par les substances hydro-  
5210 genées sous l'influence de rayons  $\gamma$  très pénétrants". In: *Comptes Rendus Hebdomadaires*  
5211 *des Séances de L'Académie des Sciences*. Vol. 194. Académie des Sciences, 1932, pp. 273–  
5212 275.
- 5213 [23] J. Chadwick. "Possible Existence of a Neutron". In: *Nature* 129 (1932), p. 312.
- 5214 [24] J. Chadwick. "Bakerian lecture. The neutron". In: *Proceedings of the Royal Society A* 142  
5215 (1933), pp. 1–25.
- 5216 [25] Max Plank. "Ueber das Gesetz der Energieverteilung im Normalspectrum". In: *Annalen Der*  
5217 *Physik* 309 (1901), pp. 553–563.
- 5218 [26] A. Einstein. "Über einen die Erzeugung und Verwandlung des Lichtes betreffenden heuris-  
5219 tischen Gesichtspunkt". In: *Annalen Der Physik* 322 (1905), pp. 132–148.
- 5220 [27] N. Bohr. "I. On the constitution of atoms and molecules". In: *The London, Edinburgh, and*  
5221 *Dublin Philosophical Magazine and Journal of Science* 26:151 (1913), pp. 1–25.
- 5222 [28] H.G.J. Moseley. "XCIII. The high-frequency spectra of the elements". In: *The London, Edin-  
5223 burgh, and Dublin Philosophical Magazine and Journal of Science* 26:156 (1913), pp. 1024–  
5224 1034.
- 5225 [29] A. Sommerfeld. "Zur Quantentheorie der Spektrallinien". In: *Annalen Der Physik* 356 (1916),  
5226 pp. 1–94.
- 5227 [30] P. Zeeman. "XXXII. On the influence of magnetism on the nature of the light emitted by a  
5228 substance". In: *The London, Edinburgh, and Dublin Philosophical Magazine and Journal of*  
5229 *Science* 43:262 (1897), pp. 226–239.
- 5230 [31] P. Zeeman. "VII. Doublets and triplets in the spectrum produced by external magnetic forces".  
5231 In: *The London, Edinburgh, and Dublin Philosophical Magazine and Journal of Science*  
5232 44:266 (1897), pp. 55–60.

## BIBLIOGRAPHY

---

- 5233 [32] P. Zeeman. “VII. Doublets and triplets in the spectrum produced by external magnetic forces.—(II.)”  
5234 In: *The London, Edinburgh, and Dublin Philosophical Magazine and Journal of Science*  
5235 44:268 (1897), pp. 255–259.
- 5236 [33] P. Zeeman. “XXI. Measurements concerning radiation-phenomena in the magnetic field.—(I.)”  
5237 In: *The London, Edinburgh, and Dublin Philosophical Magazine and Journal of Science*  
5238 45:273 (1898), pp. 197–201.
- 5239 [34] W. Gerlach and O. Stern. “Der experimentelle Nachweis der Richtungsquantelung im Mag-  
5240 netfeld”. In: *Zeitschrift für Physik* 9 (1922), pp. 349–352.
- 5241 [35] W. Pauli. “Über den Einfluß der Geschwindigkeitsabhängigkeit der Elektronenmasse auf den  
5242 Zeeman-Effekt”. In: *Zeitschrift für Physik* 31 (1925), 373–385.
- 5243 [36] W. Pauli. “Über den Zusammenhang des Abschlusses der Elektronengruppen im Atom mit  
5244 der Komplexstruktur der Spektren”. In: *Zeitschrift für Physik* 31 (1925), 765–783.
- 5245 [37] G.E. Uhlenbeck and S. Goudsmit. “Spinning Electrons and the Structure of Spectra”. In:  
5246 *Nature* 117 (1926), pp. 264–265.
- 5247 [38] W. Pauli. “Zur Quantenmechanik des magnetischen Elektrons”. In: *Zeitschrift für Physik* 43  
5248 (1927), 601–623.
- 5249 [39] L. De Broglie. “Recherches sur la théorie des Quanta”. PhD thesis. University of Paris, 1924.
- 5250 [40] E. Schrödinger. “An Undulatory Theory of the Mechanics of Atoms and Molecules”. In:  
5251 *Phys. Rev.* 28 (1927), pp. 1049–1070.
- 5252 [41] P. Dirac. “The quantum theory of the emission and absorption of radiation”. In: *Proceedings  
5253 of the Royal Society A* 114 (1928), pp. 243–265.
- 5254 [42] P. Dirac. “The quantum theory of the electron”. In: *Proceedings of the Royal Society A* 117  
5255 (1928), pp. 610–624.
- 5256 [43] J. R. Oppenheimer. “On the Theory of Electrons and Protons”. In: *Phys. Rev.* 35 (1930),  
5257 pp. 562–563.
- 5258 [44] P. Dirac. “Quantised singularities in the electromagnetic field”. In: *Proceedings of the Royal  
5259 Society A* 133 (1931), pp. 60–72.
- 5260 [45] J. R. Oppenheimer. “Note on the Theory of the Interaction of Field and Matter”. In: *Phys.  
5261 Rev.* 35 (1930), pp. 461–477.
- 5262 [46] H.A. Bethe. “The Electromagnetic Shift of Energy Levels”. In: *Phys. Rev.* 72 (1947), pp. 339–  
5263 341.
- 5264 [47] H.F.J. Dyson. “The Radiation Theories of Tomonaga, Schwinger, and Feynman”. In: *Phys.  
5265 Rev.* 75 (1949), pp. 486–502.
- 5266 [48] H. Yukawa. “On the Interaction of Elementary Particles. I”. In: *Proc. Phys. Math. Soc. Jap.*  
5267 17 (1935), pp. 48–57.
- 5268 [49] C.D. Anderson and S.H. Neddermeyer. “Cloud Chamber Observations of Cosmic Rays at  
5269 4300 Meters Elevation and Near Sea-Level”. In: *Phys. Rev.* 50 (1936), pp. 263–271.
- 5270 [50] S.H. Neddermeyer and C.D. Anderson. “Note on the Nature of Cosmic-Ray Particles”. In:  
5271 *Phys. Rev.* 51 (1937), pp. 884–886.
- 5272 [51] J.C. Street and E.C. Stevenson. “New Evidence for the Existence of a Particle of Mass Inter-  
5273 mediate Between the Proton and Electron”. In: *Phys. Rev.* 52 (1937), pp. 1003–1004.
- 5274 [52] C.M.G. Lattes et al. “Processes involving charged mesons”. In: *Nature* 159 (1947), pp. 694–  
5275 697.

- 5276 [53] C.M.G. Lattes et al. “Observations on the Tracks of Slow Mesons in Photographic Emulsions  
5277 (Part 1)”. In: *Nature* 160 (1947), pp. 453–456.
- 5278 [54] C.M.G. Lattes et al. “Observations on the Tracks of Slow Mesons in Photographic Emulsions  
5279 (Part 2)”. In: *Nature* 160 (1947), 486–492.
- 5280 [55] R. Blorklund et al. “High Energy Photons from Proton-Nucleon Collisions”. In: *Phys. Rev.*  
5281 77 (1950), pp. 213–218.
- 5282 [56] G.D. Rochester and C.C. Butler. “Evidence for the Existence of New Unstable Elementary  
5283 Particles”. In: *Nature* 160 (1947), 855–857.
- 5284 [57] A. Pais. “Some Remarks on the  $V$ -Particles”. In: *Phys. Rev.* 86 (1952), pp. 663–672.
- 5285 [58] M. Gell-Mann. “Symmetries of Baryons and Mesons”. In: *Phys. Rev.* 125 (1962), pp. 1067–  
5286 1084.
- 5287 [59] K. Nishijima and T. Nakano. “Charge Independence for  $V$ -particles”. In: *Progress of Theo-*  
5288 *retical Physics* 10 (1953), 581–582.
- 5289 [60] K. Nishijima. “Charge Independence Theory of  $V$ -Particles”. In: *Progress of Theoretical*  
5290 *Physics* 13 (1955), pp. 285–304.
- 5291 [61] M. Gell-Mann. “The interpretation of the new particles as displaced charge multiplets”. In:  
5292 *Il Nuovo Cimento* 4 (1956), 848–866.
- 5293 [62] W. Heisenberg. “Über den Bau der Atomkerne. I”. In: *Zeitschrift für Physik* 77 (1932), 1–11.
- 5294 [63] V.E. Barnes et al. “Observation of a Hyperon with Strangeness Minus Three”. In: *Phys. Rev.*  
5295 *Lett.* 12 (1964), pp. 204–206.
- 5296 [64] M. Gell-Mann. “A schematic model of baryons and mesons”. In: *Physics Letters* 8 (1964),  
5297 pp. 214–215.
- 5298 [65] G. Zweig. *An SU(3) Model for Strong Interaction Symmetry and its Breaking*. Tech. rep.  
5299 CERN-TH-401. CERN, 1964.
- 5300 [66] G. Zweig. *An SU(3) Model for Strong Interaction Symmetry and its Breaking (II)*. Tech. rep.  
5301 CERN-TH-412. CERN, 1964.
- 5302 [67] E.D. Bloom et al. “High-Energy Inelastic  $e - p$  Scattering at  $6^\circ$  and  $10^\circ$ ”. In: *Phys. Rev. Lett.*  
5303 23 (1969), pp. 930–934.
- 5304 [68] M. Breidenbach et al. “Observed Behavior of Highly Inelastic Electron-Proton Scattering”.  
5305 In: *Phys. Rev. Lett.* 23 (1969), pp. 935–939.
- 5306 [69] B.J. Bjørken and S.L. Glashow. “Elementary particles and SU(4)”. In: *Physics Letters* 11  
5307 (1964), pp. 255–257.
- 5308 [70] S. Glashow et al. “Weak Interactions with Lepton-Hadron Symmetry”. In: *Phys. Rev. D* 2  
5309 (1970), pp. 1285–1292.
- 5310 [71] J.H. Christenson et al. “Evidence for the  $2\pi$  Decay of the  $K_2^0$  Meson”. In: *Phys. Rev. Lett.* 13  
5311 (1964), pp. 138–140.
- 5312 [72] M. Kobayashi and T. Maskawa. “ $CP$ -Violation in the Renormalizable Theory of Weak Interac-
- 5313 tion”. In: *Progress of Theoretical Physics* 49 (1973), pp. 652–657.
- 5314 [73] H. Harari. “A new quark model for hadrons”. In: *Physics Letters B* 57 (1975), pp. 265–269.
- 5315 [74] B. Richter et al. “Discovery of a Narrow Resonance in  $e^+e^-$  Annihilation”. In: *Phys. Rev.*  
5316 *Lett.* 33 (1974), pp. 1406–1408.
- 5317 [75] S. Ting et al. “Experimental Observation of a Heavy Particle  $J$ ”. In: *Phys. Rev. Lett.* 33  
5318 (1974), pp. 1404–1405.

---

## BIBLIOGRAPHY

---

- 5319 [76] S.W. Herb et al. “Observation of a Dimuon Resonance at 9.5 GeV in 400 GeV Proton-  
5320 Nucleus Collisions”. In: *Phys. Rev. Lett.* 39 (1977), pp. 252–255.
- 5321 [77] S. Abashi et al. “Search for High Mass Top Quark Production in  $\bar{p}p$  Collisions at  $\sqrt{s} =$   
5322 1.8 TeV”. In: *Phys. Rev. Lett.* 74 (1995), pp. 2422–2426.
- 5323 [78] F. Abe et al. “Observation of Top Quark Production in  $\bar{p}p$  Collisions with the Collider De-  
5324 tector at Fermilab”. In: *Phys. Rev. Lett.* 74 (1995), pp. 2626–2631.
- 5325 [79] F. Tkachov. “A contribution to the history of quarks: Boris Struminsky’s 1965 JINR publi-  
5326 cation”. In: (2009).
- 5327 [80] O.W. Greenberg. “Spin and Unitary-Spin Independence in a Paraquark Model of Baryons  
5328 and Mesons”. In: *Phys. Rev. Lett.* 13 (1964), pp. 598–602.
- 5329 [81] M.Y. Han and Y. Nambu. “Three-Triplet Model with Double  $SU(3)$  Symmetry”. In: *Phys.*  
5330 *Rev.* 139 (1965), B1006–B1010.
- 5331 [82] R.P. Feynman. “The behavior of hadron collisions at extreme energies”. In: *Conf. Proc.*  
5332 C690905 (1969), pp. 237–258.
- 5333 [83] J.D. Bjorken and E.A. Paschos. “Inelastic Electron-Proton and  $\gamma$ -Proton Scattering and the  
5334 Structure of the Nucleon”. In: *Phys. Rev.* 185 (1969), pp. 1975–1982.
- 5335 [84] H. Fritzsch et al. “Advantages of the color octet gluon picture”. In: *Physics Letters B* 47  
5336 (1973), pp. 365–368.
- 5337 [85] D.J. Gross and F. Wilczek. “Ultraviolet Behavior of Non-Abelian Gauge Theories”. In: *Phys.*  
5338 *Rev. Lett.* 30 (1973), pp. 1343–1346.
- 5339 [86] H.D. Politzer. “Reliable Perturbative Results for Strong Interactions?” In: *Phys. Rev. Lett.* 30  
5340 (1973), pp. 1346–1349.
- 5341 [87] S. Bethke. “ $\alpha_s$  2002”. In: *Nuclear Physics B* 121 (2003), pp. 74–81.
- 5342 [88] E. Fermi. “Versuch einer Theorie der  $\beta$ -Strahlen. I”. In: *Zeitschrift für Physik* 88 (1934),  
5343 pp. 161–177.
- 5344 [89] W. Pauli. “Dear radioactive ladies and gentlemen”. In: *Phys. Today* 31N9 (1978), p. 27.
- 5345 [90] C.L. Cowan Jr. et al. “Detection of the Free Neutrino: a Confirmation”. In: *Science* 20 (1956),  
5346 pp. 103–104.
- 5347 [91] E.J. Konopinski and H.M. Mahmoud. “The Universal Fermi Interaction”. In: *Phys. Rev.* 92  
5348 (1953), pp. 1045–1049.
- 5349 [92] L.M. Lederman et al. “Observation of High-Energy Neutrino Reactions and the Existence of  
5350 Two Kinds of Neutrinos”. In: *Phys. Rev. Lett.* 9 (1962), pp. 36–44.
- 5351 [93] T.D. Lee and C.N. Yang. “Question of Parity Conservation in Weak Interactions”. In: *Phys.*  
5352 *Rev.* 104 (1956), pp. 254–258.
- 5353 [94] G. Gamow and E. Teller. “Selection Rules for the  $\beta$ -Disintegration”. In: *Phys. Rev.* 49 (1936),  
5354 pp. 895–899.
- 5355 [95] C.S. Wu et al. “Experimental Test of Parity Conservation in Beta Decay”. In: *Phys. Rev.* 105  
5356 (1957), pp. 1413–1415.
- 5357 [96] S. Weinberg. “A Model of Leptons”. In: *Phys. Rev. Lett.* 19 (1967), pp. 1264–1266.
- 5358 [97] Y. Nambu and G. Jona-Lasinio. “Dynamical Model of Elementary Particles Based on an  
5359 Analogy with Superconductivity. I”. In: *Phys. Rev.* 122 (1961), pp. 345–358.
- 5360 [98] Y. Nambu and G. Jona-Lasinio. “Dynamical Model of Elementary Particles Based on an  
5361 Analogy with Superconductivity. II”. In: *Phys. Rev.* 124 (1961), pp. 246–254.

- 5362 [99] J. Bardeen et al. “Microscopic Theory of Superconductivity”. In: *Phys. Rev.* 106 (1957),  
5363 pp. 162–164.
- 5364 [100] Y. Nambu. “Quasi-Particles and Gauge Invariance in the Theory of Superconductivity”. In:  
5365 *Phys. Rev.* 117 (1960), pp. 648–663.
- 5366 [101] J. Goldstone. “Quasi-Particles and Gauge Invariance in the Theory of Superconductivity”.  
5367 In: *Il Nuovo Cimento* 19 (1961), pp. 154–164.
- 5368 [102] P.W. Anderson. “Plasmons, Gauge Invariance, and Mass”. In: *Phys. Rev.* 130 (1963), pp. 439–  
5369 442.
- 5370 [103] J. Schwinger. “Gauge Invariance and Mass”. In: *Phys. Rev.* 125 (1962), pp. 397–398.
- 5371 [104] F. Englert and R. Brout. “Broken Symmetry and the Mass of Gauge Vector Mesons”. In:  
5372 *Phys. Rev. Lett.* 13 (1964), pp. 321–323.
- 5373 [105] P.W. Higgs. “Broken Symmetries and the Masses of Gauge Bosons”. In: *Phys. Rev. Lett.* 13  
5374 (1964), pp. 508–509.
- 5375 [106] G.S. Guralnik et al. “Global Conservation Laws and Massless Particles”. In: *Phys. Rev. Lett.*  
5376 13 (1964), pp. 585–587.
- 5377 [107] Wikipedia. *Standard Model*. 2018. URL: [https://en.wikipedia.org/wiki/Standard\\_Model](https://en.wikipedia.org/wiki/Standard_Model).
- 5379 [108] UA1 Collaboration. “Experimental observation of isolated large transverse energy electrons  
5380 with associated missing energy at  $s = 540 \text{ GeV}$ ”. In: *Physics Letters B* 122 (1983), pp. 103–  
5381 116.
- 5382 [109] UA2 Collaboration. “Observation of single isolated electrons of high transverse momentum  
5383 in events with missing transverse energy at the CERN pp collider”. In: *Physics Letters B* 122  
5384 (1983), pp. 476–485.
- 5385 [110] UA1 Collaboration. “Experimental observation of lepton pairs of invariant mass around  
5386  $95 \text{ GeV}/c^2$  at the CERN SPS collider”. In: *Physics Letters B* 126 (1983), pp. 398–410.
- 5387 [111] UA2 Collaboration. “Evidence for  $Z_0 \rightarrow e^+e^-$  at the CERN pp collider”. In: *Physics  
5388 Letters B* 129 (1983), pp. 130–140.
- 5389 [112] ATLAS Collaboration. “Observation of a new particle in the search for the Standard Model  
5390 Higgs boson with the ATLAS detector at the LHC”. In: *Physics Letters B* 716 (2012), pp. 1–  
5391 29.
- 5392 [113] CMS Collaboration. “Observation of a new boson at a mass of 125 GeV with the CMS  
5393 experiment at the LHC”. In: *Physics Letters B* 716 (2012), pp. 30–61.
- 5394 [114] ATLAS Collaboration and CMS Collaboration. “Combined Measurement of the Higgs Bo-  
5395 son Mass in  $pp$  Collisions at  $\sqrt{s} = 7$  and 8 TeV with the ATLAS and CMS Experiments”.  
5396 In: *Physical Review Letters* 114 (2015). 191803.
- 5397 [115] M. Tanabashi et al. (Particle Data Group). “Review of Particle Physics”. In: *Phys. Rev. D* 98  
5398 (2018), p. 030001.
- 5399 [116] A.A. Arkhipov. “Proton proton total cross-sections from the window of cosmic ray experi-  
5400 ments”. In: *Elastic and diffractive scattering. Proceedings, 9th Blois Workshop, Pruhonice,  
5401 Czech Republic*. 2001, pp. 293–304.
- 5402 [117] H. Pointcaré. “The Milky Way and the Theory of Gases”. In: *Popular Astronomy* 14 (1906),  
5403 pp. 475–488.
- 5404 [118] J.C. Kapteyn. “First Attempt at a Theory of the Arrangement and Motion of the Sidereal  
5405 System”. In: *Astrophysical Journal* 55 (1922), p. 302.

---

## BIBLIOGRAPHY

---

- 5406 [119] F. Zwicky. “Republication of: The redshift of extragalactic nebulae (First published in  
5407 1933)”. In: *General Relativity and Gravitation* 41 (2009), pp. 207–224.
- 5408 [120] F. Zwicky. “On the Masses of Nebulae and of Clusters of Nebulae”. In: *Astrophysical Journal* 86 (1937), p. 217.
- 5410 [121] H.W. Babcock. “The rotation of the Andromeda Nebula”. In: *Lick Observatory bulletin* 498  
5411 (1939), pp. 41–51.
- 5412 [122] V.C. Rubin and W.K. Ford Jr. “Rotation of the Andromeda Nebula from a Spectroscopic  
5413 Survey of Emission Regions”. In: *Astrophysical Journal* 159 (1970), p. 379.
- 5414 [123] D.H. Rogstad and G.S. Shostak. “Gross Properties of Five Scd Galaxies as Determined from  
5415 21-CENTIMETER Observations”. In: *Astrophysical Journal* 176 (1972), p. 315.
- 5416 [124] Planck Collaboration. “Planck 2015 results. XIII. Cosmological parameters”. In: *A&A* 594.A13  
5417 (2016).
- 5418 [125] N. Jarosik et al. “Seven-year Wilkinson Microwave Anisotropy Probe (WMAP\*) observa-  
5419 tions: Sky maps, Systematic errors, and Basic Results”. In: *ApJS* 192.14 (2011).
- 5420 [126] E. Verlinde. “Emergent Gravity and the Dark Universe”. In: *SciPost Phys.* 2 (2017), p. 016.
- 5421 [127] A. Maeder. “An alternative to the  $\Lambda$ CDM model: the case of scale invariance”. In: *ApJ*  
5422 834.194 (2017).
- 5423 [128] E. Corbelli and P. Salucci. “The extended rotation curve and the dark matter halo of M33”.  
5424 In: *Monthly Notices of the Royal Astronomical Society* 311 (2000), pp. 441–447.
- 5425 [129] S. Dimopoulos and H. Georgi. “Softly broken supersymmetry and SU(5)”. In: *Nuclear  
5426 Physics B* 193 (1981), pp. 150–162.
- 5427 [130] F. Tanedo. *The Hierarchy Problem: why the Higgs has a snowball’s chance in hell*. 2012.  
5428 URL: [https://www.quantumdiaries.org/2012/07/01/the-hierarchy-  
5429 problem-why-the-higgs-has-a-snowballs-chance-in-hell/](https://www.quantumdiaries.org/2012/07/01/the-hierarchy-problem-why-the-higgs-has-a-snowballs-chance-in-hell/).
- 5430 [131] G. Jungman et al. “Supersymmetric dark matter”. In: *Physics Reports* 267 (1996), pp. 10–  
5431 14.
- 5432 [132] A.H. Chamseddine et al. “Locally Supersymmetric Grand Unification”. In: *Phys. Rev. Lett.*  
5433 49 (1982), pp. 970–974.
- 5434 [133] A. Askew et al. “Searching for dark matter at hadron colliders”. In: *International Journal  
5435 of Modern Physics A* 29 (2014), p. 1430041.
- 5436 [134] N. Arkani-Hamed et al. “The hierarchy problem and new dimensions at a millimeter”. In:  
5437 *Physics Letters B* 429 (1998), pp. 263–272.
- 5438 [135] N. Arkani-Hamed et al. “Phenomenology, astrophysics, and cosmology of theories with  
5439 submillimeter dimensions and TeV scale quantum gravity”. In: *Phys. Rev. D* 59 (1999),  
5440 p. 086004.
- 5441 [136] T. Kaluza. “Zum Unitätsproblem der Physik”. In: *Sitzungsber. Preuss. Akad. Wiss. Berlin  
5442 (Math. Phys.)* 1921 (1921), pp. 966–972.
- 5443 [137] O. Klein. “The Atomicity of Electricity as a Quantum Theory Law”. In: *Nature* 118 (1926),  
5444 p. 516.
- 5445 [138] L. Randall and R. Sundrum. “Large Mass Hierarchy from a Small Extra Dimension”. In:  
5446 *Phys. Rev. Lett.* 83 (1999), pp. 3370–3373.
- 5447 [139] L. Randall and R. Sundrum. “An Alternative to Compactification”. In: *Phys. Rev. Lett.* 83  
5448 (1999), pp. 4690–4693.

- 5449 [140] M. Strassler and K. Zurek. “Echoes of a hidden valley at hadron colliders”. In: *Phys. Let. B*  
 5450 651 (2007), pp. 374–379.
- 5451 [141] A. Sakharov. “Violation of CP i variance, C asymmetry, and baryon asymmetry of the uni-  
 5452 verse”. In: *JETP Letters* 5 (1967), pp. 24–27.
- 5453 [142] M.E. Shaposhnikov and G. Farrar. “Baryon asymmetry of the Universe in the minimal stan-  
 5454 dard model”. In: *Phys. Rev. Lett.* 70 (1993), pp. 2833–2836.
- 5455 [143] V.A. Kuzmin et al. “On anomalous electroweak baryon-number non-conservation in the  
 5456 early universe”. In: *Physics Letters B* 155 (1985), pp. 36–42.
- 5457 [144] L. Canetti et al. “Matter and antimatter in the universe”. In: *New J. Phys.* 14.095012 (2012).
- 5458 [145] CMS Collaboration. “Search for black holes and sphalerons in high-multiplicity final states  
 5459 in proton-proton collisions at  $\sqrt{s} = 13$  TeV”. In: *Journal of High Energy Physics* 11 (2018).
- 5460 [146] B. Shuve and Y. Cui. “Probing baryogenesis with displaced vertices at the LHC”. In: *Journal*  
 5461 *of High Energy Physics* 2 (2015).
- 5462 [147] The ACME Collaboration. “Order of Magnitude Smaller Limit on the Electric Dipole Mo-  
 5463 ment of the Electron”. In: *Science* 343 (2014), pp. 269–272.
- 5464 [148] N. Neri et al. “On the search for the electric dipole moment of strange and charm baryons  
 5465 at LHC”. In: *The European Physical Journal C* 77 (2017), p. 181.
- 5466 [149] J. Stevens and M. Sher. “Detecting a heavy neutrino electric dipole moment at the LHC”.  
 5467 In: *Physics Letters B* 777 (2018), pp. 246–249.
- 5468 [150] R. Davis Jr. et al. “Search for Neutrinos from the Sun”. In: *Physical Review Letters* 20  
 5469 (1968), pp. 1205–1209.
- 5470 [151] B. Pontecorvo. “Neutrino Experiments and the Problem of Conservation of Leptonic Charge”.  
 5471 In: *Sov. Phys. JETP* 26 (1968), pp. 984–988.
- 5472 [152] SNO Collaboration. “Direct Evidence for Neutrino Flavor Transformation from Neutral-  
 5473 Current Interactions in the Sudbury Neutrino Observatory”. In: *Physical Review Letters*  
 5474 89.011301 (2002).
- 5475 [153] Z. Maki et al. “Remarks on the Unified Model of Elementary Particles”. In: *Progress of*  
 5476 *Theoretical Physics* 28 (1962), pp. 870–880.
- 5477 [154] P. Minkowski. “ $\mu \rightarrow e\gamma$  at a rate of one out of  $10^9$  muon decays?” In: *Physics Letters B*  
 5478 67 (1977), pp. 421–428.
- 5479 [155] R.N. Mohapatra and G. Senjanović. “Neutrino Mass and Spontaneous Parity Nonconserva-  
 5480 tion”. In: *Phys. Rev. Lett.* 44 (1980), pp. 912–915.
- 5481 [156] CERN. Geneva. LHC Experiments Committee. *CMS Physics Technical Design Report Vol-  
 5482 ume II: Physics Performance*. Tech. rep. CERN-LHCC-2006-021 ; CMS-TDR-8-2. CMS  
 5483 Collaboration, 2006.
- 5484 [157] P.W.F. Valle. “Neutrino physics overview”. In: *J. Phys.: Conf. Ser.* 53 (2006), pp. 473–505.
- 5485 [158] T. Massam et al. “Experimental observation of antideuteron production”. In: *Il Nuovo Ci-  
 5486 mento A* 63 (1965), pp. 10–14.
- 5487 [159] ALEPH Collaboration. “Determination of the number of light neutrino species”. In: *Physics*  
 5488 *Letters B* 231 (1989), pp. 519–529.
- 5489 [160] CERN, ed. (1985).
- 5490 [161] CERN, ed. (1986).
- 5491 [162] CERN, ed. (1994).

---

## BIBLIOGRAPHY

---

- 5492 [163] CERN, ed. (1998).
- 5493 [164] CERN, ed. (1999).
- 5494 [165] CERN. Geneva. LHC Experiments Committee. *Letter of Intent for A Large Ion Collider*  
5495 *Experiment [ALICE]*. Tech. rep. CERN-LHCC-93-016. ALICE Collaboration, 1993.
- 5496 [166] CERN. Geneva. LHC Experiments Committee. *ATLAS : technical proposal for a general-*  
5497 *purpose pp experiment at the Large Hadron Collider at CERN*. Tech. rep. CERN-LHCC-94-  
5498 43. ATLAS Collaboration, 1994.
- 5499 [167] CERN. Geneva. LHC Experiments Committee. *CMS : letter of intent by the CMS Col-*  
5500 *laboration for a general purpose detector at LHC*. Tech. rep. CERN-LHCC-92-003. CMS  
5501 Collaboration, 1992.
- 5502 [168] CERN. Geneva. LHC Experiments Committee. *LHCb : letter of intent*. Tech. rep. CERN-  
5503 LHCC-95-5. LHCb Collaboration, 1995.
- 5504 [169] L. Evans and P. Bryant. “LHC Machine”. In: *JINST* 3 (2008). S08001.
- 5505 [170] LHCb Collaboration. “Observation of  $J/\psi p$  Resonances Consistent with Pentaquark States  
5506 in  $\Lambda_b^0 \rightarrow J/\psi K^- p$  Decays”. In: *Physical Review Letters* 115 (2015). 072001.
- 5507 [171] LHCb Collaboration. “Observation of  $J/\psi \phi$  Structures Consistent with Exotic States from  
5508 Amplitude Analysis of  $B^+ \rightarrow J/\psi \phi K^+$  Decays”. In: *Physical Review Letters* 118 (2017).  
5509 022003.
- 5510 [172] ALICE Collaboration. *First results from proton-lead collisions*. URL: <http://aliceinfo.cern.ch/Public/en/Chapter1/results-pPb.html>.
- 5511
- 5512 [173] ATLAS Collaboration. “Observation of a New  $\chi_b$  State in Radiative Transitions to  $\Upsilon(1S)$   
5513 and  $\Upsilon(2S)$  at ATLAS”. In: *Physical Review Letters* 108 (2012). 152001.
- 5514 [174] LHCb Collaboration. “First Evidence for the Decay  $B_s^0 \rightarrow \mu^+ \mu^-$ ”. In: *Physical Review*  
5515 *Letters* 110 (2013). 021801.
- 5516 [175] CERN. Geneva. *High-Luminosity Large Hadron Collider (HL-LHC) Technical Design Re-*  
5517 *port V. 0.1*. Tech. rep. CERN-2017-007-M. 2017.
- 5518 [176] CERN. Geneva. LHC Experiments Committee. *CMS, the Compact Muon Solenoid : tech-*  
5519 *nical proposal*. Tech. rep. CERN-2015-005. 2015.
- 5520 [177] CERN. Geneva. LHC Experiments Committee. *The Phase-2 Upgrade of the CMS Muon*  
5521 *Detectors*. Tech. rep. CERN-LHCC-2017-012, CMS-TDR-016. CMS Collaboration, 2017.
- 5522 [178] M. Drees and X. Tata. “Signals for heavy exotics at hadron colliders and supercolliders”.  
5523 In: *Physics Letters B* 252 (1990), pp. 695–702.
- 5524 [179] D.A. Milstead et al. “Stable massive particles at colliders”. In: *Physics Reports* 438 (2007),  
5525 pp. 1–63.
- 5526 [180] Z. Ligeti et al. “Supermodels for early LHC”. In: *Physics Letters B* 690 (2010), pp. 280–  
5527 288.
- 5528 [181] CMS Collaboration. “Search for long-lived charged particles in proton-proton collisions at  
5529  $\sqrt(s) = 13$  TeV”. In: *Phys. Rev. D* 94 (2016), p. 112004.
- 5530 [182] V. Khachatryan et al. “Search for long-lived charged particles in proton-proton collisions at  
5531  $\sqrt{s} = 13$  TeV”. In: *Phys. Rev. D* 94 (2017). 112004.
- 5532 [183] A. Kusenko and M. Shaposhnikov. “Supersymmetric Q-balls as dark matter”. In: *Physics*  
5533 *Letters B* 418 (1998), pp. 46–54.
- 5534 [184] B. Koch et al. “Black holes at LHC?” In: *J. Phys. G: Nucl. Part. Phys.* 34 (2007). S535.

- 5535 [185] J. Schwinger. “Magnetic Charge and Quantum Field Theory”. In: *Phys. Rev.* 144 (1966).  
 5536 1087.
- 5537 [186] M Yu Khlopov et al. “Dark matter with invisible light from heavy double charged leptons  
 5538 of almost-commutative geometry?” In: *Class. Quantum Grav.* 23 (2006). 7305.
- 5539 [187] PoS, ed. *Search for Heavy Stable Charged Particles in CMS*. Vol. 084-EPS-HEP2009. 2009,  
 5540 p. 438.
- 5541 [188] L.E. Medina Medrano et al. “Studies on Luminous Region, Pile-up and Performance for  
 5542 HL-LHC Scenarios”. In: *Proc. of International Particle Accelerator Conference (IPAC’17),  
 5543 Copenhagen, Denmark, 14-19 May, 2017*. JACoW, 2017, pp. 1908–1911.
- 5544 [189] CMS Collaboration. *CMS Luminosity - Public Results*. Version 158. 2019. URL: <https://twiki.cern.ch/twiki/bin/view/CMSPublic/LumiPublicResults>.
- 5545 [190] CERN. Geneva. LHC Experiments Committee. *Technical Proposal for the Phase-II Up-  
 5546 grade of the CMS Detector*. Tech. rep. CERN-LHCC-2015-010, CMS-TDR-15-02. CMS  
 5547 Collaboration, 2015.
- 5548 [191] CERN. Geneva. LHC Experiments Committee. *The Phase-2 Upgrade of the CMS Level-1  
 5549 Trigger - Interim Report to the LHCC*. Tech. rep. CERN-LHCC-2017-013, CMS-TDR-017.  
 5550 CMS Collaboration, 2017.
- 5551 [192] CERN. Geneva. LHC Experiments Committee. *The CMS muon project : Technical Design  
 5552 Report*. Tech. rep. CERN-LHCC-97-032. CMS Collaboration, 1997.
- 5553 [193] CERN. Geneva. LHC Experiments Committee. *High-Luminosity Large Hadron Collider  
 5554 (HL-LHC) Preliminary Design Report*. Tech. rep. CERN-LHCC-94-38. CMS Collaboration,  
 5555 1994.
- 5556 [194] F. Sauli. “GEM: A new concept for electron amplification in gas detectors”. In: *Nucl. Instr.  
 5557 Meth. Phys. Res.* 386 (1997), pp. 531–534.
- 5558 [195] CERN. Geneva. LHC Experiments Committee. *CMS Technical Design Report for the Muon  
 5559 Endcap GEM Upgrade*. Tech. rep. CERN-LHCC-2015-012, CMS-TDR-013. CMS Collab-  
 5560 oration, 2015.
- 5561 [196] A. Gelmi. *CMS iRPC at HL-LHC: background study*. 2018. URL: [https://indico.cern.ch/event/732794/contributions/3021836/attachments/1657792/2654574/iRPC\\_bkg\\_study\\_Upgrade29\\_05\\_18.pdf](https://indico.cern.ch/event/732794/contributions/3021836/attachments/1657792/2654574/iRPC_bkg_study_Upgrade29_05_18.pdf).
- 5562 [197] A. Gelmi and E. Voevodina. “Background rate study for the CMS improved-RPC at HL-  
 5563 LHC using GEANT4”. In: *Nucl. Instr. Meth. Phys. Res. A* (2018).
- 5564 [198] IEEE, ed. *Petiroc, a new front-end ASIC for time of flight application*. Vol. 2013 IEEE  
 5565 Nuclear Science Symposium and Medical Imaging Conference (2013 NSS/MIC). 2014.
- 5566 [199] JINST, ed. *Petiroc and Citiroc: front-end ASICs for SiPM read-out and ToF applications*.  
 5567 Vol. Topical Workshop on Electronics for Particle Physics 2013 (TWEPP-13). 2014.
- 5568 [200] P.Bortignon. “Design and performance of the upgrade of the CMS L1 muon trigger”. In:  
 5569 *Nucl. Instr. Meth. Phys. Res.* 824 (2016), pp. 256–257.
- 5570 [201] The European Parliament and the Council of the European Union. “Regulation (EU) No  
 5571 517/2014 of 16 April 2014 on fluorinated greenhouse gases and repealing Regulation (EC)  
 5572 No 842/2006”. In: *Official Journal of the European Union* 150 (2014), pp. 195–230.
- 5573 [202] D. Piccolo. *Preliminary results of Resistive Plate Chambers operated with eco-friendly gas  
 5574 mixtures for application in the CMS experiment*. 2016. URL: <https://indico.ugent.be/event/0/session/18/contribution/28/material/slides/0.pdf>.
- 5575
- 5576
- 5577
- 5578

---

## BIBLIOGRAPHY

---

- 5579 [203] R. Santonico and R. Cardarelli. “Development of resistive plate counters”. In: *Nucl. Instr.*  
5580 *Meth. Phys. Res.* 187 (1981), pp. 377–380.
- 5581 [204] Yu.N. Pestov and G.V. Fedotovich. *A picosecond time-of-flight spectrometer for the VEPP-*  
5582 *2M based on local-discharge spark counter*. Tech. rep. SLAC-TRANS-0184. SLAC, 1978.
- 5583 [205] W.W. Ash, ed. *Spark Counter With A Localized Discharge*. Vol. SLAC-R-250. 1982, pp. 127–  
5584 131.
- 5585 [206] I. Crotty et al. “The non-spark mode and high rate operation of resistive parallel plate cham-  
5586 bers”. In: *NIMA* 337 (1993), pp. 370–381.
- 5587 [207] I. Crotty et al. “Further studies of avalanche mode operation of resistive parallel plate cham-  
5588 bers”. In: *NIMA* 346 (1994), pp. 107–113.
- 5589 [208] R. Cardarelli et al. “Avalanche and streamer mode operation of resistive plate chambers”.  
5590 In: *NIMA* 382 (1996), pp. 470–474.
- 5591 [209] R. Cardarelli et al. “Performance of a resistive plate chamber operating with pure  $CF_3Br$ ”.  
5592 In: *NIMA* 333 (1993), pp. 399–403.
- 5593 [210] M. Abbrescia et al. “Performance of a Resistive Plate Chamber operated in avalanche mode  
5594 under  $^{137}Cs$  irradiation”. In: *NIMA* 392 (1997), pp. 155–160.
- 5595 [211] M. Abbrescia et al. “Properties of C2H2F4-based gas mixture for avalanche mode operation  
5596 of resistive plate chambers”. In: *NIMA* 398 (1997), pp. 173–179.
- 5597 [212] P. Camarri et al. “Streamer suppression with SF6 in RPCs operated in avalanche mode”. In:  
5598 *NIMA* 414 (1998), pp. 317–324.
- 5599 [213] E. Cerron Zeballos et al. “Effect of adding SF6 to the gas mixture in a multigap resistive  
5600 plate chamber”. In: *NIMA* 419 (1998), pp. 475–478.
- 5601 [214] E. Cerron Zeballos et al. “A new type of resistive plate chamber: The multigap RPC”. In:  
5602 *NIMA* 374 (1996), pp. 132–135.
- 5603 [215] M.C.S. Williams. “The development of the multigap resistive plate chamber”. In: *Nucl.*  
5604 *Phys. B* 61 (1998), pp. 250–257.
- 5605 [216] H. Czyrkowski et al. “New developments on resistive plate chambers for high rate opera-  
5606 tion”. In: *NIMA* 419 (1998), pp. 490–496.
- 5607 [217] CERN. Geneva. LHC Experiments Committee. *ATLAS muon spectrometer: Technical de-  
5608 sign report*. Tech. rep. CERN-LHCC-97-22. ATLAS Collaboration, 1997.
- 5609 [218] CERN. Geneva. LHC Experiments Committee. *ALICE Time-Of-Flight system (TOF) : Tech-  
5610 nical Design Report*. Tech. rep. CERN-LHCC-2000-012. ALICE Collaboration, 2000.
- 5611 [219] The CALICE collaboration. “First results of the CALICE SDHCAL technological proto-  
5612 type”. In: *JINST* 11 (2016).
- 5613 [220] PoS, ed. *Density Imaging of Volcanoes with Atmospheric Muons using GRPCs*. International  
5614 Europhysics Conference on High Energy Physics - HEP 2011. 2011.
- 5615 [221] C. Lippmann. “Detector Physics of Resistive Plate Chambers”. PhD thesis. Johann Wolf-  
5616 gang Goethe-Universität, 2003.
- 5617 [222] W. Riegler. “Induced signals in resistive plate chambers”. In: *NIMA* 491 (2002), pp. 258–  
5618 271.
- 5619 [223] M. Abbrescia et al. “Effect of the linseed oil surface treatment on the performance of resis-  
5620 tive plate chambers”. In: *NIMA* 394 (1997), pp. 13–20.

- 5621 [224] G.Battistoni et al. “Sensitivity of streamer mode to single ionization electrons”. In: *NIMA*  
 5622 235 (1985), pp. 91–97.
- 5623 [225] M.Abbrescia et al. “Cosmic ray tests of double-gap resistive plate chambers for the CMS  
 5624 experiment”. In: *NIMA* 550 (2005), pp. 116–126.
- 5625 [226] JINST, ed. *Performance of the Resistive Plate Chambers in the CMS experiment*. The 9<sup>th</sup>  
 5626 International Conference on Positioin Sensitive Detectors. 2012.
- 5627 [227] PoS, ed. *The CMS RPC detector performance during Run-II data taking*. The European  
 5628 Physical Society Conference on High Energy Physics (EPS-HEP2017). 2018.
- 5629 [228] Honeywell International Inc. *Solstice(R) ze Refrigerant (HFO-1234ze): The Environmental  
 5630 Alternative to Traditional Refrigerants*. Tech. rep. FPR-003/2015-01. 2015.
- 5631 [229] E. Cerron Zeballos et al. “A comparison of the wide gap and narrow gap resistive plate  
 5632 chamber”. In: *NIMA* 373 (1996), pp. 35–42.
- 5633 [230] ALICE Collaboration. “A study of the multigap RPC at the gamma irradiation facility at  
 5634 CERN”. In: *NIMA* 490 (2002), pp. 58–70.
- 5635 [231] B. Bonner et al. “A multigap resistive plate chamber prototype for time-of-flight for the  
 5636 STAR experiment at RHIC”. In: *NIMA* 478 (2002), pp. 176–179.
- 5637 [232] S. Yang et al. “Test of high time resolution MRPC with different readout modes for the  
 5638 BESIII upgrade”. In: *NIMA* 763 (2014), pp. 190–196.
- 5639 [233] A. Akindinovg et al. “RPC with low-resistive phosphate glass electrodes as a candidate for  
 5640 the CBM TOF”. In: *NIMA* 572 (2007), pp. 676–681.
- 5641 [234] JINST, ed. *Development of the MRPC for the TOF system of the MultiPurpose Detector*.  
 5642 RPC2016: XII Workshop on Resistive Plate Chambers and Related Detectors. 2016.
- 5643 [235] M.C.S. Williams. “Particle identification using time of flight”. In: *Journal of Physics G* 39  
 5644 (2012).
- 5645 [236] A. Alici et al. “Aging and rate effects of the Multigap RPC studied at the Gamma Irradiation  
 5646 Facility at CERN”. In: *NIMA* 579 (2007), pp. 979–988.
- 5647 [237] M. Abbrescia et al. “The simulation of resistive plate chambers in avalanche mode: charge  
 5648 spectra and efficiency”. In: *NIMA* 431 (1999), pp. 413–427.
- 5649 [238] JINST, ed. *Description and simulation of physics of Resistive Plate Chambers*. RPC2016:  
 5650 XII Workshop on Resistive Plate Chambers and Related Detectors. 2016.
- 5651 [239] V. Francais. “Description and simulation of the physics of Resistive Plate Chambers”. PhD  
 5652 thesis. LPC - Laboratoire de Physique Corpusculaire - Clermont-Ferrand, 2017.
- 5653 [240] H. Bethe. “Zur Theorie des Durchgangs schneller Korpuskularstrahlen durch Materie”. In:  
 5654 *Annalen der Physik* 397 (1930), pp. 325–400.
- 5655 [241] International Commission on Radiation Units and Measurements. *Stopping Powers for Elec-  
 5656 trons and Positions*. Tech. rep. Report 37. 1984.
- 5657 [242] International Commission on Radiation Units and Measurements. *Stopping Power and Ranges  
 5658 for Protons and Alpha Particles*. Tech. rep. Report 49. 1994.
- 5659 [243] H. Bichsel. “A method to improve tracking and particle identification in TPCs and silicon  
 5660 detectors”. In: *NIMA* 562 (2006), pp. 154–197.
- 5661 [244] W. W. M. Allison and J. H. Cobb. “Relativistic charged particle identification by energy  
 5662 loss”. In: *Annual Review of Nuclear and Particle Science* 30 (1980), 253–298.

---

## BIBLIOGRAPHY

---

- 5663 [245] International Commission on Radiation Units and Measurements. *Average energy to pro-*  
5664 *duce an ion pair*. Tech. rep. Report 31. 1994.
- 5665 [246] I.B. Smirnov. “Modeling of ionization produced by fast charged particles in gases”. In: *NIMA* 554 (2005), pp. 474–493.
- 5666 [247] J. Phys.: Conf. Ser., ed. <https://doi.org/10.1088/1742-6596/587/1/012035> *Results of the CAL-*  
5667 *ICE SDHCAL technological prototype*. 16th International Conference on Calorimetry in  
5668 High Energy Physics (CALOR 2014). 2015.
- 5670 [248] W. Riegler et al. “Detector physics and simulation of resistive plate chambers”. In: *NIMA*  
5671 500 (2003), pp. 144–162.
- 5672 [249] I.B. Smirnov. *HEED++ simulation program*. 2010. URL: <http://ismirnov.web.cern.ch/ismirnov/heed>.
- 5674 [250] S.F. Biagi. “Monte Carlo simulation of electron drift and diffusion in counting gases under  
5675 the influence of electric and magnetic fields”. In: *NIMA* 421 (1999), pp. 234–240.
- 5676 [251] W. H. Furry. “On Fluctuation Phenomena in the Passage of High Energy Electrons through  
5677 Lead”. In: *Phys. Rev.* 52 (1937), pp. 569–581.
- 5678 [252] H. Genz. “Single electron detection in proportional gas counters”. In: *Nucl. Instr. and Meth.*  
5679 112 (1973), pp. 83–90.
- 5680 [253] M. Abbrescia et al. “Resistive plate chambers performances at cosmic rays fluxes”. In: *NIMA* 359 (1995), pp. 603–609.
- 5682 [254] M. Abbrescia et al. “Resistive plate chambers performances at low pressure”. In: *NIMA* 394  
5683 (1997), pp. 341–348.
- 5684 [255] M. Abbrescia. “Operation, performance and upgrade of the CMS Resistive Plate Chamber  
5685 system at LHC”. In: *NIMA* 732 (2013), pp. 195–198.
- 5686 [256] F. Thyssen. “Commissioning, Operation and Performance of the CMS Resistive Plate Cham-  
5687 ber System”. PhD thesis. Universiteit Gent, 2014.
- 5688 [257] M. Bianco. “ATLAS RPC certification and commissioning with cosmic rays”. PhD thesis.  
5689 Università del Salento, 2007.
- 5690 [258] M. Bianco. “ATLAS RPC certification with cosmic rays”. In: *NIMA* 602 (2009), pp. 700–  
5691 704.
- 5692 [259] M. Abbrescia et al. “Study of long-term performance of CMS RPC under irradiation at the  
5693 CERN GIF”. In: *NIMA* 533 (2004), pp. 102–106.
- 5694 [260] H.C. Kim et al. “Quantitative aging study with intense irradiation tests for the CMS forward  
5695 RPCs”. In: *NIMA* 602 (2009), pp. 771–774.
- 5696 [261] S. Agosteo et al. “A facility for the test of large-area muon chambers at high rates”. In: *NIMA*  
5697 452 (2000), pp. 94–104.
- 5698 [262] PoS, ed. *CERN GIF ++ : A new irradiation facility to test large-area particle detectors for*  
5699 *the high-luminosity LHC program*. Vol. TIPP2014. 2014, pp. 102–109.
- 5700 [263] D. Pfeiffer et al. “The radiation field in the Gamma Irradiation Facility GIF++ at CERN”.  
5701 In: *NIMA* 866 (2017), pp. 91–103.
- 5702 [264] CAEN. *Mod. V1190-VX1190 A/B, 128/64 Ch Multihit TDC*. 14th ed. 2016.
- 5703 [265] CAEN. *Mod. VI718 VME USB Bridge*. 9th ed. 2009.
- 5704 [266] A. Fagot. *GIF Cosmic Muon Monte Carlo Simulation*. 2017. URL: <https://github.com/a-fagot/Cosmics-Simulation>.
- 5705

- 5706 [267] G. Pugliese et al. “Long-term performance of double gap resistive plate chambers under  
5707 gamma irradiation”. In: *NIMA* 477 (2002), pp. 293–298.
- 5708 [268] G. Pugliese et al. “Aging study for resistive plate chambers of the CMS muon trigger detec-  
5709 tor”. In: *NIMA* 515 (2003), pp. 342–347.
- 5710 [269] M. Capeans et al. on behalf of the GIF and GIF++ User Communities. “A GIF++ Gamma  
5711 Irradiation Facility at the SPS H4 Beam Line”. CERN-SPSC-2009-029 / SPSC-P-339. 2009.
- 5712 [270] R. Guida et al. “Results about HF production and bakelite analysis for the CMS Resistive  
5713 Plate Chambers”. In: *NIMA* 594 (2008), pp. 140–147.
- 5714 [271] F. Bellini et al. “Study of HF production in BaBar Resistive Plate Chambers”. In: *NIMA* 594  
5715 (2008), pp. 33–38.
- 5716 [272] J. Eysermans. *WebDCS GIF++*. CERN. 2016. URL: <https://www.webdcs.cern.ch>.
- 5718 [273] A. Fagot and S. Carrillo. *GIF++ Offline Analysis v6*. 2017. URL: [https://github.com/afagot/GIF\\_OfflineAnalysis](https://github.com/afagot/GIF_OfflineAnalysis).
- 5720 [274] H. Reithler. *Filters for GIF++*. RWTH Aachen University, CMS-CERN. 2013. URL: <https://edms.cern.ch/document/1324028/1>.
- 5722 [275] R. Cardarelli et al. “RPC performance vs. front-end electronics”. In: *NIMA* 661 (2012),  
5723 S198–S200.
- 5724 [276] R. Cardarelli et al. “Performance of RPCs and diamond detectors using a new very fast low  
5725 noise preamplifier”. In: *JINST* 8 (2013), P01003.
- 5726 [277] J. de Urquijo et al. “Electron swarm coefficients in 1,1,1,2 tetrafluoroethane (R134a) and its  
5727 mixtures with Ar”. In: *The European Physical Journal D* 51 (2009), pp. 241–246.
- 5728 [278] A. Fagot. *GIF++ Data Acquisition Software for CMS RPC*. 2016. URL: [https://github.com/afagot/GIF\\_DAQ](https://github.com/afagot/GIF_DAQ).
- 5730 [279] W-Ie-Ne-R. *VME 6021-23 VXI*. 5th ed. 2016.
- 5731 [280] Wikipedia. *INI file*. 2017. URL: [https://en.wikipedia.org/wiki/INI\\_file](https://en.wikipedia.org/wiki/INI_file).